DEVELOPMENT AND ANALYSIS OF MICROSTRIP ANTENNAS FOR DUAL BAND MICROWAVE COMMUNICATION
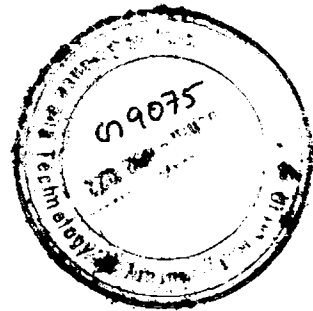
$G^a D \, 7 \, 5$

A thesis submitted by

BINU PAUL

in partial fulfilment of the requirements for the degree of

DOCTOR OF PHILOSOPHY

Under the guidance of

Prof.P.Mohanan

Centre for Research in ElectroMagnetics and Antennas
Department of Electroncis
Cochin University of Science and Technology
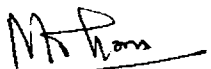Cochin - 682 022
INDIA

SEPTEMBER 2005

Dedicated

....to the Almighty
for everything.....

Certificate

Certified that this thesis entitled "**DEVELOPMENT AND ANALYSIS OF MICROSTRIP ANTENNAS FOR DUAL BAND MICROWAVE COMMUNICATION**" is a bona fide record of the research work carried out by Mrs. Binu Paul under my supervision in the Centre for Research in ElectroMagnetics and Antennas, Department of Electronics, Cochin University of Science and Technology. The results presented in this thesis or parts of it have not been presented for the award of any other degree.

Kochi - 682 022
25th September 2005

Dr.P.MOHANAN
(Supervising Teacher)
Professor
Department of Electronics
Cochin University of Science and Technology.

Declaration

I hereby declare that the work presented in this thesis entitled

"DEVELOPMENT AND ANALYSIS OF MICROSTRIP ANTENNAS FOR

DUAL BAND MICROWAVE COMMUNICATION" is based on the original

work done by me under the supervision of Prof. P. Mohanan, in the

Centre for Research in ElectroMagnetics and Antennas, Department of

Electronics, Cochin University of Science and Technology and that no

part there of has been presented for the award of any other degree.

Kochi - 682 022

25th September 2005

BINU PAUL

Acknowledgement

I remember with gratitude....

Contents

Chapter Five

NUMERICAL AND EXPERIMENTAL RESULTS...143

INTRODUCTION

Driving force behind any action is the need for it. The new and vibrant field of Microstrip antennas was initially driven by the quest for low cost conformal radiators to suit the miniaturization trend of the last decade of the century. The Wireless technology boom of the modern days has fuelled a new dimension to this field.

The chapter serves to highlight the historical developments that have led to the progress of this young antenna technology. The characteristics of a microstrip patch antenna are discussed briefly followed by an overview of the various analysis techniques that have kept pace with the technology itself. Thereafter the state of affairs that inspired the investigation presented in this thesis is stated. The chapter concludes with a description of the organization of the subsequent sections.

Wireless............*Since Hertz, J.C. Bose and Marconi.*

The term **Wireless** stood to describe the historic *Electric Wave* communication mechanism demonstrated by Heinrich Rudolph Hertz in 1886. This validated the elegant *Unified theory of electricity and magnetism* formulated by his teacher James Clerk Maxwell in the book *A treatise on Electricity and Magnetism* in the year 1873. Ten years later in February 1896, Guglielmo Marconi of Bologna, Italy demonstrated the increased signaling range (1.75 miles) achieved by Hertzian waves on using an *elevated aerial* and *earth connection*[1], initiating a commercial enterprise for wireless telegraphy. Drawing inspiration from the experiments of the great Indian scientist Jagadish Chandra Bose and other successors of Hertz, in 1901 Marconi performed the remarkable *Transatlantic Experiment*, transmitting the letter *S* (three dots in Morse code), over a distance of 700 nautical miles, thus constituting an epoch in scientific history[2]. The wavelength used was around 600 meters. Later in December 1924, Appleton and Barnett conducted a large scale experiment proving the existence of an ionosphere that reflects short waves. This achievement coupled with the availability of Vacuum tubes for commercial applications initiated an *era of radio broadcasting*. Karl Jansky's serendipitous discovery of extraterrestrial radio waves in 1932, opened a new window to the universe and he is regarded as father of *radio astronomy*. A century has passed since then and mankind has, at this point of time, embraced a *Wireless technology* to stay wire free yet *connected* to *everyone* and *everything*.

Over these years the connecting link between the Transmitter / Receiver and the outer world, underwent transformations from the simple wire and loop geometries employed by Hertz and his followers to the more recent ceramic chip configurations. They have evolved from simple *aerials* to the more complicated *Smart Antennas.*

1.1 Antennas

Antennas are an indispensable part of modern society, serving as the link between man and his environment extending to the outer space. They are virtually our electronic eyes and ears.

- **The definition**

The *IEEE Standard Definitions of Terms for Antennas* (IEEE Std 145-1983) defines the Antenna or aerial as, *a means for radiating and receiving radio waves*. From the circuit point of view, *antenna* is a load impedance connected to the transmission line, with the fictitious resistance R_r representing its Radiation resistance. In general, an *antenna* is a transition device or a transducer, between a guided wave and a free space wave. The radiation resistance may be thought of as a *virtual* resistance that does not exist physically, but is a quantity coupling the antenna to distant regions of space via *a virtual transmission line*.

- **The word**

Actually, the word *antenna* is derived from the classical Latin word *antemna* which became, in late Latin language, *antenna*. The word is uncertain etymology, but in Latin language it indicated the long pole made of wood, metal or other materials, which if placed vertically or transversally, had different uses. Later it also indicated the movable appendices of various forms and size, existing in the head portion of insects, serving as tactile and olfactory organs. The *aerial* usage in the early years of wireless communication came from the Latin word *aereum*, meaning *in the air*. The term antenna was used for the first time with the present meaning in the radio system, by Marconi in a lecture in 1909[3]. It is observed that, in Marconi's usage - *transmitting antenna* - the word was essentially a synonym for a high and thin pole meant to describe the arrangement of the system at the Poldhu

station, while a radiating structure parallel to ground was referred by him as *aerial*. The correct Latin plural is *antennae*, but English like plural *antennas* is the accepted terminology in present day technical literature.

- **The growth**

Antennas have been around for more than a century now, and seem to have an infinite variety, all operating on the same basic principles of electromagnetics[4]. From Marconi's inception and through the 1940's, antenna technology was primarily centered on wire related radiators. Later with advances in various fields of microwaves[5-6], antennas of various forms and shapes operating at different frequencies evolved. Since the late 1970's, much effort is devoted to the theoretical and experimental research on Microstrip and printed antennas. However, the alarming pace and relentless enthusiasm in embracing novel wireless communication services coupled with the demand for range extended Cellular, Wireless Local Area Network (LAN), Satellite, and Radio communication systems has led to an upsurge of interest in new approaches to antenna design for these applications.

- **The Design**

The design issues faced by an antenna engineer depend on the application being addressed, the mechanical and electrical characteristics, operating costs and environment. The mechanical parameters are size, weight, reliability, manufacturing process etc., while input impedance, operating frequency, gain, polarisation, radiation patterns, side lobe level etc. are the important electrical criteria. An aesthetically appealing design with all desirable operational characteristics is the ultimate challenge.

- **The Applications**

Antennas enjoy a wide range of applications - ranging from the classical telegraphy to the more established broadcasting to the fascinating radio astronomy. The personal communication and data communication application of antennas came upon mankind like a flash in 1990's, creating a

boom in the market, which is now literally flooded with mobile and fixed wireless devices of various types. Other potential applications include air, maritime and space navigation, search for extra terrestrial intelligence (SETI), military, medical, disaster warning and management. The more recent commercial applications include wireless gadgets ranging from simple pagers, cell phones, RF enabled toys, car locks, PC locks, GPS, Radio frequency identification (RFID) to bio chips. Active antennas, smart (intelligent or adaptive) antennas and reconfigurable antennas are just around the corner. The IEEE standard frequency allocation for various applications in the 0.3GHz-30GHz band is illustrated in table 1.1.

Band Designation	Frequency Range	Usage
VLF	3 – 30 KHz	Long- distance telegraphy, navigation
LF	30 - 300 KHz	Aeronautical navigation services, long distance communications, radio broadcasting
MF	300 – 3000 KHz	Regional broadcasting, AM radio
HF	3 – 30 MHz	Communications, broadcasting, surveillance, CB radio
VHF	30 – 300 MHz	Surveillance, T V broadcasting, FM radio
UHF	30 – 1000MHz	Cellular communications
L	1 – 2 GHz	Long range surveillance, remote sensing,
S	2 – 4 GHz	Weather, traffic control, tracking, hyperthermia, Microwave oven, W-LAN
C	4 – 8 GHz	Weather detection, long-range tracking
X	8 – 12 GHz	Satellite communications, missile guidance, mapping
Ku	12 – 18 GHz	Satellite communications, altimetry, high resolution mapping
K	18 – 27 GHz	Very high resolution mapping
Ka	27-40 GHz	Air port surveillance

Table 1.1 Frequency bands allocation for various applications

1.2 Microwave Communication

The birth of mobile radio is accepted to have occurred in 1897, when Marconi was credited with the patent for wireless telegraph [7]. Andre. G. Clavier directed the world's first successful demonstration of microwave radio transmission across the English Channel in 1931. Since then wireless communication has recorded a tremendous growth over the century. Fuelled

by the digital switching, improvements in RF circuit fabrication, enhanced capabilities to process and store multi channel voice, video and data signals and development of newer antenna modules, industry has grown many fold.

1.2.1 Glancing backwards

The milestones in the evolution of this ever-growing business [8-12] are listed in table 1.2.

1887	Electromagnetic wave propagation by Hertz
1894	Wireless telegraph by Marconi
1895	5-6mm wavelength signal transmission by J.C. Bose
1901	Transatlantic communication of S in Morse code by Marconi
1906	Radio broadcasting by Fessenden
1914	170KHz radio by the AT&T company
1921	Radio dispatch service initiated for police cars in Detroit, Michigan
1925	Ionosphere layer confirmed by Appleton, Short wave radio by Van Boetzelean
1929	*Microwave Communication* established by Andre G. Clavier
1931	600MHz radio link in Italy by Marconi, Microwave radio transmission across English channel by Clavier.
1932	50 cm Radio telephone and Teleprinter by Marconi
1933	Frequency Modulation techniques by Armstrong
1934	AM (Amplitude modulation) mobile communications systems used by hundreds of state and municipal forces in the U.S.
1935	RADAR by Watson Watt, Radio astronomy by Janskey
1943	Digitally modulated Microwave Radio by AT &T
1946	Radiotelephone connections made to PSTN (public-switched telephone network),3.7-4.2 LOS link by AT &T
1968	Development of the cellular telephony concept at Bell Laboratories
1980s	1G - First Generation – only mobile voice service – analog technology Ericsson Corporation's NMT (Nordic Mobile Telephone – 450, 900 MHz) in Scandinavian countries becomes the first cellular system. Cellular service in the US – AMPS (Advanced Mobile Phone System - 850 MHz) using FM (frequency modulation) placed in service in Chicago by Ameritech Corporation. TACS (Total Access System- 900 MHz band) introduced in Europe & China

Table 1.2 Milestones in the evolution of Microwaves and its applications

The 1990's saw the advent of Digital technology into the communication arena creating an enormous impact on personal communication services.

1.2.2 Modern wireless communication systems and antennas

The 1G analog systems of the 80's evolved into the 2G digital technology in the 90's and to the third generation of mobile communication which includes the wireless multimedia services also, as listed in table 1.3.

	1G	2G	2.5G	3G
Year	1985	1992	1995	2002
Technology	Analog	Digital	Packet switching	Intelligent signal processing
System	AMPS, TACS, NMT	DAMPS, GSM900, IS-95 CDMA	GPRS, I-Mode, EDGE	Wideband CDMA, CDMA2000, TD-CDMA
Access Technique	FDMA	FDMA,TDMA,CDMA		CDMA
Frequency (MHz)	400-900	900,1800,1900		1800-2200
Cellular range	Large	Medium		Small
Service	Voice alone	Voice, low rate data (SMS)	Higher data rate	Voice, data, video, multimedia. Single phone connected with various PSTN systems and to high data rate packet systems, World wide roaming

Table 1.3 Modern wireless communication systems

Table 1.4 shows the frequency bands allotted for modern wireless communication services along with the typically employed category of antennas[8]. Other functional land based services include, Paging (931-932MHz), Automatic Toll collection (905MHz and 5-6GHz), DBS (Direct Broadcast Satellite Systems-11.7-12.5GHz) for digital video and fast internet access, Broad band networks at 24/28/38GHz for video and internet. Fixed Wireless (FW) systems using a part of spectrum between 1GHz to 40GHz are attractive by virtue of its high bandwidth and better signal quality. The 4G or *Generation next* focuses on the broad band wireless mobile communications, which converges wireless access, wireless mobile, wireless

LAN and packet division multiplexed networks to provide value added services.

Service	Frequency band	Antenna
Cellular- US	Rx:824-849MHz Tx:869-894MHz	Base station: Dipole or patch array Handset: Monopole, sleeve dipole, Folded F or patch
GSM-900 European *Global System for Mobile communications*	Rx:925-960MHz Tx:880-915MHz	
DCS:1800-*Digital Communication System*	Rx:1805-1880MHz Tx:1710-1785MHz	
PCS:1900-*Personal Communication System*	1850-1990MHz	
UMTS 2000-*Universal Mobile Telecommunication Systems*	1920-2170MHz	
3G IMT-2000 *International Mobile Telecommunications*	IMT 2000 Core band: Rx:1885-2025MHz Tx:2110-2200MHz IMT 2000 Extension bands: 698-806 MHz, 2500-2690 MHz and 2700-2900 MHz to be available from 2005 onwards.	
W-LAN ISM-2.4 (Bluetooth™) ISM-5.2 ISM-5.8 *Industrial, Scientific, Medical*	2400-2485MHz 5150-5350MHz 5725-5850MHz	
RFID-*Radio Frequency Identification systems*	30 MHz to 2.4GHz	Loops, Folded-F, patch or monopole
GPS-*Global Positioning Systems*	1565-1585 MHz & 1227-1575 MHz	GPS Rx: Microstrip patch, bifilar helix

Table 1.4 Overview of modern wireless communication services and their antennas

1.3 Microstrip antennas

The rapid progress in wireless communications promises to make interactive voice, data and video services available anytime, anywhere. As the demand for electronic mobility grows, the need for smaller, multi-band handsets increases. Wireless communications systems come in a variety of

sizes ranging from small hand held devices to those mounted on vehicles. For optimum system performance, the antennas used must also have high radiation efficiency, small volume, desirable radiation characteristics, low loss impedance and ease of mass production.

The linear antenna (Whip antenna) and helical antenna, belonging to the class of external antennas have been the dominant radiating elements in wireless gadgets until recently. But, these antennas have remained relatively large compared to the handset itself. Thus, the handset requirements for small size, light weight, thin profile and low cost, yield internal printed antennas as suitable candidates.

Planar structures consisting of one or several dielectric layers, suitably printed with metallic traces on surfaces, were the printed geometries of the early years. These strip lines, Microstrip lines, slot lines and fin lines were primarily meant to function as transmission lines.

Microstrip geometries which radiate electromagnetic waves were originally conceived by Deschamps in the 1950's. But the idea remained as one whose *time came* only in the 70's for the want of low loss substrates with attractive properties and improved photolithographic techniques. The first practical antennas were developed by Howell and Munson [13-16]. Within three decades *Microstrip Antennas* evolved as a vibrant area.

1.3.1 The Geometry

A microstrip patch antenna in its simplest configuration consists of a radiating patch on one side of a dielectric substrate, which has a ground plane on the other side, as depicted in figure 1.1. The patch conductors, normally of copper or gold, can assume virtually any shape though rectangular and circular geometries are common. The advantages of microstrip patch antennas are:

> ➤ Light weight, low volume, thin profile configuration which easily conforms to the surface of the product or vehicle.

> ➤ Low cost, easy amenability to mass production, easy integration with MMIC's.

> ➤ Capability to produce linear and circular polarization with Broad side radiation patterns.

However the demerits include,

- Narrow bandwidth, low gain and large ohmic loss especially in feed.

- Complex feeding networks required for high performance arrays and spurious feed radiations.

- Low power handling capability and poor end fire radiation.

Various techniques are available to minimize these limitations and to achieve enhanced performance.
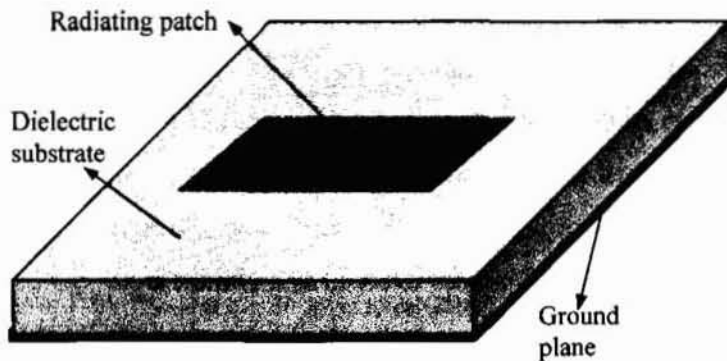
Figure 1.1 The Basic microstrip antenna geometry.

1.3.2   Radiation Mechanism

The radiation from the microstrip patch antenna (MPA) can be attributed to the fringing fields between the edges of the patch conductor and the ground plane. Figure 1.2 illustrates the fringing fields of the Quasi TEM mode that propagate in the microstrip structure.

Figure 1.2. Fringing fields in the microstrip structure

For a rectangular MPA fabricated on an electrically thin substrate (thickness, $h \ll \lambda/\sqrt{\varepsilon_r}$), and excited in the fundamental mode, the field is nearly constant along the thickness. The patch resonates along its Length, $L(L \sim \lambda_g)$ and radiates from slots or aperture of Width, W as shown in figure 1.3.a.
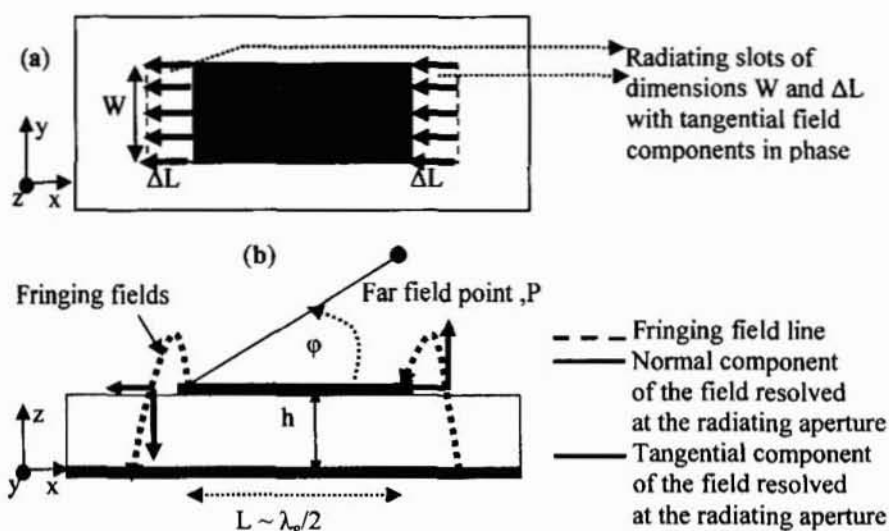
Figure 1.3 Rectangular MPA illustrating the fringing field and its resolved components
(a) Top view (b) Side view

The fields vary along the patch length, which is *about* half a wavelength ($\lambda_g/2$). The non-resonant edges of the patch are open circuits for the half wave resonance. Radiation is mainly due to the fringing fields at these open circuited edges of the patch. The electric fields at the edges can be resolved into normal (+z) and tangential (-x) components with respect to the ground plane as shown in figure 1.3.b. The patch is $\sim\lambda_g/2$ long, so that the normal components at the edges are out of phase while the tangential components are in phase. Unlike the dipole where the sinusoidal distribution

exists along the resonant length, the tangential fields at these open circuited edges are nearly constant in amplitude and phase, with resonance in the orthogonal dimension. With reference to figure 1.3.b, the normalized far field can be expressed as

$$E = \cos\left(\frac{\pi L}{\lambda_0}\cos\phi\right)$$ (1.1)

where λ_0 is the free space wavelength. For the rectangular MPA with L nearly equal to half wavelength in the dielectric (λ_g)we get

$$E_\phi = \cos\left(\frac{\pi}{2\sqrt{\varepsilon_r}}\cos\phi\right)$$ (1.2)

for $0<\phi<180°$. Edge radiations from the end of the ground plane usually reduce the radiation by 6dB at $\phi=0°$ and 180°.

1.3.3   Excitation techniques

There are various configurations that can be used to feed the microstrip antenna as shown in figure 1.4. Selection of an appropriate feed is as crucial as selection of the antenna itself. Table 1.5 illustrates the characteristics of different excitation mechanisms for microstrip antennas. Early microstrip antennas used either the coaxial probe feed or the edge fed microstrip line feed (contacting type)[16], which offers one degree of freedom for a fixed patch size and substrate. In coaxial feed excitation, inner conductor of the connector is directly connected to the patch surface while the outer conductor is grounded. Microstrip feed has the advantage of the feed lying in the same plane as the radiating patch, which facilitates easy integration with RF circuit boards but, creates spurious feed radiation. Both coaxial and microstrip feed line possess inherent asymmetries which generate higher order modes resulting in an increased cross-polarized radiation. Non-contacting feeding techniques are of importance in this context. Aperture coupling techniques are best suited when band width is of

primary concern.
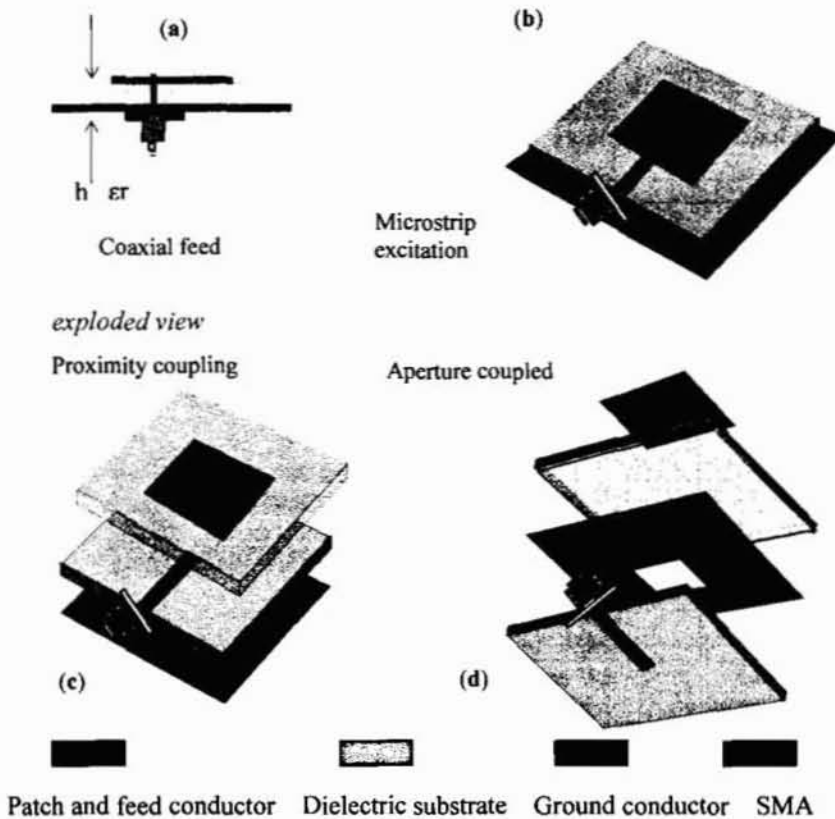
Figure 1.4 Various feed layout configurations

The Proximity coupling (electromagnetic coupling) method offers reduced feed interference to radiation and eliminates the soldering on the patch surface. Over the years several feed designs and feed modifications have been proposed by researchers with the intention to improve the impedance matching and overall antenna performance.

• Proximity coupling (Electromagnetic coupling)

This non contacting non co-planar microstrip feeding method uses a two layer configuration with microstrip feed line on the bottom layer with the radiating patch etched on the top layer. The feed line terminates in an open end underneath the patch, which is thus capacitively coupled to the source of excitation.

Characteristics	Coaxial probe excitation	Microstrip excitation (edge coupled)	Proximity coupling	Aperture coupling
Type of feed	Non planar, Contact type	Co planar Contact & non contact types	Planar Non contact type	Planar Non contact type
Spurious feed radiation	Moderate	More	Less	Less
Polarization Purity	Poor	Good for radiating edge coupling, Poor for non radiating edge coupling	Poor	Excellent
Fabrication	Drilling and soldering involved	Easy	Easy, proper alignment needed	Easy, proper alignment needed
Reliability	Poor	Better	Good	Good
Impedance matching	Easy	Poor	Very Easy	Easy
Maximum Bandwidth achieved	2-5%	9-12% for radiating edge coupling, 2-5% for non radiating edge coupling	Up to 13%[16]	~30%
Nature of the feed	Series Inductance	LC network(T shaped) with C in shunt	Series capacitance	Series inductance
Equivalent model	cylindrical band of electric current flowing on the center conductor from bottom to top along with an annular ribbon of magnetic current in the ground plane	step in width / impedance junction	capacitance in series with RLC representing the patch	Patch antenna is in series with the slot inductance

Table 1.5. Various excitation methods used for microstrip antennas.

The complete antenna configuration is thus a double layered substrate with the microstrip patch and the microstrip feed line sharing a common ground plane. The arrangement also offers an additional degree of freedom in selecting the substrates and allows independent feed optimization. The double layer arrangement can be exploited to achieve increased band width. By using a thin, high ε_r substrate for the feed, the fringing field along the length of feed line can be reduced (due to closeness of ground and feed line edges) ensuring that coupling to patch is only from the open end of the

feed line. The open end of the feed line can be terminated in a stub and the stub parameters can be used to improve the band width performance. The patch layer substrate is usually thick, and of low dielectric permittivity to enhance fringing and subsequent radiation.

Patch and feed conductor
Dielectric substrate
Ground Conductor
SMA connector
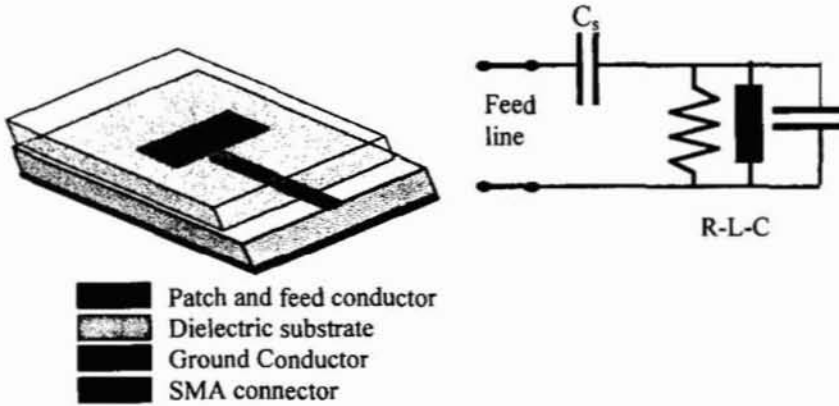
Figure 1.5 Proximity coupling method and its equivalent circuit.

The equivalent circuit for this coupling is illustrated in figure 1.5, with a capacitor C_s in series with the parallel resonant RLC circuit modeling the patch[15]. Impedance matching can be achieved by altering the patch feed overlap, length of feed line and the patch width to line width ratio [14,17]. The fundamental narrow band width limitation of MPA set by its low electrical volume is overcome here and the method can offer a bandwidth[18]. Proximity coupling type of excitation is employed in the study presented in this thesis.

1.3.4 Substrate materials

Selecting an appropriate dielectric substrate is an important design aspect. The substrate thus plays a double role: electrically, it is an integral part of the feed and antennas; mechanically, it is the support of the structure. The electrical properties include the substrate thickness, h and relative permittivity, ε_r. Uniformity and homogeneity of the substrate is of great importance. Furthermore, the parameters should remain constant for different

material batches to ensure circuit reproducibility. The change in operating frequency f, of a thin substrate microstrip antenna due solely to a small tolerance change in ε_r is given as, $\dfrac{\partial f}{f} = -\dfrac{1}{2}\dfrac{\partial \varepsilon_r}{\varepsilon_r}$, where $\varepsilon_r = \varepsilon_r' - j\varepsilon_r''$. The imaginary part of ε_r accounts for the dielectric losses represented by the loss tangent, $\tan\delta = \dfrac{\varepsilon_r''}{\varepsilon_r'}$. The dielectric losses of the substrate must be as small as possible in order to ensure an overall efficiency (typically $\tan\delta < 0.002$ is desirable). The relative frequency change due to temperature change can be expressed as $\dfrac{\partial f}{f} = -\dfrac{\partial L}{L} = -\alpha_T \partial T$ where α_T is the thermal expansion coefficient and L is the frequency determining dimension.

Physically, the substrate must have a large mechanical resistance, good shape stability and an expansion factor close to that of the metal used for the conductors. It must withstand high temperatures during soldering and present a smooth and flat surface (certain substrates tend to camber after etching). In addition, it is extremely important that there is a good adhesion between the conductor strips and the substrate that it is capable of withstanding etching and curing processes without peeling. An important factor, especially for antenna realization, is the availability of substrate in large dimensions at low cost. There is no ideal and universal substrate, but now the choice of materials is relatively broad.

• **Types of materials**

Dielectric substrate materials include ceramic, semiconductor, ferromagnetic, synthetic, composite and foams. Ceramic materials (e.g. Alumina Al_2O_3) have low loss but are hard and anisotropic. At mm wavelengths, metallic strips deposited on semiconductors (Si or GaAs) can serve as the substrate. YIG (Yttrium-Iron-Garnet) substrates whose ε_r depends on a magnetic field bias serves as a magnetically tunable substrate.

Pure synthetic materials have low and constant permittivity and low losses but the mechanical properties are less satisfactory, as most materials are rather soft and unstable with temperature and exhibits poor adhesiveness to metals. The commonly used synthetic material is PTFE or Teflon (Polytetrafluoroethylene, ε_r =2.18, tanδ =0.0003 at 10GHz). It is inexpensive, but has a low melting point (165°C), which therefore requires special soldering. By adding fibreglass (woven or random) or ceramic fillers to synthetic materials, the mechanical properties are modified and the permittivity is adjusted. They offer relative permittivity in the range from 1.03 to more than 10 and tanδ from around 0.001 to 0.002. Their mechanical properties allow easy machining, and can be etched by the standard printed circuit techniques. The woven type composites are not bendable and hence unsuited for conformal antennas. Foams consist of a lattice net enclosing air pockets with which very low dielectric constants needed for radiating elements is achieved.

- **Metallization**

The metal layers deposited on the substrate must have a very low resistivity, sufficient thickness (at least three times the skin depth, usually of the order of 10-35 microns), good solderability and good adhesion to the substrate. They must be resistant to oxidation during soldering and suit different contacting and bonding techniques. These requirements limit the choice of the metal to copper, gold, silver and aluminium. On ceramic substrates, an intermediate layer of chromium, tantalum or titanium must be added to ensure the adhesion of the metal (copper) to the substrate. This complicates the etching process, since additional etching steps and chemical baths are required.

1.3.5 Microstrip antenna configurations

Microstrip antennas can be broadly classified into four major categories namely Microstrip patch antennas, Microstrip slot antennas,

Microstrip traveling wave antennas and Printed dipole antennas whose characteristics are summarized in table 1.6.

Characte-ristics	Microstrip Patch Antennas (MPA)	Microstrip slot antennas	Microstrip traveling-wave antennas(MTA)	Microstrip Dipole antenna
Geometry	Conducting patch on one side of the substrate backed by ground plane on the other side	A flipped microstrip line configuration with an orthogonally placed aperture cut in the ground conductor serving as the radiating slot	Chain shaped periodic conductors or an ordinary TEM line on one side of the substrate backed by ground plane. The open end is terminated in matched load	Differs from MPA in their Length to width ratio. Width is typically less than $0.05\lambda_0$
Profile	Thin	Thin	Planar	Thin and small
Fabrication	Very easy	Easy	Easy	Easy
Dual Frequency	Possible	Possible	Possible	Possible
Polarisation	Linear and Circular	Linear and Circular	Elliptical	Linear
Resonance frequency	Depends on the resonant length $(L\sim \lambda_g/2)$ and Width W to some extend	Depends on the slot dimensions	Determined by the basic element and the relative spacing	Depends mainly on the strip length $(L\sim 0.317 \lambda_0)$ and is kept insensitive to the width of dipole
Band-width	Usually narrow	Generally wide 5-30%	Generally wide	~30%
Spurious Radiation	Exists -Moderate	Exists but low	Exists	Exists
Radiation patterns	Broad side Low cross–polar level	Bidirectional radiation Very low cross–polar level (<-35dB)	Main beam can be designed to be in any direction from broad side to end fire	Similar to RMPA for strip dipoles with poor cross polarization levels
Shape flexibility	Any shape	Only limited geometries are investigated till date	Limited	Usually rectangular and triangular
Types of antenna in use	Patch can have any shape:-Square,rectangle, triangle, circle, ellipse, ring, eccentric ring, U-shape, T-shape, E-shape etc	Slot can be of any shape like are circle, square,rectangle, annular,tapered etc.CPW fed slot antennas are the new entrants	Chain antenna, Rampart line antenna, Square loop antenna, Crank type antenna	Centre fed printed dipoles, bow tie dipoles, symmetrically folded dipoles

Lay out of antennas			
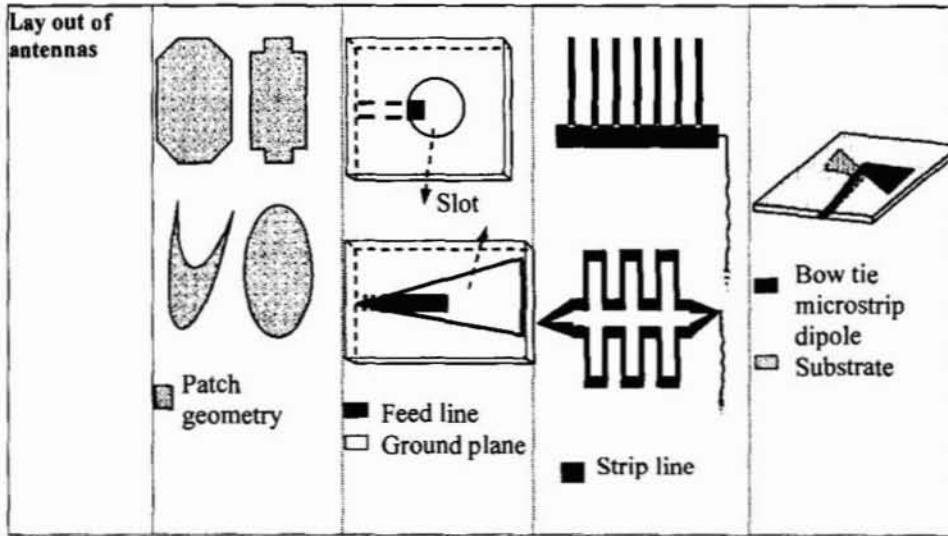
Table 1.6 Various microstrip antenna configurations

1.3.6 Standard Rectangular and Circular patches

The rectangular and circular patches are the basic and most commonly used microstrip patch antennas. A rectangular patch is characterized by length L and width W. The resonant frequency f, for TM $_{mn}$ is

$$f_{mn} = \frac{k_{mn}c}{2\pi\sqrt{\varepsilon_{eff}}} \tag{1.3}$$

where $k_{mn}{}^2 = \left(\frac{m\pi}{L}\right)^2 + \left(\frac{n\pi}{W}\right)^2$ and m,n=0,1,2...etc

To include the effect of fringing field at patch edges, effective dielectric constants are calculated for length and width separately [eqn.4.30 [16]] as,

$$\varepsilon_{eff}(W) = \frac{\varepsilon_r + 1}{2} + \frac{\varepsilon_r - 1}{2} F\left(\frac{W}{h}\right) \tag{1.4}$$

where F is given as

$$F\left(\frac{W}{h}\right) = \left(1 + 12\frac{h}{W}\right)^{-0.5} + 0.04\left(1 - \frac{W}{h}\right)^2 \qquad \text{for } \left(\frac{W}{h}\right) \le 1$$

$$= \left(1 + 12\frac{h}{W}\right)^{-0.5} \qquad \text{for } \left(\frac{W}{h}\right) \ge 1$$
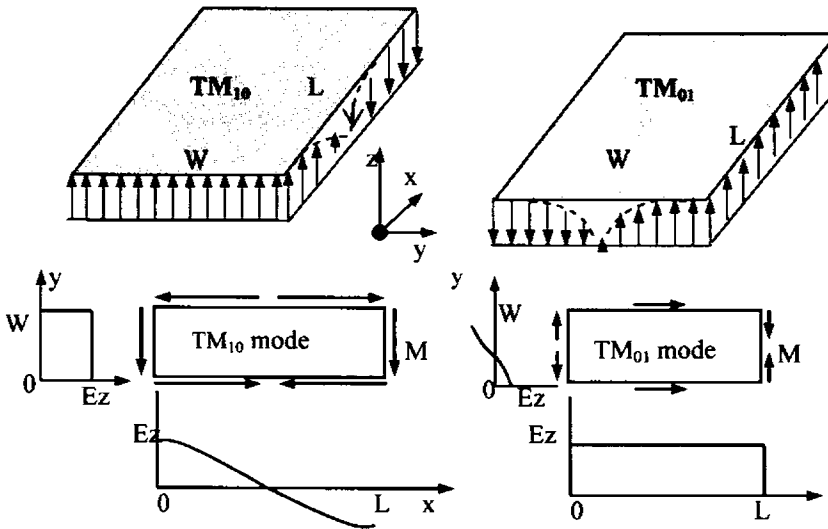
Figure 1.6 Electric Field and magnetic surface current distributions
along the periphery of a RMPA

The electric field and magnetic surface current distributions on the sidewall for TM_{10}, and TM_{01}, are illustrated in figure 1.6. For TM_{10} mode, W is the radiating edge, the magnetic currents are constant and in phase along W and out of phase along L. For TM_{01} mode, L is the radiating edge, along which the magnetic currents are constant and in phase. These fundamental modes have broadside radiation patterns and are orthogonal. TM_{10} and TM_{01} modes can be utilized to operate the rectangular patch as a dual frequency antenna also. The higher order modes have maxima off broadside. Both E plane and H plane radiation patterns are broad with field approaching zero in the end fire direction.

The geometry of the circular patch antenna (CPA) is characterized by its radius r. It is the simplest MPA geometry since all other shapes require more than one parameter to describe them. The mathematical analysis of CPA involves Bessel functions. The electric field of the resonant TM_{nm} mode in the cylindrical cavity under the circular patch is given in cylindrical co-ordinates (ρ, ϕ, z) as,

$$E_z = E_0 J_n \left(k_{nm} \rho \right) Cos \left(n\phi \right) \qquad (1.5)$$

where, J_n is the Bessel function of the first kind of order n and $k_{nm} = \dfrac{X_{nm}}{r}$

with X_{nm} being the roots of $J_n{}'(r) = 0$ and r is the radius of the CPA. The resonant frequency of the TM_{nm} mode is given by [equation 5.21[16]]

$$f_{nm} = \frac{X_{nm}c}{2\pi r\sqrt{\varepsilon_{eff}}}$$ (1.6)

based on the assumption of a perfect magnetic wall along the periphery($\rho = r$). The effect of fringing field is accounted for, by taking the effective radius of the circular patch as [16]

$$r_{eff} = r\left[1 + \frac{2h}{\pi r\varepsilon_r}\left(\ln\frac{\pi r}{2h} + 1.7726\right)\right]^{1/2}$$ (1.7)

1.3.7 Analysis of antennas

Antenna analysis provides an understanding of the operating principles that could help the design and its enhancement. The objective of the analysis is to predict the antenna characteristics both in the near field and in the far field, lending itself to the interpretation of the physical phenomena. The process is complicated by the presence of infinite radiation space, inevitable dielectric inhomogeneity, inhomogeneous boundary conditions, feed variations and above all the nature of geometry.

Problem description
(geometrical / electrical parameters)

Excitation models → Field Solver / Field Propagator derived from Maxwell's Equations with proper boundary conditions → EM Fields → Parameter Extraction → Output parameters
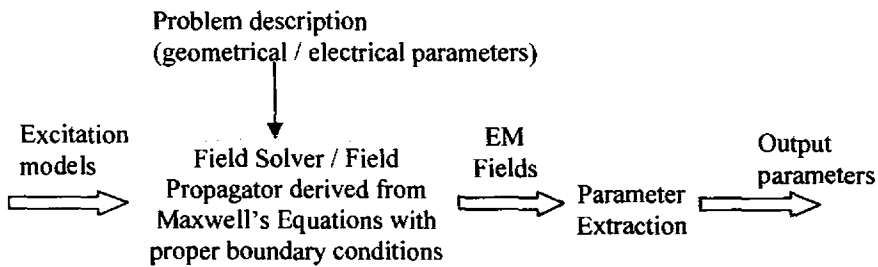
Figure 1.7 Modelling an Electromagnetic problem.

A compromise between these aspects and solution accuracy is a matter of choice. Many techniques are available in literature to choose from,

based on accuracy, simplicity and cost of analysis. The main steps involved are to describe the target geometry, electrical parameters and excitation used in the structure. As illustrated in figure 1.7, this is followed by computation of EM field in the target by solving Maxwell's equations and finally extraction of the parameters of interest.

• 1.3.7.i   Analytical methods

Analytical models were the first to be developed for microstrip antennas. Based on *simplified* assumptions they offer simple approaches well suited for understanding the physical phenomena and for computer aided design of antennas. These include the transmission line model, cavity model and multi port network models. The major draw back of the approach lies in the fact that the field along the width and substrate thickness is assumed to be uniform. Hence the method fails for thicker substrates, multi layer designs and for designs involving co planar parasitic layers.

The model categorizes the antenna space into an interior region – *consisting of the portion between the patch and ground plane with walls formed by the projection of the patch periphery onto the ground plane- and an exterior region -comprising the remainder of ground plane, substrate and region above the patch surface.* The interior is then represented as an equivalent *transmission line* or as a *cavity with effective loss tangent* and dimensions accounting for losses from the interior. The fields in the exterior comprising of radiation fields and fringing fields are described in terms of *slots / apertures of infinite width* in the interface plane.

In the transmission line model, fringing field in the radiating edge is incorporated in the edge susceptance term, and the model is not suited for non rectangular geometries. The slot width is equal to substrate thickness and slot length slightly greater than the physical length of the edge and the slots are assumed to be *on the ground plane.* Cavity model by Lo *et.al*[19] that treat the patch as *a lossy cavity,* takes care of the field variation along the non

resonant edge of the patch. The cavity is assumed to be bounded by electric walls on the top and bottom and magnetic walls on the sides. The approach is accurate only for simple geometries, since the eigen functions needed for the computation are available only for standard geometries. The electric field under the patch metallization is obtained using functions appropriate for the geometry (eqn. 2.27, [16]). For irregular geometries the patch is split into a number of regular shapes. Multiport Network Model (MNM) is an extension of the cavity model. Although the accuracy of these approximate models is limited, they can provide good initial estimates of the performance characteristics of the design and are helpful in predicting the change in these characteristics with design parameter fluctuations [20].

• 1.3.7.ii   Full wave methods

Full wave method for the analysis of an antenna, solves Maxwell's equations subject to boundary conditions at the interface. These are suitable for analyzing multilayer multipatch microstrip antennas. Accuracy, completeness and versatility are the key characteristics of these methods. They maintain rigour and accuracy at the expense of numerical simplicity and computational cost. They can handle a wide variety of antennas structures and various types of feeds. Typical full wave methods are MoM based on Integral Equations (IE), Finite element method (FEM), Finite Difference Time Domain (FDTD) method and Transmission Line Matrix (TLM) method.

• MoM based on Integral Equations (IE)

The Integral Equation (IE) method casts the solution to the antenna problem in *the form of an integral*, where the unknown is part of the integrand also. The substrate and ground plane are assumed to be infinite in lateral dimensions and the formulation of the problem is based on rigorously enforcing the boundary conditions at the air dielectric interface. Analysis carried out in spatial domain uses Sommerfield type of integral equations

whereas the spectral domain approach uses exact Green's functions, for the composite dielectric [16], in their formulations. In the Electric field Integral Equation (EFIE), boundary condition is applied to the total tangential Electric field whereas in Magnetic field Integral Equation (MFIE) boundary is expressed in terms of Magnetic fields. Mixed Potential Integral Equation (MPIE) has both scalar and vector potentials in its formulation. The integral equation is then solved using appropriate methods: either in spectral domain itself or in the space domain by taking appropriate transforms [21].

To solve IE it is *discretised* into a set of linear equations by means of the *Method of Moments* (MoM). The roots of the complex determinant of this moment matrix gives the resonant frequency, while solving the matrix yields the current distribution on the patch conductor which is then used to compute radiation pattern, polarization, directivity etc. MoM depends on expanding the unknown quantity in the equation in terms of *known basis functions* (entire domain basis functions or sub-domain basis functions) *with unknown coefficients*. The entire domain basis functions for regular geometries are obtained usually from the magnetic wall cavity eigen functions. Sub domain basis functions (valid over a *cell*) are used when arbitrary current distributions are involved, with at least 10 basis functions per wavelength. The popularly used basis functions for current include pulse basis, piecewise sinusoidal basis and roof top basis functions. The matrix evaluation involves space domain integrations (finite as well as infinite) which accounts for the mathematical complexity of the method. An improper choice of the basis functions can result in ill-conditioned matrix equations whose solution may pose convergence problems especially while handling thick substrates and finite ground plane problems. The set of basis functions should have the ability to accurately represent and resemble the anticipated unknown function, while minimizing the computational effort required [22].

• Finite Element Method (FEM)

The Finite element method is suitable for the solution of a wide class of partial differential or integral equations in almost all arbitrary geometries. FEM uses a volumetric approach which requires the entire volume of the configuration to be meshed as opposed to surface integral techniques, which require only the surfaces to be meshed. Each mesh element has completely different properties from those of neighbouring elements. In general, finite element techniques excel at modelling fine structural features in complex inhomogeneous configurations. However unbounded radiation problems are not handled as effectively as MoM. It uses both tetrahedral and prismatic elements to mesh the structure.
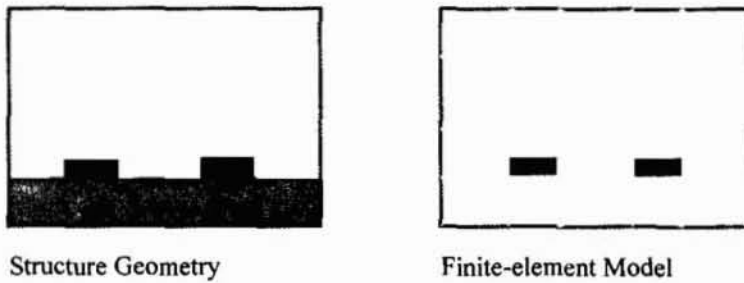
Structure Geometry   Finite-element Model
Figure 1.8 Finite Element Model

The first step in FEM analysis is to divide the configuration into a number of small homogeneous *elements* as shown in figure.1.8. The model contains information about the device geometry, excitations, material and boundary constraints. The elements are small, where fine details exist and large elsewhere. In each finite *element*, a simple (often linear) variation of the field quantity is assumed.

The corners of the *elements* are called *nodes*. The goal of the finite-element analysis is to determine the field quantities at the *nodes*. Generally, FEM solve for the unknown field quantities by *minimising a quadratic energy functional*[22]. For three-dimensional time-harmonic problems this functional may be represented as,

---

$$F = \int_v \frac{\mu \left|H^2\right|}{2} + \frac{\varepsilon \left|E\right|^2}{2} - \frac{J.E}{2j\omega} dv$$

(1.8)

where the first two terms represent the energy stored in the magnetic and electric fields, and the third term is the energy dissipated by the conduction current. Expressing H in terms of E and setting the derivative of this functional with respect to E equal to zero, an equation of the form $f(J,E) = 0$ is obtained. A kth order approximation of the function f is then applied at each node and boundary conditions enforced, resulting in the system of equations of the form,

$$[J] = [y][E]$$

(1.9)

The elements of J are referred to as the source terms, representing the known excitations. The elements of the Y-matrix are functions of the problem geometry and boundary constraints. The elements of the E-matrix represent the unknown electric field at each node, obtained by solving the system of equations. In order to obtain a unique solution, it is necessary to constrain the values of the field at all boundary nodes (e.g the metal box of the model in figure.1.8 constrains the tangential electric field at all boundary nodes to be zero). Therefore, a major weakness of FEM is that it is relatively difficult to model open configurations. However, in finite element methods, the electrical and geometric properties of each *element* can be defined independently. This permits the problem to be set up with a large number of small *elements* in regions of complex geometry and fewer but large elements in relatively open regions. Thus it is possible to model configurations that have complicated geometries and many arbitrarily shaped dielectric regions in a relatively efficient manner.

- **Transmission Line Matrix (TLM) method**

The transmission line matrix method was originally developed by Johns and Beurle. It replaces the structure by a mesh, either 2D or 3D. The nodes of the grid are interconnected by virtual transmission lines. Excitations

at the source nodes propagate to adjacent nodes through those transmission lines at each time step. Generally, dielectric loading is accomplished by loading nodes with reactive stubs, whose characteristic impedance is appropriate for the amount of loading desired. Lossy media can be modelled by introducing loss into the transmission line equations or by loading the nodes with lossy stubs. Absorbing boundaries are constructed in TLM meshes by terminating each boundary node transmission line with its characteristic impedance. Analysis is performed in the time domain. Complex, nonlinear materials are readily modelled, impulse responses and time-domain behaviour of the systems are determined explicitly, and the technique is suitable for implementation on massively parallel machines. But, voluminous problems using fine grids require excessive amounts of computation. TLM method shares the advantages and disadvantages of the FDTD method.

• Finite Difference Time Domain (FDTD)

This very powerful electromagnetic tool is capable of addressing complex antenna structures by providing a direct solution to Maxwell's equations in differential form. The FDTD formulation proposed by Yee [23] makes it highly suitable for implementation on computers. The method was further refined and *reinvented* by Taflove, in 1970's[24-25]. Simple antenna structures were first modeled using FDTD method by Reinex *et al.* [26] in 1989. Since then many improvements have been made and today it is a well established field of *Computational Electromagnetics*. As the method is time domain based, it can reveal antenna characteristics over a wide frequency range with a single run. The matrix free nature and the absence of integrals in the formulation enable the method to handle as many as 10^6 unknowns with reasonably good accuracy. The concepts and implementation details of the FDTD method used in the present investigation is discussed in chapter four.

Both TLM and FDTD techniques are very powerful and widely used. For many types of EM problems, they represent the only practical methods of analysis. Though the TLM method requires significantly more computer memory per node, it generally does a better job of modelling complex boundary geometries. On the other hand, the FDTD method is attractive because of its simple, direct approach to the solution of Maxwell's equations. Deciding whether to employ a TLM or FDTD for numerical investigation is largely a personal decision.

1.3.8   Computational Electromagnetics (CEM)

Over the years there has been a tremendous increase in the degree of sophistication in the numerical methods available for analyzing antennas. Availability of powerful computers has revolutionized the way in which electromagnetic problems are presently analysed by antenna engineers. Analytical methods can be easily incorporated in CAD based design approaches. These techniques can be a useful tool when the important EM interactions of the configuration can be anticipated.

Expert systems approach a problem in much the same way as a quick-thinking, experienced EM engineer with a calculator would. They do not actually calculate the fields directly, but instead estimate values of the parameters of interest based on a rules database. As system design procedures become more automated, expert system EM software will certainly play an important role. Nevertheless, expert systems are no better than their rules database and they are seldom used to model the complex EM interactions.

While implementing the full wave models, it is essential to ensure numerical stability and minimize numerical dispersions. The Modeling of excitation, problem space and its truncation becomes as crucial as problem itself. The power of CEM is the fact that simplifying approximations are not used for performing the differentiation and/or integration that appear in the

formulation of the problem. But the numerical techniques used for implementing these mathematical operations pose the major computational overhead. The memory requirement is determined by the variable space and the size of geometry. The method used by a particular EM analysis program plays a significant role in determining the nature of problems it can handle and accuracy of results so obtained. Electromagnetic compatibility (EMC), Antenna analysis and synthesis, Radar cross section (RCS) studies, Electromagnetic interference (EMI), Cellular phone-human body interaction, Microwave ovens, Target recognition, Hybrid / monolithic active integrated circuits etc. are the important application areas of CEM.

1.3.9 Applications

In many ways the advantages of microstrip antennas prevail over their shortcomings. Though the original applications were in the military sector, with the advent of new and cheap materials and mature fabrication methodologies, these elements have gone a long way into the commercial space. Future for these antennas reaches out to replacing all the conventional configurations. At present, they have made their presence felt in all areas of microwave communication like command and control systems, radio altimeters, satellite communication, remote sensing, biomedical radiators, intruder alarms, missiles, telemetry etc. In this *era of Information Technology*, where information and its timely communication is more crucial than ever before, the boom in personal, data and video communications owe their credit to the backbone of the industry- *the conformal and reliable microstrip antenna.* They have become a part of our *being* as much as our ears and eyes.

Various types of microstrip antennas ranging from simple elements to complicated arrays are used in mobile platforms like cars, ships, aircrafts and space shuttles. Microstrip reflectarrays [27] replace the bulky parabolic reflectors generally employed in DBS receivers. The array consisting of

simple circular or square geometries of appropriate dimensions is illuminated by the feed horn to provide the HPBW and gain required for DBS.

Mobile system antenna application includes the antennas for base stations, handsets and those for automobiles. For base stations generally requiring *sector* beams, *multibeam arrays* consisting of broadband elements is employed. In vehicles, simple circular patch serves as the cabin antenna and the annular slot serves as a good roof top antenna for sending power at low elevation angles. In handheld portable gadgets such as pagers and cellular phones numerous new approaches like PIFA[28] have been proposed and implemented successfully.

Microstrip configurations are used efficiently in Radars also (e.g. portable man-pack radar to detect moving targets and vehicles). Secondary surveillance radar working at 1030 MHz and 1090MHz and having cosecant squared pattern is made using suitable circular patches. It gives both sector beams and pencil beams which can be electronically switched. SAR consists of two identical microstrip arrays. In the field of medicine, microstrip antennas are used in early detection of tumor and to induce hyperthermia, while treating malignant tumors. The list is by no means exhaustive and the number is sure to multiply many fold in time.

1.3.10 Dual Band Applications

The dawn of the new century came upon us with a new *revolution* in wireless systems, centered on personal and data communication. This prompted study with stress on the improvement of technical performance of such systems. Many a times, operation in two or more discrete but rather closely spaced bands, with arbitrary separation between bands is sought after. Various Cellular systems operating in the L band constitute the main driving force in world communication scenario. *Cell phones operable in two or more different bands* without raising issues pertaining to the different technologies are a major application. *Cell phones that accommodate a GPS receiver* is yet

another dual band application that has triggered interests. While majority of standard GPS receivers use the L1-GPS frequency, differential GPS systems for surveying and precision location require both L1 and L2 bands. A dual band microstrip element with good gain and low elevation angles is therefore required at reasonable price for the above application. Majority of wireless gadgets at present occupy the spectrum from 800-2000MHz where the wavelength is relatively large. To keep pace with the miniaturization trends in these appliances, compact antennas are highly desirable. With increased demand for data communication in Local Area Networks, Wireless LAN (W-LAN) is now more popular, widely setup and off late standardized with regard to frequency allocation. This in turn has triggered a dual band application wherein *cell phones are desired to be* BLUETOOTH™ *enabled* - the wire free technology for data communication, being named so after the Danish king Herald Bluetooth.

As mobile communication evolves into the 3G wireless, with thrust on Wideband wireless access to advanced multimedia or Internet services from a single handheld module, an important issue that is being addressed is the reuse of existing base station sites in view of limited space availability. This calls for both base station and mobile unit *antennas that serve 2G and 3G band of services.*

Above described state of affairs has inspired the investigation of a dual band antenna and the outcome is presented in this thesis.

1.4 Outline of the present work

The numerical and experimental investigation towards the development of patch antennas suitable for dual band communication applications is presented. Microstrip Patch Antenna with Octagon shaped geometry excited using proximity coupling methods and exhibiting dual polarisation characteristics is the main theme of study. Antennas with varying dimensions are investigated using the powerful and robust Finite-Difference Time-Domain method. The influence of feed dimensions and substrate properties upon the antenna performance is looked into with emphasis on resonant frequency, 2:1 VSWR bandwidth, gain and half power beam width. The FDTD method employed provides an insight into the spatial and temporal field behaviour within the geometry and also helps in identifying the resonant modes. The GPS /DCS /PCS /BLUETOOTH™ applications influenced the choice of dual bands.

Conformal FDTD method is used to model the inclined edges of the patch geometry. Resonant frequency and Radiation patterns predicted using CFDTD tool compares well against the experimental observations. Results presented in this thesis highlight the characteristics of a dual band dual polarised Octagonal microstrip patch antenna suitable for integration into a BLUETOOTH™ enabled DCS-1800 cell phone.

The influence of slot perturbation on the resonance frequency is discussed. By modifying the standard equations of circular microstrip patch antennas derived from the cavity model, design relations are developed which help to estimate the resonant frequency of a simple Octagonal geometry.

1.5 Organization of the thesis

The relevant works in the field of Microwave antennas are reviewed in Chapter two, with due emphasis on Dual band Microstrip Patch Antennas. The chapter also presents an overview of advances in the FDTD based computational Electromagnetics.

Chapter three briefly outlines the experimental setup used for the measurement of S parameters, Gain, Polarisation patterns and Radiation patterns.

Chapter four highlights the fundamental mathematical concepts behind the FDTD method. A brief description of the Conformal FDTD method adopted to incorporate the inclined edge of the Octagonal geometry and the PMC approach taken to reduce the size of computational domain is presented. Steps involved in the implementation of CFDTD are also addressed.

The results of the theoretical and experimental investigations are presented in Chapter five. The field distribution at the resonant modes of the antenna is illustrated. The far field radiation patterns predicted using the CFDTD approach are compared with the experimental observations and simulation results obtained using IE3D™. The influence of antenna dimensions and feed line dimensions upon the characteristics is also presented. This is followed by a design relation for the resonant frequency of a simple octagonal geometry.

The conclusions drawn from the experimental and theoretical studies are presented in Chapter six. Suggestions for future work in the field are also made.

References:

1. W.J.G. Beynon, "Marconi, radio waves and the ionosphere," *Radio Science*, vol.10, no.7, pp.657-664, July 1975.
2. John D. Kraus, "Antennas since Hertz and Marconi," *IEEE Trans. Antennas Propagat.*, vol.33, no.2, pp.131-136, February 1985.
3. Giuseppe Pelosi, Stefano Selleri and Barbara Valotti, "Antennae," *IEEE Antennas Propagat. Mag.*, vol.42, no.1, pp. 61-63, February 2000.
4. John D. Kraus and Ronald J. Marhefka, "Antennas - For all applications," The McGraw-Hill Companies Inc., New York, 2002.
5. D.L. Sengupta and T.K. Sarkar, "Maxwell, Hertz, The Maxwellians and the Early history of Electromagnetic waves," *IEEE Antennas Propagat. Soc. Int. Symp.*, Boston, vol.1, pp.14-21, July 2001.
6. A.C. Schell, "Antenna developments of the 1950s to the 1980s," *IEEE Antennas Propagat. Soc. Int. Symp.*, Boston, vol.1, pp. 30-33, July 2001.
7. Andy D Kucar, "Mobile Radio: An overview," *IEEE Communications Magazine*, pp.72-85, November 1991.
8. David M. Pozar, "An overview of wireless systems and antennas," *IEEE Antennas Propagat. Soc. Int. Symp.*, Salt lake city, vol.2, pp.566-569, July 2000.
9. T.K.Sarkar, M.Salazar Palma and D.Sengupta, "A Chronology of developments of wireless communication and Electronics from 1831-1920," *IEEE Antennas Propagat. Soc. Int. Symp.*, Boston, vol.1, pp.2-5, July 2001.
10. M.Salazar Palma, T.K.Sarkar and D.Sengupta, "A Chronology of developments of wireless communication and Electronics from 1921-1940," *IEEE Antennas Propagat. Soc. Int. Symp.*, Boston, vol.1, pp. 6-9, July 2001.
11. Harold Sobol and Kiyo Tomiasu, "Milestones of Microwaves." *IEEE Trans. Microwave Theory Tech.*, vol.MTT-50(3), pp.594-611, March 2002.
12. Bernard Sklar, "Digital Communications – Fundamentals and Applications," Pearson Education Asia, 2nd edition 2003.
13. J.R.James and P.S.Hall, "Handbook of Microstrip antennas - volume 1," edited, Peter Peregrinus Ltd.,U.K.
14. David M. Pozar, "Microstrip Antennas," *Proc. IEEE.*, vol.80, no.1, pp.79-91, January 1992.
15. J.Q.Howell , "Microstrip Antennas," *IEEE. Int. Symp. Digest on Antennas and Propagation*, Williamsburg Virginia, pp.177-180, 1972.
16. Ramesh Garg, Prakash Bhartia, Inder Bahl and Apisak Ittipiboon, "Microstrip Antenna Design Handbook," Artech House publishers , London, 2001.
17. Constatine A. Balanis, "Antenna theory - Analysis and design," John Wiley & Sons Inc., New York, second edition 2002.
18. D.M. Pozar and B. Kaufman, "Increasing the bandwidth of a microstrip antenna by proximity coupling," *Electron Lett.*, vol.23, pp.368-369, April 1987.
19. Y.T. Lo, D. Solomon and W.F. Richards, "Theory and experiments on microstrip antennas," *IEEE Trans. Antennas Propagat.*, vol.27, pp.137-145, 1979.
20. Kai Fong Lee and Wei C, "Advances in microstrip antennas," edited, John Wiley & sons Inc., New York, 1997.

21. Eikichi Yamashita and Raj Mittra, "Variational Method for the Analysis of Microstrip Lines," *IEEE Trans. Microwave Theory Tech.*, vol.MTT-16(4), pp.251-256, April 1968.

22. Constantine A. Balanis, "Advanced Engineering Electromagnetics," John Wiley and Sons, USA, 1989.

23. K.S. Yee, "Numerical solution of initial boundary value problems involving Maxwell's equations in isotropic media," *IEEE Trans. Antennas Propagat.*, vol. 14, pp.302-307, May 1966.

24. Allen Taflov, "Reinventing Electromagnetics: Emerging applications and FDTD computation," *IEEE Computational Science and Engineering*, pp.24-34, Winter 1995.

25. Allen Taflov, "Numerical issues regarding finite-difference time-domain modelling of Microwave structures," *Time-Domain Methods for Microwave structures – Analysis and Design, IEEE Press*, Edited by Tatsuo Itoh and Bijan Houshmand, pp.59-75.

26. A. Reinex and B. Jecko, "Analysis of microstrip patch antennas using finite difference time domain method," *IEEE Trans. Antennas Propagat.*, vol.37, pp. 1361-1369, November 1989.

27. Ronald D. Javor, Xiao Dong Wu and Kai Chang, "Design and performance of a microstrip reflectarray antenna," *IEEE Trans. Antennas Propagat.*, vol.43, pp. 932-939, September 1995.

28. C.R. Rowell and R.D. Murch, " A compact PIFA suitable for dual frequency 900/1800MHz operation," *IEEE Trans. Antennas Propagat.*, vol.46, pp.596-598, 1998.

REVIEW OF LITERATURE

The need to replace bulky, heavy and difficult to manufacture waveguide structures was one of the main motivations for the endeavours which lead to the invention of printed structures. Early structures were essentially triplate or striplines. Subsequently, other line structures were invented, each type having its own advantages and disadvantages. Today the most widely used type is probably the Microstrip line. Microstrip geometries which radiate electromagnetic waves were originally contemplated in the 1950's.

This chapter serves to review the significant advances in the design and modelling of Microstrip antennas since its origin. Due emphasis is given to dual band and dual polarized antennas used for Mobile Communication applications. An overview of advances in FDTD based numerical analysis is also presented.

2.1 The Origin of Microstrip Radiators

Microstrip geometries which radiate electromagnetic waves were originally contemplated in the 1950's. The realization of radiators which are compatible with Microstrip transmission line is nearly contemporary with its introduction in 1952 by Grieg and Englemann [1]. The earliest known realization of a Microstrip like antenna integrated with Microstrip transmission line was developed in 1953 by Deschamps [2]. By 1955, Gutton and Baissinot patented a Microstrip antenna design [3]. Early Microstrip lines and radiators were specialized devices developed in laboratories. No commercially available printed circuit boards with controlled dielectric constants and low loss were developed during this period. The investigation of Microstrip resonators which were also efficient radiators languished. The theoretical basis of Microstrip transmission lines continued to be the object of academic inquiry [4]. Stripline received more interest as a planar transmission line at the time because it supported TEM wave and allowed for easier analysis, design and development of planar Microwave structures. This may have been the one of the reasons for the Microstrip not achieving immediate popularity in the 1950's. The development of Microstrip transmission line analysis and design methods continued in the mid to late 1960's by Wheeler [5] and Purcel *et al.* [6-7]. In 1969 Denlinger noted that rectangular and circular Microstrip resonators could radiate efficiently [8]. Denlinger described the radiation mechanism of a rectangular Microstrip resonator as arising from the discontinuities at each end of a truncated Microstrip transmission line. Previous researchers had noted that in some cases 50% of the power in a Microstrip resonator would escape as radiation. It was noted the percent of radiated power to total input power increased as the substrate thickness of the Microstrip radiator increased. Denlinger's explored only the effect of increasing the substrate thickness until approximately 70% of the input power was radiated into space. Denlinger

also investigated radiation from a resonant circular Microstrip disc. He noted that at least 75% of the power was radiated by one circular resonator under study. In late 1969, Watkins described the fields and currents of the resonant modes of circular Microstrip structures [9]. The Microstrip antenna concept finally began to receive closer examination in the early 1970's when aerospace applications, such as spacecraft and missiles, produced the impetus for researchers to investigate the utility of conformal antenna designs. In 1972 Howell articulated the basic rectangular Microstrip radiator fed with Microstrip transmission line at a radiating edge [10]. The Microstrip resonator with considerable radiation loss was now described as a Microstrip antenna. A number of antenna designers received the design with considerable caution. It was difficult to believe a resonator of this type could radiate, with > 90% efficiency. The narrow bandwidth of the antenna seemed to severely limit the number of possible applications to which the antenna could prove useful. By the late 1970's many of these objections had not proven to derail the use of Microstrip antennas in numerous aerospace applications. In 1981 Microstrip antennas had become so ubiquitous that they were the subject of a special issue of the IEEE Transactions on Antennas and Propagation [11]. Today a farrago of designs have been developed which can be bewildering for designers who are new to the subject.

Itoh and Goto [12-13] modified the printed antenna with strips and slots to obtain dual frequency and circular polarization. Their antenna consisted of two different length strips and a slot excited by microstrip feed. The optimum parameters for the dual frequency operation were theoretically obtained and compared with the experimental data. Das *et al.* [14] modified the ordinary circular patch antenna configuration by slightly depressing the patch conically into the substrate, to obtain much larger bandwidth compared to ordinary antenna.

V. Palanisamy and R. Garg [15] presented two new geometries, which could be used as substitutes for rectangular microstrip antennas. They

presented the theoretical and experimental results of rectangular ring and H-shaped antennas. Bhatnagar *et al.* [16] proposed a broadband microstrip antenna configuration consisting of a triangular patch placed parasitically over a driven patch. A technique for achieving dual frequency operation in microstrip antennas was developed by Wang and Lo [17]. By placing shorting pins at appropriate locations in the patch, they were able to vary the ratio of the two band frequencies from 3 to 1.8.

C. K. Aanandan and K. G. Nair [18] presented the development of a compact and broadband microstrip antenna configuration using a number of parasitic elements, gap-coupled to a driven patch to get improvement in bandwidth. D. M. Pozar and B. Kaufman [19] presented a broadband (13% BW) proximity coupled microstrip antenna configuration consisting of a microstrip patch coupled to a microstrip feed line below the patch. J. L. Drewniak and P.E. Mayes [20] proposed a simple, low-profile, broadband (30% impedance bandwidth) antenna with circularly polarized radiation.

G. Kossiavas et al. [21] presented C-shaped microstrip radiating element operating in the UHF and L bands. Its dimensions are found to be smaller than those of conventional square or circular elements. Supriyo Dey *et al.* [22] modified the geometry of an ordinary microstrip circular patch antenna by putting two sectoral slots shunted by conducting strips to get reduced resonant frequency. This method enabled them to match the antenna using conventional microstrip feed and also achieve 19% reduction in resonant frequency. Zhang *et .al*[23] studied the feasibility of miniaturisation of the antennas used for microcellular and personal communications by using barium titanate as superstrate in microstrip antennas designed for 900 MHz and 1800 MHz bands.

S. Dey *et al.* [24] proposed the design of a compact, low-cost wide band circularly polarized antenna suitable for personal communication applications. The configuration consists of four shorted rectangular patches. Two of them are fed directly and the others are fed parasitically.

Jacob George *et al.* [25] proposed a broad band low profile microstrip circular patch antenna. Four sectoral slots are cut on the circular patch antenna with a uniform inter sectoral angle 90^0 and a slot angle 8^0. The antenna requires about 59.8% lesser area compared to an ordinary circular patch antenna resonating at the same frequency. R. Waterhouse [26] presented a probe fed circular microstrip antenna incorporating a single shorting pin, which significantly reduced the overall size of the antenna. A proximity coupled rectangular microstrip antenna giving circular polarization was demonstrated by H. Iwasaki [27]. A practical antenna suitable for applications in phased arrays with an axial ratio of less than 0.3dB was realized.

J. George *et al.* [28] developed a compact drum shaped microstrip antenna with considerable reduction in size and radiation characteristics similar to those of an equivalent rectangular patch antenna. H.T. Chen [29] experimentally studied the characteristics of compact microstrip antennas and compared them with those of conventional microstrip antennas. Compactness achieved through the placement of shorting pin and through meandering were studied. Lo *et al.* [30] used a high permittivity substrate for the design of a miniature microstrip antenna. Return loss, radiation pattern and antenna gain were measured and presented for a 1.66GHz antenna. The patch size was greatly reduced to one fifth of that of the conventional microstrip antenna.

Economou and Langley [31] proposed a circular patch antenna equivalent to a simple monopole, suitable for mobile vehicle applications and W-LANs. Jacob George *et al.* [32] investigated the possibility of enhancing the bandwidth of a microstrip antenna through dielectric resonator loading.

A miniaturized C-patch antenna excited by means of a coaxial probe was described by Zaid *et al.* [33]. The antenna consisting of two stacked C-shaped elements connected together with a vertical conducting plane was designed on an air substrate. Kin-Lu Wong and Ming-Huang Chen

[34] described a circularly polarized single-feed small circular Microstrip antenna with four equally spaced slits inset at the patch boundary. 50% size reduction was achieved with respect to a conventional patch antenna. An L-probe fed circular patch antenna with 24% impedance bandwidth and 7.5 dBi average gain was demonstrated by Luk *et al.* [35].

Chia-Luan Tang and Kin-Lu Wong [36] presented the design of a probe fed equilateral triangular ring microstrip antenna for circular polarization. Designs for bandwidth enhancement were investigated by Sean M.Duffy [37] and Kin-Fai Tong *et al.*[38]. J.Y. Sze and K. L. Wong [39] presented a slotted rectangular microstrip antenna for bandwidth enhancement with the loading of a pair of right angle slots and a modified U-shaped slot in the patch. Manju Paulson *et al.* [40] demonstrated a compact microstrip antenna with circular polarization radiation. This configuration provides an area reduction of 42% compared to a standard rectangular patch antenna at the same frequency, and a 3dB CP bandwidth of ~1%. Jui-Han Lu and Kin-Lu Wong [41] experimentally studied a single-feed circularly polarised equilateral-triangular microstrip antenna with a tuning stub, achieving 22% area reduction with respect to a regular triangular antenna. This configuration had a wider impedance bandwidth (5.5%) and a higher front-to-back radiation ratio.

Fan Yang *et al.* [42] presented wide-band E-shaped Patch antennas for wireless communications by incorporating two parallel slots in the patch area. The bandwidth was increased beyond 30%. Lee *et al.* [43] reported linearly and circularly polarized corrugated circular microstrip patch antennas for miniaturization at 1.575 GHz (GPS). Jang [44] presented a broadband T-shaped microstrip-fed U-slot coupled patch antenna exhibiting 76.8% bandwidth. Chen [45] proposed a compact circularly polarised square microstrip antenna with slotted ground plane.

Debatosh Guha presented a comprehensive survey of the developments in microstrip antenna research [46]. Shackelford *et al.* [47]

examined several designs for small-size wide-bandwidth microstrip antennas through simulation and experiment. Che-Wei Su and Kin-Lu Wong [48] conducted an experimental study on a circularly polarised microstrip antenna with a rectangular ground plane to determine the effects of the ground plane dimensions on the polarisation characteristics. They concluded that the aspect ratio of the ground plane is an important factor for achieving good circular polarization radiation. Chi Yuk Chiu *et al.* [49] proposed two different geometries (U-slot and L-slit) to improve the impedance bandwidth of a quarter wave patch antenna. Upto 53% and 28% bandwidth was obtained. Boccia *et al.* [50] reported a shorted elliptical patch antenna for GPS applications with improved multipath rejection capability. Qinjiang Rao [51] proposed an improved design for an aperture coupled microstrip antenna for size miniaturization and high radiation efficiency. The structure used a thin dielectric layer as a back-reflector for blocking back-radiation instead of a metal plate with an additional dielectric layer. Kin-Lu Wong *et al.* [52] proposed a planar metal plate monopole folded into a low profile structure and a matching tuning portion for achieving a wide bandwidth. A hybrid antenna consisting of an annular dielectric resonator antenna combined with a quarter wave monopole producing an ultra wideband response was presented by Lapierre *et al.* [53].

2.2 Dual Frequency Microstrip Antennas

The advent of third generation mobile has spurred the interest in antenna design. To deal with the increasing demand for mobile applications and cater to the different standards around the world, future mobile terminals will need broadband or multi-band antennas capable of providing multi-mode operation. Dual-band operation is underway to become an industry standard for mobile communication terminals.

Choon Sae Lee *et al.* [54] presented the detailed design scheme of a planar dual-band microstrip antenna. The antenna comprised of multiple

layers with metallic strips placed at one of the dielectric interfaces under the radiating patch to achieve field modification. Liu and Hall [55] suggested a planar dual band inverted F-antenna operating at 0.9GHz and 1.8GHz for hand held portable telephones. The dual-band antenna was almost the same size as a conventional inverted F-antenna operating at 0.9GHz, and had better than 17dB isolation between bands. Sanad [56] developed a compact dual frequency microstrip antenna consisting of a driven element and five small parasitic patches distributed in two stacked layers suitable for application in cellular phones. A broad band dual frequency circular sided microstrip antenna providing two independent ports with orthogonal polarization and gain comparable to that of a standard circular patch antenna was proposed by Deepukumar *et al.*[57]. The antenna offered excellent isolation between its ports. A formula for calculating the resonant frequencies of the two ports was also proposed. Sanchez-Hernandez *et al.* [58] presented a dual-band circularly polarized microstrip antenna with a single feed by using two spur-line band-stop filters within the perimeter of the microstrip patch. This is obtained without increasing either the size or the thickness of the patch.

The design of a single-feed, reduced-size dual frequency rectangular microstrip antenna with a cross slot of equal length was presented by Kin-Lu Wong and Kai-Ping Yang [59]. The frequency ratio of the two operating frequencies was mainly determined by the aspect ratio of the rectangular patch. Kin-Lu Wong and Wen-Shan Chen[60] experimentally studied the characteristics of a single-feed dual-frequency compact microstrip antenna with a shorting pin. Chia-Luan Tang *et al.*[61] demonstrated a small circular microstrip antenna with dual frequency operation by using a single shorting pin and a single probe feed. This dual-frequency design resulted in a much reduced antenna size and provided a tunable ratio of ~2.55-3.83 for the two operating frequencies.

A dual-frequency triangular microstrip antenna with a shorting pin

was designed by Shan-Cheng Pan and Kin-Lu Wong [62]. By varying the shorting pin position in the microstrip patch, a large tunable frequency ratio of about 2.5-4.9 was provided. Kin-Lu Wong and Wen-Shan Chen [63] reported a slot-loaded bow-tie microstrip antenna for dual-frequency operation. Various frequency ratios, within the range 2-3, of the two operating frequencies could be obtained by varying the flare angle of the bow-tie patch. Kin-Lu Wong and Gui-Bin Hsieh [64] described a dual-frequency circular microstrip antenna with a pair of arc-shaped slots operating in the frequency range 1.38-1.58 GHz. Jui-Han Lu and Kin-Lu Wong [65] demonstrated a dual frequency rectangular microstrip antenna design consisting of a rectangular patch loaded with two parallel slots close to the radiating edges and meandered with slits at the non-radiating edges, with frequencies tunable in the range 1.8-2.4 GHz.

J. George *et al.*[66] presented a single feed dual frequency compact microstrip antenna with a shorting pin. This antenna configuration gave a large variation in frequency ratio of the two operating frequencies, without increasing the overall size of the antenna. A single-feed dual-band circularly polarized microstrip antenna was demonstrated by Gui-Bin Hsieh *et al*[67]. By embedding two pairs of arc-shaped slots of proper lengths close to the boundary of a circular patch, and protruding one of the arc-shaped slots with a narrow slot, the circular microstrip antenna could perform dual-band CP radiation using a single probe feed. Details of similar dual frequency antenna designs and experimental results are presented by a team of researchers under Kin Lu Wong [68-70].

Kin-Lu Wong and Jia-Yi Sze [71] presented a dual-frequency slotted rectangular microstrip antenna with a pair of properly bent narrow slots close to its non-radiating edges. The two operating frequencies had parallel polarization planes and similar broadside radiation patterns, and the frequency ratio of the two frequencies was controlled by the bent angle of the embedded slots. A dual-frequency planar antenna for cellular telephone

handsets (0.9 and 1.8 GHz bands) was designed by Chiba *et al.*[72]. This antenna had almost the same size as a conventional internal antenna operating in the 0.9 GHz band. Hoorfar *et al.*[73] demonstrated the design of a three-layer proximity-coupled microstrip antenna structure for dual frequency operation at two GPS frequencies (1.228 GHz and 1.575 GHz). A small dual patch antenna with 5% bandwidth and less than -15dB cross-polarisation level was designed by Chair *et al.*[74]. The resonant frequency was reduced by 39% when compared with a basic single layer patch antenna with the same projection area. Lee *et al.* [75] presented a compact, dual-band dual polarization antenna capable of generating two distinct frequencies with different polarisation and radiation pattern characteristics: a monopolar mode for terrestrial cellular communication and a circularly polarized, upward oriented pattern for satellite mobile. Bandwidths of 2 and 4%, respectively, have been obtained in the two modes.

A wideband microstrip antenna with dual-frequency and dual-polarisation operation was proposed by Yeunjeong Kim *et al.*[76]. This enabled the transmission and reception of differently polarized wideband signals simultaneously with a single antenna system. The measured bandwidths for 15dB return loss at dual frequencies were 9.02 and 12.4%, respectively. Jui-Han Lu[77] designed a dual frequency rectangular microstrip antenna with a pair of step-slots embedded close to its non-radiating edges. The two operating frequencies have the same polarization planes and similar broadside radiation characteristics. By adjusting the step ratio of the step-slots, the frequency ratio of the two operating frequencies was tunable in the range ~1.23-1.63. The design of a single-feed equilateral-triangular microstrip antenna was proposed by Jui-Han Lu[78]. A bent slot of 60° was loaded close to each triangle tip to achieve dual frequency operation.

A Dual-band Meander antenna with two passive ground-attached metallic strips for wireless telephones was proposed by Williams *et al.* [79]. Experimental studies on compact dual-band dual-polarized compact

microstrip antenna were presented by Sona *et al.* [80]. The antenna structure could also be modified to achieve the desired ratio between the two resonant frequencies. Pekka Salonen *et al.* [81] described a dual-band planar inverted-F antenna using a novel top plate geometry. The effect of the various physical parts upon the antenna characteristics was also described. Maci and Gentili has provided a critical overview of possible solutions for dual-frequency patch antennas [82]. Kai-Ping Yang and Kin-Lu Wong [83] achieved dual-band circularly-polarized designs by inserting T-shaped and Y-shaped slits along the patch edges and patch corners of a square microstrip antenna.

Salonen *et al.* [84] suggested L and U slot configurations for dual band PIFA suited for 2.4GHz and 5.2GHz bands. The radiation patterns were also affected by the shape of PIFA and slots. Reed *et al.* [85] achieved size reduction of 50% for their antenna by incorporating slots in the geometry and suggested that a rule of thumb for determining the period of slits is 2-2.5 times slit width. Manju Paulson *et al.* [86] presented a compact dual-band, dual polarized microstrip antenna for terrestrial communication and satellite mobile communication. Wu *et al* [87] proposed a stacked patch antenna with dual feed for DCS/GPS application with an overall thickness of ~14mm.The antenna gain was in the order of 3dBi.

Tung *et al* [88] has proposed a shorted microstrip antenna for 2.4/5.2GHz WLAN with the coaxial probe exciting the configuration etched on FR4 substrate with an air gap introduced between patch layer and ground. The geometry gives a maximum gain of ~ 4dBi for the 2.4GHz band. A slot-loaded compact arrow-shaped microstrip antenna with a pair of narrow slots close to its radiating edges for dual frequency operation was presented by Sona *et al.* [89]. The two frequencies exhibit similar radiation characteristics. The ratio between the two operating frequencies could be tuned in the range 1.14-1.24, which is much smaller than that offered by similar designs. A planar inverted-L patch antenna for 2.4/5.2GHz dual-band operation was

proposed by Yen-Liang Kuo and Kin-Lu Wong [90]. Wang [91] summarized various methodologies for achieving dual-frequency microstrip patch antennas and presented two antenna designs suitable for IMT-2000 applications.

Marta Martinez-Vazquez *et al.* [92] proposed a compact dual-band antenna for mobile handsets. The antenna consisted of a rectangular patch with a shorting pin and a spur-line filter added for dual band characteristics. Chen [93] described a microstrip-fed dual-frequency printed triangular monopole to obtain various frequencies in the range 1.37-1.75 GHz. The F shaped internal antenna, of dimensions 10 x15mm^2, proposed by Yeh and Wong [94] exhibited dual frequency operation in the 2.4/5.2GHz WLAN application, though the gain offered was less than 3dBi. A dual frequency Rhombic microstrip antenna was proposed by Lin *et al.* [95] where compactness was achieved by incorporating slits and shorting posts. Tung *et al.*[96] proposed printed monopole suited for 2.4/5.2GHz WLAN with the 50Ω line directly exciting the monopole etched on FR4 substrate. The geometry gave a gain of ~ 4dBi and 5dBi in the two bands.

Su *et al.* [97] proposed a slot configuration with reasonable gain for 2.4/5.2GHz WLAN with 50Ω coaxial line feeding the antenna, suitable for mounting along perimeter of display etc. of WLAN modules. Jouko Heikkinen and Markku Kivikoski [98] presented a novel dual-frequency circularly polarized rectifying antenna for wireless power transmission at 2.45GHz and 5.8GHz. Gadzinea and Slobodzian [99] described the concept of a compact dual-band dual-port Microstrip base station antenna for GSM900 and GSM1800 mobile communication systems. Ching-Yuan Chiu *et al.*[100] proposed a shorted, folded planar monopole antenna for application in GSM/DCS dual-band mobile phones.

A simple monopole configuration for WLAN bands was proposed by Kuo and Wong [101] with gain around 2dBi in both bands. The circular MPA with an offset ring slot proposed by Jan [102] offers single feed dual

band operation. The frequency ratio can be varied by varying the ratio of radii of MPA and the ring slot. The single layer dual frequency H shaped geometry [103] with U slots embedded near the radiating edges offer TM_{10} and TM_{30} resonant modes at 900MHz and 1.8GHz respectively. The antenna has an overall patch area of 70 x 42mm^2 on a substrate with $\varepsilon_r = 2.8$. A wide band internal antenna design supporting the IEEE 802.11a WLAN applications (5.2/5.8GHz) is proposed by Ali *et al.* [104].

Ciais *et al.* [105] described an internal planar inverted F antenna which combines shorted parasitic patches, capacitive slots to support multi band operation. It is suitable for mobile phones and WLAN standards. Chen *et al.*[106] proposed a CPW fed monopole antenna operating in the DCS1800 and 2.45GHz bands with the operating bands being determined by various arms of the monopole. But the measured gain is 1.4dBi and 2.4dBi respectively for the bands. Sudha, Vedavathy and Bhat [107] proposed a wideband single feed patch antenna with nearly square patches offering circular polarization characteristic by the excitation of two orthogonal resonant modes. The impedance band width at 1.99GHz was nearly 22%, with good Axial ratio within the band. The gain offered in the entire band was also high. The low profile planar dipole antenna proposed by Chen and Sun [108] for 2.4GHz operation had a truncated and tapered ground plane for its feed line portion. The novel geometry offered good bandwidth and ~4dBi gain.

Moon and Park [109] proposed a PIFA suited for 2.4/5GHz band applications. The antenna is CPW fed and has a height of 0.8mm but offers lower gain for the 2.4GHz band. The dual band PIFA configuration [110] proposed by Guo *et al.* covered four application bands namely, GSM900, DCS1800, PCS1900 and UMTS2000. The configuration had 8mm foam between the radiating element and the ground plane and offered less than 4dBi gain. Dual band operation suitable for UMTS and WLAN was achieved with CPW feed in an antenna with meandered geometry by Liu *et al.* [111]

on FR4 substrate. The diamond shaped printed antenna proposed by Rafi and Shafai [112] was characterised by 50% band width, by virtue of the V slot in it, and very good gain from 3.69GHz to 6.2GHz.

The arms of the printed dipole perturbed by spur line offered dual frequency operation suited for 2.4 and 5.2GHz bands, in the configuration proposed by Chen *et al.* [113]. The special feed arrangement for the dipole offered adequate band widths for these applications. The CPW fed antenna proposed by Chen and Hsu [114] offered ~4dBi gain at 5.8GHz suited for RFID tags. Wang *et al.* [115] proposed a printed compact dual band antenna suited for the 2.4GHz and ISM band applications. On FR4 substrate the geometry occupies a volume of 15x40x1 mm^3 with low gain of 1.4dBi in the lower band.

Chen [116] presented a study on CPW fed and microstrip fed dual band annular ring antenna operating in DCS and 2.45GHz bands with peak gain of 5.8dBi and 5.6dBi respectively. Wong *et al.*[117] proposed a dual band antenna configuration, for the 2.45GHz and 5.2/5.8GHz WLAN application, suited for integration into the Laptop. The antenna offered broad patterns and gain around 5dBi for the higher band. Dual polarized broad band proximity coupled antenna by Gao *et al.*[118] used H slots in the ground plane to feed the patch. Band widening was achieved by using an air gap between the feed and patch substrates. The isolation achieved was -34dB with good broad side radiation.

Li *et al.* [119] illustrate the design of a folded antenna with short at one edge and offering a wideband of operation covering the PCS, DECT and DCS bands. The overall height of the configuration was 8mm and additional tuning posts were also incorporated. Lin and Huang [120] proposed a compact dual band antenna for GPS and DCS application comprising of a truncated square patch supporting the GPS and an annular ring patch supporting the DCS in its TM$_{21}$ mode. The TM$_{21}$ mode resonance is lowered to the desired value, by cutting radial slots in the ground plane. The single

layer monopole printed antenna for dual ISM band designed by Chen *et al.* [121] incorporated an end stepped feed strip to achieve frequency tuning for both bands and band broadening in the upper band. The serial slot in the geometry was crucial in determining the lower resonance and its bandwidth. The antenna offered omni directional patterns with low gain in the lower band.

Liu *et al.*[122] introduced a rectangular notch to expand the impedance bandwidth of a dual band planar monopole antenna for PCS/WLAN systems. The antenna was shaped like letter Y and offered 14.4% and 34.1% band widths in the respective bands. Zhang *et al.*[123] designed a dual band WLAN printed dipole antenna, where the approach was to obtain a full resonance frequency in the 2.4GHz band while the secondary resonance in the 5GHz band was achieved using a simple matching network. Li *et al.*[124] proposed a two layer patch antenna fed by dual L probes for wideband response in the 890MHz and 2.45GHz bands. The lower layer patch operated in the lower band while the smaller upper patch operated in the 2.45GHz band offering 26%and 42% bandwidths.

2.3 Microstrip Antenna Analysis

Various analytical methods based on simplifying assumptions, as outlined in section 1.3.7, aided the study of antenna characteristics in the early days. With the advent of computers numerical methods which offered more accurate estimates evolved as discussed below

Robinson [125] presented the graphical calculations of the resonant frequency of microstrip cavities where the resonant frequency was determined for a particular structure or resonances within a band. Wolff and Knoppik [126] described a simple method to calculate the capacitances of rectangular and circular microstrip disk capacitors. The resonant frequencies were calculated from a resonator model employing an effective width/length or radius respectively, filled with a medium of a dynamic dielectric constant.

Dahele [127] discussed the appropriate correction factor to use in the resonant frequency formula of an equilateral triangular Patch antenna obtained from the cavity model with perfect magnetic walls.

Ramesh Garg and Stuart A. Long [128] derived an improved formula for the resonant frequencies of the triangular Microstrip patch antenna by substituting an equivalent side length to produce an effective side length. Dearnley and Barel [129] compared the three variations of the cavity model to determine the resonant frequencies of a rectangular microstrip antenna. It was shown that the uncertainties in the dimensions of the patch and the properties of the substrate greatly influenced the final result. Xu Gang [130] obtained an appropriately corrected formula for the resonant frequencies of Microstrip antenna elements based on the evaluation of effective dielectric constant. Antoszkiewicz and Shafai [131] investigated the effects of feed probe and ground plane size on the resonant frequency and impedance characteristics of circular Microstrip patches. The resonant frequency was calculated assuming a magnetic wall at the edge of the patch. Mishra and Pattnaik [132] derived an expression for the resonant frequency of a wedge shaped Microstrip antenna. Bhattacharyya [133] applied the principle of reciprocity to obtain the equivalent circuit of an electromagnetically coupled rectangular patch antenna. The equivalent circuit was developed from the concept of voltage and current discontinuities in the transition region. Wei Chen, Kai-Fong Lee and Dahele [134] presented theoretical and experimental studies of the resonant frequencies of the equilateral triangular microstrip antenna. A curve fitting formula yielding the resonant frequency of the lower order mode was the major contribution. Rengarajan [135] presented a simple and accurate technique for determining the resonance frequency of the dominant odd and even modes of elliptical microstrip antennas and resonators.

Kumprasert and Kiranon [136] developed a simple and accurate formula for the resonant frequency of the equilateral triangular Microstrip

Patch Antenna using an approximate solution of the capacitance of circular Microstrip disk to account for the fringing fields. They later formulated the resonant frequency of a circular disk Microstrip antenna [137] as a function of the effective radius and fringing capacitance.

Rajanish and Vedavathy [138] developed a modified expression for calculating the resonant frequency of higher order modes for circular microstrip antennas, by generalizing the expression for the resonant frequency in a cavity model. Ribero and Damiano [139] provided fast and accurate expressions for the resonance frequency of an ellipsoidal structure operating in the TM_{10} mode, making use of a computer algebra system to generate the polynomial expression of the zeros of the characteristic equations. Ray and Girish Kumar [140] proposed a generalized method to determine the effective dielectric constant and edge extension for predicting the resonant frequency of various microstrip antennas by equating their area to that of the equivalent rectangular microstrip antennas. Rabindra K. Mishra [141] devised a simple method for determining the bandwidth of rectangular patch antenna using the idea of transmission line and cavity model, without using an iterative procedure.

Debatosh Guha [142] presented an improved analytical model for calculating the resonant frequency of circular microstrip antennas with and without air gaps. Unlike the previous models, the method was applicable to a wide range of antenna diameters and substrate parameters. Paulson *et al*[143] discussed a simple technique for calculating the resonant frequencies of a compact arrow-shaped microstrip antenna, by modifying the standard design equations of a rectangular patch antenna. Verma and Nasimuddin [144-145] presented a modified cavity model to compute the resonance frequency and bandwidth of a rectangular patch antenna on a thick substrate. Rajanish and Vedavathy [146] presented a generalized expression for calculating the resonant frequency of microstrip antennas by including a correction factor for higher order modes.

Following the introduction of the Microstrip antenna, analysis methods were desired to determine the approximate resonant resistance of a basic rectangular Microstrip radiator. The earliest useful model introduced to provide approximate values of resistance at the edge of a Microstrip antenna is known as the transmission line model introduced by Munson [147]. This model provides insight into the simplest Microstrip antenna design, but is not complete enough to be useful when more than one resonant mode is present. The radiation mechanism of an open circuited Microstrip termination was studied by James and Wilson [148]. They observed that the terminal plane region is the dominant radiating aperture. Agarwal and Bailey [149] modeled the Microstrip radiating structure as a fine wire grid and solved for the current using Richmond's reaction theorem. In the late 1970's, Lo *et al.* [150] developed a model of the Rectangular Microstrip Antenna as a lossy resonant cavity. Microstrip disc antenna has also been analysed by Derneryd [151] by calculating the radiation conductance, antenna efficiency and quality factor associated with the circular disc antenna. Hammer *et al.* [152] developed an aperture model for calculating the radiation fields of microstrip antennas. This model accounts for radiation from all the edges of the patch and could give the radiation field and the radiation resistance of any mode in a microstrip resonator antenna.

Microstrip antennas, despite their simple geometry, proved to be very challenging to be analyzed using exact methods. In the 1980's, the Method of Moments (MoM) was the first numerical analysis method with which computers could provide enough memory and CPU speed to practically analyze Microstrip antennas [153-157]. Fred Gardiol [158] presented an overview of mixed potential integral equation methods for multilayered structures. Sriram and Vedavathy [159] presented a novel analysis scheme utilizing the advantages of the conformal mapping technique and the cavity model to analyze multilayer dielectric microstrip antennas. Abegaonkar *et al.*[160] studied the field configurations for

electromagnetically coupled microstrip patch antenna using CST Microwave Studio.

A comprehensive review of the Microstrip antenna technology till 1981 was provided by Carver *et al.*[161]. In the early 80's Itoh *et al.*[162] presented a full wave method for the analysis of open printed circuit structures. Kuester *et al.*[163] reported a thin substrate approximation applied to microstrip antennas. The formulae obtained were found to be useful in simplifying the expression for the microstrip antenna parameters considerably.

Sengupta [164] derived an expression for the resonant frequency of a rectangular patch antenna. Accuracy of the expressions for the patches of different sizes were compared with measured results. The rectangular microstrip antenna has been extensively analysed by Lier *et al.*[165] for both finite and infinite ground plane dimensions. Pues *et al.*[166] presented a more accurate and efficient method for the analysis of rectangular microstrip antennas. They modified transmission line model by incorporating the mutual coupling between the equivalent slots and by considering the influence of the side slots on the radiation conductance. Penard and Daniel [167] used the cavity model for the analysis of open and hybrid microstrip antennas. Das *et al.*[168] analysed the modal fields and radiation characteristics of microstrip ring antennas. The experiments conducted at 1.8GHz were compared with the theoretical patterns. Richards *et al.*[169] analysed the annular, annular sector and circular sector microstrip antennas. The model expansion cavity model was used to predict the performance factors. The experiments done at L band for various antenna dimensions were reported.

Chu and S.K. Chaudhuri [170] combined modal analysis and the Finite Difference Time Domain method in the study of dielectric waveguide problems. Karmakar [171] obtained the equivalent circuit of an electromagnetically coupled patch antenna using reciprocity. Kishk [172]

presented the analysis of a spherical annular microstrip antenna. The input impedance of the patch was computed using the generalized transmission line model and Method of moments was used for the computation of the radiation patterns.

Kashiwa *et al.*[173] demonstrated the analysis of rectangular microstrip antennas mounted on the curved surface using the curvilinear FDTD method. The numerical results agreed well with almost all the experimental results and this confirmed the validity of the technique. The near fields of single layer microstrip patch antennas was computed through an iterative method by Bokhari *et al.*[174]. A combination of mixed potential integral equation method, the FFT algorithm and the biconjugate gradient resulted in an efficient numerical solution. S. Dey and R. Mittra[175] presented the design and development of a compact microstrip patch antenna. The length of the antenna was only one eight of the effective wavelength at resonance. They used method of moments for the analysis of the current distribution on the patch surface.

Iti Saha Misra and S.K. Chowdhury [176] performed a study of impedance and radiation properties of a concentric microstrip triangular-ring antenna and its modeling techniques using FDTD method, avoiding the staircase approximation. The improvement of computational power and memory size of personal computers during the 1990's made numerical methods such as the Finite Element Method (FEM) and Finite Difference Time Domain method (FDTD), which require much more memory than Moment Method solutions, workable for everyday use by designers [177-178]. Holter and Steyskal [179] presented a new technique for the FDTD analysis of periodic infinite phased arrays, by implementing periodic boundary conditions which reduced the computational volume to that of a single unit cell. Guha and.Siddique [180] presented a new CAD model to calculate the resonant frequency of inverted microstrip circular patch antennas.

2.4 Overview of progress in FDTD based numerical analysis

The finite difference method was first developed by A. Thom in 1920's under the title, *the method of squares*, to solve the nonlinear hydrodynamic equations [181]. The simple and elegant discretization of differential form of Maxwell's Equations by K.S. Yee [182] in 1966 initiated the application of the tool in electromagnetics. Since then there were soaring advances in the field. The fundamental concepts as applied to the present work is discussed, in chapter four of the thesis. The discussion below highlights the successful extensions and applications of the method.

The Cartesian coordinate systems used in the method may lead to errors while handling smooth geometries. Yee proposed a non orthogonal grid scheme in 1987. Several attempts have been made to implement alternative orthogonal coordinate systems [183-184]. Sub gridding techniques, where information is passed between coarse and fine grids were proposed by Kunz and Simpson [185] as *general FDTD*. The sub gridding, which is numerically stable, proposed by Zivanovic, Yee and Mei [186], which uses coarse grid in the whole domain while fine grid is introduced only around the discontinuities. A simple modification of Yee's FDTD algorithm allowing the time reversal in FDTD simulation thereby permitting numerical microwave synthesis was put forth in 1993 by Sorrentino and Mezzanotte [187]. Uehara and Kagoshima applied FDTD tool to analyze a microstrip phased array antenna [188].

FDTD modeling of complicated materials has gained much attention. Luebbers *et al.*[189] had proposed a recursive convolution (RC) scheme to model Debye media, by relating the electric flux density and electric field through a convolution integral. FDTD was extended successfully to model nonlinear active regions [190] by Toland and Itoh in 1993. In 1996 Sullivan [191] showed the use of Z transform in implementing

the FDTD for nonlinear media.

A straight forward and general approach for implementing local grids in FDTD calculations, with good accuracy was proposed by Chevlier *et al.*[192]. The highly accurate sub gridding algorithm by Okoniewski *et al.* [193] offers good accuracy with less than -60 dB reflections from the mesh interfaces. The method to replace the grid discontinuity with an equivalent circuit presented in [194] is simple yet accurate. In 1998, Oguz *et al.*[195] proposed an efficient and accurate method for incident wave excitation in the FDTD method. They employed different signal processing tools to reduce the errors.

Kar and Wahid [196] performed the FDTD analysis of a microstrip patch antenna with dual feed lines. The antenna studied was a square patch on substrate of thickness 0.6cm and permittivity 2.55. The ports were fed with Gaussian pulses 90° out of phase to obtain circular polarisation. Shift in the resonance frequency obtained by a short or open in the feed lines was also looked into.

J. Gomez-Tagle *et al.*[197] performed the active impedance analysis of finite phased array microstrip antennas using the finite difference time domain method. A rigorous feed model was also presented and the results validated through experiment. Korner [198] presented a 3-D refractive index adaptive gridding algorithm for finite-difference time-domain methods.

Cangellaris and Zhao [199] suggested a rapid FDTD scheme which does not involve time stepping, in 1999, by combining FDTD method with non symmetrical Lanczos eigen value algorithm. Techniques to handle late time instability and stability of absorbing boundary conditions was discussed in [200-201]. FDTD algorithms not involving the CFL constrain were suggested in [202-203]. It was based on the Alternating Direction Implicit (ADI) method, which allowed the minimum cell size to be much smaller than the wavelength and involve different discretization schemes for alternate time steps. Railton [204] modeled inductance and capacitance associated

with the fringing fields that exist around the discontinuities by altering the permittivity associated with the transverse E field nodes and the permeability associated with transverse H field nodes. Oguz *et al.*[205] also developed methods to reduce the sinusoidal steady state errors in the numerical calculations. A modeling approach to incorporate a two port networks, with S parameters, in the FDTD method was presented by Xiaoning *et al.*[206] based on time domain Y parameters to describe the network characteristics. It could be extended to N port networks also. Accurate modeling of a practical lossy substrate necessitates the termination of the simulation region with an ABC suitably matched to the lossy dielectrics. Wittwer and Ziolkowski [207] discussed the effect of dielectric loss in FDTD simulation and suggested a lossy material mode ABC as the termination.

Yong-Woong Jang [208] presented the numerical simulation using FDTD methods and experimental implementation of a wide-band T-shaped microstrip-fed twin-slot array antenna. The dependence of the design parameters on the bandwidth characteristics was investigated. Reduced finite difference time domain (RFDTD) method proposed by Kondylis *et al.* [209] eliminated the necessity of subdividing the computational domain into sub regions. It reduced the number of required field computations to four, by employing a specific sequence for the spatial update of the field components. Investigations performed by Zhao and Alinikula [210] on the performance of the resistive voltage source (RVS) used in FDTD analysis indicated that reflections caused by RVS could be reduced if effective impedance was used in the computations, instead of actual physical impedance. A comparison of the ADI − FDTD method with other FDTD schemes and an estimate of the truncation error was discussed by Garcia *et al.* [211].

A study of EMI filters with ferrites was presented by Xiaoning *et al.* [212]. Zhao [213] discussed an unconditionally stable FDTD (US-FDTD) approach, where the field components where defined only at n and $n+1$ time steps. The left and right hand side of the FDTD equations were rearranged by

him to ensure maximum accuracy in respect of time. The approach was claimed to be more accurate than ADI-FDTD. Makinen *et al.* [214] developed a coaxial probe feed model for FDTD, based on transmission line, in order to increase the modeling accuracy. James *et al.* [215] explained the scheme for hardware implementation of 3D FDTD algorithm, to speed up the simulation.

An enhanced FDTD method to handle the sharp edges in the domain based on FDTD contour path sub cell approach was discussed by Seyed and Esselle [216]. It offers lower reflections for a broad band of frequencies. A three dimensional algorithm with PML absorbing boundary condition for the wave equation in time domain suited for inhomogeneous lossy media was proposed by Rickard *et al.* [217]. Javier Gomez-Tagle *et al.* [218] performed the FDTD Analysis of Finite-sized Phased Array Microstrip Antennas. Their main contribution was the determination of the active impedance for different scan conditions. By allowing the PML variables to vary at different exponential rates and by applying lossy termination walls, the performance of the PML was improved by Rickard and Georgieva [219].

Simpson and Taflov [220] explored ELF propagation about earth sphere using FDTD tool. Akyurtlu and Werner [221] used the FDTD tool for modeling the EM wave interactions with bi-Isotropic medium in the BI-FDTD scheme formulated by them. The nonstandard finite difference model by Cole [222] is accurate with very low solution error, as against the ordinary FDTD scheme. The novel 3D CPFDTD scheme for modeling objects nonconformally aligned within the FDTD grids proposed by Chavannes [223] enabled improved modeling of antennas rotated within a FDTD grid plane.

Venkatrayalu *et al.* [224] modeled an ultra wideband dielectric horn antenna using FDTD. Hany *et al.* [225] proposed a modified 3D scheme referred to as $M3d_{24}$ which used second order time and fourth order space discretization to achieve low dispersion. Zhao [226] performed an analysis

on the influence of aspect ratio of the Yee's unit cell on the numerical dispersion in an FDTD domain. For fixed mesh resolution, higher aspect ratio showed that phase velocity error converged to acceptable limits. This has implications especially in the ADI-FDTD method where cells with higher aspect ratio is desirable than a cubic cell.

Based on the original Enguist - Majda ABC a simple procedure for implementing the boundary condition for the FDTD modeling of lossy and dispersive media in presented by Kosmas and Rappaport [227]. The higher order US-FDTD suggested by Xiao *et al.* [228] based on the weighted finite difference method offered very low numerical dispersion. Fu and Tan [229] successfully developed a split–step FDTD scheme with second order temporal accuracy and fourth order spatial accuracy and unconditional stability. Rickard and Nikolova [230] suggested an enhancement to PML which offers as low as -60dB reflection even for six layers and reliable performance in the proximity of discontinuities.

Simon and Kishk [231] proposed an asymptotic strip boundary condition (ASBC) for the FDTD domain wherein they modified the effective permittivity based on the spacing to width factor of the strips. Accurate results for Schumann resonant frequencies of the earth was computed by Soriano *et al.* [232], in their study of the earth's atmosphere using the FDTD tool. Tao, Wenhua Yu and Mittra [233] discussed the different excitation sources with emphasis on the considerations to be given to incident current source as applicable to a practical lossy substrate. Recently Marrone and Raj Mittra [234] proposed a stable 3D-FDTD algorithm employing *Cell method* for analyzing complex structures without posing severe constrains on the maximum time step.

Chun *et al.*[235] proposed a fourth order finite difference time domain like algorithm named as integro-difference time-domain (IDTD). It uses the integral form of Maxwell's equation with due emphasis on spatial variation of EM field *within* each cell instead of the *difference between*

adjacent cells used in the Yee algorithm. It yielded a dispersion, which was only 6% of that arising from the second order system. Recently Yoonjae [236] performed the study of field distribution and radiation pattern of a plasma column antenna using the FDTD technique.

References:

1.   D.D Grieg and H.F. Englemann, "Microstrip—A New Transmission Technique for the Kilomegacycle Range," *Proc. IRE*, vol.40, no.10, pp.1644-1650, 1952.

2.   G.A. Deschamps, "Microstrip Microwave Antennas," *The Third Symposium on The USAF Antenna Research and Development Program, University of Illinois*, Monticello, Illinois, October 18-22, 1953.

3.   H. Gutton and Baissinot, "Flat Aerial for Ultra High Frequencies," *French Patent* no. 703113, 1955.

4.   Wu, Tsun, Tai, "Theory of the Microstrip," *Journal of Applied Physics*, vol.28, no.3, pp.299-302, March 1957.

5.   H.A. Wheeler, "Transmission Line Properties of Parallel Strips Separated by a Dielectric Sheet," *IEEE Trans. Microwave Theory Tech.*, vol.MTT-13, pp.172-185, March 1965.

6.   R.A. Purcel, D.J. Masse and C.P. Hartwig, "Losses in Microstrip," *IEEE Trans Microwave Theory Tech.*, pp.342-350, June 1968.

7.   R.A. Purcel, D.J. Masse and C.P. Hartwig, Errata: "Losses in Microstrip" *IEEE Trans Microwave Theory Tech.*, pp.1064, December 1968.

8.   Edgar J. Denlinger, "Radiation from Microstrip Radiators," *IEEE Trans Microwave Theory Tech.*, pp. 235-236, April 1969.

9.   J. Watkins, "Circular Resonant Structures in Microstrip," *Electron Lett.*, vol.5, no.21, pp.524-525, October 16 1969.

10.   J. Q. Howell, "Microstrip Antennas," *IEEE International Symposium Digest on Antennas and Propagation*, Williamsburg Virginia, pp.177-180, 1972.

11.   *IEEE Trans. Antennas Propagat.*, January 1981.

12.   K. Itoh and N. Goto, "Dual frequency circularly polarized printed circuit antennas composed of strips and slots," *IEE Proc.*, Pt. H, vol.130, pp.170-174, 1983.

13.   K. Itoh, "Circularly polarized printed antenna with wide axial ratio bandwidth using strip dipoles and slots," *IEE Proc.*, Pt.H, vol.130, pp.397-401, 1983.

14.   N. Das and J.S. Chatterjee, "Conically depressed microstrip patch antenna," *IEE Proc.* Pt. H., vol.130, pp. 193-196, 1983.

15.   V. Palanisamy and R. Garg, "Rectangular ring and H-shaped microstrip antennas -alternatives to rectangular patch antenna," *Electron. Lett.*, vol.21, no.19, pp.874-876, 1985.

16.   P.S. Bhatnagar, J.P. Daniel, K. Mahdjoubi and C. Terret, "Experimental study on stacked triangular microstrip antennas," *Electron. Lett.*, vol.22, pp.864-865, 1985.

17.   Bao F. Wang and Yuen T. Lo, "Microstrip antennas for dual frequency operation," *IEEE Trans. Antennas Propagat.*, vol.32, pp.938-943, September 1984.

18.   C.K. Aanandan and K.G. Nair, "Compact broadband microstrip antenna," *Electron. Lett.*, vol.22, no.20, pp.1064-1065, 1986.

19.   D.M. Pozar and B. Kaufman, "Increasing the bandwidth of a microstrip antenna through proximity coupling," *Electron Lett.*, vol.23, pp.368-369, April 1987.

20.   J. L. Drewniak and P.E. Mayes, "ANSERLIN: a broadband, low-profile circularly polarized antenna," *IEEE Trans. Antennas Propagat.*, vol.37, no.3, pp.281-288, March 1989.

21.   G. Kossiavas, A. Papiernik, J.P. Boisset, and M. Sauvan, "The C-Patch: A Small Microstrip Element," *Electron. Lett.*, vol.25, no.4, pp.253-254, 1989.

22. Supriyo Dey, C.K. Aanandan, P. Mohanan, and K.G. Nair, "A New Compact Circular Patch antenna," *IEEE Antennas Propagat. Soc. Int. Symp.,* Washington, pp.822-825, June 1994.

23. Y. Zhang, T.K. Lo and Y. Hwang, "A dielectric-loaded miniature antenna for microcellular and personal communications," *IEEE Antennas Propagat. Soc. Int. Symp.,* California, pp.1152-1155, June 1995.

24. S. Dey, S. Chebolu, R. Mittra, I. Park, T. Kobayashi and M. Itoh, "A Compact Microstrip Antenna for CP," *IEEE Antennas Propagat. Soc. Int. Symp.,* California, pp.982-985, June 1995.

25. Jacob George, P. Mohanan and K.G. Nair, "A Broadband Low Profile Microstrip Circular patch Antenna," *IEEE Antennas Propagat. Soc. Int. Symp.,* California, pp. 700-703, June 1995.

26. R. Waterhouse, "Small Microstrip Patch antenna," *Electron. Lett.,* vol. 31, No. 8, pp.604-605, 1995.

27. H. Iwasaki, "A circularly polarized rectangular microstrip antenna using single-fed proximity couple method," *IEEE Trans. Antennas Propagat.,* vol.43, pp.895-896, August 1995.

28. J. George, M. Deepukumar, C.K. Aanandan, P. Mohanan and K. G. Nair, "New compact microstrip antenna," *Electron. Lett.,* vol.32, no.6, pp.508-509, March 1996.

29. H.T. Chen, "Experimental results of compact microstrip antennas," *IEEE Antennas Propagat. Soc. Int. Symp.,* Montreal, pp.932-935, 14-17 April 1997.

30. T. K. Lo, C. O. Ho, Y. Hwang, E. K. W. Lam, and B. Lee, "Miniature aperture-coupled microstrip antenna of very high permittivity," *Electron. Lett.,* vol.33, no.1, pp.9-10, 1997.

31. L. Economou and R.J. Langley, "Patch antenna equivalent to simple monopole," *Electron. Lett.,* vol.33, no.9, pp. 727-728, April 1997..

32. Jacob George, C.K. Aanandan, P. Mohanan, K.G. Nair, H. Sreemoolanadhan and M.T. Sebastian, "Dielectric-resonator-loaded microstrip antenna for enhanced impedance bandwidth and efficiency," *Microwave and Opt. Technol. Lett.,* vol.17, no.3, pp.205-207, February 1998.

33. L. Zaid, G. Kossiavas, J.Y. Dauvignac and A. Papiernik, "Very Compact Double C-Patch Antenna," *Electron. Lett.,* vol.34, no.10, pp.933-934, May 1998.

34. Kin-Lu Wong and Ming-Huang Chen, "Single-feed small circular Microstrip antenna with circular polarization," *Microwave and Opt. Technol. Lett.,* vol.18, no.6, pp.394-397, August 1998.

35. K.M. Luk, L.K. Au Young, C.L. Mak and K.F. Lee, "Circular patch antenna with an L-shaped probe," *Microwave and Opt. Technol. Lett.,* vol.20, no.4, pp.256-257, February 1999.

36. Chia-Luan Tang and Kin-Lu Wong, "A modified equilateral-triangular-ring microstrip antenna for circular polarization," *Microwave and Opt. Technol. Lett.,* vol.23, no.2, pp.123-126, October 1999.

37. Sean M. Duffy, "An enhanced bandwidth design technique for electromagnetically coupled microstrip antennas," *IEEE Trans. Antennas Propagat.,* vol.48, no.2, pp.161-164, February 2000.

38. Kin-Fai Tong, Kwai-Man Luk, Kai-Fong Lee and Richard Q. Lee, "A broadband U-slot rectangular patch antenna on a microwave substrate," *IEEE Trans. Antennas Propagat.,* vol.48, no.6, pp. 954-960, June 2000.

39.   J.Y Sze and K.L. Wong, "Slotted rectangular microstrip antenna for bandwidth enhancement," *IEEE Trans. Antennas Propagat.*, vol.48, no.8, pp.1149-1152, August 2000.

40.   Manju Paulson, Sona O. Kundukulam, C.K. Aanandan, P. Mohanan and K. Vasudevan, "Circularly Polarised compact microstrip antenna," *Microwave and Opt. Technol. Lett.*, vol.26, no.5, pp.308-309, September 2000.

41.   Jui-Han Lu and Kin-Lu Wong, "Single-feed circularly polarised equilateral-triangular microstrip antenna with a tuning stub," *IEEE Trans. Antennas Propagat.*, vol.48, no.12, pp.1869-1872, December 2000.

42.   Fan Yang, Xue-Xia Zhang, Xiaonong Ye and Yahya Rahmat-Samii, "Wide-band E-shaped Patch antennas for wireless communications," *IEEE Trans. Antennas Propagat.*, vol. 49, no.7, pp.1094-1100, July 2001.

43.   S. Lee, J. Woo, M. Ryu and H. Shin, "Corrugated circular microstrip patch antennas for miniaturization," *Electron. Lett.*, vol.38, no.6, pp.262-263, 14 March 2002.

44.   Y.W. Jang, "Broadband T-shaped microstrip-fed U-slot coupled patch antenna," *Electron. Lett.*, vol.38, no.11, pp.495-496, May 2002.

45.   H.C. Chen, "Compact circularly polarised microstrip antenna with slotted ground plane," *Electron. Lett.*, vol.38, no.13, pp.616-617, June 2002.

46.   Debatosh Guha, "Microstrip and Printed antennas: recent trends and developments," Proc. *International conference on telecommunication in Modern Satellite, Cables and Broadcasting sevices*, (TELSIKS),University of NiS, Serbia and Montenegro, pp.39-43, 1-3 October 2003.

47.   Aaron K. Shackelford, Kai-Fong Lee and K.M. Luk, "Design of small-size wide-bandwidth microstrip patch antennas," *IEEE Antennas and propagat. Mag.*, vol.45, no.1, pp.75-83, February 2003.

48.   Che-Wei Su and Kin-Lu Wong, "Circularly polarised microstrip antenna with a rectangular ground plane," *Microwave and Opt. Technol. Lett.*, vol.37, no.2, pp.93-95, April 2003.

49.   Chi Yuk Chiu, Kam Man Shum, Chi Hou Chan and Kwai Man Luk, "Bandwidth enhancement technique for quarter-wave patch antennas," *IEEE Antennas and wireless propagation Lett.*, vol.2, pp.130-133, 2003.

50.   L. Boccia, G. Amendola and G.Di Massa, "A shorted elliptical patch antenna for GPS applications," *IEEE Antennas and wireless propagation Lett.*, vol.2, pp.6-8, 2003.

51.   Qinjiang Rao, Tayeb A. Denidni and Ronald H.Johnston, "Miniaturised Aperture-coupled microstrip antennas," *IEEE Antennas Propagat. Soc. Int. Symp., Monterrey*, July 2004.

52.   Kin-Lu Wong, Ting-Chih Teeng and Pay-Ling Teng, "Low-profile ultra-wideband antenna for mobile phone applications," *Microwave and Opt. Technol. Lett.*, vol.43, no.1, pp.7-9, October 2004.

53.   M. Lapierre, Y.M.M. Antar, A. Ittipiboon and A. Petosa, "Ultra Wideband Monopole/Dielectric Resonator Antenna," *IEEE Microwave and wireless components Lett.*, vol.15, no.1, pp.7-9, January 2005.

54.   Choon Sae Lee, Vahakn Nalbandian and Felix Schwering, "Planar dual-band microstrip antenna," *IEEE Trans. Antennas Propagat.*, vol.43, no.8, pp.892-894, August 1995.

55.   Z.D. Liu and P.S. Hall, "Dual-band Antenna for Hand Held Portable Telephones," *Electron. Lett.*, vol.32, no.7, pp.609-610, March 1996.

56.   M. Sanad, "A Compact Dual-Broadband Microstrip Antenna having both Stacked and planar Parasitic Elements," *IEEE Antennas Propagat. Soc. Int. Symp.*, Maryland, pp.6-9, July 1996.

57.   M. Deepukumar, J. George, C.K. Aanandan, P. Mohanan and K.G. Nair, "Broadband Dual Frequency Microstrip Antenna," *Electron. Lett.*, vol.32, no. 17, pp.1531-1532, August 1996.

58.   D. Sanchez-Hernandez, G. Passiopoulos, M. Ferrando, E.de los Reyes and I. D. Robertson, "Dual-Band Circularly Polarized Antenna with a Single Feed", *Electron. Lett.*, vol.32, no.25, pp.2296-2298, December 1996.

59.   K.L. Wong and K.P. Yang, "Small dual frequency microstrip antenna with cross slot," *Electron. Lett.*, vol.33, no.23, pp 1916-1917, 1997.

60.   Kin-Lu Wong and Wen-Shan Chen, "Compact microstrip antenna with dual frequency operation," *Electron. Lett.*, vol.33, no.8, pp 646-647, April 1997.

61.   C.L. Tang, H.T. Chen and K.L. Wong, "Small Circular Microstrip Antenna with Dual Frequency Operation," *Electron. Lett.*, vol.33, no.13, pp.1112-1113, 1997.

62.   Shan-Cheng Pan and Kin-Lu Wong, "Dual-frequency triangular microstrip antenna with a shorting pin," *IEEE Trans. Antennas Propagat.*, vol.45, no.12, pp.1889-1891, December 1997.

63.   Kin-Lu Wong and Wen-Shan Chen, "Slot-Loaded Bow-Tie Microstrip Antenna for Dual-Frequency Operation", *Electron. Lett.*, vol.34, no.18, pp.1713-1714, September 1998.

64.   Kin-Lu Wong and Gui-Bin Hsieh, "Dual-frequency circular microstrip antenna with a pair of arc-shaped slots," *Microwave and Opt. Technol. Lett.*, vol.19, no.6, pp. 410-412, December 1998.

65.   Jui-Han Lu and Kin-Lu Wong, "Slot-loaded, meandered rectangular microstrip antenna with compact dual-frequency operation," *Electron. Lett.*, vol.34, no.11, pp.1048-1049, May 1998.

66.   J. George, K. Vasudevan, P. Mohanan and K.G. Nair, "Dual Frequency Miniature Microstrip Antenna", *Electron. Lett.*, vol.34, no.12, pp.1168-1170, June 1998.

67.   Gui-Bin Hsieh, Ming-Huang Chen and Kin-Lu Wong, "Single-feed dual-band circularly polarized microstrip antenna", *Electron. Lett.*, vol.34, no.12, pp.1170-1171, June 1998.

68.   Jui-Han Lu and Kin-Lu Wong, "Single-feed dual-frequency equilateral triangular microstrip antenna with a pair of spur lines," *Electron. Lett.*, vol.34, no. 12, pp.1171-1173, June 1998.

69.   Chia-Luan Tang, Jui-Han Lu and Kin-Lu Wong, "Circularly polarized equilateral-triangular microstrip antenna with truncated tip," *Electron. Lett.*, vol.34, no.13, pp.1277-1278, June 1998.

70.   Wen-Shyang Chen, Chen-Kun Wu and Kin-Lu Wong, "Compact circularly polarized microstrip antenna with bent slots," *Electron. Lett.*, vol.34, no.13, pp.1278-1279, June 1998.

71.   Kin-Lu Wong and Jia-Yi Sze, "Dual-Frequency Slotted Rectangular Microstrip Antenna", *Electron. Lett.*, vol.34, no.14, pp.1368-1370, July 1998.

72.   N. Chiba, T. Amano and H. Iwasaki, "Dual-Frequency Planar Antenna for Handsets", *Electron. Lett.*, vol.34, no.25, pp.2362-2363, December 1998.

73.   A. Hoorfar, G. Girard and A. Perotta, "Dual frequency circularly polarized proximity-fed microstrip antenna," *Electron. Lett.*, vol.35, no.10, pp.759-761, May 1999.

74.   R. Chair, K. M. Luk and K.F. Lee, "Small Dual Patch Antenna", *Electron. Lett.*, vol.35, no.10, pp.762-764, May 1999.

75.   E. Lee, P.S. Hall and P. Gardiner, "Compact Dual-Band Dual-Polarisation Microstrip Patch Antenna", *Electron. Lett.*, vol.35, no.13, pp.1034-1036, June 1999.

76.   Yeunjeong Kim, Wansuk Yun and Youngjoong Yoon, "Dual-Frequency and Dual Polarisation Wideband Microstrip Antenna", *Electron. Lett.*, vol.35, no. 17, pp. 1399-1400, August 1999.

77.   Jui-Han Lu, "Single-Feed Dual-Frequency Rectangular Microstrip Antenna with pair of Step-Slots", *Electron. Lett.*, vol.35, no.5, pp.354-355, March 1999.

78.   Jui-Han Lu, "Novel dual frequency design of single-feed equilateral-triangular microstrip antenna," *Microwave and Opt. Technol. Lett.*, vol.22, no.2, pp.133-136, July 1999.

79.   T. Williams, M. Rehman and M.A. Stuchly, "Dual-band Meander antenna for wireless telephones," *Microwave and Opt. Technol. Lett.*, vol.24, no.2, pp.81-85, January 20 2000.

80.   Sona O. Kundukulam, Manju Paulson, C.K. Aanandan, P. Mohanan and K. Vasudevan, "Dual-band dual-polarised compact microstrip antenna", *Microwave and Opt. Technol. Lett.*, vol.25, no.5, pp.328-330, June 2000.

81.   Pekka Salonen, Mikko Keskilammi and Markku Kivikoski, "Single-feed dual-band planar inverted-F antenna with U-shaped slot," *IEEE Trans. Antennas Propagat.*, vol.48, no.8, pp.1262-1264, August 2000.

82.   S. Maci and G. Biffi Gentili, "Dual-Frequency Patch Antennas," *IEEE Antennas and Propagat. Mag.*, vol.39, no.6, pp.13-19, August 2000.

83.   Kai-Ping Yang and Kin-Lu Wong, "Dual-band circularly-polarized square microstrip antenna," *IEEE Trans. Antennas Propagat.*, vol.49, no.3, pp.377-381, March 2001.

84.   P. Salonen, M. Keskilammi and M. Kivikoski, "New slot configurations for dual band planar inverted F antenna," *Microwave and Opt. Technol. Lett.*, vol.28, no.5, pp.293-298, March 2001.

85.   W. Reed, L. Desclos, C. Terret and S. Toutain, "Patch antenna size reduction by means of inductive slots," *Microwave and Opt. Technol. Lett.*, vol.29, no.2, pp.79-81, April 2001.

86.   Manju Paulson, Sona O. Kundukulam, C.K. Aanandan and P. Mohanan, "A new compact dual-band dual-polarised microstrip antenna", *Microwave and Opt. Technol. Lett.*, vol.29, no.5, pp.315-317, June 2001.

87.   J.Y. Wu, J.S. Row and K.L. Wong, "A compact dual band microstrip patch antenna for DCS/GPS operations," *Microwave and Opt. Technol. Lett.*, vol.29, no.6, pp.410-412, June 2001.

88.   H.C.Tung and K.L.Wong, "A shorted microstrip antenna for 2.4/5.2GHz dual band operation," *Microwave and Opt. Technol. Lett.*, vol.30, no.6, pp.401-402, September 2001.

89.   Sona O Kundukulam, Manju Paulson, C.K. Aanandan and P. Mohanan, "Slot-loaded compact microstrip antenna for dual-frequency operation", *Microwave and Opt. Technol. Lett.*, vol.31, no.5, pp. 379-381, December 2001.

90.   Yen-Liang Kuo and Kin-Lu Wong, "A planar inverted-L patch antenna for 2.4/5.2 GHz dual-band operation," *Microwave and Opt. Technol. Lett.*, vol.31, no.5, pp.394-397, December 2001.

91.   Y.J. Wang, "Design of dual-frequency microstrip patch antennas and application for IMT-2000 mobile handsets," Proc. *Progress in Electromagnetics Research*, PIER 36, pp.265-278, 2002.

92. Marta Martinez-Vazquez, Matthias Geisster, Dirk Heberling, Antonio Martinez-Gonzalez and David Sanchez-Hernandez, "Compact dual-band antenna for mobile handsets," *Microwave and Opt. Technol. Lett.*, vol.32, no.2, pp. 87-88, January 20 2002.

93. H.M. Chen, "Microstrip-fed dual-frequency printed triangular monopole," *Electron. Lett.*, vol.38, no.13, pp.619-620, June 2002.

94. S.H. Yeh and K.L Wong, "Integrated F shaped Monopole antenna for 2.4/5.2GHz dual band operation," *Microwave and Opt. Technol. Lett.*, vol.34, no.1, pp.24-26, July 2002.

95. Y.F. Lin, C.C. Kuo and H.M. Chen, "Compact dual frequency shorted Rhombic microstrip antenna with a pair of slits," *Microwave and Opt. Technol. Lett.*, vol.34, no.3, pp.183-186, August 2002.

96. H.C. Tung, S.T. Fang and K.L. Wong, "Printed dual band monopole antenna for 2.4/5.2GHz WLAN access point," *Microwave and Opt. Technol. Lett.*, vol.35, no.42, pp.286-288, November 2002.

97. C.M. Su, H.T. Chen, F.S. Chang and K.L. Wong, "Dual band slot antenna for 2.4/5.2GHz WLAN operation," *Microwave and Opt. Technol. Lett.*, vol.35, no.42, pp.306-308, November 2002.

98. Jouko Heikkinen and Markku Kivikoski, "A novel dual-frequency circularly polarized rectenna," *IEEE Antennas and Wireless Propagat. Lett.*, vol.2, 2003.

99. A. Gadzinea and P. Slobodzian, "Concept of a compact dual-band dual-port Microstrip base station antenna for mobile communication systems," *Microwave and Opt. Technol. Lett.*, vol.36, no.3, pp.218-221, February 5 2003.

100. Ching-Yuan Chiu, Pey-Ling Teng and Kin-Lu Wong, "Shorted, folded planar monopole antenna for dual-band mobile phone," *Electron. Lett.*, vol.39, no.4, pp.1301-1302, September 2003.

101. Y.L. Kuo and K.L. Wong, "Printed double T – monopole antenna for 2.4/5.2 GHz dual band WLAN operations," *IEEE Trans. Antennas Propagat.*, vol.51, no.9, pp.2187-2192, September 2003.

102. J.Y. Jan, "Single layer single feed dual frequency circular microstrip antenna with an offset open ring slot," *IEEE Trans. Antennas Propagat.*, vol. 51, no.10(Part II), pp.3010-3012, October 2003.

103. Dongsheng Qi, Binhong Li, Yahin Zhang and Haitao Liu, "A compact novel slot loaded dual frequency H shaped antenna," *Microwave and Opt. Technol. Lett.*, vol.40, pp.248-250, February 2004.

104. M. Ali, T. Sittironnarit, H.S. Hwang, R.A. Sadler and G.J. Hayes, "Wideband/Dual-band packaged antenna for 5-6GHz WLAN application," *IEEE Trans. Antennas Propagat.*, vol.52, no.2, pp.610-615, February 2004.

105. P. Ciais, R. Staraj, G. Kossiavis and C. Luxey, "Compact internal multiband antenna for mobile phones and WLAN standards," *Electron. Lett.*, vol.40, no.15, April 2004.

106. H.D. Chen and H.T. Chen, "A CPW fed dual frequency monopole antenna," *IEEE Trans. Antennas Propagat.*, vol.52, no.4, pp.978-982, April 2004.

107. T. Sudha, T.S. Vedavathy and N. Bhat, "Wideband single fed circularly polarized patch antenna," *Electron. Lett.*, vol.40, no.11, pp.648-649, May 2004.

108. G.Y. Chen and J.S. Sun, "Low profile planar dipole antenna," *Electron. Lett.*, vol.40, no.13, pp.790-791, June 2004.

109. J.I. Moon, D.U. Sim and S.O. Park, "Compact PIFA for 2.4/5GHz dual ISM applications," *Electron. Lett.*, vol.40, no.14, pp.844-845, July 2004.

110.   Y.X. Guo, M.Y.W. Chia and Z.N. Chen, "Miniature built-in multiband antennas for mobile handsets," *IEEE Trans. Antennas Propagat.*, vol.52, no.8, pp.1936-1944, August 2004.

111.   W.C. Liu and W.R. Chen, "CPW-fed compact meandered patch antenna for dual band operation," *Electron. Lett.*, vol.40, no.18, pp.1094-1095, September 2004.

112.   Gh.Z Rafi and Shafai, "Wide band V slotted diamond shaped microstrip patch antenna," *Electron. Lett.*, vol.40, no.19, pp.1166-1167, September 2004.

113.   H.M Chen, J.M. Chen, P.S. Cheng and Y.F. Lin, "Feed for dual band printed dipole antenna," *Electron. Lett.*, vol.40, no.21, pp.1320-1320, October 2004.

114.   S.Y. Chen and P. Hsu, "CPW fed folded slot antenna for 5.8GHz RFID tags," *Electron. Lett.*, vol.40, no. 24, pp.1516-1517, November 2004.

115.   S.H. Wang, J.I. Moon, W.I. Kwak and S.O. Park, "Printed compact dual band antenna for 2.4 and 5GHz ISM band applications," *Electron. Lett.*, vol.40, no. 25, pp.1568-1569, December 2004.

116.   J.S. Chen, "Dual frequency annular ring slot antennas fed by CPW feed and microstrip line feed," *IEEE Trans. Antennas Propagat.*, vol.53, no.1(Part II), pp.569-571, January 2005.

117.   K.L. Wong, L.C. Chou and C.M. Su, "Dual band flat plate antenna with a shorted parasitic element for laptop applications," *IEEE Trans. Antennas Propagat.*, vol.53, no.1(Part II), pp.539-544, January 2005.

118.   S. Gao and A. Sambell, "Dual polarized broad band microstrip antennas fed by proximity coupling," *IEEE Trans. Antennas Propagat.*, vol.53, no.1(Part II), pp. 526-530, January 2005.

119.   P. Li, K.L. Lau and K.M. Luk, "Wideband folded shorted patch antenna with low profile," *Electron. Lett.*, vol.41, no.3, pp.112-113, February 2005.

120.   S.Y. Lin and K.C. Huang, "A compact microstrip antenna for GPS and DCS application," *IEEE Trans. Antennas Propagat.*, vol.53, no.3, pp.1227-1229, March 2005.

121.   I.F. Chen, C.M. Peng and S.C. Liang, "Single layer printed monopole antenna for dual ISM operation," *IEEE Trans. Antennas Propagat.*, vol.53, no.4, pp. 1274-1277, April 2005.

122.   W.C. Liu and C.F Hsu, "Dual band CPW fed Y-shaped monopole antenna for PCS/WLAN application," *Electron. Lett.*, vol.41, no.7, pp.390-391, March 2005.

123.   Z. Zhang, M.F. Iskander, J.C. Langer and J. Mathews, "Dual band WLAN dipole antenna using an internal matching circuit," *IEEE Trans. Antennas Propagat.*, vol.53, no.5, pp.1813-1818, May 2005.

124.   P. Li, K.M. Luk and K.L. Lau, "A Dual feed Dual band L-probe patch antenna," *IEEE Trans. Antennas Propagat.*, vol.53, no.7, pp.2321-2323, July 2005.

125.   G.H. Robinson, "Resonant frequency calculations for Microstrip cavities," *IEEE Trans. Microwave Theory Tech.*, pp.665-666, July 1971.

126.   Ingo Wolff and Norbert Knoppik, "Rectangular and circular Microstrip disk capacitors and resonators," *IEEE Trans. Microwave Theory Tech.*, vol.22, no. 10, pp. 857-864, October 1974.

127.   Jashwant S. Dahele and Kai Fong Lee, "On the resonant frequencies of the triangular Patch antenna," *IEEE Trans. Antennas Propagat.*, vol.35, no.1, pp. 100-101, January 1987.

128. Ramesh Garg and Stuart A. Long, "An improved formula for the resonant frequencies of the triangular Microstrip patch antenna," *IEEE Trans. Antennas Propagat.*, vol.36, no.4, pp.570-571, April 1988.

129. Russel W. Dearnley and Alain R.F. Barel, "A comparison of models to determine the resonant frequencies of a rectangular Microstrip antenna," *IEEE Trans. Antennas Propagat.*, vol.37, no.1, pp.114-118, January 1989.

130. Xu Gang, "On the resonant frequencies of Microstrip Antenna," *IEEE Trans. Antennas Propagat.*, vol.37, no.2, pp.245-247, February 1989.

131. K. Antoszkiewicz and Lotfollah Shafai, "Impedance characteristics of circular Microstrip patches," *IEEE Trans. Antennas Propagat.*, vol.38, no.6, pp.42-946, June 1990.

132. R.K. Mishra and S.S. Pattnaik, "Resonant frequency of wedge shaped Microstrip Antenna," *Electron. Lett.*, vol.26, no.13, pp.912-913, 21 June 1990.

133. A. Bhattacharyya, "Electromagnetically coupled patch antenna – theoretical and experimental investigations," *Microwave Opt. Technol. Lett.*, vol.5, no.3, pp.115-118, March 1992.

134. Wei Chen, Kai-Fong Lee and Jashwant S. Dahele, "Theoretical and experimental studies of the resonant frequencies of the equilateral triangular microstrip antenna," *IEEE Trans. Antennas Propagat.*, vol.40, no.10, pp.1253-1256, October 1992.

135. S.R. Rengarajan, "Resonance frequency of elliptical microstrip antennas," *Electron. Lett.*, vol.29, no.12, pp.1066-1067, 10 June 1993.

136. Nirun Kumprasert and Wiwat Kiranon, "Simple and accurate formula for the resonant frequency of the equilateral triangular Microstrip Patch Antenna," *IEEE Trans. Antennas Propagat.*, vol.42, no.8, pp.1178-1179, August 1994.

137. Nirun Kumprasert and Wiwat Kiranon, "Simple and accurate formula for the resonant frequency of the circular Microstrip Disk Antenna," *IEEE Trans. Antennas Propagat.*, vol. 43, no.11, pp.1331-1333, November 1995.

138. Rajanish and T.S. Vedavathy, "Resonant frequency of higher order modes for circular microstrip antennas," *Proc. Asia Pacific Microwave Conference (APMC-'99)* pp.936-939, 1999.

139. Jean-Marc Ribero and Jean-Pierre Damiano, "Determination of the resonance frequency of an ellipsoidal structure," *Microwave Opt. Technol. Lett.*, vol.23, no.1, pp.64-65, October 5 1999.

140. K.P. Ray and Girish Kumar, "Determination of the resonant frequency of microstrip antennas," *Microwave Opt. Technol. Lett.*, vol.23, no.2, pp.114-17, October 20 1999.

141. Rabindra K. Mishra, "Simple method for determining the bandwidth of rectangular patch antenna," *IEEE Antennas Propagat. Soc. Int. Symp., Salt lake city*, Uttah, pp.1402-1404, 17-21 July 2000.

142. Debatosh Guha, "Resonant frequency of circular microstrip antennas with and without air gaps," *IEEE Trans. Antennas Propagat.*, vol.49, no.1, pp.55-59, January 2001.

143. M. Paulson, S.O. Kundukulam, C.K. Aanandan and P. Mohanan, "Resonance frequencies of compact microstrip antenna," *Electron. Lett.*, vol.37, no.19, pp.1151-1153, 13 September 2001.

144. A.K. Verma and Nasimuddin, "Resonance frequency of rectangular microstrip antenna on thick substrate," *Electron. Lett.*, vol.37, no.23, pp.1373-1374, 8 November 2001.

145.   A.K. Verma and Nasimuddin, "Resonance frequency and bandwidth of rectangular microstrip antenna on thick substrate," *IEEE Microwave and wireless component letters*, vol.12, no.2, pp.60-62, February 2002.

146.   Rajanish and T.S. Vedavathy, "A generalized expression for resonant frequency of circular microstrip antennas," *Proc. Asia Pacific Microwave Conference (APMC-2000)* Dec 3-6, 2000.

147.   R.E. Munson, "Conformal Microstrip Antennas and Microstrip Phased Arrays," *IEEE Trans. Antennas Propagat.*, vol. 22, no.1, pp.235-236, January 1974.

148.   J.R. James and C.J. Wilson, "Microstrip antennas and arrays Part-I: Fundamental actions and limitations, "*IEE Proc. Microwaves, Opt. And Antennas*, vol.1, pp.165-174, 1977.

149.   P.K. Agarwal and M.C. Bailey, "An analysis technique for microstrip antennas," *IEEE Trans. Antennas Propagat.*, vol.25, pp.756-759, 1977.

150.   Y.T. Lo, D. Solomon, and W.F. Richards, "Theory and Experiment on Microstrip Antennas," *IEEE Trans. Antennas Propagat.*, vol.27, pp.137-149 1979.

151.   G. Derneryd, "Analysis of the microstrip disc antenna element," *IEEE Trans. Antennas Propagat.*, vol.27, pp.660-664, 1979.

152.   P. Hammer, D. Van Bouchante, D. Verschraevan and A. Van de Capelle, "A model for calculating the radiation field of microstrip antennas," *IEEE Trans. Antennas Propagat.*, vol.27, pp.267-270, 1979.

153.   E.H. Newman and P. Tulyathan, "Analysis of microstrip antennas using moment methods," *IEEE Trans. Antennas Propagat.*, vol.29, pp.47-53, 1981.

154.   J.R. Mosig and F.E. Gardiol, "Analytical and Numerical Techniques in the Green's Function Treatment of Microstrip Antennas and Scatterers," *IEE Proceedings*, vol. 130, Pt. H., no.2, pp.175-182, March 1983.

155.   K. Mahdjoubi, J. P. Daniel and C. Terret, "Dual frequency disc antennas studied by cavity method", *Electron. Lett.*, vol.22, pp.125-126, 1986.

156.   J.R Mosig, "Arbitrarily Shaped Microstrip Structures and Their Analysis with a Mixed Potential Integral Equation," *IEEE Trans. Microwave Theory Tech.*, vol. 36, no.2, February 1988.

157.   L.T. Hildebrand and Derek A. McNamara, "A Guide to Implementation Aspects of the Spatial-Domain Integral Equation Analysis of Microstrip Antennas," *Applied Computational Electromagnetics Journal*, vol.10, no.1, pp. 40-51 March 1995.

158.   Fred E. Gardiol, "Mixed potential integral equation methods for multilayered structures," *Proc. Mathematical Methods in Electromagnetic Theory (MMET)*, Ukraine, pp.16-27, September 10-13,1996.

159.   S. Sriram and T.S. Vedavathy, "Novel analysis scheme to analyze multilayer dielectric microstrip antennas," *Proc. Asia Pacific Microwave Conference (APMC-1999)*, pp.924-927, November 30-December-6, 1999.

160.   Mahesh P. Abegaonkar, Yu-Kang Heo and Young-Ki Cho, "Field configurations for electromagnetically coupled microstrip patch antenna," *IEEE Antennas Propagat. Soc. Int. Symp., Colombus* USA, vol.3, pp.128-131, 22-27 June 2003.

161.   K.P. Carver and J.W. Mink, "Microstrip antenna technology," *IEEE Trans. Antennas Propagat.*, vol.29, pp.2-24, 1981.

162.   T. Itoh and W. Menzel, "A full-wave analysis method for open microstrip structures," *IEEE Trans. Antennas Propagat.*, vol.29, pp.63-68, 1981.

163.   E. F. Kuester, R.T. Johak, and D.C. Chang, "The Thin Substrate Approximation for Reflection from the End of the Slab Loaded Parallel Plate Wave Guide with

Application to Microstrip patch", *IEEE Trans. Antennas Propagat.,* vol.30, pp. 910-917, 1982.

164. D.L. Sengupta, "Approximate expression for the resonant frequency of a rectangular patch antenna", *Electron. Lett.,* vol.19, pp.834-835, 1983.

165. E. Lier and K.R. Jakobsen, "Rectangular microstrip patch antennas with infinite and finite ground plane dimensions," *IEEE Trans. Antennas Propagat.,* vol.31, pp.978-984, November 1983.

166. H. Pues and Van De Capelle, "Accurate transmission-line model for the rectangular microstrip antenna," *IEE Proc.,* vol.131, Pt.H., pp334-340, 1984.

167. E. Penard and J.P. Daniel, "Open and hybrid microstrip antennas," *IEE Proc.,* Part II, vol.131, pp.38-44, 1984.

168. S.K. Das and S.P. Mathur, "Radiation characteristics of higher order modes in microstrip ring antenna," *IEE Proc.,* Part II, vol.131, pp.102-106, 1984.

169. W.F. Richards, J.D. Ou and S.A. Long, "A theoretical and experimental investigation of annular sector and circular sector microstrip antennas," *IEEE Trans. Antennas Propagat.,* vol.32, pp.864-867, 1984.

170. S.T. Chu and S.K. Chaudhuri, "Combining modal analysis and the Finite Difference Time Domain method in the study of dielectric waveguide problems," *IEEE Trans. Microwave Theory Tech.,* vol.38, no.11, November 1990.

171. Nemal C. Karmakar, "Electromagnetically coupled patch antenna – theoretical and experimental investigations," *Microwave and Opt. Technol. Lett.,* vol.5, no.3, pp.115-118, March 1992.

172. A. Kishk, "Analysis of spherical annular microstrip antennas," *IEEE Trans. Antennas Propagat.,* vol.41, pp.338-343, March 1993.

173. T. Kashiwa, T. Onishi and I. Fukai, "Analysis of microstrip antennas on a curved surface using the conformal grids FDTD method", *IEEE Trans. Antennas Propagat.,* vol.42, pp.423-427, March 1994.

174. S.A. Bokhari, J.F. Zucher, J.R. Mosig and F.E. Gardiol, "Near fields of microstrip antennas," *IEEE Trans. Antennas Propagat.,* vol.43, pp.188-197, February 1995.

175. S. Dey and R. Mittra, "Compact microstrip patch antenna," *Microwave and Opt. Technol. Lett.,* vol.13, no.1, pp.12-14, September 1996.

176. Iti Saha Misra and S.K. Chowdhury, "Study of impedance and radiation properties of a concentric microstrip triangular-ring antenna and its modeling techniques using FDTD method," *IEEE Trans. Antennas Propagat.,* vol.46, no.4, pp. 531-538, April 1998.

177. Allen Taflov Ed., "Advances in Computational Electrodynamics: The Finite-Difference Time-Domain Method," Artech House, 1998.

178. Allen Taflov and Susan C. Hagness, "Computational Electrodynamics: The Finite-Difference Time-Domain Method," Second Edition, Artech House, 2000.

179. H. Holter and H. Steyskal, "Broadband FDTD analysis of infinite phased arrays using periodic boundary conditions," *Electron. Lett.,* vol.35, no.13, pp.758-759, May 1999.

180. D. Guha and J.Y. Siddique, "New CAD model to calculate the resonant frequency of inverted microstrip circular patch antennas," *Microwave and Opt. Technol. Lett.,* vol.35, no.6, pp.434-437, December 20 2002.

181. M.N.O Sadiku, "Numerical Techniques in Electromagnetics," 2nd edition, CRC press LLC, 2001.

182.   K.S. Yee, "Numerical solution of initial boundary value problems involving Maxwell's equations in isotropic media," *IEEE Trans. Antennas Propagat.*, vol.14, pp. 302-307, May 1966.

183.   A.C. Cangellaris and D.B. Wright, "Analysis of the numerical error caused by the stair stepped approximation of a conducting boundary in FDTD simulations of electromagnetic phenomena," *IEEE Trans. Antennas Propagat.*, vol.39, pp. 1518-1525, 1991.

184.   R. Holland, "Pitfalls in staircase meshing," *IEEE Trans. on Electromagnetic Compatibility*, vol. EMC-35, pp 434-439, 1993.

185.   K.S. Kunz and L. Simpson, "A technique for increasing the resolution of finite difference solution of Maxwell's equation," *IEEE Trans. on Electromagnetic Compatibility*, vol. EMC-23, pp 419-422, 1981.

186.   Svetlna S. Zivanovic, Kane S. Yee and Kenneth K. Mei, "A subgridding method for the Time Domain Finite Difference method to solve Maxwell's equations," *IEEE Trans. Microwave Theory Tech.*, vol.MTT-39(3), pp.471-479, March 1991.

187.   Roberto Sorrentino, Luca Roselli and Paolo Mezzanotte, "Time reversal in finite difference time domain method," *IEEE Microwave and Guided wave Lett.*, vol.3, no.11, pp.402-404, November 1993.

188.   K. Uehara and K. Kagoshima, "Rigorous analysis of microstrip phased array antennas using a new FDTD method," *Electron Lett.*, vol.30, no.2, pp.100-101, January 1994.

189.   R.J Luebbers, F. Hunsberger, K.S. Kunz, R.B. Standler and M. Schneider, "A frequency dependant finite difference time domain formulation for dispersive materials," *IEEE Trans. on Electromagnetic Compatibility*, vol. EMC-32, pp. 222-227, 1990.

190.   B. Toland, B. Houshmand and T. Itoh, "Modelling of Non linear active regions with the FDTD method," *IEEE Microwave and Guided wave Lett.*, vol.3, no.9, pp.333-335, September 1993.

191.   Dennis M. Sullivan, "Z-transform theory and the FDTD method," *IEEE Trans. Antennas Propagat.*, vol.44, pp.28-34, January 1996.

192.   Michael W. Chevlier, R.J. Leubbers and Vaughn P. Cable , "FDTD local grid with material traverse," *IEEE Trans. Antennas Propagat.*, vol.45, pp.411-424, March 1997.

193.   Michal Okoniewski, Ewa Okoniewska and Maria A. Stuchly, "Three dimensional sub-gridding algorithm for FDTD," *IEEE Trans. Antennas Propagat.*, vol.45, pp.422-429, March 1997.

194.   K.M. Krishnaiah and C.J. Railton, "Passive equivalent circuit of FDTD: An application to sub - gridding," *Electron Lett.*, vol.33, no.15, pp.1277-1278, July 1997.

195.   Ugur Oguz, Levent Gurel and Orhan Arikan, "An efficient and accurate technique for the incident wave excitations in the FDTD method," *IEEE Trans. Microwave Theory Tech.*, vol. MTT-46(6), pp.869-882, June 1998.

196.   M. Kar and P.F. Wahid, "The FDTD analysis of a microstrip patch antenna with dual feed lines," *Proc. IEEE Southeast conference*, April 24-26 1998.

197.   J. Gomez-Tagle, C.G. Christodoulu, P.F. Wahid, T. Miles and A. Wall, "Active impedance analysis of finite phased array microstrip antennas using the finite difference time domain method," *Proc. IEEE Antennas Propagat. Soc. Int. Symp.(APS-URSI), Atlanta, Georgia*, pp.2024-2026, 21-26 June 1998.

198. T.O. Korner, "3-D refractive index adaptive gridding for finite-difference time-domain methods," *Microwave and Opt. Technol. Lett.,* vol.23, no.2, pp.109-114, October 20 1999.

199. A.C. Cangellaris and Li Zhao, "Rapid FDTD Simulation without time stepping," *IEEE Microwave and Guided wave letters,* vol.9, no.9, pp.4-6, January 1999.

200. Cheih Tsao Hwang and Ruey Beei Wu, "Treating late time instability of hybrid Finite element/ Finite difference time domain method" *IEEE Trans. Antennas Propagat.,* vol.47, pp.227-232, February 1999.

201. Omar M. Ramahi, "Stability of Absorbing Boundary Conditions," *IEEE Trans. Antennas Propagat.,* vol.47, pp.593-599, April 1999.

202. Takefumi Namiki, "A new FDTD algorithm based on Alternating Direction Implicit method," *IEEE Trans. Microwave Theory Tech.,* vol. MTT-47(10), pp. 2003-2007, October 1999.

203. Fenghua Zheng, Zhizhang Chen and Jiazong Zhang, "A Finite Difference Time Domain method without involving the Courant stability conditions," *IEEE Microwave and Guided wave Lett.,* vol.9, no.11 pp.441-446, November 1999.

204. Chris J. Railton, "The inclusion of fringing capacitance and inductance in FDTD for the robust, accurate treatment of material discontinuities," *IEEE Trans. Microwave Theory Tech.,* vol.MTT-48(12), pp.2283-2288, December 2000.

205. Levent Gurel and Ugur Oguz, "Signal Processing techniques to reduce the sinusoidal steady state error in the FDTD method," *IEEE Trans. Antennas Propagat.,* vol.48, pp.585-592, April 2000.

206. Xiaoning Ye and James L. Drewniak, "Incorporating Two port networks with S - parameters into FDTD," *IEEE Microwave and Wireless components Lett.,* vol.11(2), pp.77-78, February 2001.

207. David C. Wittwer and Richard W. Ziolkowski, "The effect of dielectric loss in FDTD simulations of microstrip structures," *IEEE Trans. Microwave Theory Tech.,* vol. MTT-49(2), pp.250-262, February 2001.

208. Yong-Woong Jang, "Wide-band T-shaped microstrip-fed twin-slot array antenna," ETRI Journal, vol.23, no.1, pp.33-38, March 2001.

209. George D. Kondylis, Franco de Flavis, Gregory J. Pottie and Tatsuo Itoh, " A memory efficient formulation of the finite difference time domain method for the solution of Maxwell equations," *IEEE Trans. Microwave Theory Tech.,* vol. MTT-49(7), pp.1310-1320, July 2001.

210. A.P. Zhao and P. Alinikula, "Investigations of the performance of the resistive voltage source used for the FDTD analysis of microstrip circuits," *Microwave and Opt. Technol. Lett.,* vol.30, no.6, pp.378-381, September 2001.

211. Salvador Gonzalez Garcia, Tae Woo Lee and Susan C. Hagness, "On the accuracy of the ADI-FDTD method," *IEEE Antennas and Wireless Propagat. Lett.,* vol.1, pp.31-34, 2002.

212. Xiaoning Ye and James Drewniak, "FDTD modeling incorporating a two port network for I/O line EMI filtering design," *IEEE Trans. on Electromagnetic Compatibility,* vol. EMC-44, pp. 175-180, February 2002.

213. A. Zhao, "More accurate and efficient unconditionally stable FDTD method," *Electron Lett.,* vol.38, no.16, pp.862-864, August 2002.

214. R. Makinen,V. Kangas, J. Lahitnen and M. Kivikovski, "A coaxial probe feed model for FDTD," *Microwave and Opt. Technol. Lett.,* vol.34, no.3, pp.193-198, August 2002.

215.   James P. Durbano, Fernando E. Ortiz, John R. Humphrey, Mark S. Mirotznik and Dennis W. Prather, "Hardware implementation of a three dimensional finite difference time domain algorithm," *IEEE Antennas and Wireless Propagat. Lett.*, vol.2, pp.54-57, 2003.

216.   Seyed Mahmoudreza Foroughipour and Karu P.Esselle, "The Theory of a singularity Enhanced FDTD method for diagonal metal edges," *IEEE Trans. Antennas Propagat.*, vol.51, pp.312-321, February 2003.

217.   Yotka S Rickard, Natalia K Georgieva, and Wei Ping Huang, "Application and optimization of PML ABC for the 3D wave equation in time domain," *IEEE Trans. Antennas Propagat.*, vol.51, pp. 286-295, February 2003.

218.   Javier Gomez-Tagle, Parveen F. Wahid, Michael T. Chryssomallia and Christos G. Christodoulu, "FDTD Analysis of Finite-sized Phased Array Microstrip Antennas," *IEEE Trans. Antennas Propagat.*, vol.51, no.8, pp.2057-2062, August 2003.

219.   Y.S. Rickard and N.K. Georgieva, "Problem independent enhancement of PML ABC for the FDTD method," *IEEE Trans. Antennas Propagat.*, vol.51,no.10(Part II), pp. 3002-3006, October 2003.

220.   J.J Simpson and A. Taflov, "Three dimensional modeling of impulsive ELF propagation about the earth sphere," *IEEE Trans. Antennas Propagat.*, vol.52, no.2, pp. 443-451, February 2004.

221.   A. Akyurtlu and D.H. Werner, "BI-FDTD: A novel finite difference time domain formulation for modelling of wave propagation in a Bi-Isotropic medium using the technique," *IEEE Trans. Antennas Propagat.*, vol.52, no.2, pp.416-425, February 2004.

222.   J.B. Cole, "High accuracy FDTD solution of the absorbing wave equation and conducting Maxwell's equations based on a non standard finite difference model," *IEEE Trans. Antennas Propagat.*, vol.52, no.3, pp.725-729, March 2004.

223.   N. Chavannes and N. Kuster, "A novel 3D- CPFDTD scheme for modeling grid nonconformally aligned transmitter structures," *IEEE Trans. Antennas Propagat.*, vol.52, no.5, pp.1324-1334, May 2004.

224.   N.V. Venkatrayalu, C.C. Chen, F.L. Teixeira and R. Lee, "Numerical modeling of Ultrawideband dielectric horn antennas using FDTD," *IEEE Trans. Antennas Propagat.*, vol.52, no.5, pp.1318-1323, May 2004.

225.   Hany-E-Abd-E-Raouf, E.A. El-Diwani, Abd-El-Hadi-Ammar and Fatma-M-El-Hefnawi, "A low dispersion 3D second order in time fourth order in space FDTD scheme (M3d$_{24}$)," *IEEE Trans. Antennas Propagat.*, vol.52, no.7, pp. 1638-1646, July 2004.

226.   A.P. Zhao, "Rigorous analysis of the influence of the aspect ratio of Yee's unit cell on the numerical dispersion property of the 3D and 3D FDTD methods," *IEEE Trans. Antennas Propagat.*, vol.52, no.7, pp.1630-1637, July 2004.

227.   P. Kosmas and C. Rappaport, "A simple absorbing boundary condition for FDTD modeling of lossy and dispersive media based on the one way wave equation," *IEEE Trans. Antennas Propagat.*, vol.52, no.9, pp.2476-2479, September 2004.

228.   Fei Xiao, Xiaohong Tang and Haihong Ma, "High order US-FDTD based on the weighted finite difference method," *Microwave and Opt. Technol. Lett.*, vol.45, no.2, pp.142-144, April 2005.

229.   W. Fu and E.L. Tan, "Compact higher order split-step FDTD method," *Electron Lett.*, vol.41, no.7, pp. 397-399, March 2005.

230. Y.S. Rickard and N.K. Nikolova, "Enhancing the PML Absorbing boundary conditions for the wave equation," *IEEE Trans. Antennas Propagat.*, vol.53, no.3, pp.1242-1246, March 2005.

231. A.E. Simon and A.A. Kishk, "Asymptotic strip boundary condition in the Finite Difference Time Domain method," *IEEE Trans. Antennas Propagat.*, vol.53, no.3, pp.1187-1193, March 2005.

232. A. Soriano, E.A. Navarro, D.L. Paul, J.A. Porti, J.A. Morente and I.J. Craddock, "Finite Difference Time Domain simulation of Earth – Ionosphere resonant cavity: Schumann resonances," *IEEE Trans. Antennas Propagat.*, vol.53, no.4, pp.1535-1541, April 2005.

233. Tao Su, Wenhua Yu and Raj Mittra, "A new look at FDTD excitation sources," *Microwave and Opt. Technol. Lett.*, vol.45, no.3, pp.203-207, May 2005.

234. Massimiliano Marrone, and Raj Mittra, "A new stable hybrid three dimensional generalized finite difference time domain algorithm for analyzing complex structures," *IEEE Trans. Antennas Propagat.*, vol.53, no.5, pp.1729-1737, May 2005.

235. S.T Chun and J.Y. Choe "A higher order FDTD method in integral formulation," *IEEE Trans. Antennas Propagat.*, vol.53, no.7, pp.2237-2246, July 2005.

236. Yoonjae Lee and Suman Ganguly, "Analysis of a plasma column antenna using FDTD," *Microwave and Opt. Technol. Lett.*, vol.46, no.3, pp.252-259, August 2005.

METHODOLOGY

The chapter serves to highlight the basic facilities used for experimental investigation. The fabrication method used for antenna is outlined. The experimental set up and procedure for measuring the antenna radiation characteristics are also described.

3.1 Basic facilities utilised

A succinct description of the equipments and facilities utilized for the measurements of antenna characteristics is presented.

3.1.1 HP 8510C Vector Network Analyzer

HP 8510C Vector Network Analyser (NWA) is a versatile equipment capable of making rapid and accurate measurements in the frequency and time domain. It consists of the 32 bit microcontroller MC68000 and has 1MB RAM and 512kB ROM. The NWA can measure the magnitude and phase of Scattering (S) parameters for frequencies upto 50GHz with a resolution of 1Hz. It has the optional ability to take Inverse Fourier transform of the measured frequency data to give the time domain response. The NWA consists of a microwave generator, S parameter test set, signal processor and the display unit, as illustrated in figure 3.1. The synthesised sweep generator, HP83651B, uses an open loop YIG tuned element to generate the RF stimulus. It can synthesise frequencies from 10MHz up to 50GHz. The frequencies can be synthesized in *Step* mode or *Ramp* mode depending on the desired measurement accuracy [1]. The antenna under test (AUT) is connected to the two port S parameter Test unit, HP8514B. This module isolates the incident (test), reflected and / or transmitted signals (namely a1,b1,a2,b2) at the two ports. The signals are then down converted to an intermediate frequency of 20MHz and fed to the IF detector. These signals are suitably processed to display the magnitude and phase information of S parameters in Log magnitude, Linear magnitude, Smith Chart or Polar formats. These constituent modules of the NWA are connected using HPIB system bus. A completely automated data acquisition is made possible using the MATLAB ™ based *CremaSoft* - the software developed indigenously at the Centre for Research in ElectroMagnetics and Antennas (CREMA), Department of Electronics, CUSAT.
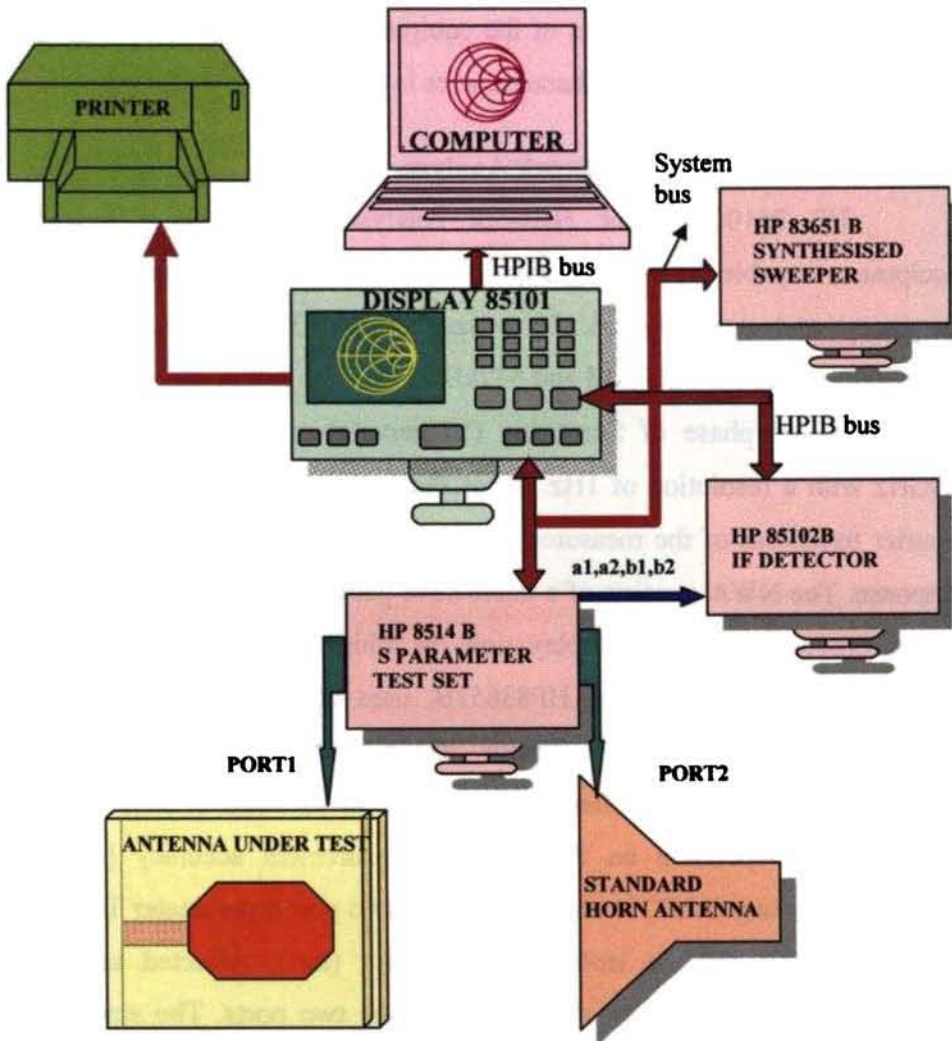
Figure 3.1 Schematic diagram of HP8510C Network Analyzer

3.1.2   Anechoic Chamber

The anechoic chamber provides a *quiet zone* needed to simulate free space environment required in pattern measurements. The absorbers used in building the chamber are made from high quality, low density foam, impregnated with dielectrically / magnetically lossy medium. The walls of

the chamber (24'x 12'x10') used for measurements is properly shaped (tapered chamber) and covered with carbon black impregnated Poly Urethane foam based pyramidal, wedge, or flat absorbers of appropriate sizes. The PU foam structure gives the geometrical impedance matching while the dispersed carbon gives the required attenuation (up to -40dB) for a wide frequency (500MHz-18GHz) range. The chamber is made free of EMI by surrounding it with thin Aluminium sheet.

3.1.3 Automated turn table assembly for *Far* field measurements

The turn table kept in the *quiet zone* consists of a stepper motor driven rotating platform, for mounting the Antenna Under Test (AUT). The microcontroller based *antenna positioner*, STIC 310C is used for rotating the AUT, for studying the radiation characteristics. The AUT is used as a receiver and a standard wideband (1-18GHz) ridged Horn antenna is used as transmitter for pattern measurements. Properly shielded cables connect the antennas to the NWA. Antenna positioner is interfaced to the computer and the antenna can be rotated 360° in CW or CCW direction with any stepping angle ($\geq 1°$), using *CremaSoft*.

3.1.4 Automated *Electric probe* assembly for *Near* field measurements

The electric probe assembly mounted on a Planar Near field scanner consists of two stepper motors, A and B. They can be controlled individually using *CremaSoft*, allowing the probe platform to be moved in the horizontal and vertical directions. Both motors are rotated to position the probe to the home grid point in the scan area for the DUT. Stepper A is energized to move the probe assembly in the horizontal plane, until the electric probe reaches the scan area boundary. With DUT connected to port 1 and electric probe connected to port 2 of the S parameter test set, S21 measurement is made at each spatial step. On reaching the boundary of the required scan area, stepper B is rotated to move the platform vertically up wards. Thereafter the S21 measurement is repeated with stepper A rotating in the

reverse direction. The entire near field aperture of interest is scanned and the Magnitude and phase information at each frequency point in the specified band is saved. This data is further processed to display the near field strength and to plot the far field pattern. Appendix B describes the setup and measurement procedure in detail.

3.2   Fabrication of Octagonal patch antenna
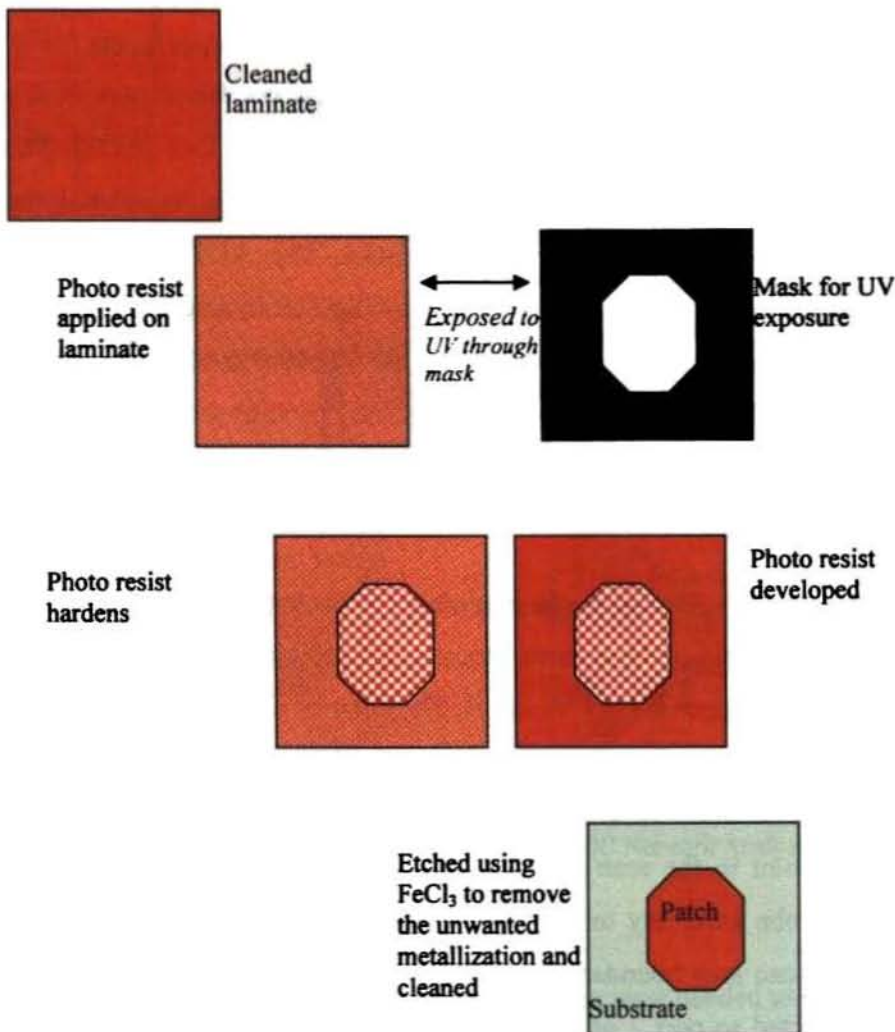
Figure 3.2 Steps in photolithographic technique for antenna fabrication

The CAD drawing of the –ve mask for antenna geometry and feed line is prepared and printed on *butter* paper. A copper clad laminate of suitable dimension is thoroughly cleaned and dried. The photo resist material is applied on the antenna/feed side of the substrate to form a uniform coating. It is then exposed to UV radiation through the mask. Due care is taken to ensure that the ground conductor on the opposite side of feed substrate is in tact. Photo resist in the exposed portions now *hardens*. The unexposed portions are dissolved away by the photo resist developer whereas the patch and feed line regions, which were exposed, are protected by the hardened photo resist. The laminate is then carefully rinsed with water to wash off the unexposed photo resist. The unwanted copper, on the patch and feed side of the substrate, is then etched away using Ferric Chloride ($FeCl_3$). Laminate is then cleaned using an abrasive to remove the hardened resist. Figure 3.2 illustrates the steps involved in the fabrication.

3.3   Experimental setup
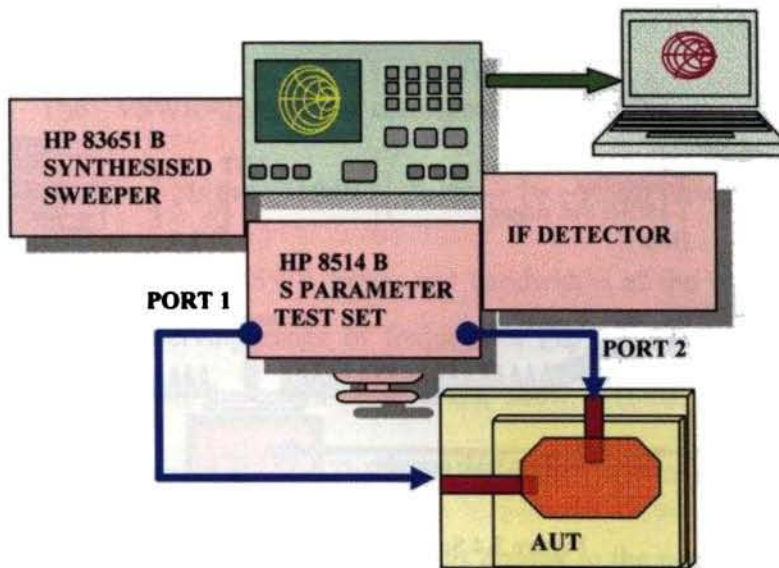
Figure 3.3 Set up for measuring the Reflection characteristics using HP8510C Network analyzer

Schematic of the setup used to measure the reflection and radiation characteristics is illustrated in figures 3.3 and 3.4 respectively. Pattern measurement is done inside the *anechoic* chamber after a thorough investigation of the input characteristics.
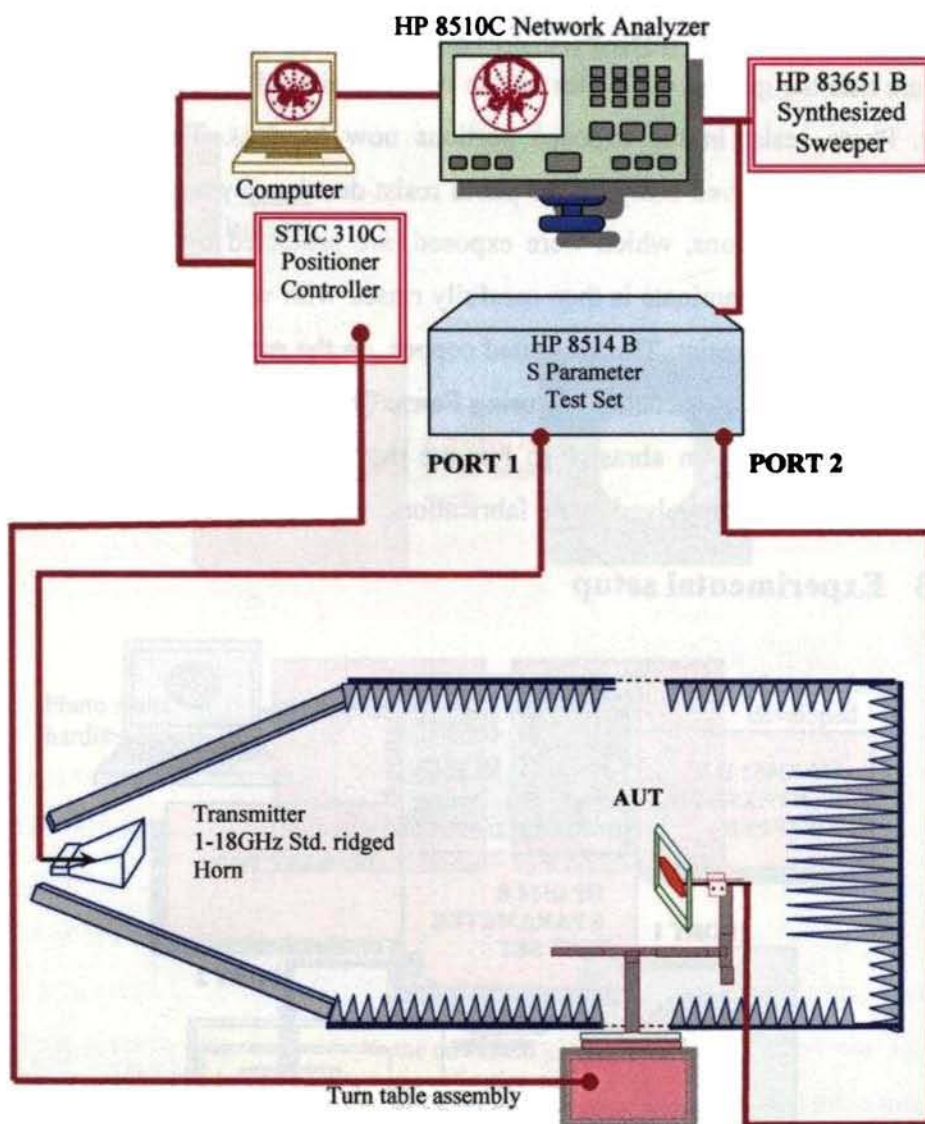
Figure 3.4 Set up for measuring the Radiation characteristics using HP8510C Network Analyzer

3.4 Measurement Procedure

The experimental procedure followed in determining various antenna parameters is discussed below:

3.4.1 S parameters, Resonance frequency and Bandwidth

The network analyzer is *calibrated* for *Full two port* by connecting the standard *short, open* and *thru* loads suitably. Proper phase delay is introduced while calibrating, to ensure that the reference plane for all measurements in the desired band is actually at 0°, thus taking care of probable cable length variations. The two ports of the Octagonal antenna are then connected to the ports of the S parameter test unit as shown in figure 3.3. The magnitude and phase of S11, S22 and S21 are measured and stored in ASCII format using the *CremaSoft*. S11 and S22 indicate the return loss at the two ports of the antenna geometry and S21 indicates the isolation between the ports of the antenna. The resonant frequencies (f_r) at the two ports is determined from the return loss curves in *LOG MAG* form, by identifying those frequencies for which the curve shows maximum *dip*. It can be noted from the stored data also.

The VSWR=2, which corresponds to reflection coefficient, $\rho = \dfrac{VSWR - 1}{VSWR + 1} \equiv \dfrac{1}{3}$, is the ~ -10dB $\left[\left(20\log\dfrac{1}{\rho}\right) = -9.5dB\right]$ level in the *LOG MAG* display. Thus 2:1VSWR bands and bandwidths at the two ports are determined by observing range of frequencies (Δf_r) about the resonant frequency for which the return loss curves, show $\leq$-10dB. The fractional bandwidth is calculated as $\dfrac{\Delta f_r}{f_r}$. The input impedance at resonance frequency is determined directly from the *Smith chart* display in the network analyzer, where after calibration the centre corresponds to 50Ω.

3.4.2 Radiation patterns

Pattern measurement is performed within the anechoic chamber using the set up shown in figure 3.4. The Octagonal patch antenna is mounted on the rotating platform of the turn table assembly kept in the *quiet zone*. Measurements are performed in the *receiving mode* for the AUT, which is kept in the far field of the Standard wideband ridged Horn antenna. The radiation patterns of the AUT at multiple frequency points can be measured in a single rotation of the positioner using *CremaSoft*. Before measurement is commenced, the T_x and R_x are aligned such that the R_x is in the *line of sight* of the T_x. AUT is connected to port 2 and Horn is connected to port 1 of the S parameter test. Analyzer is configured to make S21 measurement in the *Step* mode with proper *Averaging*.

With antennas aligned at *boresight* for maximum reception, a *THRU RESPONSE* calibration is performed for the frequency band of interest and saved in the *Cal* set. Switching to time domain, *GATE* is turned *on* in the analyzer, with a *gate span* depending on the largest dimension of the AUT. This procedure eliminates the spurious reflections from neighbor hood that are likely to corrupt the measured data. AUT is aligned in a near boresight position with polarization matched, the *Boresight* option in the *CremaSoft* is invoked to rotate the AUT to accurately determine the direction of maximum radiation. After the above sequence, the *Calibrate* option prompts for the frequency band and number of frequency points within the band for which S21 *cal* is to be done for pattern measurement of the AUT.

The positioner controller is then set to *home*. The analyzer is switched back to frequency domain, and the controlling software for pattern measurement is invoked which prompts for the start, stop and step angles. Software sequences the following operations:

➢ Rotate the AUT in the horizontal plane by the specified step angle

➢ Measure S21 at each frequency step within the specified start and

stop frequency range

> ➢ Acquire data and rotate the AUT by the step angle to cover the full 360°

Measurements are repeated in the principal planes for both the co-polar and cross polar orientations of the AUT and Horn, with calibration *on*. The gated response at each angular position is therefore normalized with respect to boresight trace. From the stored data, half power beam width, cross polar level, back lobe level etc. in the respective planes are estimated.

3.4.3 Gain

The gain of the AUT is measured in the boresight direction. Gain-transfer method utilizing a reference antenna of known gain is employed to determine the absolute gain of the AUT [2-4]. The experimental set up and measurement procedure for determining the gain is similar to radiation pattern measurement. A standard antenna with known gain G_R operating in the same band as AUT, is used as the reference antenna. S21 measurement done using reference antenna (as receiver) and the wideband Horn (as transmitter), is saved as the reference power. A *THRU RESPONSE* calibration is performed for the frequency band of interest and saved in a new *Cal* set. This acts as the reference (0dB) gain response. The reference antenna is replaced with AUT, retaining the physical alignment. S21 is measured then with the new calibration *on* and the power received (P_T in dB) is recorded. Display on the Network Analyzer indicates the relative gain in dB of the AUT with respect to the reference antenna. The gain G_T of the AUT is calculated from the stored data based on *Friis transmission formula* as,

$$G_T(dB) = G_R(dB) + P_T(dB) \qquad (3.1)$$

3.4.4   Polarisation pattern

Polarization of an antenna in a given direction is the polarization of the wave radiated (or transmitted) by the antenna, which is that property of an electromagnetic wave describing the time varying direction and relative magnitude of the electric field vector at a fixed location in space, and the sense in which it is traced as observed along the direction of propagation [2-4]. The polarization characteristic of an antenna is represented by its polarization pattern which is the spatial distribution of the polarisation of the field vector radiated by an antenna measured over the radiation sphere.

To measure the polarization pattern along the axis of the antenna beam, the linearly polarized standard Horn antenna and test antenna are aligned so that orientation of AUT's co-polar electric field matches with that of the Horn. The AUT connected to port 1 of the S parameter test setup is kept stationary, while the Horn antenna mounted on the turn table is rotated about its axis using the positioner controller. The Horn antenna is connected to port 2 of the S parameter test set and S21 measurement is performed after each rotation of the Horn. The data so acquired is plotted in polar coordinates with respect to angle of rotation to reveal the polarisation pattern of the AUT. The ellipse drawn inscribed within the polarization pattern is the polarization ellipse for the antenna in the specified direction.

3.4.5   Planar *Near* field measurement

The probe assembly mounted on a twin stepper motor driven XY scanner is used to scan the electric field strength in the near field of the DUT. The DUT is mounted on a fixed platform and probe, under computer control, is positioned accurately at each grid point in the measurement plane, in the near field region. The measurement set up and the procedure adopted is described in detail in Appendix B.

3.5 Simulation tool IE3D™

The Integral equation based simulation tool, IE3D™ from Zeland Inc.[5], is used to simulate the characteristics of the Octagonal patch antenna. The Conformal FDTD predicted results compared reasonably well with simulation results also. The simulation results are presented along with numerical and experimental observations in Chapter five, for the dual frequency Octagonal patch antenna.

References:

1. HP8510C Network Analyzer, Operating and service manual, Hewlett-Packard company, Santa Rosa, CA,USA
2. C.A.Balanis, "Antenna Theory: analysis and design," Second edition, John Wiley & Sons, Inc., Singapore, 2004.
3. Fred Gardiol, "Microstrip Circuits," John Wiley & Sons, Inc., 1994.
4. C.G.Christodoulou and Parveen F. Wahid, "Fundamentals of Antennas: Concepts and Applications," Prentice Hall India, New Delhi, India, 2001.
5. IE3D User's manual, Zeland Software Inc., CA, USA, Dec 1999.

Numerical Investigations:

Concepts and implementation based on FDTD

The fundamental mathematical concepts of Finite Difference Time Domain (FDTD) technique are discussed first in this chapter, with due emphasis on the procedure adopted for determining the spatial and temporal parameters employed in the code. The Conformal FDTD method used in this thesis, to analyze the slant edge of the Octagonal microstrip patch antenna under study, is then explained highlighting the assumptions taken in the implementation of the algorithm. Thereafter the steps involved in extracting the antenna parameters of interest are explained briefly. This is followed by a brief description of the theoretical aspect involved in predicting the resonant modes and the far field response from the computed near field data.

4.1 Introduction

Analyzing any electromagnetic problem demands, solving Maxwell's equations, subject to appropriate electromagnetic boundary conditions at every point along the material discontinuity. For few simple geometries, closed form analytic solutions can be arrived at, after exhaustive mathematical computations. But, for most realistic problems one must resort to computational electromagnetic methods (CEM). Amongst the various approaches developed to date towards this end, the Finite Difference Time Domain Method (FDTD) has received maximum attention and popularity by virtue of its inherent simplicity and capability to accurately model large inhomogeneous volume. Following are the striking features of this powerful Electromagnetic modeling, simulation and analysis tool:

➤ Simple to implement yet robust

➤ Large structures ($\sim 10^5$ wavelengths in extent) can be analyzed in reasonable time frames

➤ Facilitates easy extraction of temporal, broadband spectral and spatial response by using suitable post processing tools

➤ Applicable to a wide range of EM problems including arbitrary 3D geometries

➤ Algorithm extremely suited to implementation on parallel computers

4.2 Fundamental concepts of FDTD

FDTD algorithm was initially proposed by Kane S. Yee for the simulation of two dimensional electromagnetic scattering problems. Since the landmark paper by Yee in 1966[1] many researchers have contributed immensely to extend the method to many areas of Science and Technology, as outlined in Chapter two. FDTD provides a direct solution of time dependant Maxwell's equations for the Electric and Magnetic field intensities in a finite, piece wise homogenous space. Through these years it has been

used to solve all kinds of electromagnetic problems including microstrip geometries[2].
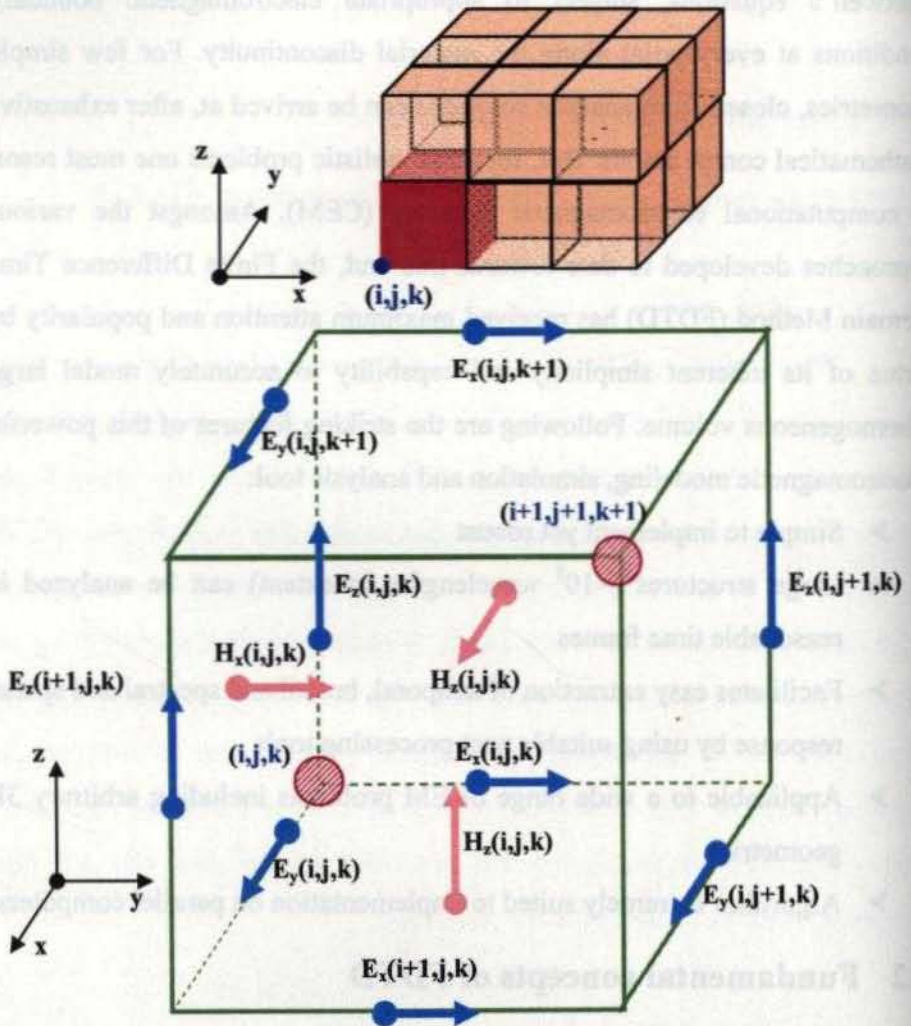
Figure 4.1 Yee cell showing the E and H field vector component placement

The main advantage of the tool, in addition to its simplicity and versatility, is the fact that by exciting the microstrip geometry using a single pulse, large amount of information can be extracted from the resulting time domain fields. The building block of the FDTD model is the Yee cell in which the Electric ($\vec{E}$) fields and Magnetic ($\vec{H}$) fields are regularly

interleaved as shown in figure 4.1. The electromagnetic structure is modeled by discretising its complete geometry and composition with a stack of Yee cells of appropriate material parameters. The various issues to be addressed while using the FDTD approach are convergence, stability, accuracy and consistency.

4.2.1 Implementation

The Ampere's law and Faraday's law incorporated using curl operators in the Maxwell's set of equations are discretised using central difference approximations of the spatial and time derivatives. To this end, the orthogonal $\vec{E}$ field components (E_x, E_y and E_z) are staggered onto the edges of Yee cell, where as the orthogonal $\vec{H}$ field components (H_x, H_y and H_z) are distributed onto the face centers. By correctly applying appropriate initial and boundary values we ensure that the Maxwell's Divergence equations are always satisfied in the FDTD scheme [18]. On incorporating the constitutive relations, the two curl equations fundamental to the FDTD becomes,

$$\nabla \times \vec{E} = -\mu \frac{\partial \vec{H}}{\partial t} \tag{4.1}$$

$$\nabla \times \vec{H} = \varepsilon \frac{\partial \vec{E}}{\partial t} + \sigma \vec{E} \tag{4.2}$$

where $\vec{E}$ and $\vec{H}$ are the Electric field and Magnetic field intensities, ε is the permittivity, μ is the permeability and σ is the conductivity of the medium. Under Cartesian co-ordinate systems, these can be expanded as,

$$\frac{\partial H_x}{\partial t} = \frac{-1}{\mu}\left[\frac{\partial E_z}{\partial y} - \frac{\partial E_y}{\partial z}\right] \tag{4.1.a}$$

$$\frac{\partial H_y}{\partial t} = \frac{-1}{\mu}\left[\frac{\partial E_x}{\partial z} - \frac{\partial E_z}{\partial x}\right] \tag{4.1.b}$$

$$\frac{\partial H_z}{\partial t} = \frac{-1}{\mu}\left[\frac{\partial E_y}{\partial x} - \frac{\partial E_x}{\partial y}\right] \tag{4.1.c}$$

$$\frac{\partial E_x}{\partial t} = \frac{1}{\varepsilon}\left[\frac{\partial H_z}{\partial y} - \frac{\partial H_y}{\partial z} - \sigma E_x\right] \qquad (4.2.a)$$

$$\frac{\partial E_y}{\partial t} = \frac{1}{\varepsilon}\left[\frac{\partial H_x}{\partial z} - \frac{\partial H_z}{\partial x} - \sigma E_y\right] \qquad (4.2.b)$$

$$\frac{\partial E_z}{\partial t} = \frac{1}{\varepsilon}\left[\frac{\partial H_y}{\partial x} - \frac{\partial H_x}{\partial y} - \sigma E_z\right] \qquad (4.2.c)$$

In Cartesian coordinates the partial differential equations of a function F(x,t), can be expressed as a set of algebraic equations, using the *centered difference approximations* for space and time derivatives *i.e.* differential equations can be expressed as algebraic equations as,

$$\frac{\partial F}{\partial x} = \frac{F(x + \frac{\Delta x}{2}, t) - F(x - \frac{\Delta x}{2}, t)}{\Delta x} \qquad (4.3)$$

$$\frac{\partial F}{\partial t} = \frac{F(x, t + \frac{\Delta t}{2}) - F(x, t - \frac{\Delta t}{2})}{\Delta t} \qquad (4.4)$$

The error associated with such an approximation with respect to the actual derivative is denoted as *truncation error*. Its value evaluated using Taylor's expansion is found to be proportional to discretisation parameter, Δx (for eqn. 4.3). To implement these equations, in a Yee cell of dimensions $\Delta x \times \Delta y \times \Delta z$, the three electric field components and the corresponding three magnetic field components are interleaved by half the discretisation length ($\Delta x/2$, $\Delta y/2$ and $\Delta z/2$). This arrangement, illustrated in figure 4.1, is crucial in obtaining the centered difference approximation for the space derivative.

Similarly, the centered difference for the time derivative is achieved by *alternatively* calculating the electric and magnetic fields at every half time step ($\Delta t/2$) as illustrated in figure 4.2.a. Since the space derivative of the staggered E and H fields are taken only at discrete time instants spaced at half time step between the instants at which time derivatives are computed, the algorithm has earned for itself the name *leap frog algorithm*. The above

concept is depicted in figure 4.2.b.
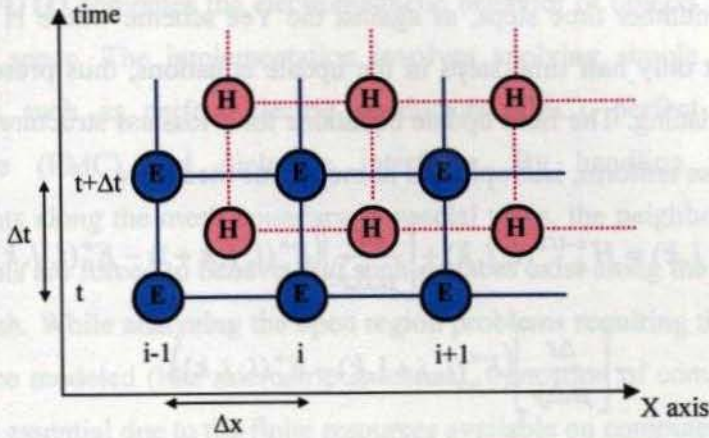
Figure 4.2.a Discretisation in space and time scheme
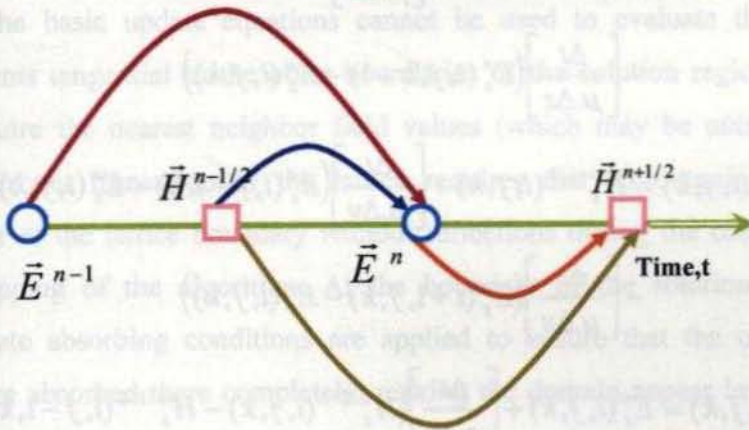
Figure 4.2.b Leap - frog time integration scheme

The figure clearly illustrates that fields are advanced in time by using information from the opposite field type at an intermediate time point. The method is thus explicit, as it depends only on fields from earlier instants. The half step staggered ($\pm \frac{1}{2}$) space indices in H field notation of the original scheme by Yee was later modified by Sheen et al.[2], with the subscript indices i, j and k implicitly denoting the $\pm \frac{1}{2}$ space indices. This simplified the notation, rendering the formulas to be directly implemental on computers. The typical field representation used in this thesis for the x component, of the Electric field in the (i, j, k) cell at the n th time step is E^n_x (i, j, k)

where t = n.Δt, x = i.Δx, y = j.Δy, z = k.Δz. Both E and H fields are defined at whole number time steps, as against the Yee scheme where H fields are defined at only half time steps in the update equations, thus preserving the time interlacing. The field update equations for a lossless structure placed in a piecewise uniform, isotropic and homogenous media are,

$$H_x^{n+1/2}(i,j,k) = H_x^{n-1/2}(i,j,k) + \left[\frac{\Delta t}{\mu.\Delta z}\right]\left(E_y^n(i,j,k+1) - E_y^n(i,j,k)\right)$$

$$-\left[\frac{\Delta t}{\mu.\Delta y}\right]\left(E_z^n(i,j+1,k) - E_z^n(i,j,k)\right) \qquad (4.5.a)$$

$$H_y^{n+1/2}(i,j,k) = H_y^{n-1/2}(i,j,k) + \left[\frac{\Delta t}{\mu.\Delta x}\right]\left(E_z^n(i+1,j,k) - E_z^n(i,j,k)\right)$$

$$-\left[\frac{\Delta t}{\mu.\Delta z}\right]\left(E_x^n(i,j,k+1) - E_x^n(i,j,k)\right) \qquad (4.5.b)$$

$$H_z^{n+1/2}(i,j,k) = H_z^{n-1/2}(i,j,k) + \left[\frac{\Delta t}{\mu.\Delta y}\right]\left(E_x^n(i,j+1,k) - E_x^n(i,j,k)\right)$$

$$-\left[\frac{\Delta t}{\mu.\Delta x}\right]\left(E_y^n(i+1,j,k) - E_y^n(i,j,k)\right) \qquad (4.5.c)$$

$$E_x^{n+1}(i,j,k) = E_x^n(i,j,k) + \left[\frac{\Delta t}{\varepsilon.\Delta y}\right]\left(H_z^{n+1/2}(i,j,k) - H_z^{n+1/2}(i,j-1,k)\right)$$

$$-\left[\frac{\Delta t}{\varepsilon.\Delta z}\right]\left(H_y^{n+1/2}(i,j,k) - H_y^{n+1/2}(i,j,k-1)\right) \qquad (4.5.d)$$

$$E_y^{n+1}(i,j,k) = E_y^n(i,j,k) + \left[\frac{\Delta t}{\varepsilon.\Delta z}\right]\left(H_x^{n+1/2}(i,j,k) - H_x^{n+1/2}(i,j,k-1)\right)$$

$$-\left[\frac{\Delta t}{\varepsilon.\Delta x}\right]\left(H_z^{n+1/2}(i,j,k) - H_z^{n+1/2}(i-1,j,k)\right) \qquad (4.5.e)$$

$$E_z^{n+1}(i,j,k) = E_z^n(i,j,k) + \left[\frac{\Delta t}{\varepsilon.\Delta x}\right]\left(H_y^{n+1/2}(i,j,k) - H_y^{n+1/2}(i-1,j,k)\right)$$

$$-\left[\frac{\Delta t}{\varepsilon.\Delta y}\right]\left(H_x^{n+1/2}(i,j,k) - H_x^{n+1/2}(i,j-1,k)\right) \qquad (4.5.f)$$

4.2.2 Boundary conditions

FDTD computes the electromagnetic behavior of objects in a finite region of space. The implementation involves applying simple boundary conditions such as perfect electric conductors (PEC), perfect magnetic conductors (PMC) and dielectric interfaces. By handling the field components along the mesh boundary in special ways, the neighboring field components are forced to behave *as if* such surfaces exist along the boundary of the mesh. While analyzing the open region problems requiring the infinite space to be modeled (like microstrip antennas), truncation of computational domain is essential due to the finite resources available on computers. Size of the computational volume is chosen carefully based on the problem under study. The basic update equations cannot be used to evaluate the field components tangential to the outer boundaries of the solution region since they require the nearest neighbor field values (which may be outside the mesh). Proper truncation of the lattice requires that an outgoing wave disappear at the lattice boundary without reflections during the continuous time stepping of the algorithm. At the boundary of the solution region appropriate absorbing conditions are applied to ensure that the outgoing waves are absorbed there completely, making the domain appear infinite in extent, with numerical back reflections at a minimum. In the absence of such *Absorbing Boundary Conditions* (ABCs), the back reflections may propagate back to the region under study and induce computational errors perturbing the final response.

- **Perfect Electric Conductor Boundary**

In materials with finite conductivity the update equation for the electric field component is

$$E^n = E^{n-1}\left[\frac{1 - \sigma\Delta t/2\varepsilon}{1 + \sigma\Delta t/2\varepsilon}\right] + \left[\frac{1}{1 + \sigma\Delta t/2\varepsilon}\right]\left[\frac{\Delta t}{\varepsilon}\right]\left(\nabla \times H^{n-1/2}\right) \qquad (4.6)$$

With $\sigma \gg 1$ eqn. 4.6 reduces to $E^n \approx - E^{n-1}$ which is mathematically stated as

$\vec{a}_n \times \vec{E} = 0$ where $\vec{a}_n$ is the surface normal vector. Thus, if the E components tangential to a PEC boundary are initialized to zero (E_{tan}=0), they will remain *nearly* zero throughout the iterations. Thus FDTD grid is constructed with *conductor boundaries in the geometry coinciding with cell edges.* Appropriate tangential E components are therefore initialized to zero and maintained as *zero* throughout the iterations to realize the E_{tan}= 0 condition for the perfect electric conductor. PEC type condition is assigned to boundaries (*e.g.* ground plane of the microstrip geometry) as well as to Yee cells inside the mesh to model zero thickness metal surfaces (*e.g.* strip line and patch surfaces).

• **Perfect Magnetic Conductor Boundary**

In order to model a perfect magnetic conductor or to invoke a symmetry condition H_{tan}= 0 is applied. Analogous with PEC boundary implementation, the PMC boundary must pass through the middle of the Yee cell. This approach needs both unit cell and half cell mesh handling. This is avoided by positioning the PMC at the FDTD cell edge itself as described in section 4.4.1.

• **Dielectric interface Boundary**

At the interface between two media the discretisation of Maxwell's equation becomes invalid. This is because of the fact that in the difference equations only a single value for the material constants (ε and μ) is used, though there are actually two separate values ($\varepsilon_1, \varepsilon_2$ and μ_1, μ_2) on either side of the interface. Simplest approach is to let all cells to be homogenous *i.e.* to ignore the surface. The equivalent medium parameter approach was introduced by Zhang and Mei by considering the fact that tangential E field is continuous if the interface is aligned with the FDTD cell boundary. For non-magnetic media, considering a constant x surface at $i\Delta x$, eqn. 4.1.a-c and 4.2.a remains unchanged, while ε in eqn. 4.2.b-c changes. Rewriting and adding eqn. 4.2.b for the two media we get,

$$\left(\frac{\partial E_y}{\partial t}\right)_1 + \left(\frac{\partial E_y}{\partial t)}\right)_2 = \frac{1}{\varepsilon_1}\left[\left(\frac{\partial H_x}{\partial z} - \frac{\partial H_z}{\partial x}\right)_1 - \sigma_1\left(E_y\right)_1\right]$$

$$+ \frac{1}{\varepsilon_2}\left[\left(\frac{\partial H_x}{\partial z} - \frac{\partial H_z}{\partial x}\right)_2 - \sigma_2\left(E_y\right)_2\right] \qquad (4.7.a)$$

At the constant x surface where $(E_y)_1 \approx (E_y)_2 \approx (E_y)_{x=i\Delta x}$, eqn. 4.7.a can be rearranged and compared with eqn. 4.2.b to obtain

$$\varepsilon_1\left(\frac{\partial E_y}{\partial t}\right)_1 + \varepsilon_2\left(\frac{\partial E_y}{\partial t}\right)_2 = 2\varepsilon_{equi}\left(\frac{\partial E_y}{\partial t}\right)_{x=i\Delta x} \qquad (4.7.b)$$

$$\sigma_1\left(E_y\right)_1 + \sigma_2\left(E_y\right)_2 = 2\sigma_{equi}\left(E_y\right)_{x=i\Delta x} \qquad (4.7.c)$$

Thus we get the condition that at the interface,

$$\varepsilon_{eff} = \frac{\varepsilon_1 + \varepsilon_2}{2} \qquad (4.7.d)$$

which is applied in the present analysis.

4.2.2.i   Early ABCs

The principle behind ABC is that by using an appropriate function to estimate the electric field components on the surface of the FDTD mesh, the EM fields should appear to be *absorbed* into the boundary surface. This is an area of active research and a variety of methods are available like Field extrapolation approach, Impedance condition approach, Surface integral approach, Bayliss-Turkel annihilation operator, One-way wave equation approach, Higdon ABC, Absorbing material approach (numerical anechoic chamber), Mur's ABC and Perfectly Matched Layer(PML) approach. A *hard* lattice truncation condition does not take into account the values of fields of any *possible* outgoing wave. A *soft* lattice truncation assigns linearly increasing values of conductivity near the lattice boundary so that gradual absorption of the outgoing wave is achieved.

The perfectly conducting type of hard lattice truncation proposed by Yee was consistent with his application only. The early ABCs suffered large reflections, limiting the efficiency of the FDTD tool. The field extrapolation

approach by Taylor used fields from two interior nodes to approximate the field at the boundary. Averaging approach based on an average of fields in the neighborhood and a Radiation boundary approach where field at boundary was approximated as far field value was in use. The annihilation operator used to determine the field located along the truncated boundary provided less than 10^{-1} back reflections.

The One – way wave equation approach developed by Engquist and Majda uses a partial differential equation which permits wave propagation only in one direction[5-6]. This method can perform as an exact analytic ABC for outgoing waves at any incident angle, but its direct application in numerical form is not possible due to a square root operation of the second order spatial and temporal derivatives involved in it. G.Mur[3] proposed a finite difference implementation scheme for the Engquist - Majda ABC which has been proven by many researchers to be a practical and efficient ABC with reflection of the order of 10^{-3} for normal incidence.

The more accurate PML approach proposed by Berenger [4] involves 12 field components and is computationally more demanding. The reflection from PML ABC is of the order of 10^{-8} for broad incident angles. This method proposed in 1994 is regarded as one of the most significant advances in FDTD development since its inception in 1966. At any point, a truncation cannot be exact because any particular outgoing plane wave *cannot be* assumed to be plane and normally incident on the lattice boundary and the local angle of incidence of a wave, relative to the boundary at a particular boundary point is unknown. Also different waves with different incidence angles may arrive simultaneously. Thus plainly stated any ABC is only an approximation that *reduces* the effective lattice boundary reflections to an acceptable level. The basic concept behind the lower order *soft* truncation scheme that relates the field at boundary nodes to values one cell within and which is less memory savvy, developed by Mur is discussed below.

4.2.2.ii   Mur's ABC

Mur's method rely on the fact that *most* of the electromagnetic waves will be outgoing at the boundary sufficiently far from the region of interest. Consider the one dimensional wave equation for a field component F, with phase velocity c,

$$\left(\frac{\partial^2}{\partial x^2} - \frac{1}{c^2} \frac{\partial^2}{\partial t^2} \right) F = 0 \tag{4.8}$$

The $-$ve x propagating waves can be obtained by factorizing it as

$$\left(\frac{\partial}{\partial x} - \frac{1}{c} \frac{\partial}{\partial t} \right) \left(\frac{\partial}{\partial x} + \frac{1}{c} \frac{\partial}{\partial t} \right) F = 0 \tag{4.8.a}$$

and equating the first term to zero. These one way wave equations can serve as ABCs.
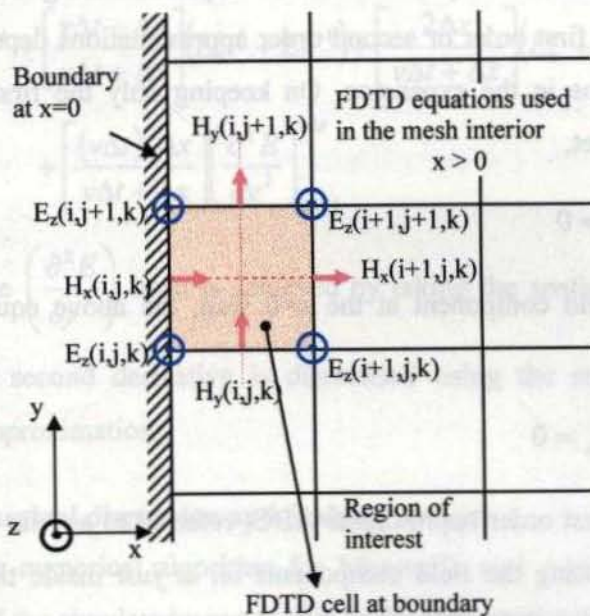
Figure 4.3 Computational domain truncated with Mur's ABC applied at the boundary

For the computational region x > 0 shown in figure 4.3, consider the two dimensional wave equation given by

$$\left(\frac{\partial^2}{\partial x^2} + \frac{\partial^2}{\partial y^2} - \frac{1}{c^2} \frac{\partial^2}{\partial t^2} \right) F = 0 \tag{4.9}$$

On factorizing eqn. 4.9 we get,

$$\left(\frac{\partial}{\partial x} - \sqrt{\frac{1}{c^2}\frac{\partial^2}{\partial t^2} - \frac{\partial^2}{\partial y^2}}\right)\left(\frac{\partial}{\partial x} + \sqrt{\frac{1}{c^2}\frac{\partial^2}{\partial t^2} - \frac{\partial^2}{\partial y^2}}\right)F = 0 \qquad (4.10)$$

Equating each of the factors of F to zero gives the one – way wave equations. Thus the ABC at the x =0 boundary is given by equating the first term to zero, which on rearranging gives

$$\left(\frac{\partial}{\partial x} - \frac{1}{c}\frac{\partial}{\partial t}\sqrt{1 - \frac{\dfrac{\partial^2}{\partial y^2}}{\dfrac{1}{c^2}\dfrac{\partial^2}{\partial t^2}}}\right)F = 0 \qquad (4.10.a)$$

Similar conditions can be derived at other boundary planes also. The square root operator in these equations can be expanded using Taylor's series, resulting in the first order or second order approximations depending on the number of terms in the expansion. On keeping only the first term in the expansion we get,

$$\left(\frac{\partial}{\partial x} - \frac{1}{c}\frac{\partial}{\partial t}\right)F = 0 \qquad (4.10.b)$$

For Electric field component at the x=0 wall, the above equation can be written as

$$\left(\frac{\partial}{\partial x} - \frac{1}{c}\frac{\partial}{\partial t}\right)E_{tan} = 0 \qquad (4.10.c)$$

This is Mur's first order approximate ABC(referred to as Mur-1) and it can be discretised using the field components *on* or *just* inside the mesh wall yielding an explicit finite difference update equation,

$$E_0^{n+1} = E_1^n + \left[\frac{c\Delta t - \Delta x}{c\Delta t + \Delta x}\right]\left(E_1^{n+1} - E_0^n\right) \qquad (4.10.d)$$

where E_0 represents the tangential electric field component(E_z) *on* the mesh wall and E_1 represents the tangential electric field component one node *inside* the mesh wall. Mur-1 conditions are used in the present analysis for

truncating the domain.

θ	0°	5°	15°	30°	45°	85°
$R(\theta)$	0	1.9×10^{-3}	1.7×10^{-2}	7.2×10^{-2}	17.2×10^{-2}	84×10^{-2}

Table 4.1 Variation of back reflections with respect to incident angles

Table 4.1 shows the ratio of reflected to incident waves, $R(\theta)$, for various incident angles. When Mur-1 is applied it is seen that the ABC works fine for normal incidence. Since the normal incidence assumption is not valid for the fringing fields which propagate tangential to the walls, the boundary walls on the sides are kept far enough to ensure that fringing fields are negligible there. Discretising eqn. 4.10.a, using the two–point difference approximations centered at $x = \Delta x/2$ and $t = n.\Delta t$ yields second order Mur condition referred to as Mur-2,

$$E_0^{n+1} = -E_1^{n-1} + \left[\frac{v\Delta t - \Delta x}{v\Delta t + \Delta x} \right] \left(E_0^{n-1} + E_1^{n+1} \right) + \left[\frac{2\Delta x}{v\Delta t + \Delta x} \right] \left(E_0^n + E_1^n \right)$$

$$+ \left[\frac{(v\Delta t)^2 \Delta x}{v\Delta t + \Delta x} \right] \left(\frac{\partial^2 E}{\partial y^2} \right)_{\Delta x/2}^{n\Delta t} \tag{4.11}$$

Centering the $\left(\dfrac{\partial^2 E}{\partial y^2} \right)$ term is achieved by taking the spatial average about $(0, \Delta x)$. The second derivative is discretised using the standard centered difference approximations.

4.2.3 Numerical dispersion and Stability criteria

The numerical algorithm for Maxwell's curl equations can cause dispersion of the simulated wave modes in the computational domain. This is because of the fact that the phase velocity of a numerical wave in the FDTD grid can differ from its physical phase velocity *i.e.* for an analysis involving vacuum medium, the phase velocity of the numerical wave could be different from vacuum speed of light. This phenomenon is known as *Numerical Dispersion* which can lead to non physical results such as broadening and

ringing of single pulse waveforms, imperfect cancellation of multiple scattered wave and pseudo-refraction. The phase velocity of the numerical wave mode is a function of wavelength, the direction of propagation and size of the cell.

Considering the time varying solution for the one dimensional wave equation of eqn. 4.8 as

$$F(x,t) = e^{j(\omega t - kx)} \tag{4.12}$$

we see that wave number $k = \dfrac{\omega}{V_p}$, where V_p is the phase velocity ($V_p \equiv c$ for vacuum). Hence the wave number is linearly proportional to frequency, ω. The difference form of the above solution is

$$F_i^{n+1} = e^{j(\omega n \Delta t - \widetilde{k} i \Delta x)} \tag{4.12.a}$$

where $\widetilde{k}$ is the wave number of a sinusoidal traveling wave of frequency ω, which exists in the FDTD solution space due to discretisation. On applying Euler's identity we get the following non linear relation between wave number and frequency.

$$\cos(\omega \Delta t) = 1 + \left(\frac{c\Delta t}{\Delta x}\right)^2 \left[\cos\left(\widetilde{k}\Delta x\right) - 1\right] \tag{4.13}$$

Thus the simulated wave propagating through the solution space undergoes phase errors, since it either accelerates or slows down with respect to the actual wave in a physical space. When both Δt, $\Delta x \to 0$, $\widetilde{k} \to \pm \dfrac{\omega}{c}$ which is equal to the analytical case. But such a small spatial or time increment is practically not feasible. The magic time step $c\Delta t = \Delta x$, causes no numerical dispersion, but has implications in stability. With a spatial sampling rate $\Delta x = \lambda / 10$, we get the

Numerical wave number, $\widetilde{k} \approx \dfrac{0.6364}{\Delta x}$ (4.14.a)

and Numerical phase velocity, $\tilde{V}_p \approx 0.9873c$ (4.14.b)

On increasing the sampling rate to $\lambda/20$, phase velocity becomes,

$$\tilde{V}_p \approx 0.9968c \qquad (4.14.c)$$

with a phase error of ~11° over a distance of 10λ. Thus it can seen that even with 20 cells per wavelength, for large computational volume phase errors can result from numerical dispersion producing incorrect results. In the analysis presented in this thesis, the rule- of- thumb, employed [5] is

$$\Delta x, \Delta y, \Delta z \leq \frac{\lambda_{min}}{20} \qquad (4.15)$$

where λ_{min} is the wavelength of the expected highest significant harmonic in the model.

In the implementation of FDTD, as time marching continues according to Yee algorithm, it is important to ensure that the electric and magnetic field values do not grow beyond bounds. FDTD algorithm allows propagation only from one cell to its neighbor in one time step. Hence at any point within the FDTD grid, over a period of one time step, the propagating wave must not pass through more than one spatial cell. Thus the method is useful only when the solutions of difference equations are convergent and stable. *Stability* is therefore stated as a set of conditions under which the error generated by the finite difference approximations is finite and does not grow in an unbounded fashion as time stepping progresses. It can be expressed in terms of a mathematical relation, that requires the time increment Δt to have a specific bound, relative to the spatial discretisation Δx, Δy and Δz, referred to as the *stability criteria*.

Considering the complete solution of eqn. 4.8 in finite difference form as $F_i^n = \xi^n e^{-j\tilde{k}i\Delta x}$ (4.16)

a growing (unstable) solution occurs if $|\xi| > 1$ *.i.e* when $v\Delta t > \Delta x$. Thus in one dimensional FDTD code, $v\Delta t \leq \Delta x$ is the condition required for stability.

This is referred to as Courant stability criteria, which ensures that the FDTD grid is causally connected, where speed of light binds the rate of propagation within the mesh.
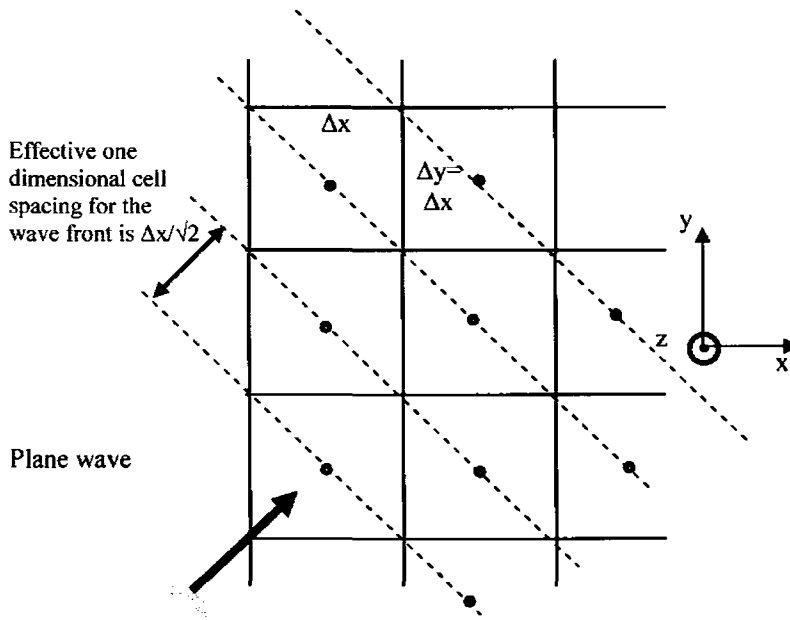
Figure 4.4 A 2D square cell FDTD mesh with propagation along the diagonal

Consider a plane wave propagating along the mesh diagonals in a two dimensional square cell FDTD mesh as shown in figure 4.4. Projecting the lines of constant phase onto an equivalent one dimensional mesh results in an effective mesh spacing of $\dfrac{\Delta x}{\sqrt{2}}$, requiring the time step to be reduced accordingly for ensuring stability in this *smaller effective mesh*. For a cubical grid case the effective mesh spacing reduces to $\dfrac{\Delta x}{\sqrt{3}}$.

In general, for a linear, isotropic, non dispersive dielectric medium, the time increment for the 3D-rectangular grid FDTD obey the following bound, referred to as the Courant- Friedrichs- Lewy (CFL) stability criteria.

$$v\Delta t \leq \cfrac{1}{\sqrt{\dfrac{1}{\Delta x^2} + \dfrac{1}{\Delta y^2} + \dfrac{1}{\Delta z^2}}} \qquad (4.17)$$

For most cases when the equality holds, the discretised wave most closely approximates the actual wave propagation. When the solution space contains several dielectric materials with different values for v, rule-of-thumb is to use the maximum value of v. The approach used in this thesis is to set the time step limit based on 99.5% of the maximum wave phase velocity that exist in the grid. For non-linear materials and for materials with high conductivity, time step lesser than Courant limit is usually employed. However the CFL stability criteria has many limitations:

> It does not account for dielectric discontinuity

> It assumes infinite computational domain *i.e.* effect of ABC on stability is not taken care of

> It does not consider lumped linear and non-linear models to be included in the domain

4.2.4   Excitation Source modeling

The FDTD grid space can be driven via an internal source or incident field depending on the problem at hand. A proper excitation to a particular structure will excite the field distribution closest to that of physical structure while an improper excitation can lead to spurious solutions that may not physically exist. Compact internal sources commonly used are the driven current and driven voltage sources. A simple driven voltage gap consisting of a voltage source imposed over a single-cell wide gap in the +z direction, is commonly used as the antenna feed. It can be represented mathematically as,

$$E_z^n(i, j, k = const) = \left[\frac{V(t = n\Delta t)}{\Delta z} \right] \qquad (4.18)$$

A current source when applied, is imposed at the same spatial point as the

electric field but at a time point corresponding to that of the magnetic field. In scattering and coupling applications, an incident field of plane wave is used as the source. To extract the response over a band of frequencies, after the transient analysis, a pulsed source must be employed in the time domain as opposed to a sinusoidal one. The width of the time domain excitation pulse is chosen depending on the frequency bandwidth of interest. A wide time domain pulse results in narrow frequency band response. To avoid unnecessary noise appearing in the FDTD generated response, excitation pulse and its spectrum must have smooth roll off and low side lobes. Pulses commonly used include Raised cosine pulse, Blackmann-Harris pulse and Gaussian pulse.

A raise cosine pulse consists of a single cycle of a cosine wave with a bias of 1, given by $R(t) = 1 - \cos(2\pi F_b t)$ for $0 < t < 1/F_b$, and zero else where. The spectrum has an effective bandwidth of $2F_b$. The Gaussian pulse given by eqn. 4.19.a extends for all time.

$$G(t) = \exp\left(-\pi(2F_b t)^2\right)$$ (4.19.a)

The Gaussian half width defined as T is given by $T = 1/(2F_b)$, with $G(T)=4.3\%$ of maxima. The spectrum of Gaussian pulse given by eqn. 4.19.b shows an effective bandwidth of $2F_b$, with $\check{G}(F_b) = 45.6\%$ of maxima.

$$\check{G}(f) = \frac{1}{2F_b}\exp\left(-\pi\left[\frac{f}{2F_b}\right]^2\right)$$ (4.19.b)

In the parade of the FDTD method, all functions are assumed to be causal. In order to satisfy the zero initial condition as required in FDTD scheme at the zeroth time step, the time origin of the Gaussian pulse must be shifted by τ_d where $\tau_d \geq T$. The time delayed Gaussian excitation used in the present analysis is given by [6]

$$G(t) = \exp\left(-\left(\frac{t - \tau_d}{T}\right)^2\right)$$ (4.19.c)

with the parameters τ_d and T chosen appropriately. The discrete form of eqn. 4.19.c is

$$G(n\Delta t) = \exp\left(-\left(\frac{n\Delta t - \tau_d}{T}\right)^2\right)$$

(4.20)

where $T = N\Delta t, \tau_d = 3T$. It indicates that the Gaussian is sampled N times during the pulse half width T. The above defined pulse is centered at τ_d with the $1/e$ characteristic decay at T. A smooth transition from zero to the maximum value of 1 is ensured by taking the delay τ_d as $3T$.
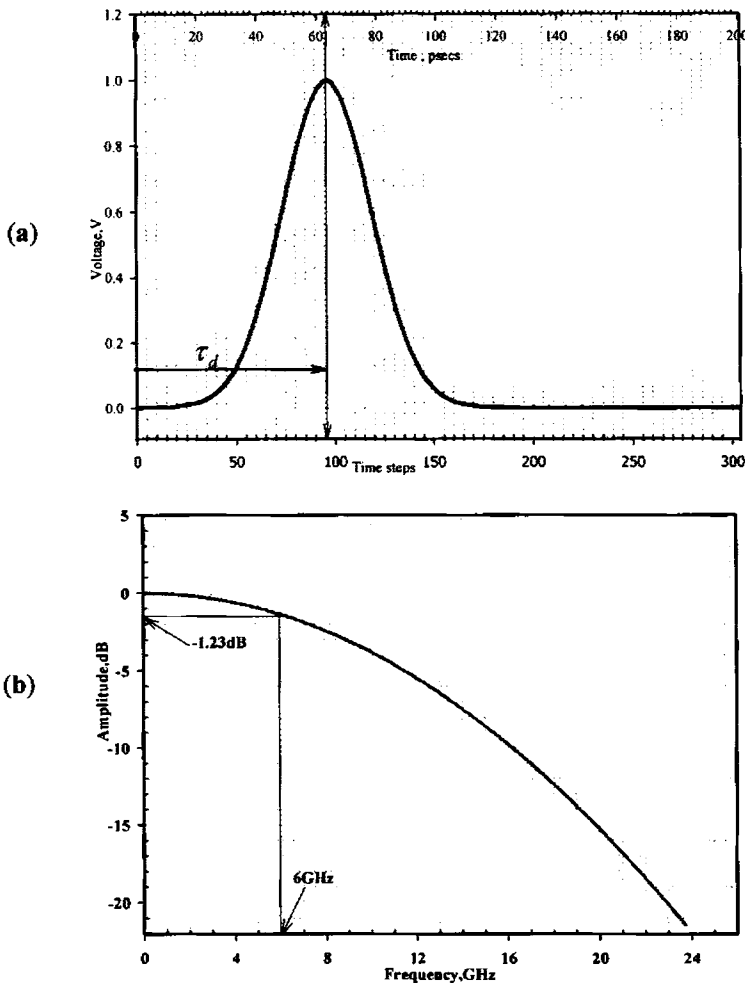
Figure 4.5 Gaussian pulse launched into the domain and its Spectrum illustrating the useful bandwidth

Considering 6GHz as the highest frequency of interest, and allowing a tolerance factor of 4, N=30 is used in the present study. The Gaussian pulse and its spectrum defined by these parameters are shown in figure 4.5.a, b respectively. From figure 4.5.b it is seen that the selected pulse provides relatively high signal levels up to the frequency of interest and that the spectrum rolls off smoothly to less than -20 dB at frequencies (>30GHz) for which the selected cell dimensions is less than $\lambda/10$. The parameter N can be changed to achieve sharper frequency roll off.

The z component of the E field at source location on the microstrip feed line as shown in figure 4.6.a, is excited with the +z directed Gaussian voltage source. The transition from source point to the microstrip feed line can be modelled as a tapered transition or a straight line transition as depicted in figure 4.6.b and c, with latter chosen for the present analysis.
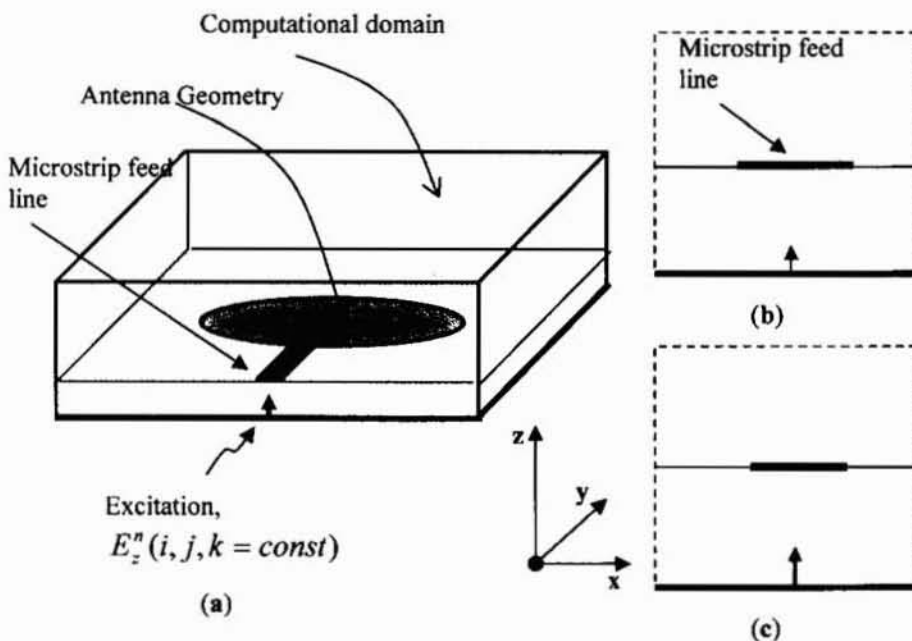
Figure 4.6 Computational domain with voltage source exciting the microstrip feed line
(a)Domain showing feed line patch and the source point
(b)Tapered transition from source location to microstrip conductor
(c)Straight transition from source location to microstrip conductor

The source point becomes virtually short circuited, with zero tangential electric field for the wave, once the transient pulse has fallen to zero in amplitude. Thus as time marching proceeds, even though the Gaussian pulse has subsided, any reflection from the geometry under study, traveling back to the source point might get reflected back into the computational domain. The only way to dissipate this energy due to average dc content of the Gaussian is by radiation, absorption in a lossy media or absorption in lumped loads. This necessitates longer simulation interval for the system to converge. To circumvent this problem, the approach proposed by Sheen *et al.*[2] consisted of extending the microstrip feed line all the way to the end of the FDTD mesh with the excitation being provided by a *wall* of electric fields which were to be replaced with ABC after the pulse has been fully launched. Luebbers *et al.* [7] proposed a more realistic simple gap feed model as shown in figure 4.7, based on a Gaussian voltage source with a finite internal source resistance R_s instead of the *hard source* model where the source had no internal source resistance.
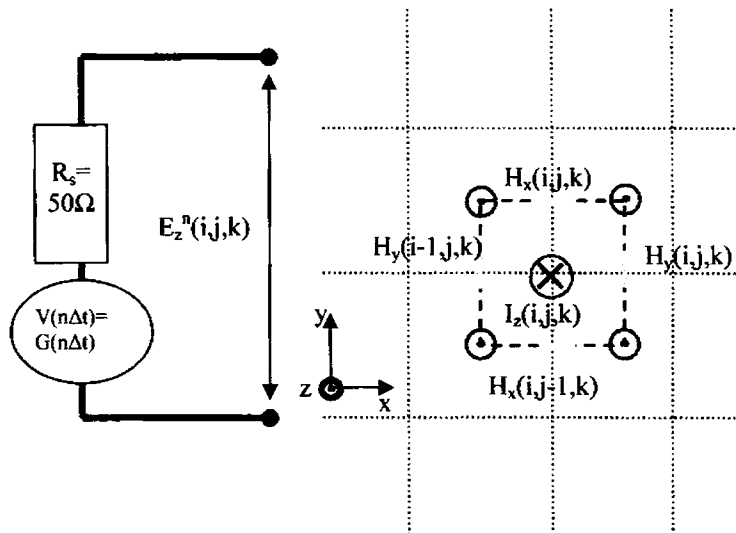
Figure 4.7 Simple gap feed model with matched Gaussian excitation

The resistance is assumed to be lumped and it serves two functions:

> Series internal resistance when the voltage source is activated

> Matched termination when the source is deactivated

The Electric field component at the source point, derived based on Ampere's circuital law and Ohm's law, is given as

$$E_z^n(i,j,k = const) = \left[\frac{V(t = n\Delta t)}{\Delta z}\right] + \left[\frac{I_z^{n-1}(i,j,k)R_s}{\Delta z}\right] \quad (4.21.a)$$

where

$$I_z^{n-1}(i,j,k) = \left(H_x^{n-1}(i,j-1,k) - H_x^{n-1}(i,j,k)\right)\Delta x$$

$$+ \left(H_y^{n-1}(i,j,k) - H_y^{n-1}(i-1,j,k)\right)\Delta y \quad (4.21.b)$$

This expression is derived from Maxwell's curl equation (eqn.4.2) neglecting the displacement term and assuming that resistance is lumped[5-6]. The ½ time step offset between the V^n and I^{n-1} used in the above expression does not introduce appreciable error in the FDTD calculations.
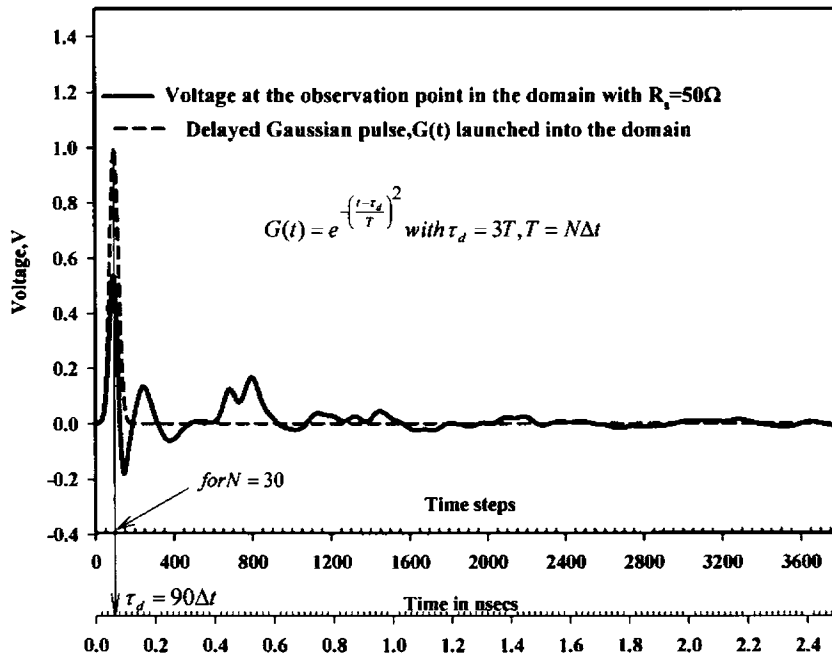
Figure 4.8 Voltage at the source point due to matched Delayed Gaussian pulse source in the domain

In FDTD calculations involving $R_s=50\Omega$, source point voltage waveform is no longer purely Gaussian, as illustrated in figure 4.8, since the voltage across the resistance is also included. It is also observed that the system converges in fewer than 5000 time steps for the geometry under study. The source resistance is matched to the characteristic impedance (50Ω) of the microstrip feed line so that the nonphysical retroreflections of the numerical waves at the source point is minimized. For very large R_s, instability can result due to the fact that the displacement current through the FDTD cell containing the source is neglected.

4.2.5 Flow chart illustrating Yee algorithm

The finite difference equations (eqn. 4.5.a-f) are used with the above described boundary, stability and source criteria to analyze the propagation of a sufficiently broad, matched, delayed Gaussian pulse excitation launched into the geometry. The flow chart illustrating the steps in implementing the Yee's FDTD scheme for solving Maxwell's equations on the computer is depicted in figure 4.9. Before commencing the time marching procedure to update the fields, problem must be suitably defined. This primarily involves defining the geometry under study. The grid cell dimensions are selected so that material boundaries coincide with the cell edges and satisfy eqn. 4.15. The material properties of the cells lying at the interface of dielectric media are modified following the equivalent medium rule given by eqn. 4.7.d. The time increment is computed satisfying the stability criteria described in eqn. 4.17. In this thesis, feed lines, ground plane and patch surface are defined using the PEC boundary condition, neglecting their thickness. FDTD mesh is constructed such that all H fields lie inside the final grid while outer edges of the domain have tangential E components. The Mur-1 boundary is applied at a suitable distance from the structure. The source is setup by assigning the delayed Gaussian time distribution to the selected E_z field component in the domain.

```
                    ┌─────────────┐
                    │    Start    │
                    └─────────────┘
```

❖   Problem space setup
•   *Describing the geometry*
•   *Describing the material properties*
•   *Estimate spatial increment and temporal increment Δx,*
     Δy, Δz, Δt
•   *Estimate the no of iterations ,K*
•   *Set time $t=0$, Time step, $n = 0$;*

❖   Set up initial E and H field in the domain as zero
❖   Define the excitation, E^n_z (i,j,k) at the selected feed point
       in the domain over the complete simulation interval.

n=n+1

❖   Update H field (i.e $H^{n+1/2}$) *inside* the domain following the
       Yee equations
❖   Update E field (i.e E^{n+1}) *inside* the domain following the
       Yee equations
❖   Apply PEC, PMC, ABC wherever needed to update E
       fields *at* the boundaries.
❖   Save the desired field values

No ◄──────   Maximum time steps,
              K, reached?   ────► Yes   (A)

Figure 4.9 The Flow chart of Yee scheme for FDTD method
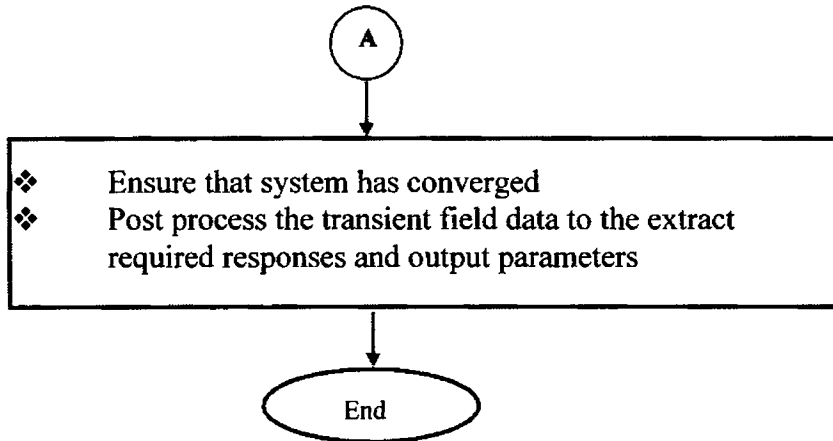
Figure 4.9 *(contd)* The Flow chart of Yee scheme for FDTD method

The time iterating procedure is then initiated for the desired number of time steps. The plane of symmetry in the geometry is identified and PMC condition is applied while updating the fields. For those cells containing the slant edges of the patch, referred to as distorted Yee cells, the field components are modified employing conformal FDTD algorithm described in section 4.3.3 suitably. Once the time marching ends and desired fields are saved, the Scattering (S) parameters are computed suitably as detailed in section 4.5. By monitoring the voltage and current waveforms over the entire time interval at the source point, the convergence of the system is ensured. From a suitably sampled near field data, the far field characteristics and modes of resonance are extracted as detailed in section 4.6.

4.3 Methods for modeling inclined/curved edges

Microstrip patches with patch edges parallel to grid lines can be accurately modeled using the classical Yee FDTD approach if the grid is sufficiently fine. This scheme employing uniform orthogonal gridding in the Cartesian coordinate system forces inclined and curved boundaries of the geometry to be approximated using various methods. To maintain the geometrical fidelity, the choice is to have a *globally variable* array of cells that tracks even the finest spatial detail, but at the expense of computer

resources and complex mesh generation in addition to the risk of instability. An alternate approach is to approximate the physical properties of the fine spatial details by incorporating them into the adjacent *local* cells of a uniform mesh. Curvilinear co-ordinate variants of FDTD, finite volume FDTD and discrete surface integral method allow greater geometric flexibility but incur a higher computational cost. Sub-gridding methods and conformal methods modify the difference equations locally while preserving the computational efficiency and simple formulation of the Yee lattice. The metal is assumed to have zero thickness.

4.3.1   Staircase approach

In the FDTD grid based on Yee algorithm, the microstrip surface edges that are not parallel to the FDTD cell edges are approximated as either completely covered by metal or as completely uncovered. This leads to the metallic edge being defined by a *staircase* boundary as shown in figure 4.10 which is a continuous chain of zero valued E_x and E_y components in the grid that forms a *best fit* to the contour.
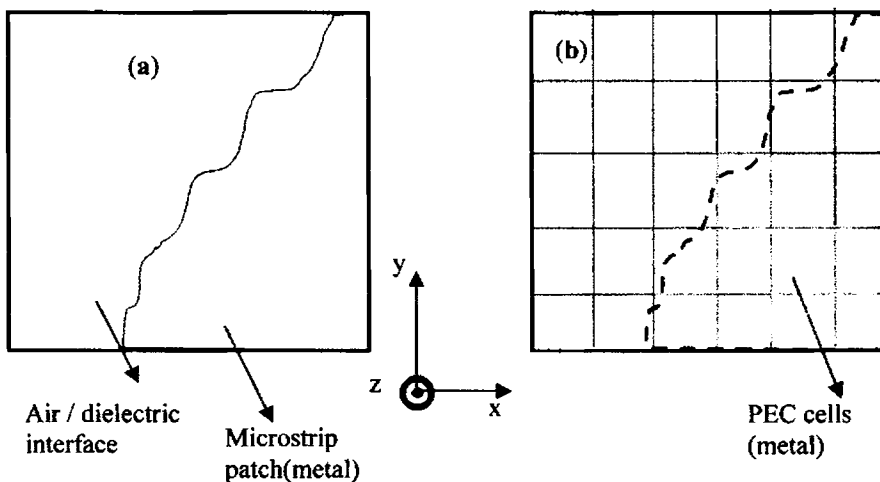
Figure 4.10 Stair case meshing
(a) Top view showing the curved boundary
(b)Top view of the FDTD mesh defining the curved boundary

The update equations for the grid will remain the same as the conventional one. In such an approach, defining an irregular boundary involves complex

mesh generation overhead. This approach compromises on the accuracy of result and demands very fine gridding. Since practical geometries rarely have contour lines that fit on the discrete grid points of the mesh, application of exact field boundary conditions at the material interfaces is nearly impossible, which in turn leads to errors.

4.3.2   Contour path FDTD (CP-FDTD)

The principle behind the classical Yee scheme is a direct approximation of the point wise derivatives of Maxwell's curl equations. Based on Ampere's law and Faraday's law in the *integral* form, the coupling of these two laws, can be graphically interpreted by the intersection of two electrically small, spatially orthogonal contours as depicted in figure 4.11.a.
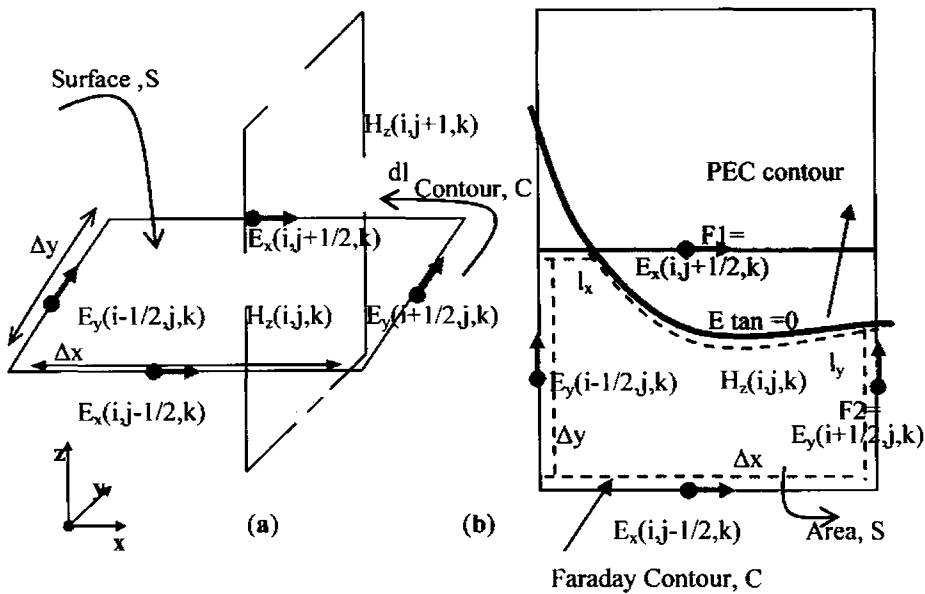
Figure 4.11 Contour path FDTD meshing
(a)Chain linked orthogonal contours illustrating Faraday's law for time stepping
(b)Applying CP-FDTD to a distorted cell

The FDTD mesh is thus a 3D *chain link* array of intersecting orthogonal contours and surface curvature is incorporated by deforming the contour path at selected meshes to conform to the curvature. Using Stokes theorem and assuming that field at the midpoint of one side of the contour C equals the

average value of that field component along that side[19], Ampere's law along the closed contour C defining the surface S is given as

$$\mu A\left(\frac{H_z^{n+1/2}(i,j,k) - H_z^{n-1/2}(i.j.k)}{\Delta t}\right) =$$

$$\left(E_x^n(i,j+1/2,k) - E_x^n(i,j-1/2,k)\right)\!\Delta x +$$

$$\left(E_y^n(i-1/2,j,k) - E_y^n(i+1/2,j,k)\right)\!\Delta y \qquad (4.22)$$

where $A=\Delta x\Delta y$, the cell face area. By setting tangential E components lying on the patch surface to zero, the above equation is used to update the magnetic field components at the centre of distorted cells. All other components are updated using the normal Yee algorithm.

- **Contour path modeling of two dimensional PEC curved surface**

The implementation of CP-FDTD scheme leads to either *shrinking* or *stretching* of the selected grid cells, due to the *nearest neighbour approximation* or *collinear borrow* involved. The H_z component enclosed by the distorted contour is evaluated at its usual grid position and it is assumed to be the average value of the magnetic field within the area bounded by the contour. Along the contour of the PEC boundary, E $_{tan}=0$. For the distorted cell shown in figure 4.11.b, with field components F1 and F2 lying on edges of Yee cell defining the patch area (PEC), the field of the affected contour segment in the eqn. 4.22 is simply taken to be the corresponding E field value one space cell further away from the surface in the collinear direction [5]. The area, A in eqn. 4.22 is suitably redefined as the area S within the Faraday contour. The mesh generation routine therefore must calculate the area of cell within the Faraday contour and also the intercept points of the PEC contour with the grid lines. Although the method is simple, CP-FDTD leads to instabilities due to the non-causal and non-reciprocal *nearest neighbour* approximation. The improved schemes proposed to obviate this

instability involve complex bookkeeping, mesh generation and programming [8-9].

4.3.3   Conformal FDTD

Instead of a single grid defining the structure under analysis, Yee *et al.*[10] proposed a system of overlapping grids (OGFDTD), with the locally curvilinear grid in the neighbor hood of curved surface and a normal Cartesian grid elsewhere. The overlapping zone of the two is kept away from the surface boundary and the grid fields there are computed by suitable spatial interpolation. This hybrid method is more accurate than CPFDTD but incurs increased computational time, cost and is difficult to implement. The modified locally Conformal FDTD approach used in this thesis to model the inclined edge of the microstrip patch antenna is based on the simple scheme initially proposed by Dey *et al.*[11-12]. All electric field update equations are same as those in the conventional FDTD scheme while the magnetic field update equations for cells adjacent to the metallic boundary are modified only slightly to include geometric factors. The *cost* of this simple scheme is a reduction of the Courant limit in order to obtain a stable solution. The method is reported to be stable except when distorted cell is extremely small (<5%) compared to the undistorted cell.

4.3.3.i   Update equations

The update equation for the E field is same as in regular FDTD scheme. For instance the E_x component for the FDTD cell depicted in figure 4.12 is given as

$$E_x^{n+1}(i,j,k) = E_x^n(i,j,k) +$$

$$\left(\frac{\Delta t}{\varepsilon \Delta y}\right)\left(H_z^{n+1/2}(i,j+1,k) - H_z^{n+1/2}(i,j,k)\right) -$$

$$\left(\frac{\Delta t}{\varepsilon \Delta z}\right)\left(H_y^{n+1/2}(i+1,j,k) - H_y^{n+1/2}(i,j,k)\right) \qquad (4.23.a)$$

The update equation for H_z deviates from the conventional equation[11-12]

and is given as

$$H_z^{n+1/2}(i,j,k) = H_z^{n-1/2}(i,j,k) + \left(\frac{\Delta t}{\mu A_z(i,j,k)}\right)$$

$$\times (\{E_x^{n(i,j,k)} l_x(i,j,k) - E_x^n(i,j-1,k) l_x(i,j-1,k)\} +$$

$$\{- E_y^n(i,j,k) l_y(i,j,k) + E_y^n(i-1,j,k) l_y(i-1,j,k)\}) \qquad (4.23.b)$$

where A_z is the face area of the distorted cell excluding the metallic region, l_x and l_y are the affected cell lengths along the x and y directions respectively, outside the metallic region. Since the entire field values are updated without borrowing from adjacent cells, the associated stability problem is not present in this scheme as long as the time step is less than 75% of the Courant limit for the undistorted cell in the grid.
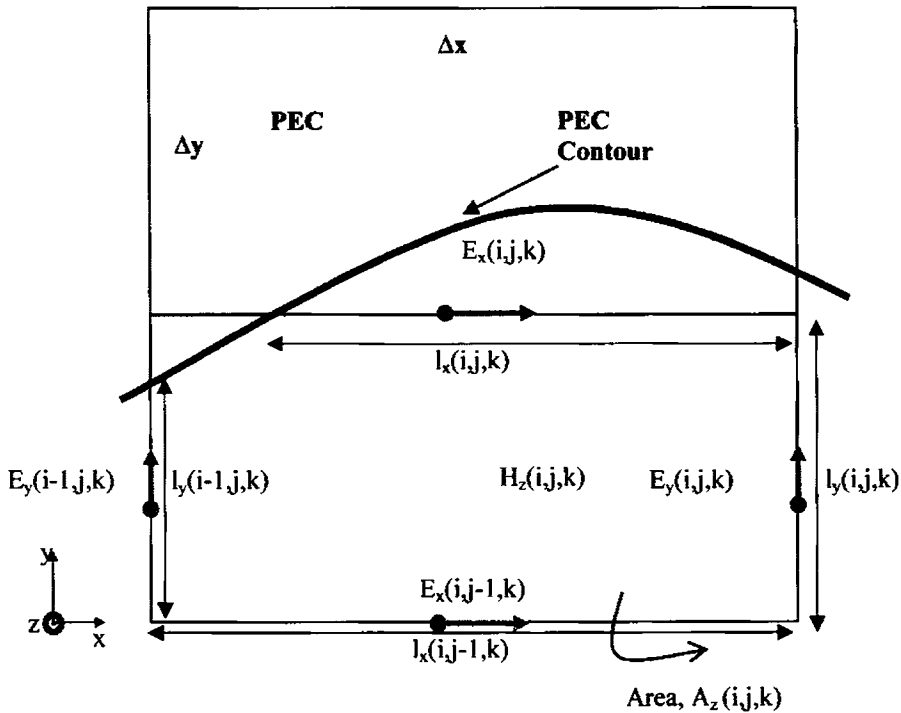
Figure 4.12 E and H field distribution for Conformal FDTD scheme.

Extremely distorted cells (with the maximum side length to area ratio > 12) can generate instability that spreads over the entire grid as time progresses. The backward – weighted averaging scheme in conjunction with the above

update equation is employed in distorted cells that are likely to seed instability. Any cell having non zero cell length and non zero face area is updated normally. For other cells if the normalized cell area is less than 0.075 or if the ratio of maximum cell length to cell face area is greater than 12, then present H field values are saved in buffer. The new set of H field values are computed using the eqn. 4.23.b and averaged with the corresponding values in the buffer to obtain the final value of the H fields for that update. This backward averaging ensures stability. For cell containing two different dielectric media, the effective dielectric constant is computed by taking the weighted volume average of the two dielectrics as[13]

$$\varepsilon_{eff} = V_z(i,j,k)\varepsilon_{r1} + (1 - V_z(i,j,k))\varepsilon_{r2} \tag{4.24}$$

where $V_z(i,j,k)$ is the fractional volume of the $(i,j,k)^{th}$ cell that contains the dielectric material ε_{r1} and ε_{r2} is the dielectric constant of the medium. The phase error in the system can be reduced by incorporating the CP-FDTD scheme within CFDTD[14] in those cells that violate the geometry restrictions for CFDTD.

A robust, computationally efficient and numerically stable conformal FDTD method proposed by Wenhua et al. [15-17] is employed in the present study, where the H field update equation (eqn. 4.23.b) employs the entire cell area instead of the distorted cell area as given below.

$$H_z^{n+1/2}(i,j,k) = H_z^{n-1/2}(i,j,k) + \left(\frac{\Delta t}{\mu \Delta x(i)\Delta y(j)}\right)$$

$$\times (\{- E_x^{n(i,j,k)}\delta_x(i,j,k) + E_x^n(i,j+1,k)\delta_x(i,j+1,k)\} +$$

$$\{E_y^n(i,j,k)\delta_y(i,j,k) - E_y^n(i+1,j,k)\delta_y(i+1,j,k)\}) \tag{4.25}$$

In this method the E and H field components of the distorted cell are located at same position as that in the normal FDTD, but Faraday contour extend over the entire FDTD cell edge rather than over the distorted contour, as shown in figure 4.13. To implement the scheme the distorted cell lengths (δ) located outside the PEC area is calculated based on the PEC-Cartesian grid

line intercept and E field on the edge of distorted cells is calculated using the normal Yee update equations assuming that the deformed cells are *filled* with the media located outside the PEC region. For analyzing 2D planar structures involving perfect electric conductors, this method which uses the information regarding the cell edges, is a better choice than the weighted area and weighted volume approaches.
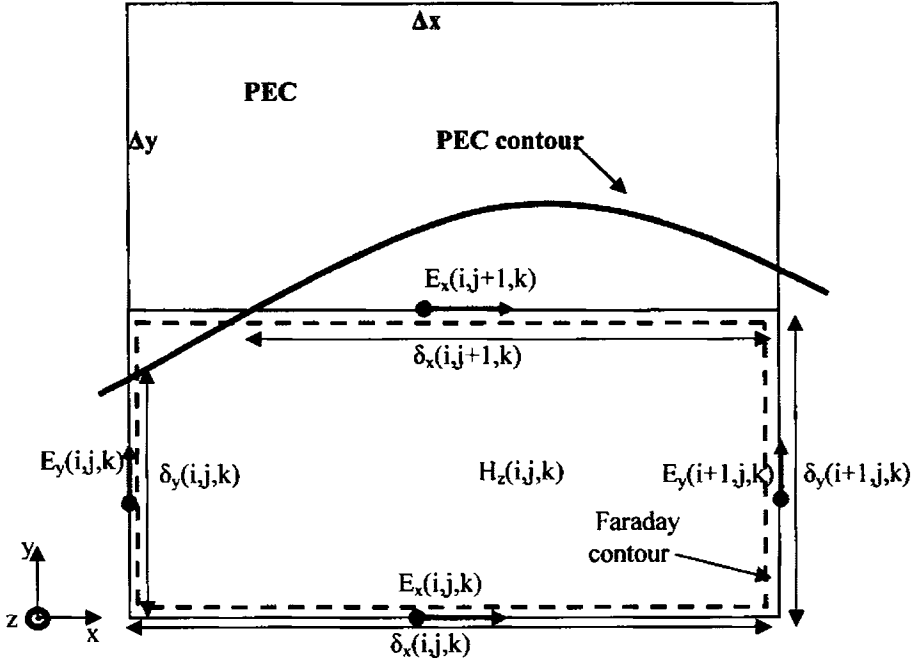
Figure 4.13 E and H field distribution for modified CFDTD

4.3.3.ii   Assumptions taken in the present analysis

While implementing the above described CFDTD algorithm, the following conditions are found necessary in avoiding late time instability:

$$\Delta t = 0.75 \times \frac{0.995}{c\sqrt{\dfrac{1}{\Delta x^2} + \dfrac{1}{\Delta y^2} + \dfrac{1}{\Delta z^2}}}$$

$$\delta_x = 0, \text{ for } \frac{\delta_x}{\Delta x} < \frac{1}{15} \text{ and } \delta_y = 0, \text{ for } \frac{\delta_y}{\Delta y} < \frac{1}{15}$$

To implement this the cell lengths in the patch and feed layers of the domain

are defined as arrays of size equal to that of E or H in that layer.

4.4 Full spatial domain computation *vs* reduced domain

In a FDTD computational domain of cell size Nx x Ny x Nz, the simulation time can be halved if the total number of cells in any of the 3 directions can be halved. By applying the PMC wall along the *plane of symmetry* in the geometry as shown in figure 4.14, the spatial domain can be reduced by 50% resulting in a memory efficient and fast implementation of CFDTD.
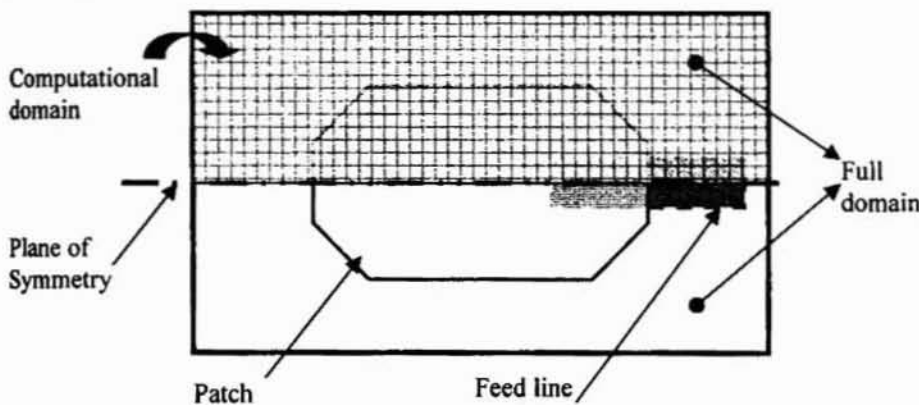
Figure 4.14 Geometry of the antenna with FDTD grid overlaid highlighting the effective computational volume.

4.4.1 Concept of PMC

A PMC wall helps in reducing the computational domain size. Instead of selecting the H boundary through the middle of Yee Cell, PMC edge can be positioned along the cell edge as shown in figure 4.15.a, giving the update equation for the E_y component (1D) on the cell edge as

$$\frac{\partial E_y}{\partial t} = \left[\frac{1}{\Delta x}\right]\left[\frac{1}{\varepsilon}\right](H_{z1} - H_{z2}) \qquad (4.26.a)$$

Exploiting the fact that PMC boundary is equivalent to an anti-symmetry condition on H_z, the fictitious H_z component on the other side of the wall (H_{z2}) is taken to be equal and opposite to H_{z1} (*i.e.* $H_{z2} = - H_{z1}$) thereby giving tangential E_y component at the boundary as

$$\frac{\partial E_y}{\partial t} = \left[\frac{2H_z}{\varepsilon.\Delta x}\right]$$ (4.26.b)

The PMC boundary condition can be mathematically stated as $\vec{a}_n \times \vec{H} = 0$.

i.e. $H_{tan} = 0$ or $E_{norm} = 0$ on the wall. Equivalently E_{tan} and H_{norm} are continuous across the wall.
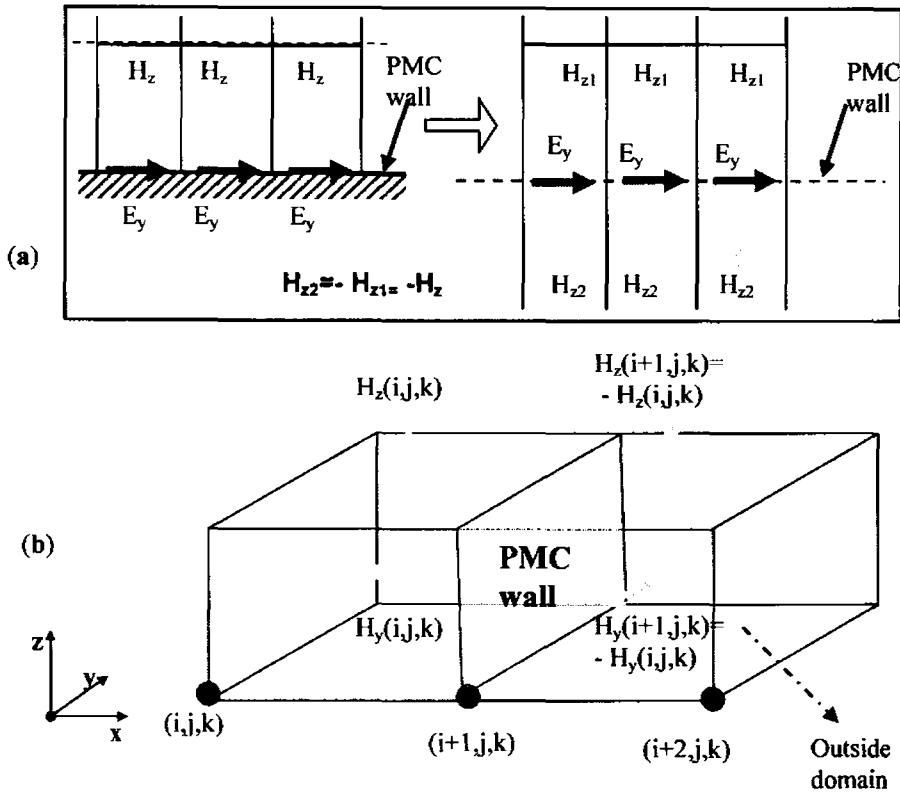
Figure 4.15 Field component distribution at PMC wall

4.4.2 Application of PMC wall in the present analysis

The PMC wall is applied in the present analysis, along the plane of symmetry as illustrated in figure 4.15.b. Instead of simulating the whole model, it is only necessary to simulate the fields in one of the symmetric parts. The $H_{tan} = 0$ condition pertaining to tangential H field at the wall is chosen since it allows easy implementation in the program. The tangential H field components exterior to the domain, needed to update the E field along

the edge coinciding with PMC is therefore equal in magnitude and opposite in polarity to that of the cell inside. On implementing H_{tan} =0, the required condition on the normal H field is realized implicitly.

4.5 Extraction of antenna characteristics

FDTD algorithm performs the transient analysis of the problem under investigation. Field, voltage or current samples are taken from fixed points in the FDTD grid and Fast Fourier Transform is used to compute the frequency domain information. Further post processing can be done to estimate the S parameters, Resonant frequencies and 2:1VSWR bandwidth. The procedure outlined below, based on the method proposed by Luebbers *et al.*[7] is used to extract the parameters.

4.5.1 Return loss

The voltage V^n = V(n.Δt) at the input port location is computed and saved from the E_z field component at that grid point over the entire simulation time interval(K steps). Similarly the current I^{n-1} is also computed based on Ampere's law applied to the tangential H loop around the feed point. The samples are suitably padded with P (P>>K) zeros and the FFT is computed separately. The Input impedance of the antenna is computed as ratio of the FFT of voltage derived from E field values at the feed point, over the entire time steps, to the FFT of current at the same point, derived from the H field values.

$$Z_{in}(\omega) = \frac{FFT(V^n, P)}{FFT(I^{n-1}, P)} \tag{4.27}$$

where V^n is given by eqn. 4.18 and I^{n-1} is given by eqn. 4.21.b

Assuming the characteristic impedance (Z_0) of the feed line ($Z_0 = R_s$),

reflection coefficient is given as $\Gamma(\omega) = \dfrac{Z_{in} - Z_0}{Z_{in} + Z_0}$ \hfill (4.28)

Return loss in dB, $S_{11} = 20\log_{10}\Gamma(\omega)$ \hfill (4.29)

4.5.2   Resonant frequency and 2:1VSWR band width

By processing return loss data computed at the input port ,the fundamental resonance frequency of the antenna is identified as the lowest ω with minimum S_{11}. The 2:1VSWR band and bandwidth corresponding to the -10dB return loss is also estimated from the above data.

4.5.3   Isolation between the ports

In a dual port antenna configuration, the isolation (S_{21}) between the ports is defined as V $_{refl\ at\ port\ 2}$ / V $_{inc\ at\ port\ 1}$. At the location of port 2 in the domain the Ez field values are sampled over the entire period, with source at port 1 activated keeping port 2 source *off*. The internal resistance R_s of port 2 voltage source is retained in the domain to serve as the matched load termination for port 2. The Isolation characteristics is calculated from the voltage induced on a 50Ω resistance at port 2, derived from the local H field values, and the voltage impressed at port 1.

$$V_{reflatport2} = E_z(atport2)\Delta z - R_s I_s(atport2) \qquad (4.30)$$

S_{21} is computed from $\dfrac{FFT(Vreflatport2, P)}{FFT(V_{n\Delta t} atport1, P)}$

4.6   Far field computation

Theoretical analysis of radiators is usually carried out by formulating a theoretical model which closely approximates the actual antenna and then employing a suitable mathematical technique. In such cases discrepancies creep in depending on the extent to which the antenna and /or the equations are approximated. FDTD approach of solving the Maxwell's equations being straight forward, and easily adaptable to any geometry, stands as a good alternative in predicting the far field due to a radiating structure[20]. From the transient near-field values, the required far field transient and/or frequency domain results can be easily computed using suitable near field to far field transformations *i.e* there is *no* need to extend

the FDTD grid to a far field point. By post processing the complex time harmonic electric and magnetic currents flowing on a closed surface in the domain, the far field results are computed. Using a pulse excitation and by applying a running Discrete Fourier Transform(DFT) in every time step, on the tangential field components at each frequency of interest, far field results at multiple frequencies can be extracted[19]. This method requires more computational effort if the number of frequencies involved is high, as it involves complex multiplication at each cell on the transformation surface. In applications requiring the transient and/or broadband frequency domain far field results at different observation angles, the fully transient approach involving the fast Fourier transform (FFT) is desirable. For small geometries this can be implemented by storing the transient tangential field components on the transformation surface. In general the transient far zone potentials, due to the tangential electric and magnetic fields on a closed surface in the computational domain, at each angle of interest can be directly computed by a running summation[21] at each time step.

4.6.1   Theoretical background

A near field surface as shown in figure 4.16.a inside the FDTD lattice is defined as the transformation surface for far field projections. This near field surface is chosen in a layer above the patch layer and is taken to be rectangular for easy implementation of the far field projection algorithm in the FDTD. The tangential E and H fields on this surface (E_A and H_A) are sampled and converted to equivalent surface currents as

$$\vec{J}_s = \vec{a}_n \times \vec{H}_A \qquad\qquad\qquad (4.31.a)$$

$$\vec{M}_s = \vec{E}_A \times \vec{a}_n \qquad\qquad\qquad (4.31.b)$$

where $\vec{a}_n$ is the unit outward normal surface vector($\vec{a}_n = \hat{z}$). The far field at any point outside this surface is computed using electric ($\vec{F}$) and magnetic ($\vec{A}$) vector potentials derived from these surface currents. The presence of

the ground plane is incorporated by applying the image theory, which doubles the effective magnetic current density. In the far field, the E fields transverse to direction of propagation is given as

$$E_\theta = -\mu \frac{\partial A_\theta}{\partial t} - \frac{1}{c}\frac{\partial F_\phi}{\partial t} \qquad\qquad\qquad (4.32.a)$$

$$E_\phi = -\mu \frac{\partial A_\phi}{\partial t} + \frac{1}{c}\frac{\partial F_\theta}{\partial t} \qquad\qquad\qquad (4.32.b)$$

where A and F denote the vector potentials and θ, Φ denote the coordinates in the spherical coordinate system.
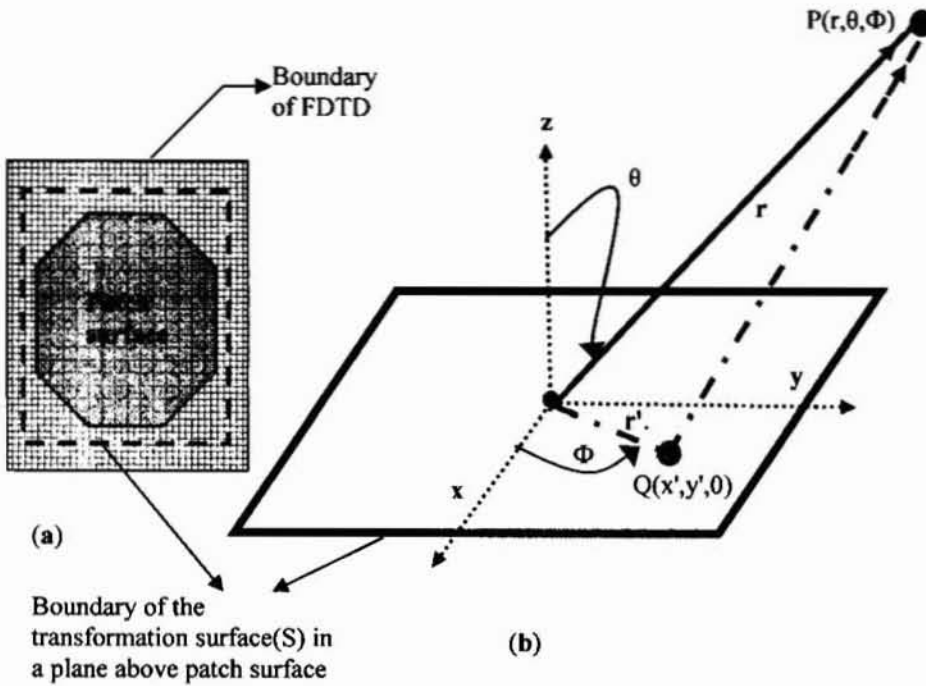
Figure 4.16 The Transformation surface chosen for radiation pattern computation using FDTD.
(a)Transformation surface layout
(b)Q is the spatial point on the transformation surface and P is the far zone point

Simple averaging is used to collocate the spatially staggered FDTD fields. Magnetic surface current density is used to compute the electric potential $\vec{F}$ [equation 1.9 [22]] over the surface. The electric field in free space with characteristic impedance η_0 for the patch under study is written as (with $e^{j\omega t}$ variation assumed and suppressed)[21]

$$\vec{E}(r,\theta,\phi) = j\omega\eta_0(F_\theta\vec{a}_\phi - F_\phi\vec{a}_\theta)$$ (4.32.c)

The far field components E_θ and E_Φ are derived by the rectangular to spherical transformation as

$$E_\theta = j\omega.\eta_0.(F_x.Sin(\phi) - F_y Cos(\phi))$$ (4.33.a)

$$E_\phi = j\omega.\eta_0.Cos(\theta)(F_x Cos.(\phi) + F_y.Sin(\phi))$$ (4.33.b)

With the following assumptions,

> the antenna radiates into the z >0 region from the planar surface in the z=0 plane(transformation surface), as indicated in figure 4.16.b

> r is in the far field *i.e.* (r >> $((x')^2+(y')^2)^{1/2}$) and $k_0 r$ >>1 where $k_0=2\pi/\lambda_0$

> transformation surface defined is such that the tangential electric fields are negligible outside its boundary,

eqn. 4.32.c now becomes

$$\vec{E} = \frac{je^{(-jk_0r)}}{\lambda r}\left\{\left(\cos(\theta)\left(f_x\cos(\phi) + f_y\sin(\phi)\right)\vec{a}_\phi\right) - \left((f_x\sin(\phi) - f_y\cos(\phi))\vec{a}_\theta\right)\right\}$$

where

$$f_* = \iint_S E_*(x',y',0) \times$$
$$\left\{e^{jk_0}\left(x'\sin(\theta)\cos(\phi) + y'\sin(\theta)\sin(\phi)\right)\right\} \times dx' dy'$$ (4.34)

and S is the planar surface selected. The E field components $(E_*(x', y',0))$ over the surface S can be computed by sampling the tangential E field components, over N time steps corresponding to one period of the sinusoidal excitation at the frequency of interest, as proposed by Zimmerman *et al.*[23].

$$E(x',y',z = 0) = \left(\frac{1}{N}\right)\sum_{n=1}^{N} E(n)e^{\left(\frac{j2\pi n}{N}\right)}$$ (4.35)

where $E(n)$ corresponds to the instantaneous tangential E field components $(E_x^n$ and $E_y^n)$ sampled at the point Q(x',y',0) at the nth time step.

4.6.2   Selection of excitation and near field aperture

The excitation source used in the present study is a single frequency sinusoid for extracting the patterns at the resonance frequency. The Gaussian excited normal FDTD is run initially to determine the resonance frequency of the antenna. The frequency so obtained is used as f_0, in the FDTD run for pattern computation. The source voltage V(t) used for the simulation is given by

$$V(n\Delta t) = \sin(2\pi f_0 n\Delta t) \tag{4.36}$$

The surface S is chosen to be in the near field, with dimensions suitable to ensure that tangential E_x^n and E_y^n components are negligible outside its boundary as illustrated in figure 4.16.b. In the FDTD domain for the present analysis, near field aperture is taken as the rectangular surface, S lying in a plane four cells above the xy plane containing the patch PEC in the FDTD grid. In the x and y directions the surface, S spans beyond the patch region by more than two times the number of cells representing substrate thickness.

4.6.3   E plane and H plane patterns

To extract the principal plane pattern data at the resonance frequency, the FDTD mesh is excited using a single frequency sinusoid and the system is allowed to reach steady state. For one period of the sinusoid involving N time steps, the E_x^n and E_y^n components are sampled from the surface S. At each spatial point (x'=i.Δx, y'=j.Δy) on this surface, a running Fourier series summation of these samples is done, as given by eqn. 4.35, to remove the time dependence from the sampled tangential E fields. The E_θ and E_ϕ are then computed for the principal E and H planes, corresponding to Φ= 0°and 90°, using the eqn.4.34. The surface integration over S is implemented as summation over S and far field is computed at discrete θ values. Figure 4.17 depicts the steps involved in far field computation using the FDTD approach.

```
                          ╭───────────╮
                         (    Start    )
                          ╰───────────╯
                                │
                                ▼
   ┌────────────────────────────────────────────────────────────┐
   │  ❖   Problem space setup                                    │
   │  •   Estimate the no of iterations needed to reach the      │
   │      sinusoidal steady state                                │
   └────────────────────────────────────────────────────────────┘
                                │
                                ▼
   ┌────────────────────────────────────────────────────────────┐
   │  ❖   Set up E and H fields in the domain                    │
   │  ❖   Define the sinusoidal excitation at resonant frequency,│
   │      Eⁿ_z (i,j,k) at the selected feed point in the domain  │
   │      over the complete simulation interval.                 │
   └────────────────────────────────────────────────────────────┘

        n=n+1
    ◄──────────────────────────────────►
                                │
                    ┌───────────────────────────┐
                    │   ❖   Update all fields    │
                    └───────────────────────────┘
                                │
                                ▼
              No         ╱─────────────────╲
         ◄───────────── ╱   Steady state    ╲
                        ╲   reached?         ╱
                         ╲─────────────────╱
                                │  Yes
   ┌────────────────────────────────────────────────────────────┐
   │  ❖   Initialize an iteration counter ,M, for one period of  │
   │      the sinusoidal cycle                                   │
   └────────────────────────────────────────────────────────────┘
                                │
                                ▼
                              ( B )

  ( A )
```

Figure 4.17 The Flow chart of FDTD method for pattern computation

B

❖ Perform series summation on the time domain data for every
point in the transformation surface ,S

❖ Store the tangential near field data so computed for the
surface S

One period counter=0?   M=M-1,n=n+1

Yes   No

No
A Maximum time
steps reached?

Yes

❖ Perform the NF - FF transform on the stored tangential field
data to compute the far field components

❖ Plot the near field data to identify the resonance modes

End
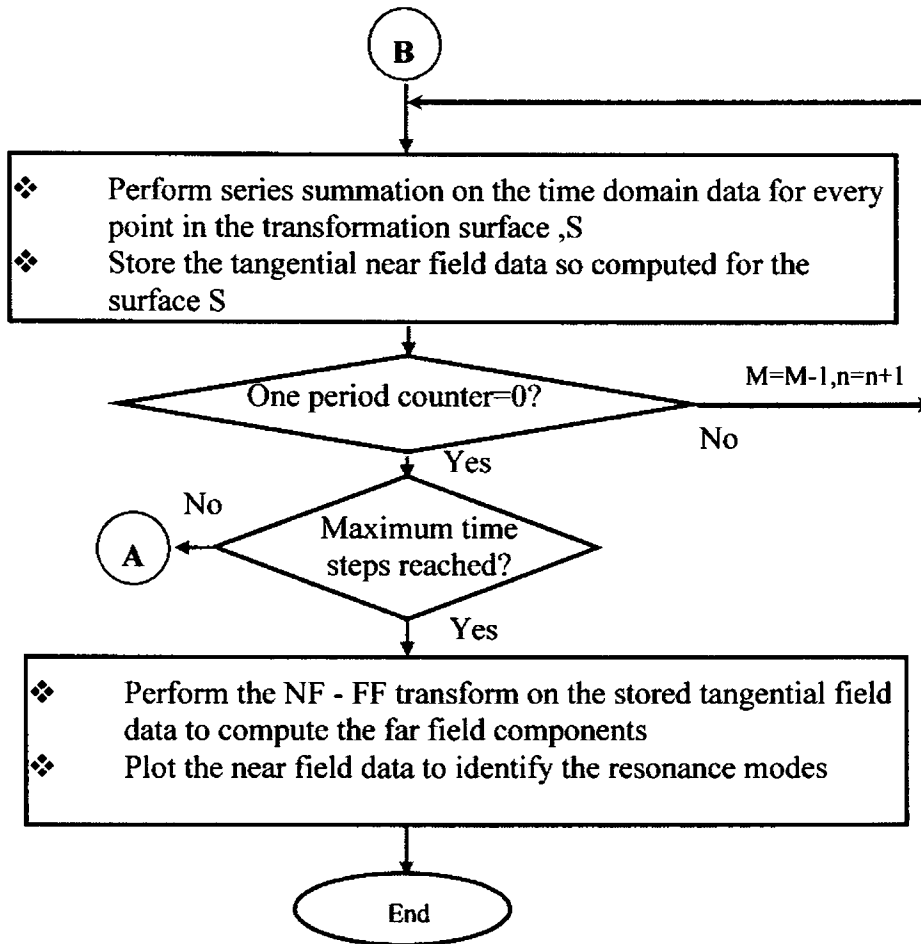
Figure 4.17 *(contd.)* The Flow chart of FDTD method for pattern computation

4.6.4 Modes of resonance

The time independent H_x and H_y over the surface S is arrived at by following the procedure explained above for the E_x and E_y computation. The modes of resonance of the geometry at the chosen frequency of excitation can be inferred from a pictorial representation of these fields normalized suitably, as illustrated in Chapter five.

4.7 Conclusions

The constraints on spatial and temporal parameters used in the Numerical investigations of the Octagonal MPA is discussed in this chapter in addition to a brief outline of the fundamental concepts and implementation of the CFDTD approach. The antenna characteristics extracted from these investigations is presented along with experimental observations in Chapter five.

References:

1. K.S.Yee, "Numerical solution of initial boundary value problems involving Maxwell's equations in isotropic media," *IEEE Trans. Antennas Propagat.*, vol. 14, pp.302-307, May 1966.

2. David M. Sheen, Sami M. Ali, Mohamed D. Abouzahra and Jin Au Kong, "Application of the three dimensional finite difference time domain method to the analysis of planar microstrip circuits," *IEEE Trans. Microwave Theory Tech.*, vol.MTT-38(7), pp.849-857, July 1990.

3. G.Mur, "Absorbing boundary conditions for the finite difference approximations of the time domain electromagnetic field equations," *IEEE Trans. Electromagnetic Compatibility*, vol.23, no.4, pp.377-382, November 1981.

4. Jean Pierre Berenger, "A perfectly matched layer for the absorption of electromagnetic waves," *Journal of computational physics*, 114, pp.185-200, 1994.

5. Allen Taflov, "Computational electromagnetics: The Finite Difference Time Domain method," Artech house publishers, London, 1995.

6. Karl S. Kunz and Raymond J. Luebbers, "The finite difference time domain method for electromagnetics," CRC press, New York 1993.

7. R.J. Luebbers and H.S. Langdon, "A simple feed model that reduces time steps needed for FDTD antenna and microstrip calculations," *IEEE Trans. Antennas Propagat.*, vol. 44, pp.1000-1005, July 1996.

8. C.J. Railton, I.J. Craddock and J.B. Schneider, "Improved locally distorted CPFDTD algorithm with provable stability," *Electron Lett.*, vol.31, no.18, pp. 1585-1586, August 1995.

9. Yikyu Min, Byungsoo Kil and Sangseol Lee, "A novel contour path finite difference tie domain (CPFDTD) algorithm for modeling objects with curved surfaces," *Microwave Opt. Technol. Lett.*, vol.28, no.4, pp.285-287, February 2001.

10. K.S.Yee, J.S.Chen and A.H.Chang, "Conformal finite difference time domain (FDTD) with overlapping grids," *IEEE Trans. Antennas Propagat.*, vol.40, pp. 1068-1075, 1992.

11. Supriyo Dey and Raj Mittra, " A locally conformal finite difference time domain (FDTD) algorithm for modeling three dimensional perfectly conducting objects," *IEEE Microwave Guided Wave Lett.*, vol.7, pp.273-2750, September 1997.

12. Supriyo Dey and Raj Mittra, "A modified locally conformal finite difference time domain algorithm for modeling three dimensional perfectly conducting objects," *Microwave Opt. Technol. Lett.*, vol.17, no.6, pp. 349-352, April 1998.

13. Supriyo Dey and Raj Mittra, "A conformal finite difference time domain technique for modeling cylindrical dielectric resonators," *IEEE Trans. Microwave Theory Tech.*, vol. MTT-47(9), pp.1737-1739, September 1999.

14. John B. Schneider and Christopher L. Wagner, "Analytic analysis of the CP-FDTD and C-FDTD methods for offset planar boundaries," *IEEE Antennas Propagat., Soc. Int. Symp.*,vol.4, pp.1816-1819, June 1998.

15. Wenhua Yu and Raj Mittra, "A conformal FDTD algorithm for modeling perfectly conducting objects with curve-shaped surfaces and edges," *Microwave Opt. Technol. Lett.*, vol.7, no.2, pp.136-138, October 2000.

16. Wenhua Yu and Raj Mittra, "A conformal FDTD software package modeling antennas and microstrip circuit components," *IEEE Antennas Propagat. Mag.,* vol.42, pp.28-39, October 2000.

17. Wenhua Yu and Raj Mittra, "A conformal finite difference time domain technique for modeling curved dielectric surfaces," *IEEE Microwave Wireless Comp., Lett.,* vol.11, no.1,pp.25-28, January 2001.

18. Andrew F Peterson, Scott L Ray and Raj Mittra, "Computational methods for electromagnetics," University Press, India, 2001,ch. 12.

19. Allen Taflov and Morris Brodwin, "Numerical solution of steady state electromagnetic scattering problems using the time dependent Maxwell's equations," *IEEE Trans. Microwave Theory Tech.,* vol.MTT-23(8), pp.623-630, August 1975.

20. J.G. Maloney, G.S. Smith and W.R. Scott Jr., "Accurate computation of radiation from simple antennas using finite difference time domain method," *IEEE Trans. Antennas Propagat.,* vol.38, pp.1059-1068, 1990.

21. Raymond J. Luebbers, Karl S. Kunz, Micheal Schneider and Forrest Hunsberger, "A finite difference time domain near zone to far zone transformation," *IEEE Trans. Antennas Propagat.,* vol.39, pp.429-433, April 1991.

22. Ramesh Garg, Prakash Bhartia, Inder Bahl, Apisak Ittipiboon, "Microstrip Antenna Design Handbook," Artech House Publishers, 2001, ch.1,2,3 and 5

23. Martin L. Zimmerman and Richard Q. Lee, "Use of the FDTD method in the design of microstrip antenna arrays," *Int. Journal of Microwave and Millimeter wave Comp. aided Engg.,* vol.4, no.1, pp.58-66, 1994.

Numerical and Experimental results

The outcome of conformal FDTD algorithm based numerical computation performed on Octagonal microstrip patch antenna, is presented in this Chapter. The predicted results are verified experimentally for Octagonal microstrip patch antennas suitable for selected dual band applications. Brief discussion on the experimental observations of antenna characteristics is also presented.

The Chapter begins with an introduction to the Octagonal MPA under investigation, followed by the illustration of the computation domain defined to perform the numerical investigations. The CFDTD code implemented in MATLAB™ uses the optimised spatial and temporal parameters based on the theoretical aspects outlined in Chapter three. This is followed by a description of the computational and experimental outcome of the characteristics of antennas suitable for Mobile-Bluetooth application. Experimental observations of the characteristics of the dual band antenna excited using a single coaxial probe is highlighted first, followed by the outcome of the exhaustive study performed on Electromagnetically excited dual feed dual band Octagonal MPA suited for the above application. Overview of results of an Octagonal MPA suited for Mobile-GPS receiver application is then presented. The effect of slot perturbation is then discussed. The Chapter concludes with an empirical formula for designing a regular Octagonal microstrip patch antenna.

5.1 Introduction

Wireless access to different services from a single handheld module, is an important issue that is being addressed in the present scenario. Dual frequency capability is important for most of the present day and future wireless systems. This demands a single *antenna that serves different frequency bands allotted to different services*.

A simple Octagonal microstrip patch antenna (OMPA) configuration that suits the above purpose is the theme of present work. Conformal Finite Difference Time Domain (CFDTD) algorithm is used to predict the antenna characteristics which are then experimentally verified. The spatial and temporal parameters of the CFDTD code, implemented in MATLAB™, are optimized based on the theoretical aspects discussed in section 4.2. The outcome of exhaustive numerical and experimental investigations performed on the Octagonal MPA, is presented in the following sections. The antenna geometry and feed configurations are discussed initially followed by the observations and inferences.

- **Geometry of the Octagonal microstrip patch antenna**
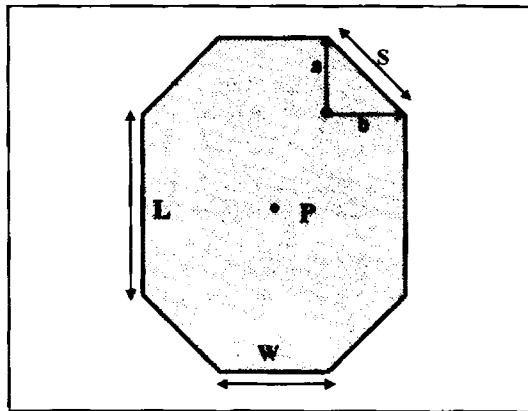
Figure 5.1.1 Geometry of Octagonal Microstrip Patch Antenna

The geometry of the *Octagonal* MPA is illustrated in figure 5.1.1. It consists of an octagonal patch with length L, width W and slant edge dimension S

(constitutive dimensions being a,b). The geometric centre of the patch is denoted as P. The patch is etched on a substrate of thickness h and dielectric permittivity ε_r. The Octagonal patch antenna resonates at two frequencies determined primarily by the L and W dimensions of the geometry. The dimension S serves as an additional parameter that helps in trimming the resonant frequencies to the desired value.

• The CFDTD *Problem* and optimum code parameters

Conformal FDTD algorithm described in Chapter four is employed for the study and optimization of the Octagonal Microstrip Patch Antenna configuration. The CFDTD problem is set up treating the patch surface, feed lines and ground metallisation as Perfect Electric Conductors (PEC).
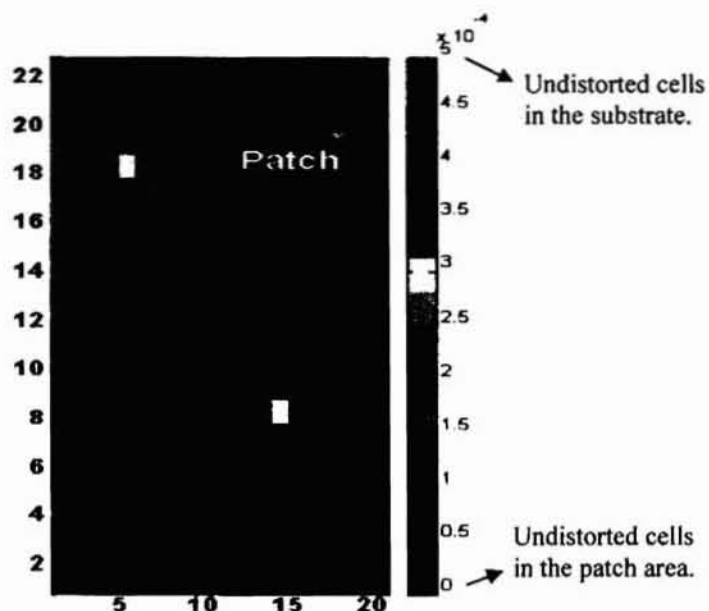
Figure 5.1.2 Inclined edge of the Octagonal Microstrip Patch Antenna showing the distorted cells of the CFDTD computation domain

Figure 5.1.2 illustrates the inclined edge of the geometry. Color bar in the figure indicates the color scheme used to distinguish between the distorted Yee cell size along the edge and the normal undistorted Yee cell size assigned to patch interior region and substrate regions. In the development of

the CFDTD code, Δx and Δy in the PEC regions are assigned zero value. The distorted Yee cells are given special attention based on the *conformal* scheme outlined in section 4.3.3. The steps taken to ensure numerical stability in the system are explained in section 4.2.3.

The feed is modeled as a resistive voltage source oriented in the +z direction. The time delayed Gaussian distribution, discussed in section 4.2.4, is assigned to the E_z component at the feed point of the patch. Mur's Absorbing Boundary Conditions (ABC) are applied in the x, y and z directions at $30 \times 30 \times 15$ cells away from the geometry. Table 5.1.1 highlights the optimized temporal and spatial parameters used in the source code implemented in MATLAB™ environment for CFDTD computation. The Gaussian half width and time delay are chosen following the criteria highlighted in section 4.2.4. The grid size along the x and y directions in the CFDTD domain are chosen to facilitate description of the geometry with minimum discretisation error. The cell size along the z direction is chosen ensuring that there are finite number of Yee cells along the substrate thickness (*e.g.* four cells in the case of FR4 substrate of thickness h=1.6mm). The time step is chosen as indicated in section 4.3.3.ii.

Temporal parameters	Spatial parameters
Gaussian Pulse Half width $T = N\Delta t = 21\ ps$ Time delay $\tau_d = 3T$	Undistorted Cell Dimensions $\Delta x = 0.5mm$, $\Delta y = 0.5mm$, $\Delta z = 0.4mm$ (for substrate thickness $h = 1.6mm$)
Time step $\Delta t = 0.66\ ps$ Number of time steps : 4000 Simulation interval : 2.64ns	Distorted Cell Dimensions $\delta_x = 0$, for $\dfrac{\delta_x}{\Delta x} < \dfrac{1}{15}$ $\delta_y = 0$, for $\dfrac{\delta_y}{\Delta y} < \dfrac{1}{15}$ else the actual value is computed depending on the ratio a/b

Table 5.1.1 Optimized CFDTD code parameters

5.1.1   Coaxially fed Dual frequency Octagonal MPA

Coaxial feeding technique explained in section 1.3.3 is used to couple energy to the Octagonal MPA. Feed point may be located on the edges of the patch or inside the patch. In the CFDTD computation domain the feed point location is varied to optimize the position for good impedance (50Ω) match for both resonant frequencies. As in the case of a conventional microstrip antenna the coaxial feed located along the edges excites modes depending on the dimension of the chosen excitation edge. A suitably located single feed point F_P inside the patch at a distance of f_x and f_y from the geometric centre P of the patch, offers impedance match for both resonant frequencies. Figure 5.1.3 shows the geometry of the Octagonal MPA with the coaxial feed set up, illustrating the location of the feed point.
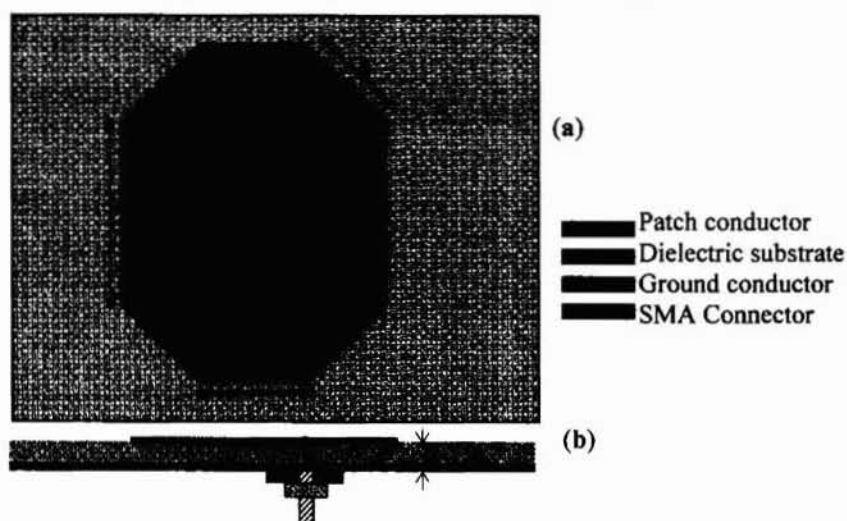
Figure 5.1.3 Coaxially fed Octagonal MPA layout
(a) The Geometry illustrating the feed point and antenna parameters
(b) Side view illustrating the Feed set up

The characteristics of Coaxially fed Octagonal MPA configuration suitable for Mobile-Bluetooth dual frequency application, is predicted numerically and verified experimentally for different dielectric substrates. Operating band of *DCS 1800* is 1.71GHz-1.88GHz, whereas Bluetooth applications work in the 2.4GHz-2.485GHz band. From the results of the Conformal FDTD study, presented in table 5.1.2, it is found that the optimum dimensions of the

coaxially fed Dual band Octagonal MPA configuration, with resonance frequencies that suit the above requirement, is L = 25.5mm, W= 11mm, a = 10mm, b=10mm, for the patch on FR4 substrate with h=1.6mm, ε_r=4.28 (Antenna 1). For GML 2032 laminate with h=0.762mm, ε_r=3.2, the optimized dimensions are L = 31mm, W= 15.5mm, a= 10mm and b=10mm (Antenna 2). The relative permittivity of FR4 and GML 2032 are verified using cavity perturbation method. Discussions below portray the characteristics of the two antenna configurations.

	Antenna dimensions				Resonant frequency	
	Length, L (mm)	Side, a (mm)	Side, b (mm)	Width W (mm)	Fr_1 (GHz)	Fr_2 (GHz)
FR4 Substrate (h=1.6mm ε_r=4.28)	10	4	8	6	3.56	4.37
	13	10	10	10	2.5	2.65
	15	10	10	10	2.38	2.62
	19	10	10	10	2.12	2.56
	20	10	10	15	2	2.25
	22	10	10	9	2	2.6
	24	10	10	10	1.88	2.52
	25	9	9	17	1.85	2.15
	25	10	10	15	1.78	2.2
	25	10	10	12	1.8	2.35
	25	12	10	12	1.7	2.35
	25	9	8	11	1.9	2.75
	25	8	9	11	1.95	2.6
	25	10	8.5	9.5	1.85	2.8
	25	10	10	8	1.85	2.65
	25.5	**10**	**10**	**11**	**1.83**	**2.43**
	26	10	10	12	1.75	2.4
	27	10	10	23	1.65	1.8
	27	10	10	7	1.8	2.75
	30	10	10	20	1.55	1.9
	30	10	10	15	1.6	2.15
	30	10	10	10	1.65	2.45
GML 2032 Substrate (h= 0.762mm ε_r=3.2)	25	9	9	17	2.04	2.53
	29	9	9	16	1.88	2.6
	30	10	10	15	1.85	2.5
	30	10	10	12	1.85	2.75
	30	9	9	10	1.9	3.09
	31	**10**	**10**	**15.5**	**1.785**	**2.43**
	31	10	10	15	1.8	2.5

Table 5.1.2 Resonant frequency of coaxially fed Octagonal MPA computed using Conformal FDTD

*   Characteristics of the coaxially fed Octagonal MPA

Figure 5.1.4 shows the computed and measured return loss characteristics of the coaxially fed Octagonal MPA for two different substrates. The measured and computed lower resonance frequencies (TM_{10} mode) of antenna 1 when fed at f_x= 7mm and f_y = 11mm are, 1.8375GHz and 1.8306GHz respectively with 2:1VSWR bandwidth of 1.52% and 1.37%. The measured and computed TM_{10} mode frequencies exhibited by antenna 2 fed at f_x= 7mm and f_y = 8mm are, 1.81GHz and 1.785GHz respectively, with fractional bandwidths of 1.38% and 1.12%. The measured and computed higher resonance frequencies (TM_{01} mode) of the antenna 1 are 2.3975GHz and 2.43GHz respectively. The respective 2:1VSWR bandwidths are 1.85% and 1.44%. The corresponding measured and computed TM_{01} mode results exhibited by antenna 2 are 2.46GHz and 2.43GHz with fractional bandwidths of 1.43% and 1.44%. The effective resonating length for the two modes is observed to be longer than 'L' or 'W' as the case may be, and it is dependant also on the slant edge dimension 'S'. Maximum error between the measured and computed resonances for the two antennas is +1.93%, as indicated in table 5.1.3, validating the CFDTD predictions. Measured variation in the input impedance in the resonant bands of the two configurations is illustrated in figure 5.1.4.b. Validity of the CFDTD is further confirmed by the Smith Chart plot. It is very clear from figure 5.1.4.b,d that phase of the computed return loss is in agreement with the experimental results. The slight difference between the CFDTD and measured results may be due to the non uniform substrate characteristics, finite diameter of the centre conductor of the SMA connector and the effect of the solder on patch surface, which are not included in the CFDTD model.

Antenna 1

(a)

(b)

—○— TM$_{10}$ mode Start freq 1.823GHz
Measured   Step freq 6MHz
••○•• TM$_{01}$ mode Start freq 2.3656GHz
           Step freq 11.5MHz
••○•• TM$_{10}$ mode Start freq 1.8GHz
CFDTD   Step freq 4.5MHz
••◇•• TM$_{01}$ mode Start freq 2.4GHz
           Step freq 7.5MHz
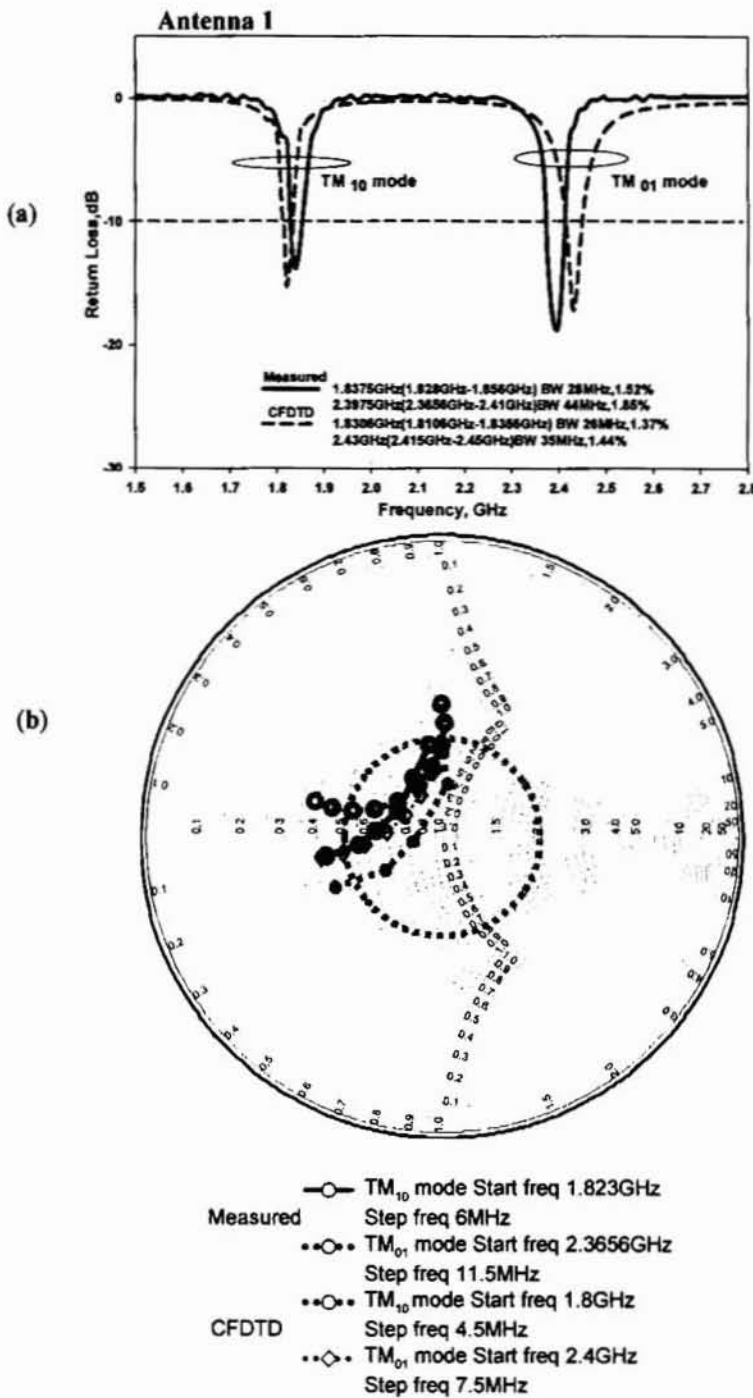
Figure 5.1.4 Input characteristics of coaxially fed Octagonal MPA (Antenna 1)
Antenna 1: L = 25.5mm, W= 11mm, a= 10mm, b=10mm, f$_x$=7mm, f$_y$=11mm,
h=1.6mm, ε$_r$=4.28
(a)Return Loss in the two resonant modes of the antennas
(b) Input impedance variation in the resonant bands of the antennas

Antenna 2

(c)

(d)

Measured
—○— TM$_{10}$ mode Start freq 1.795GHz
       Step freq 7MHz
··○·· TM$_{01}$ mode Start freq 2.435GHz
       Step freq 10MHz

CFDTD
··○·· TM$_{10}$ mode Start freq 1.76GHz
       Step freq 5MHz
··◇·· TM$_{01}$ mode Start freq 2.4GHz
       Step freq 2.5MHz
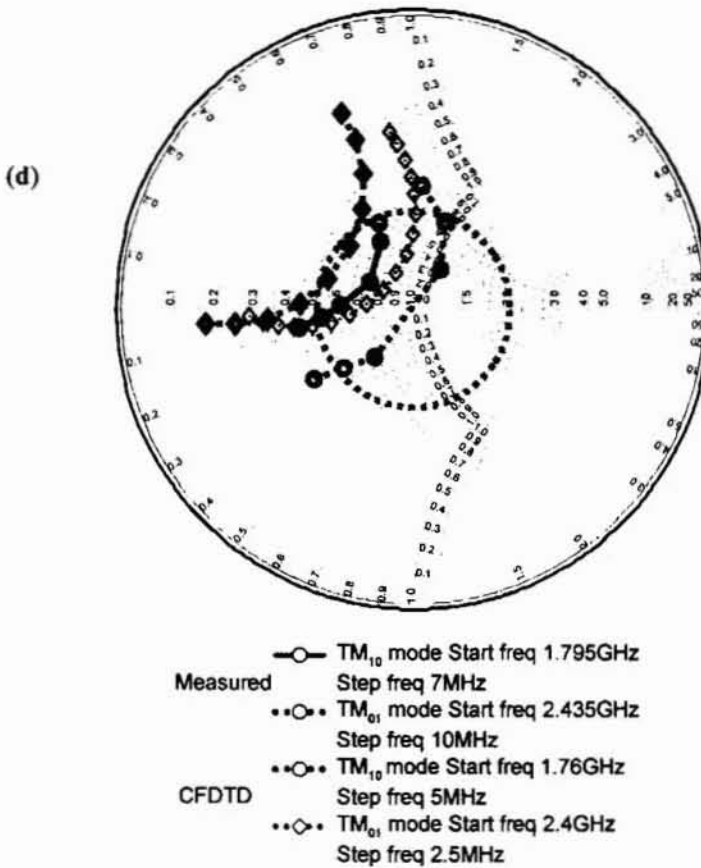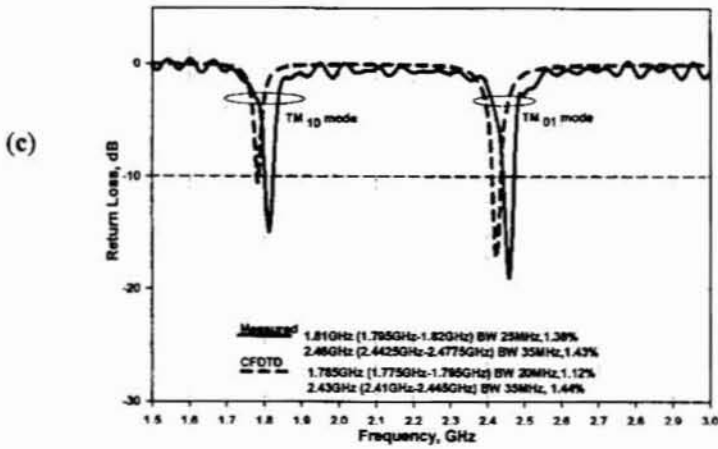
Figure 5.1.4 *(contd.)* Input characteristics of coaxially fed Octagonal MPA (Antenna 2)
Antenna 2: L = 31mm, W= 15.5mm, a= 10mm, b=10mm, f$_x$=7mm, f$_y$=8mm,
h=0.762mm, ε$_r$=3.2
(c)Return Loss in the two resonant modes of the antennas
(d) Input impedance variation in the resonant bands of the antennas

Antenna 1

(a)

(b)

Antenna 2

(a)

(b)

Computed Eplane co_polar — Expt Eplane co_polar

···· Computed Eplane cross_polar ···· Expt Eplane cross polar

Computed H plane co_polar — Expt Hplane co_polar

··●· Computed H plane cross_polar ··+· Expt Hplane cross_polar
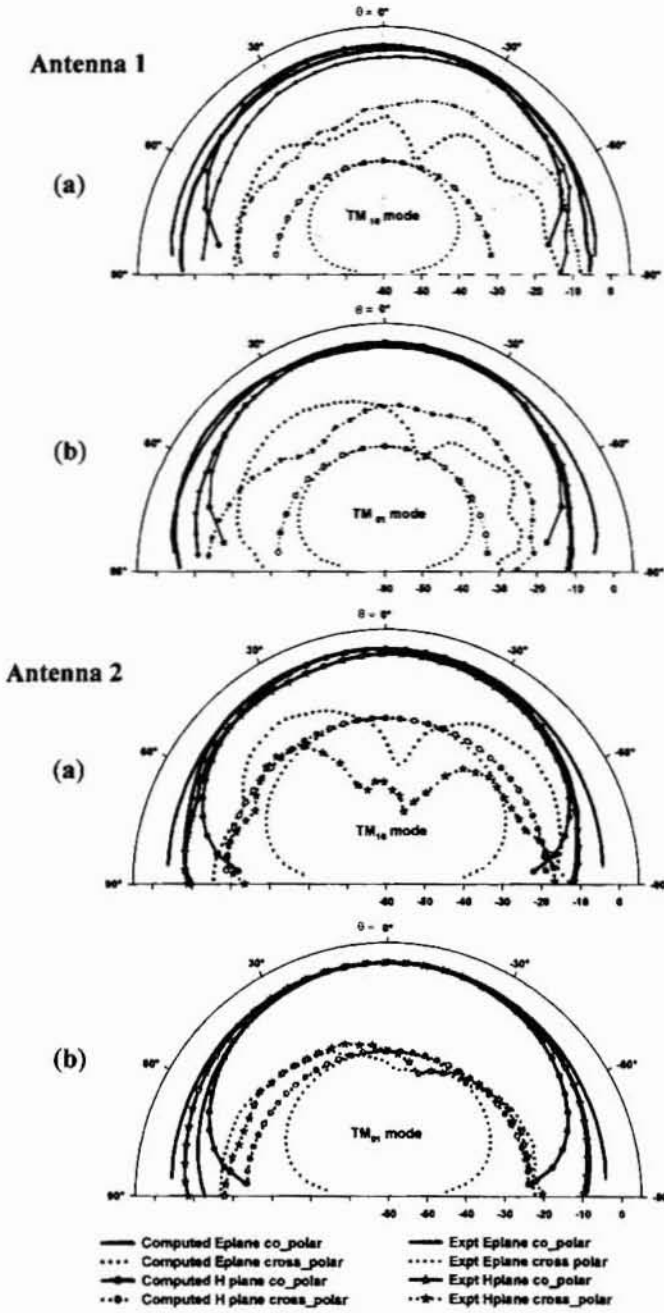
Figure 5.1.5 CFDTD computed and measured patterns of
Coaxial fed Octagonal MPA

Antenna 1: L = 25.5mm, W= 11mm,a= 10mm, b=10mm,f_x=7mm, f_y=11mm,
h=1.6mm,ε_r=4.28

Antenna 2: L = 31mm, W= 15.5mm, a= 10mm, b=10mm, f_x=7mm, f_y=8mm,
h=0.762mm, ε_r=3.2

(a)E plane and H plane patterns of TM_{10} mode

(b) E plane and H plane patterns of TM_{01} mode

Both antennas show good radiation characteristics with broad patterns in their principal E planes as illustrated in figure 5.1.5 and summarised in table 5.1.3. The computed cross polar level in the bore sight is better than -25dB for both modes in case of antenna1 where as TM_{10} mode of antenna2 shows poor cross polarization characteristics. Due to the inherent asymmetry in the coaxial fed antenna configuration, the measured average cross-polar level especially in the H plane for antenna 1 is high for both modes whereas for antenna 2, the measured values are better than -20dB. As shown in figure 5.1.6, the decoupling between the two resonant mode frequencies in the boresight is a moderate 14dB for TM_{10} mode whereas it is 17dB for the TM_{01} mode, in the case of antenna 1. For antenna 2, the values are 19dB and 23.8dB respectively. The shaded regions in these figures correspond to the respective 2:1 VSWR bands.

(a)
Antenna 1

(b)
Antenna 2
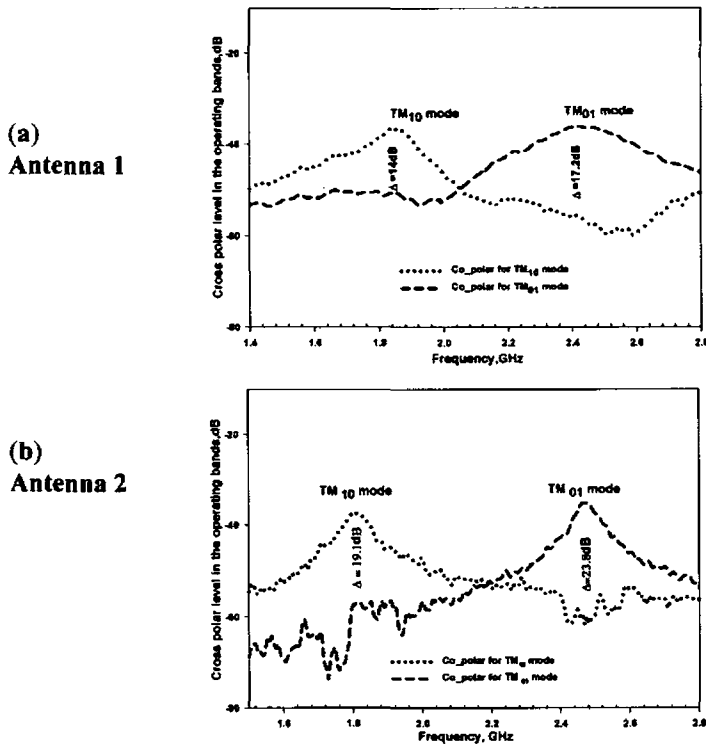
Figure 5.1.6 Decoupling between the modes of coaxially fed Octagonal MPA
(a) L = 25.5mm, W= 11mm, a= 10mm, b=10mm, f_x=7mm, f_y=11mm, h=1.6mm, ε_r=4.28
(b) L = 31mm, W= 15.5mm, a= 10mm, b=10mm, f_x=7mm, f_y=8mm, h=0.762mm, ε_r=3.2

The antenna offers moderate gain in the desired frequency bands as shown in figure 5.1.7. For antenna 1 the TM_{10} mode exhibits a peak gain of 7.1dBi whereas TM_{01} mode shows 7.3dBi gain. Antenna 2 shows a peak gain of 8.1dBi in the TM_{01} band and 7.66dBi in the TM_{10} mode. The resonant modes exhibit linear orthogonal polarization. The plane of polarization for TM_{10} mode is tangential to side 'L' and the polarization plane of TM_{01} mode is tangential to side 'W'. Figure 5.1.8 illustrates the computed surface current density on the
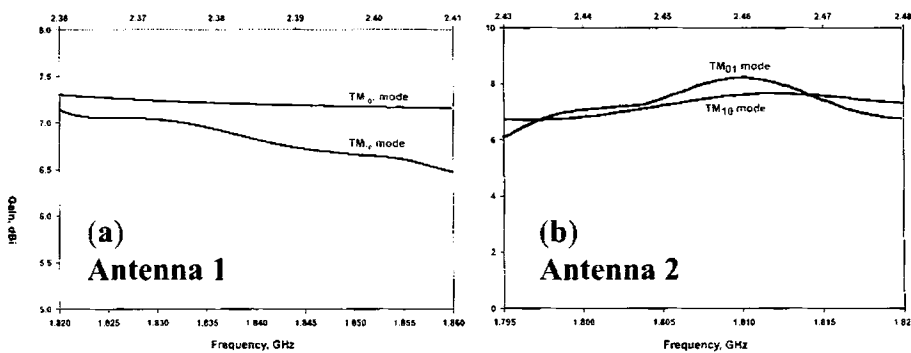
Figure 5.1.7 Gain of coaxial fed Octagonal MPA

(a) Antenna 1: L = 25.5mm, W= 11mm, a= 10mm, b=10mm, f_x=7mm, f_y=11mm, h=1.6mm, ε_r=4.28

(b) Antenna 2: L = 31mm, W= 15.5mm, a= 10mm, b=10mm, f_x=7mm, f_y=8mm, h=0.762mm, ε_r=3.2

Table 5.1.3 summarizes the antenna parameters along with the computed and measured antenna characteristics for the two cases. As illustrated, the numerically predicted results agree very closely with the experimental observations. The slight deviations may be due to the finite domain size constraint in the CFDTD computation and also due to the variations that creep in due to non ideal substrate characteristics and etching tolerances. The CFDTD domain extends only 30 cells (15mm) beyond the patch metallization, in the x and y planes. The overall size of the antenna substrate used for measurements is 100 x 100 mm^2. This may also lead to the

difference between computed and measured values.
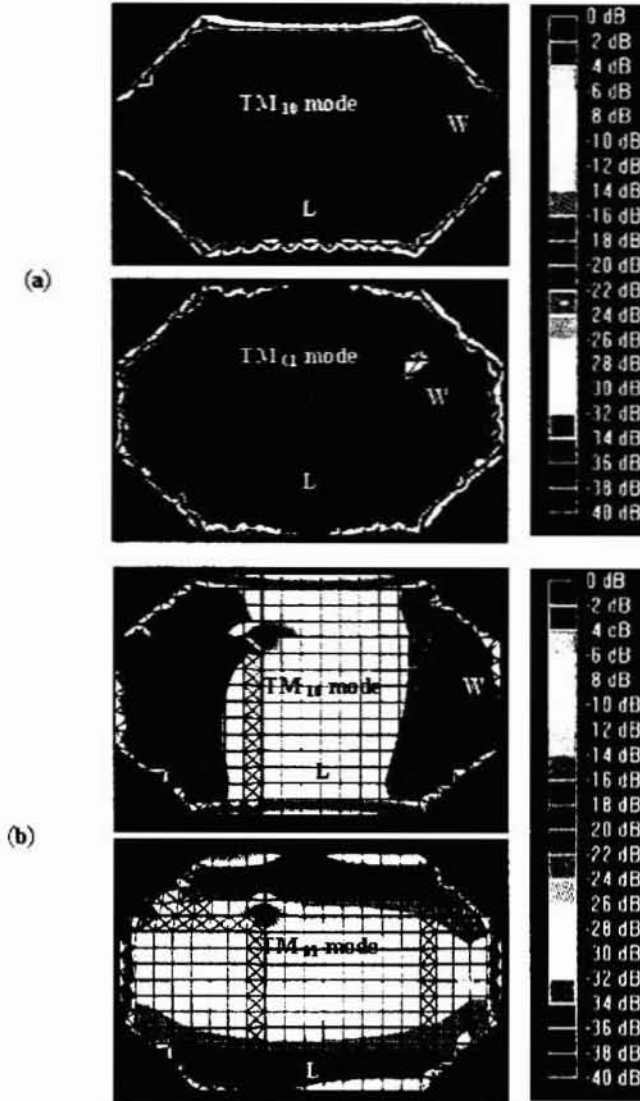
Figure 5.1.8 Surface current distribution corresponding to the two resonant
modes
of the coaxial fed Octagonal MPA
(a) Antenna 1: L = 25.5mm, W=11mm, a= 10mm, b=10mm, f_x=7mm,
f_y=11mm
h=1.6mm, ε_r=4.28
(b) Antenna 2: L = 31mm, W=15.5mm, a= 10mm, b=10mm, f_x=8mm,
f_y=7mm h=0.762mm, ε_r=3.2

Parameters	Antenna 1 (FR4)		Antenna 2 (GML 2032)	
Substrate parameters	$\varepsilon_r = 4.28$		$\varepsilon_r = 3.2$	
	h = 1.6 mm		h = 0.762 mm	
Patch Dimensions	L=25.5mm W =11mm a = 10mm b = 10 mm		L=31mm W = 15.5mm a = 10mm b =10mm	
Feed Position	$f_x = 7mm$ $f_y = 11mm$		$f_x =7mm$ $f_y =8mm$	
Results	TM $_{10}$ mode	TM $_{01}$ mode	TM $_{10}$ mode	TM $_{01}$ mode
Numerical Results — Frequency	1.8306GHz	2.43GHz	1.785GHz	2.43GHz
Numerical Results — Band	1.8106GHz-1.8356GHz	2.415GHz-2.450GHz	1.775GHz-1.795GHz	2.41GHz-2.445GHz
Numerical Results — Bandwidth	26MHz, 1.37 %	35MHz, 1.44 %	20MHz, 1.12 %	35MHz, 1.44%
Measured Results — Frequency	1.8375GHz	2.3975GHz	1.81GHz	2.46GHz
Measured Results — Band	1.8280GHz-1.8560GHz	2.3656GHz-2.4100GHz	1.795GHz -1.82GHz	2.4425GHz -2.4775GHz
Measured Results — Bandwidth	28MHz, 1.52 %	44MHz, 1.85%	25MHz, 1.38%	35MHz, 1.43%
Fractional error in resonance frequency	+0.37%	-1.37%	+1.93%	+1.22%
Cross Polar Level — numerical	-30.4dB	-27dB	-17.6dB	-22.7dB
Cross Polar Level — measured	E plane -19dB H plane -13dB	E plane -16dB H plane -16dB	E plane -22dB H plane -30dB	E plane -26dB H plane -22dB
Polarisation plane	Tangential to 'L'	Tangential to 'W'	Tangential to 'L'	Tangential to 'W'
HPBW	E plane 100° H plane 85°	E plane 114 ° H plane 86 °	E plane 100° H plane 93°	E plane 100° H plane 88°
Gain	Peak 7.1dBi Avg. 6.8dBi	Peak 7.3dBi Avg. 7.2dBi	Peak 7.66dBi Avg. 6.78dBi	Peak 8.1dBi Avg.7.07dBi

Table 5.1.3 Summary of the characteristics of the coaxial fed Octagonal MPA on different substrates

5.1.2 Electromagnetically excited single port Octagonal MPA for Dual frequency operation

The Coaxially fed single port Octagonal MPA discussed in the previous section offers dual frequency operation with 2:1VSWR bandwidth of the order of 1-2%. Using thicker substrates, the bandwidth can be enhanced to some extent. However this leads to excitation of surface waves and performance deterioration. Increased cross-polar radiation is yet another disadvantage of the coaxial technique. The electromagnetic coupling method offers less feed interference to radiation and also eliminates the soldering on the patch surface.

Single microstrip feed line of length F_L and width w, designed with a 50Ω characteristic impedance, serves as the feed of the antenna configuration. The Octagonal patch geometry is etched on one side of patch layer substrate, while the metallization on other side of the patch substrate is removed, resulting in the configuration depicted in figure 5.1.9.

Patch and feed conductor
Dielectric substrate
Ground conductor
SMA Connector

(a)

(b)
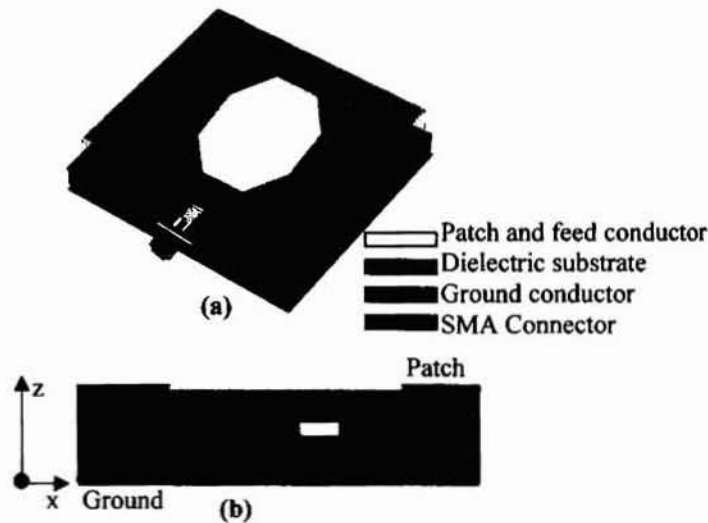
Figure 5.1.9 Electromagnetically excited Octagonal MPA with single feed
(a) The Antenna configuration (b) Side view

Different single feed configurations studied to achieve dual frequency excitation are illustrated in figure 5.1.10. Fx and Fy indicate the distance of the *open end* of the feed line from the geometric centre P, of the patch. The relative position of the open end of the feed line with respect to patch determines the impedance match at the port.
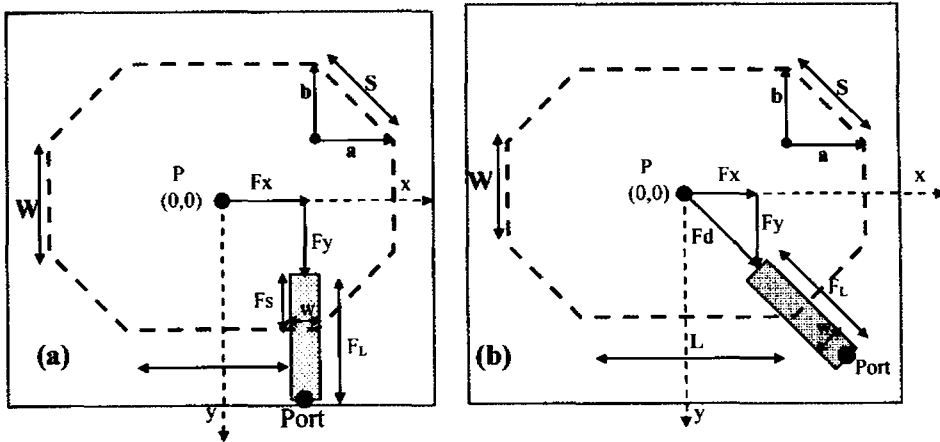
Figure 5.1.10 Feed configurations of the electromagnetically excited
single port Octagonal MPA
(a) Laterally offset feed
(b) Corner feed set up with open end of the feed at distance F_d from the patch centre

Variation in the return loss characteristics of the Octagonal MPA with respect to the feed position, for the two feed arrangements is presented below. For FR4 substrate, the width w of the feed line with characteristic impedance 50Ω is w=3mm. Length of the feed line is chosen as F_L=25mm. From the results of the Conformal FDTD study, presented in table 5.1.4, it is found that the optimum dimensions of the single port Dual band Octagonal MPA configuration, with resonance frequencies that suit the above requirement, is L = 24mm, W= 10mm, a = 10mm, b=10mm, for the patch on FR4 substrate with h=1.6mm, ε_r=4.28. The optimum position of feed for dual frequency excitation in Octagonal MPA is determined based on CFDTD computation.

Antenna dimensions (h=1.6mm,ε_r=4.28)				Resonant frequency	
Length, L (mm)	Side, a (mm)	Side, b (mm)	Width W (mm)	Fr$_1$ (GHz)	Fr$_2$ (GHz)
15	10	10	10	2.3	2.5
15	10	10	15	2.15	2.15
20	10	10	10	2	2.45
20	10	10	15	1.95	2.1
22	10	10	12	1.9	2.3
23	10	10	10	1.85	2.4
23	10	10	12	1.85	2.3
24	**10**	**10**	**10**	**1.8**	**2.4**
24	9	10	10	1.9	2.4
24	10	9	10	1.8	2.35
24	10	10	12	1.8	2.35
25	10	10	12	1.75	2.25
25	10	10	15	1.75	2.1
30	10	10	15	1.55	2.05
30	10	10	20	1.55	1.87

Table 5.1.4 Resonant frequency of Octagonal MPA computed using CFDTD

✶   Characteristics of the electromagnetically excited single port Octagonal MPA

• Laterally offset feed configuration

Single port configuration with the feed line laterally offset with respect to x and y axis, as shown in figure 5.1.10.a, offers dual frequency characteristics. For the feed line positions depicted in figure 5.1.11, return loss characteristics of the antenna in the two resonant modes are obtained numerically. The figure indicates the loci A,B,C,D and E traced by the open end of the feed line, along with the corresponding Fx and Fy values for different feed positions (P1 to P10). The computed and measured return loss characteristics exhibited by Octagonal MPA of dimensions L=24mm, W=10mm and a= b= 10mm with feed and patch layers on FR4 substrate (h=1.6mm and ε_r = 4.28) is shown in figure 5.1.12. For feed positions lying on Loci A and B, impedance matching is exhibited only for TM$_{01}$ mode, as

illustrated in figure 5.1.12.a-b. Loci C and D offers impedance matching for both TM_{10} mode and TM_{01} modes as shown in figure 5.1.12.c-d. Only TM_{10} mode exhibits good impedance match for positions lying on Locus E as indicated in figure 5.1.12.e. Dual frequency behaviour with good reflection characteristics is exhibited when the open end of the feed line is at Fx=15mm and Fy=5mm, which corresponds to P3 in locus D. Reflection for both modes increases as the tip of the feed moves along the locus D from P1 to P6 in the +ve y direction.
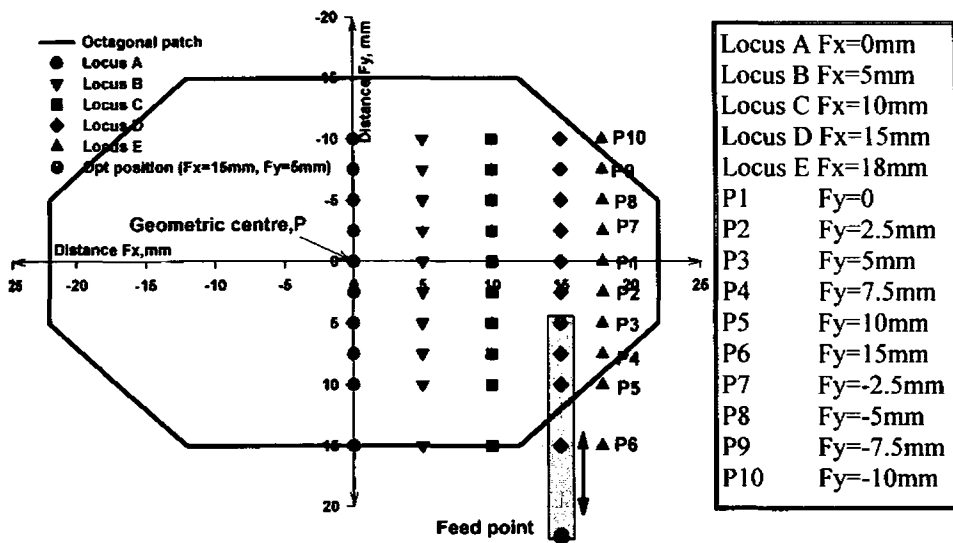
Figure 5.1.11 Illustration of feed positions for single port electromagnetically excited Octagonal MPA with laterally offset feed. P is the geometric centre of the patch L = 24mm, W= 10mm, a= 10mm, b=10mm, F_L=25mm, h=1.6mm, ε_r=4.28

The measured and computed return loss characteristics observed for the numerically estimated optimum feed end position (Fx=15mm, Fy=5mm *i.e* P3 of locus D) is illustrated in figure 5.1.13.a. The antenna exhibits dual resonance with resonant frequencies at 1.795GHz and 2.425GHz. Corresponding -10dB return loss bands are 1.765GHz - 1.810GHz and 2.4GHz - 2.47GHz respectively for the two modes with 2.51% and 2.89% BW. The fractional error between the computed and measured resonances is -0.56% and -1.65% respectively for the two modes.
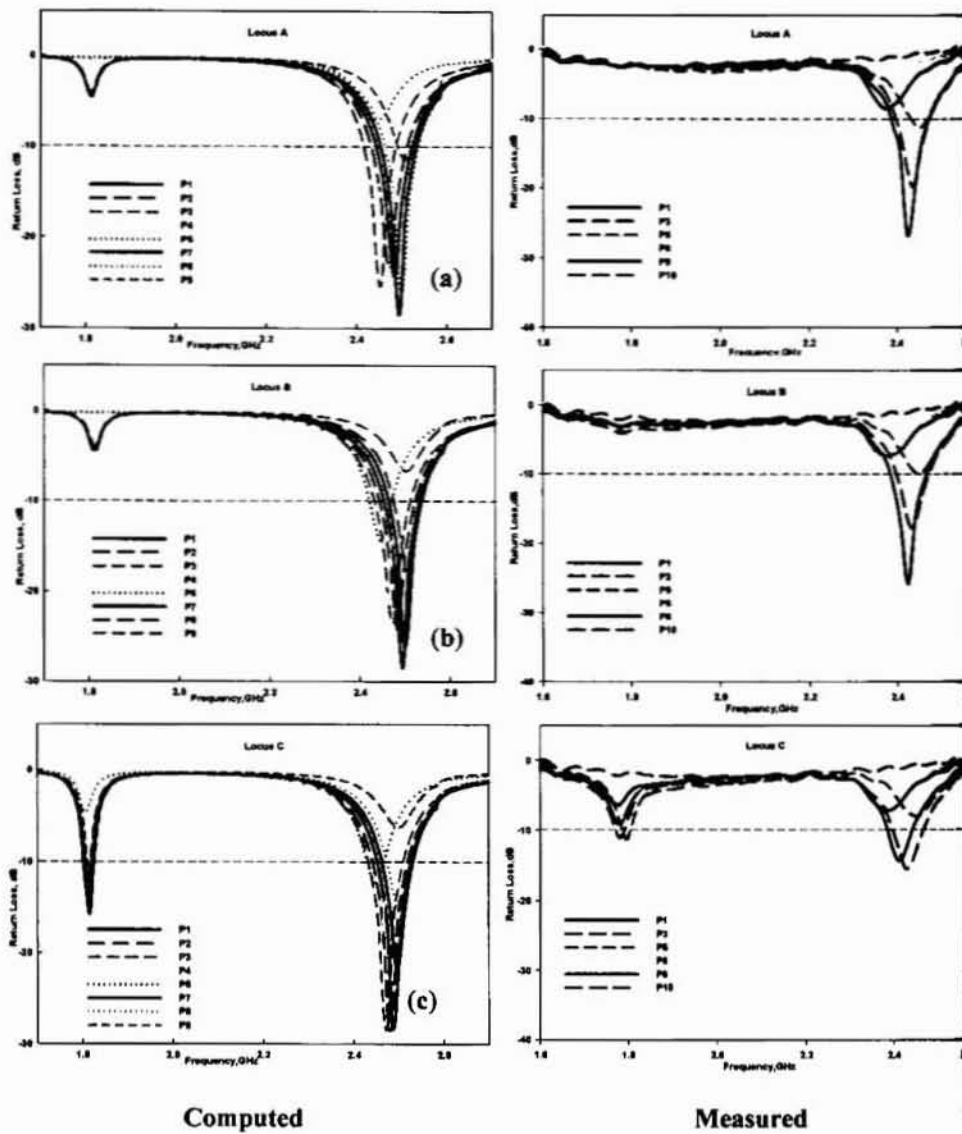
Computed   Measured

Figure 5.1.12 CFDTD computed and measured reflection characteristics of electromagnetically excited single port Octagonal MPA with laterally offset feed moving along different loci
L = 24mm, W= 10mm, a= 10mm, b=10mm, F$_L$=25mm, h=1.6mm, ε_r=4.28
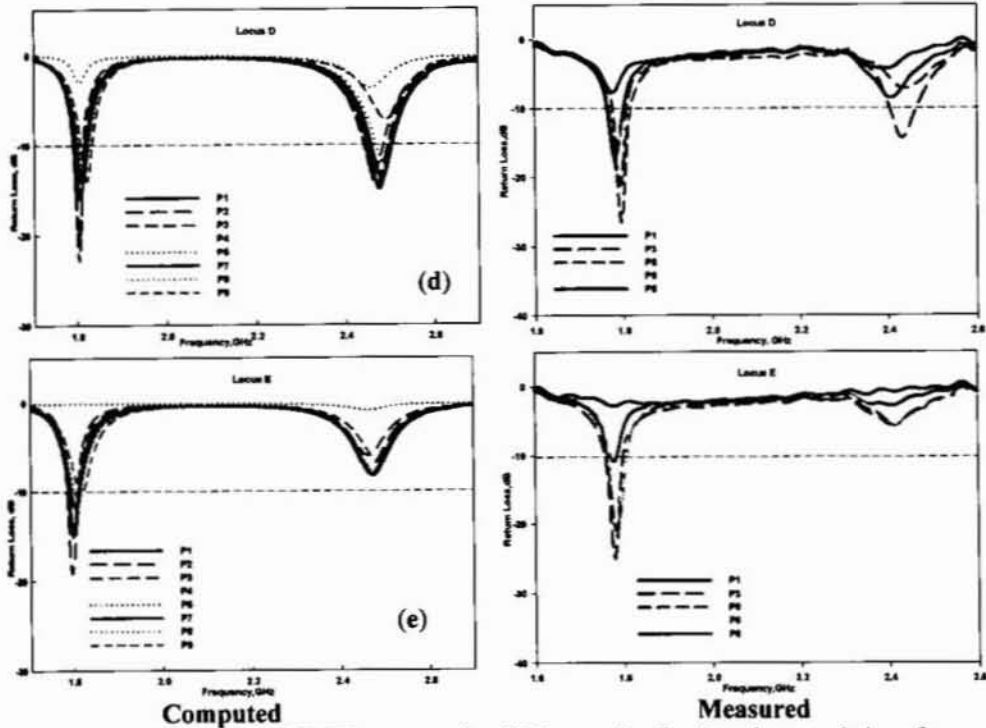
Figure 5.1.12 (*contd*) CFDTD computed and Measured reflection characteristics of electromagnetically excited single port Octagonal MPA with laterally offset feed moving along different loci.

L = 24mm, W= 10mm, a= 10mm, b=10mm, F_L=25mm, h=1.6mm, ε_r=4.28

Figure 5.1.13.a Characteristics of electromagnetically excited single port Octagonal MPA with laterally offset feed, Fx=15mm, Fy=5mm

L = 24mm. W= 10mm. a= 10mm. b=10mm. F_1=25mm h=1.6mm. ε_r=4.28
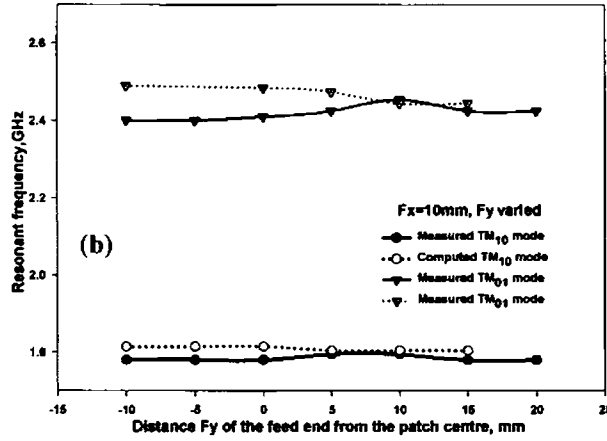
Figure 5.1.13.b CFDTD computed and measured variation in the resonant frequency for single port electromagnetically excited Octagonal MPA using a laterally offset feed with Fx=10mm and Fy varied

L = 24mm, W= 10mm, a= 10mm, b=10mm, F_L=25mm, h=1.6mm, ε_r=4.28
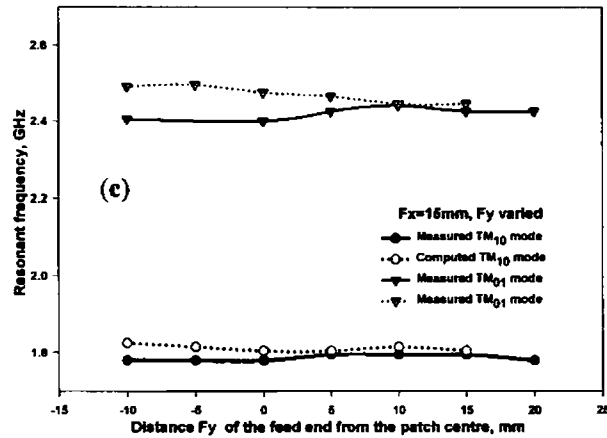
Figure 5.1.13.c CFDTD computed and measured variation in the resonant frequency for single port electromagnetically excited Octagonal MPA using a laterally offset feed with Fx=15mm and Fy varied

L = 24mm, W= 10mm, a= 10mm, b=10mm, F_L=25mm, h=1.6mm, ε_r=4.28

The variation in the resonance frequency of the two modes, for different feed end positions corresponding to Fx=10mm (locus C) and Fx=15mm (locus D) is illustrated in figure 5.1.13.b-c. The measured and computed values in all case show reasonably good agreement. The TM_{10} mode resonance exhibits linear polarization along the L dimension while the TM_{01} mode is polarized linearly along the direction tangential to W. Decoupling between the two

resonant frequencies along the boresight is 10dB and 6dB respectively for the two modes as shown in figure 5.1.13.a. The radiation patterns of the Octagonal patch antenna with laterally offset feed is given in figures 5.1.13.d -e. In both planes the patterns show poor cross polar level.
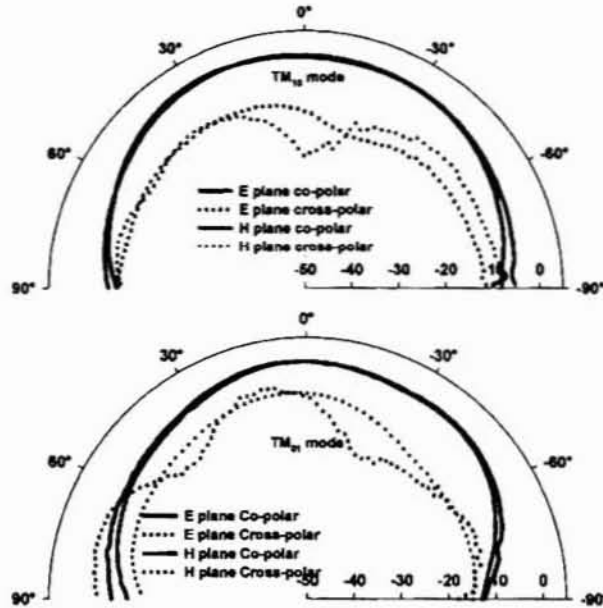
Figure 5.1.13 (*contd.*) Radiation Patterns of the electromagnetically excited single port
Octagonal MPA with laterally offset feed
L = 24mm, W= 10mm, a= 10mm, b=10mm, Fx=15mm, Fy=5mm,F_L=25mm
h=1.6mm, ε_r=4.28
(d) E plane and H plane patterns of TM_{10} mode
(e) E plane and H plane patterns of TM_{01} mode

• Corner fed configuration

Dual frequency behavior is exhibited by the single port corner fed
configuration shown in figure 5.1.10.b, where feed line is orthogonal to side
S. Reflection characteristics of the configuration is studied numerically for
various feed positions. Figure 5.1.14 illustrates the three loci, A, B and C
traced by the open end of the feed line about side S, while the Fx and Fy
values corresponding to different feed end positions (P1 to P10) is indicated
in the table 5.1.5.
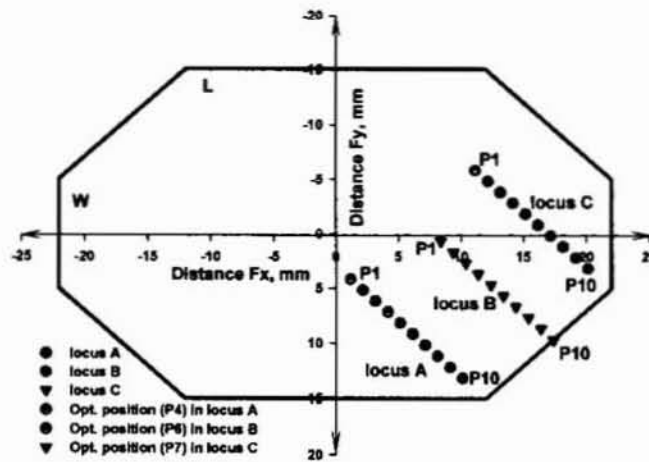
Figure 5.1.14 Illustration of feed positions for corner fed electromagnetically excited
single port Octagonal MPA
L = 24mm, W= 10mm, a= 10mm, b=10mm, F_L=25mm, h=1.6mm, ε_r=4.28

The computed return loss characteristics exhibited by the antenna for
different positions, P1 to P10, along these loci is shown in figures 5.1.15 a-c
(within table 5.1.5). The antenna dimensions are L=24mm, W=10mm and a=
b= 10mm and feed layer and patch layer substrate is FR4 with h=1.6mm and
ε_r = 4.28. From these computations the optimum position for dual frequency
operation with good reflection characteristics is Fx =4.2mm and Fy = 7.2mm
(P4 of locus A). Most of the feed positions along loci B and C show poor
impedance match for the second resonance. It is observed that impedance
matching for either frequencies improve as feed position is moved from
locus C to locus A.

Posi tion	Locus A			Freq (GHz) TM$_{10}$ mode with Return loss in dB	Freq (GHz) TM$_{01}$ mode with Return loss in dB	Variation in return loss characteristics
	Fx mm	Fy mm	Fd mm			
P1	1.2	4.2	4.3	1.83(-14)	2.49(-16)	
P2	2.2	5.2	5.6	1.82(-15)	2.49(-18)	
P3	3.2	6.2	6.9	1.82(-18)	2.48(-17)	
P4	4.2	7.2	8.3	1.82(-21)	2.48(-16)	
P5	5.2	8.2	9.7	1.82(-21)	2.47(-14)	
P6	6.2	9.2	11	1.82(-18)	2.47(-12)	
P7	7.2	10.2	12.4	1.82(-12)	2.47(-9)	
P8	8.2	11.2	13.8	1.82(-8)	2.47(-6)	
P9	9.2	12.2	15.2	1.82(-4)	2.49(-4)	
P10	10.2	13.2	16.6	--	--	

Figure 5.1.15.a

Posi tion	Locus B			Freq (GHz) TM$_{10}$ mode with Return loss in dB	Freq (GHz) TM$_{01}$ mode with Return loss in dB	
	Fx mm	Fy mm	Fd mm			
P1	8.4	0.7	8.4	1.82(-8.7)	2.49(-7.3)	
P2	9.4	1.7	9.6	1.82(-9)	2.49(-7.0)	
P3	10.4	2.7	10.7	1.82(-10)	2.48(-7.1)	
P4	11.4	3.7	12	1.82(-12)	2.48(-6.8)	
P5	12.4	4.7	13.3	1.81(-15.8)	2.48(-6)	
P6	13.4	5.7	14.6	1.81(-28)	2.48(-5)	
P7	14.4	6.7	15.9	1.81(-17)	2.48(-4)	
P8	15.4	7.7	17.2	1.8(-8)	2.48(-2)	
P9	16.4	8.7	18.6	1.8(-3.6)	2.48(-1)	Figure 5.1.15.b
P10	17.4	9.7	19.9	--	--	

Posi tion	Locus C			Freq (GHz) TM$_{10}$ mode with Return loss in dB	Freq (GHz) TM$_{01}$ mode with Return loss in dB	
	Fx mm	Fy mm	Fd mm			
P1	11.2	-5.8	12.6	1.82(-6.4)		
P2	12.2	-4.8	13.1	1.82(-6.8)		
P3	13.2	-3.8	13.7	1.81(-7.1)		
P4	14.2	-2.8	14.4	1.81(-8.8)		
P5	15.2	-1.8	15.3	1.81(-10)	No match	
P6	16.2	-0.8	16.2	1.8(-14)		
P7	17.2	0.2	17.2	1.81(-20)		
P8	18.2	1.2	18.2	1.81(-12)		
P9	19.2	2.2	19.3	--		Figure 5.1.15.c
P10	20.2	3.2	20.4	--		

Table 5.1.5 Variation of return loss characteristics with different feed end positions for electromagnetically excited single port Octagonal MPA
L=24mm, W=a=b=10mm, F$_L$=25mm, h =1.6mm, ε_r=4.28

Figure 5.1.16 shows the experimentally measured and predicted return loss characteristics of the above configuration. The single port corner fed antenna exhibits dual resonance at 1.8538GHz and 2.4863GHz. Corresponding -10dB return loss bands are 1.83GHz - 1.876GHz and 2.4381GHz - 2.53GHz respectively for the two modes with 2.48% and 3.7% BW. The TM_{10} mode resonance exhibits linear polarization along the L dimension while the TM_{01} mode is polarized linearly along the direction tangential to W. The cross polar levels in the boresight direction, measured at the two resonant frequencies are 13.6dB and 10.96dB respectively as shown in figure 5.1.16. Single port corner fed Octagonal MPA configuration offers good bandwidth but rather poor cross polar levels as shown. The radiation patterns in the principal planes of the antenna for the two resonant modes are broad as indicated in figure 5.1.17.
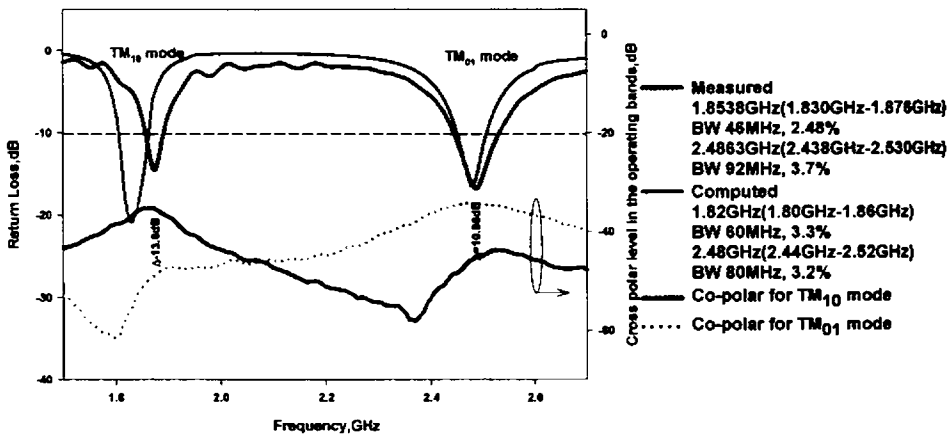
Figure 5.1.16 Characteristics of corner fed electromagnetically excited single port Octagonal MPA

L = 24mm, W= 10mm, a= 10mm, b=10mm, Fx=4.2mm, Fy=7.2mm,F_L=25mm
h=1.6mm, ε_r=4.28
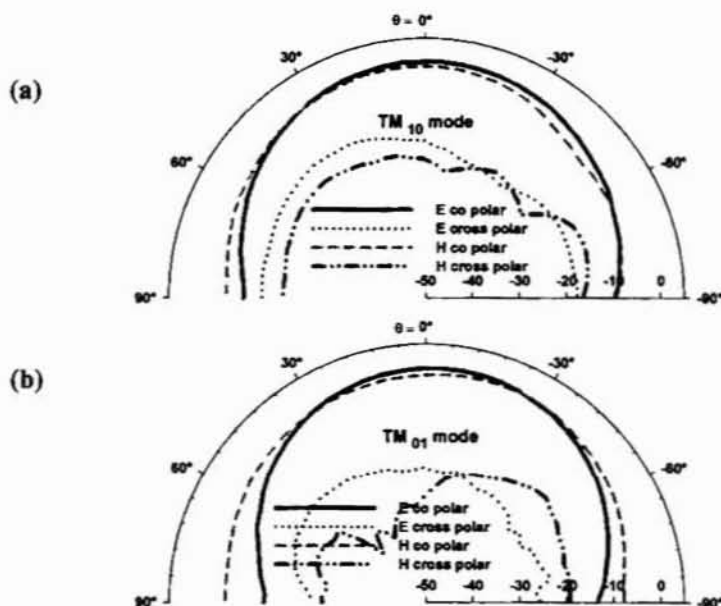
Figure 5.1.17 Radiation Patterns of the corner fed electromagnetically excited single
port Octagonal MPA
L = 24mm, W= 10mm, a= 10mm, b=10mm, Fx=4.2mm, Fy=7.2mm,F_L=25mm
h=1.6mm, ε_r=4.28
(a) E plane and H plane patterns of TM_{10} mode
(b) E plane and H plane patterns of TM_{01} mode

Table 5.1.6 summarises the measured and computed reflection characteristics
of the single feed dual band Octagonal MPA configurations. Single port
electromagnetically excited Octagonal MPA exhibits improved 2:1 VSWR
band widths when compared with coaxial excitation technique. Polarisation
of the two modes is along planes tangential to the dimensions L and W of the
antenna, but low cross polar level isolation between the modes is a major
disadvantage of these configurations.

Parameters		Laterally offset fed single port electromagnetically excited Octagonal MPA		Corner fed single port electromagnetically excited Octagonal MPA	
Substrate parameters		εr = 4.28, h = 1.6 mm		εr = 4.28, h = 1.6 mm	
Patch Dimensions		L= 24mm W = 10mm a= 10mm b = 10mm		L=24mm W =10mm a=10mm b =10mm	
Feed Dimensions		F_L=25mm,w=3mm		F_L=25mm,w=3mm	
Feed Position		Fx = 15mm Fy = 5mm		Fx =4.2mm Fy =7.2mm	
Results		TM $_{10}$ mode	TM $_{01}$ mode	TM $_{10}$ mode	TM $_{01}$ mode
Numerical Results	Frequency	1.805GHz	2.465GHz	1.82GHz	2.48GHz
	Band	1.790GHz - 1.815GHz	2.430GHz- 2.515GHz	1.80GHz - 1.86GHz	2.44GHz- 2.52GHz
	Bandwidth	25MHz, 1.39 %	85MHz, 3.45 %	60MHz, 3.297 %	80MHz, 3.226%
Measured Results	Frequency	1.795GHz	2.425GHz	1.8538GHz	2.4863GHz
	Band	1.765GHz - 1.810GHz	2.40GHz - 2.47GHz	1.83GHz - 1.876GHz	2.438GHz- 2.530GHz
	Bandwidth	25MHz, 2.51 %	70MHz, 2.89%	46MHz, 2.48%	92MHz, 3.7%
Fractional error in resonance frequency		-0.56%	-1.65%	+1.82%	+0.25%
Measured decoupling between the two modes		-10dB	-6dB	-13.6dB	-10.96dB
Polarisation plane		Tangential to 'L'	Tangential to 'W'	Tangential to 'L'	Tangential to 'W'

Table 5.1.6 Summary of the characteristics of the electromagnetically excited single port dual frequency Octagonal MPA configurations

5.2 Electromagnetically excited dual port Octagonal microstrip patch antenna for dual frequency operation

The dual port dual frequency Octagonal MPA is excited by *Electromagnetic coupling* using two orthogonal 50Ω microstrip feed lines is illustrated in figure 5.2.1.a.
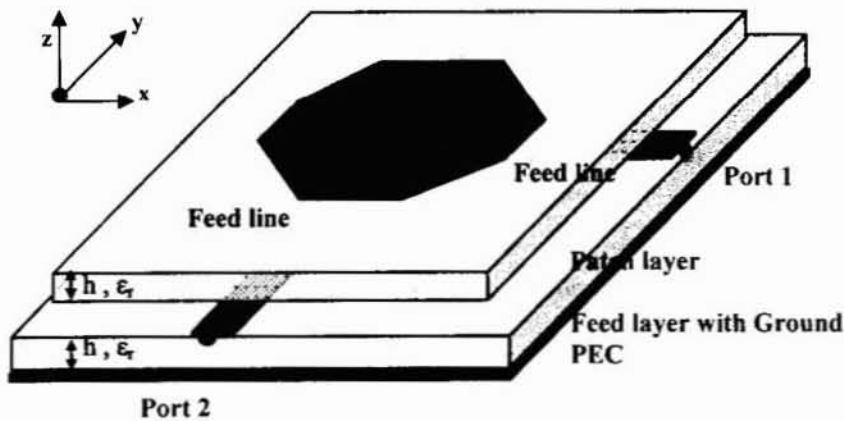
Figure 5.2.1.a Geometry of the electromagnetically excited dual port Octagonal MPA

The top view of the feed layer configuration as illustrated in figure 5.2.1.b. P is the geometric centre of the patch with length L, width W and slant edge dimension S, etched on a substrate of thickness, h and relative permittivity, ε_r. The side view of the configuration is illustrated in figure 5.2.1.c. The feed lines for Port 1 and Port 2 are of lengths FL_1 and FL_2 respectively. Fd_1 and Fd_2 indicate the distance between the *open end* of the feed lines and the geometric centre P, of the patch. The feed – patch overlap distance, F_1 and F_2, determines the impedance match at the respective ports. Feed lines are also fabricated on FR4 substrate of thickness h =1.6mm and dielectric constant ε_r = 4.28.
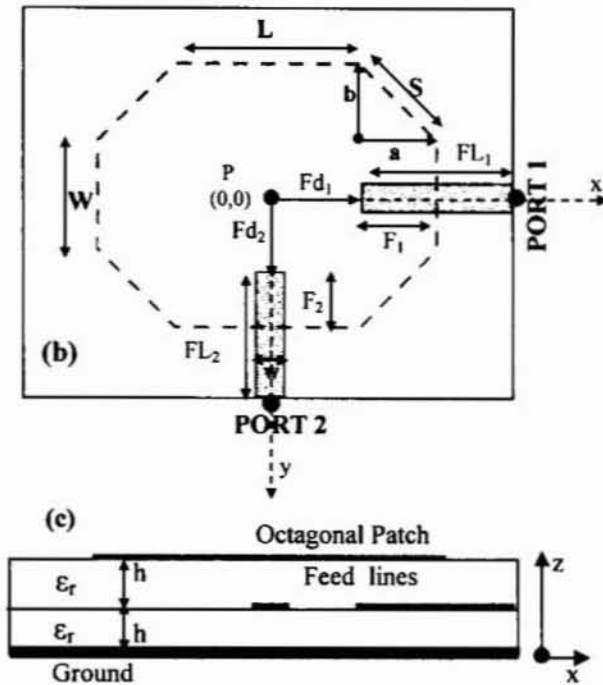
Figure 5.2.1 *(contd)* Feed layer of Electromagnetically excited Octagonal MPA
(b) Top view (c) Side view

✱ Conformal FDTD computational domain and its implementation

Conformal FDTD computational domain is set up treating the patch, feed lines and ground as perfect electric conductors (PEC). Numerical stability of the system is ensured by applying proper spatial and temporal constraints as explained in section 4.2.3. The optimized temporal and spatial parameters (table 5.1.1) used in the MATLAB™ source code for the single feed configuration is applicable for dual port problem also. Figure 5.2.2.a illustrates the full computational domain needed to analyze the dual feed octagonal patch with the Absorbing Boundary Conditions (ABC) in the x, y and z directions applied 30x30x15 cells away from the geometry.

Figure 5.2.2.b illustrates the top view of the CFDTD grid scheme employed in the full domain computation, for an Octagonal microstrip patch

antenna configuration, of dimensions L = 24.5mm, W= 9.5mm, a= 10mm, b=10mm, fabricated on FR4 substrate with ε_r=4.28, h=1.6mm.
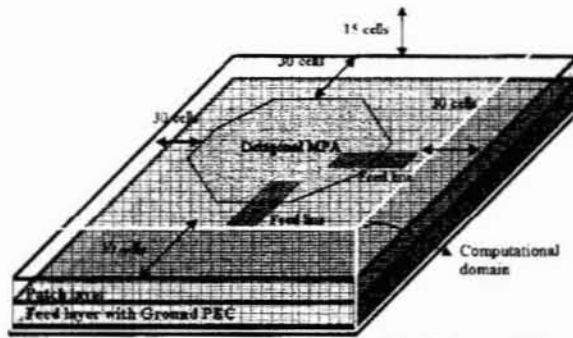
Figure 5.2.2.a The CFDTD computational domain for the Octagonal MPA
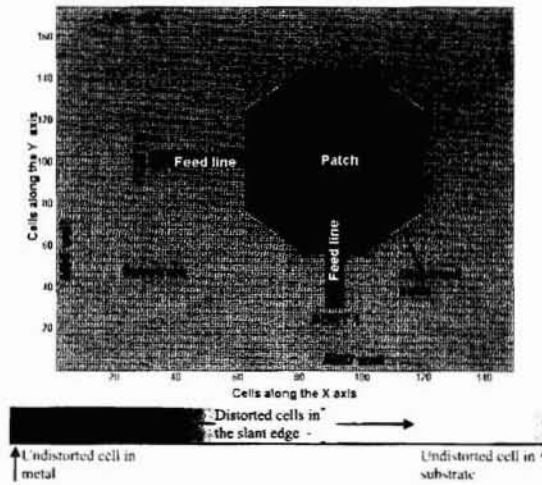
Figure 5.2.2.b The CFDTD grid scheme of Octagonal microstrip patch

The feed lines, fabricated on the same substrate is of dimensions w=3mm, $FL_1 = 0.31\lambda_d$, $FL_2 = 0.42\lambda_d$. The size of the full domain Nx x Ny x Nz is 150x175x23, for CFDTD grid with undistorted cells of dimensions x=0.5mm, y=0.5mm and z=0.4mm. To reduce the overall computational time and volume, PMC criteria explained in section 4.4 is employed. The top view of the reduced domain used in computation is depicted in figure 5.2.3. The distorted cells along the slant edge are of size different from the normal
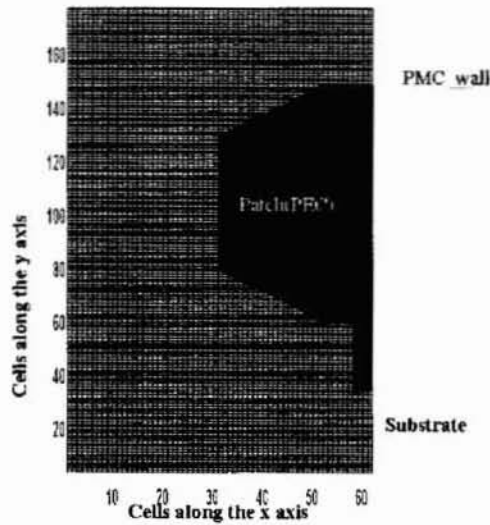
Figure 5.2.3 PMC based reduced computational domain employed for implementing the conformal FDTD

	CPU time in minutes	Computational domain size	% error wrt measured values for the two resonances
Full domain analysis	95minutes	150x175x23 ( )	-1.67%,+1.27%
PMC approach	38minutes	64x175x23 ( )	-0.8%,+1.0%

Table 5.2.1 Performance comparison between the PMC approach and the FULL domain CFDTD analysis of Octagonal patch antenna fabricated on FR4 substrate.
L = 24.5mm, W= 9.5mm, a= 10mm, b=10mm, w=3mm, FL_1= 0.31 λ_d FL_2=0.42 λ_d
h=1.6mm ε_r=4.28 (Executed on a P IV 3.2GHz machine with 512MB RAM)

The slant edge of the Octagon having the distorted cells is given special attention based on the CFDTD scheme. A comparison of the time elapsed in CFDTD computation by the two approaches is indicated in table 5.2.1. PMC approach is employed in the study performed on the Octagonal MPA configuration, since it offers a reduction in CPU time without affecting the accuracy of the result, along with the reduced memory overhead.

5.2.1 Effect of Antenna dimensions on the resonant frequency of the Octagonal geometry

The influence of antenna dimensions on the resonant frequencies of the geometry is discussed in detail in this section. The cases analysed include:

Case A: Variation with respect to L, with a $\equiv$ b and L+2a = W+2b = K where K is a constant

Case B: Variation with respect to L, with a $\equiv$ b, L+2a = K1, W+2b = K2 where K1 and K2 are constants

Case C: Variation with respect to L, with W, a and b kept constant

Case D: Variation with respect to W, with L, a and b kept constant
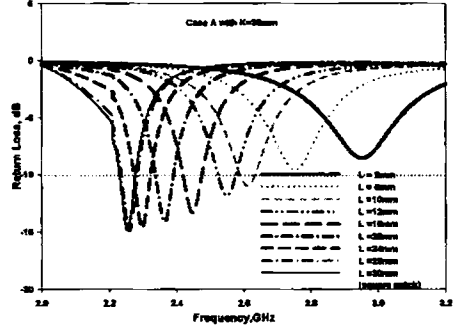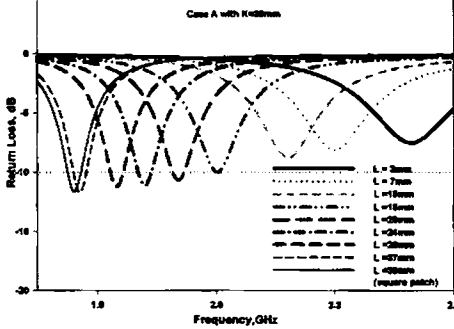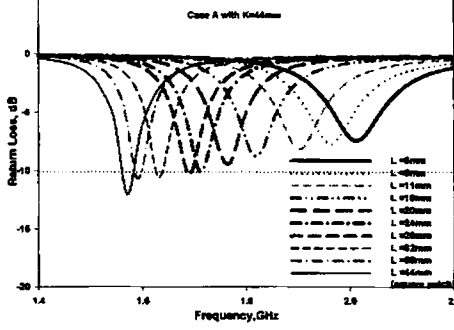
Case E: Variation with respect to α (α = a =b) with L and W kept constant

Case F: Variation with respect to α = a (or b) with L, W and b (or a) kept constant

Conformal FDTD is employed to evaluate the influence of these dimensions on the resonant frequencies excited at the two ports of the antenna. The laminate chosen is FR4 with ε_r = 4.28 and h = 1.6mm. For case A computed with different K values, identical resonances are observed for both ports of the octagonal geometry. The Octagonal patch antenna exhibits a higher resonant frequency than the inscribing square patch with side K as shown in table 5.2.2. This indicates that the overall resonant length of the octagonal geometry is shorter than its L+2a or W+2b dimensions.

K, mm	L, mm	α, mm	Freq, GHz	Variation in Resonant frequency
30	2	14	2.97	
	6	12	2.76	
	10	10	2.59	
	12	9	2.55	
	16	7	2.45	
	20	5	2.37	
	24	3	2.3	
	28	1	2.26	
	30	0	2.25	

Figure 5.2.4.a,b

K, mm	L, mm	α, mm	Freq, GHz	Variation in Resonant frequency
39	3	18	2.33	
	7	16	2.2	
	10	14.5	2.12	
	16	11.5	2	
	20	9.5	1.94	
	24	7.5	1.88	
	28	5.5	1.83	
	37	1	1.77	
	39	0	1.76	

Figure 5.2.4.c,d

K, mm	L, mm	α, mm	Freq, GHz	Variation in Resonant frequency
44	6	19	2.01	
	8	18	1.97	
	11	16.5	1.91	
	16	14	1.82	
	20	12	1.77	
	24	10	1.71	
	26	9	1.69	
	32	6	1.63	
	38	3	1.59	
	44	0	1.56	

Figure 5.2.4.e,f

Table 5.2.2 Computed variation of resonant frequency of the Octagonal patch antenna inscribed within square of side dimension K (Case A)

Substrate parameters are h =1.6mm, ε_r=4.28

K, mm	Variation in return loss characteristics
30	 **Figure 5.2.5.a**
39	 **Figure 5.2.5.b**
44	 **Figure 5.2.5.c**

Table 5.2.2 *(contd)* Computed variation of return loss characteristics of the Octagonal patch antenna inscribed within square of side dimension K (Case A)

Substrate parameters are h =1.6mm, ε_r=4.28

By using curve fitting algorithms, an empirical relation is arrived at for the resonant frequency of octagonal patches, in terms of L, coming under case A, and is represented in equation 5.2.1.

$$F_r = F_0 + m_1 e^{(-nL.)}$$ (5.2.1)

where F_r is the resonant frequency of the patch in GHz. Equation 5.2.2 gives the empirical relation expressed in terms of α for the same case.

$$F_r = F_0 + m_2 e^{(2n\alpha)}$$ (5.2.2)

F_0, m_1, m_2 and n is given in table 5.2.3 for different K values. Equation 5.2.3 gives a simple relation for the calculation of F_0 with K=L+2*a=W+2*b.

$$F_0 = 4.8435 e^{(-0.0278K)}$$ (5.2.3)

Parameters in the eqn. 5.2.1-3	K=30mm	K=39mm	K=44mm
m_1	0.9718	0.7963	0.7493
m_2	0.1394	0.1093	0.1319
n	0.0647	0.0509	0.0395
F_0	2.1025	1.6455	1.4212

Table 5.2.3 Design equation parameters

Figures 5.2.4.a,c,e shows the variation in resonant frequency with respect to L (L=W), for different K values. Figures 5.2.4.b,d,f illustrate the frequency variations against the corresponding α values(α=a=b). The design curves obtained using the curve fitting approach is also shown in these figures. In figures 5.2.5.a-c, the computed variation in return loss characteristics with respect to length L, for different K values is shown in comparison with the characteristics of a square patch of dimension K.

Figure 5.2.6 illustrates the measured variation in return loss characteristics with respect to feed length for different K values, in comparison with the predicted result. The results shown correspond to a typical L value for each K case. The measured values agree closely with computed results.

Typical example for K=30mm case with L=13mm

Return Loss, dB

CFDTD computed

Expt

Expt

(a)

Frequency, GHz

Expt

CFDTD

Feed length 0.66λ_d 2.516GHz (2.47GHz-2.560GHz) BW 90MHz,3.68%
Feed length 0.86λ_d 2.509GHz (2.47GHz-2.545GHz) BW 75MHz,3.0%
Feed length 1.05λ_d 2.530GHz (2.49GHz-2.570GHz) BW 80MHz,3.16%
Feed length 1.38λ_d 2.506GHz (2.45GHz-2.540GHz) BW 90MHz,3.6%
Feed length 1.71λ_d 2.485GHz (2.44GHz-2.560GHz) BW120MHz,4.8%
Feed length 0.45λ_d 2.52GHz (2.46GHz-2.57GHz) BW 110MHz,4.35%

Typical example for K=39mm case with L=16mm

Return Loss, dB

CFDTD computed

Expt

Expt

CFDTD

(b)

Frequency, GHz

Feed length 0.53λ_d 2.006GHz(1.979GHz-2.033GHz) BW 54MHz,2.67%
Feed length 0.69λ_d 2.005GHz(1.962GHz-2.030GHz) BW 68MHz,3.4%
Feed length 0.84λ_d 2.035GHz(2.001GHz-2.073GHz) BW 72MHz,3.6%
Feed length 1.11λ_d 2.006GHz(1.970GHz-2.050GHz) BW 80MHz,4.0%
Feed length 1.39λ_d 2.020GHz(1.986GHz-2.055GHz) BW 69MHz,3.4%
Feed length 0.35λ_d 2.000GHz (1.975GHz-2.035GHz) BW 60MHz,3.0%

Typical example for K=44mm case with L=16mm

Return Loss, dB

CFDTD

Expt

Expt

CFDTD

(c)

Frequency,GHz

Feed length 0.48λ_x 1.825GHz(1.845GHz-1.800GHz) BW 45MHz,2.47%
Feed length 0.62λ_x 1.810GHz(1.780GHz-1.835GHz) BW 55MHz,3.04%
Feed length 0.77λ_x 1.870GHz(1.830GHz-1.900GHz) BW 70MHz,3.74%
Feed length 1.02λ_x 1.840GHz(1.810GHz-1.870GHz) BW 50MHz,2.73%
Feed length 1.27λ_x 1.795GHz(1.765GHz-1.825GHz) BW 60MHz,3.24%
Feed length 0.32λd 1.820GHz(1.805GHz-1.830GHz) BW 25MHz,1.37%

Figure 5.2.6 CFDTD computed and measured return loss characteristics
for different K values
(a)L=13mm, K=30mm (b)L=16mm,K=39mm (c) L=16mm,K=44mm
h=1.6mm,ε_r=4.28

With K=44mm, measured return loss for different L values, ranging from 5mm to 38mm, is shown in figure 5.2.7.a. The good agreement between the CFDTD computed and measured results for this example, is illustrated in figure 5.2.7.b. It is observed that resonance frequency decreases as the value of L increases.
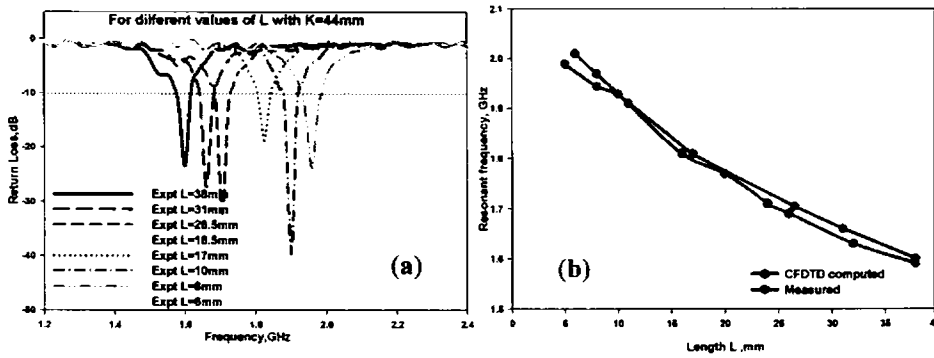
Figure 5.2.7 Reflection characteristics for different L values, with K=44mm
(a) Return Loss variation wrt L values (b) Resonant frequency variation wrt L values
h=1.6mm, ε_r=4.28, L varies from 5mm to 38mm

For case B, keeping a ≡ b, L is varied and variation of the two resonant frequencies of the geometry is studied and compared with TM_{10} and TM_{01} resonant frequencies of a rectangular patch of dimensions K1xK2. The K1 and K2 values are chosen so that the corresponding rectangular patches resonate at frequencies that are in the proximity of Mobile-Bluetooth bands.
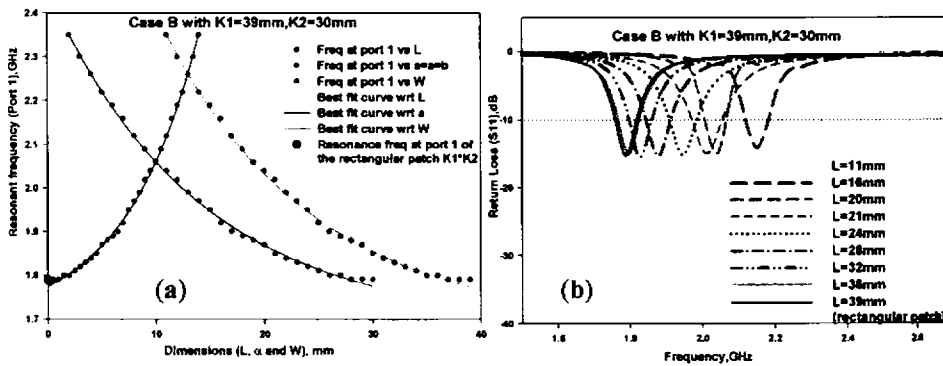
Figure 5.2.8 Reflection characteristics at Port 1 for K1=39mm and K2=30mm
(a) Resonant frequency variation wrt L values (b) Return Loss variation wrt L values
h=1.6mm, ε_r=4.28, L varies from 11mm to 39mm

From computations with K1=39mm and K2=30mm, the resonance frequency at port 1 is found to decrease as L increases towards K1, as shown in figure 5.2.8.a. The figure shows the frequency variations against the corresponding α and W values also. The computed return loss characteristics at port 1 resonance is indicated in figure 5.2.8.b, in comparison with the rectangular patch of dimensions K1xK2. Port 2 of the antenna configuration shows a

higher resonant frequency, as indicated in figure5.2.8.c. The figure illustrates the frequency variation with respect to L. The computed return loss at port 2 is indicated in figure 5.2.8.d. The computed isolation between the ports for different L values is found to be better than -30dB at port 1 resonances while it is better than -25dB at port 2 as indicated in figure 5.2.8.e.
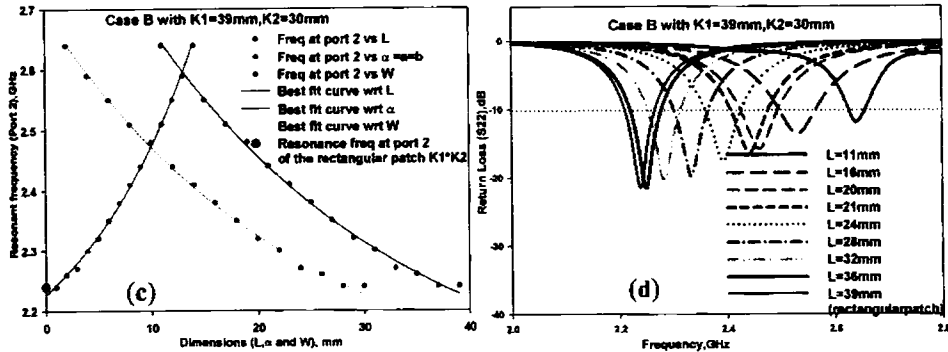
Figure 5.2.8 (*contd.*) Reflection characteristics at Port 2 for K1=39mm and K2=30mm
(c) Resonant frequency variation wrt L values (d) Return Loss variation wrt L values
h=1.6mm, ε_r=4.28, L varies from 11mm to 39mm
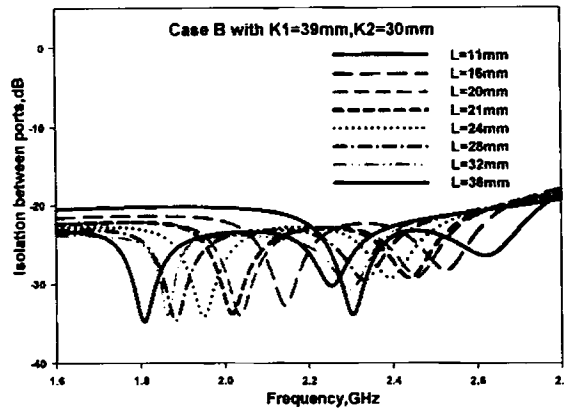
Figure 5.2.8 (*contd.*) (e) Isolation characteristics for K1=39mm and K2=30mm

Figures 5.2.9.a-e show the corresponding results obtained computationally with K1=44mm and K2=30mm, for L values ranging from 14mm to 40mm. It is observed that port 1 resonance increases as L value decreases where as port 2 resonance is decided primarily by W. To ascertain the influence of individual dimensions on the two resonant frequencies, computations are done as indicated by cases C to F listed above.
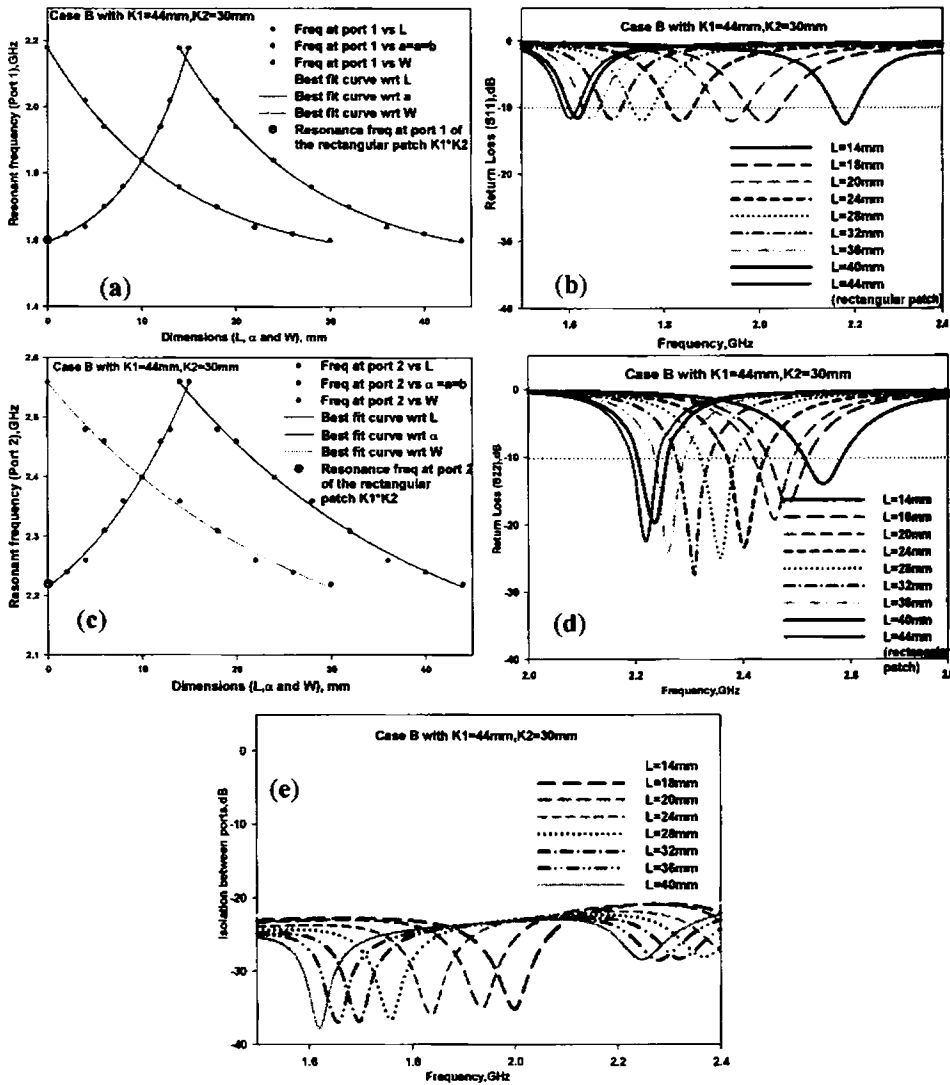
Figure 5.2.9 Input characteristics for K1=44mm and K2=30mm
(a) Port 1 Resonant frequency variation wrt L (b) S11 wrt L
(c)Port 2 Resonant frequency variation wrt L (d) S22 wrt L (e) S21 wrt L
L varied from 14mm to 20mm, h=1.6mm, ε_r=4.28

Influence of L on resonant frequency with W, a, b kept constant, is illustrated in figure 5.2.10.a. Computed values agree reasonably well with the measured results. It is seen experimentally that a 30% change in length L causes ~5% variation in port 1 resonance and ~2.6% in port 2 resonance. Numerically, 57% length variation leads to 5.5% change in port 1 frequency and a 2.2% variation in port 2 frequency. Keeping L, a, b constant, a 35% variation in W

gives 1.3% variation in port 1 resonance whereas port 2 resonance exhibits 4.64% change in the measured resonant frequencies as illustrated in figure 5.2.10.b.
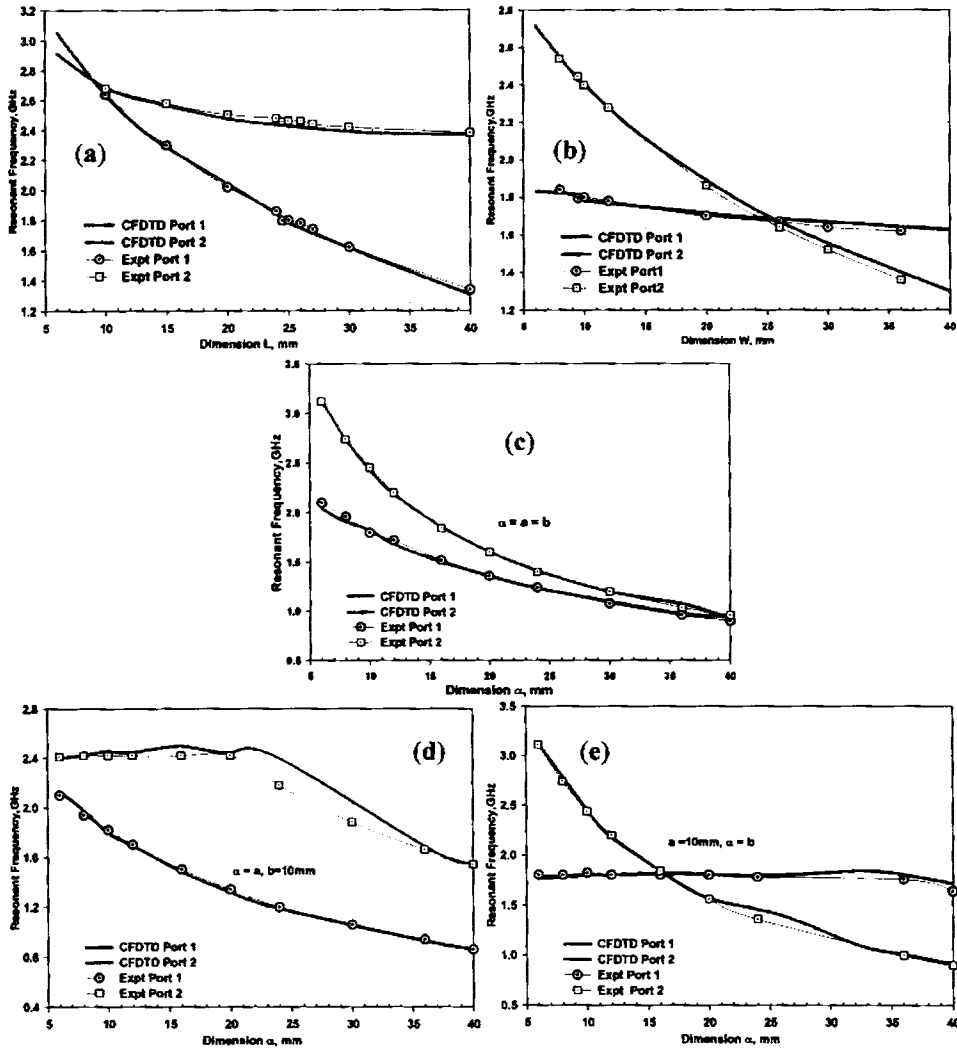
Figure 5.2.10 Resonant frequency variation with respect to patch dimensions
(a) Variation wrt L values with W=9.5mm, a=b=10mm
(b) Variation wrt W values with L=24.5mm, a=b=10mm
(c) Variation wrt α = a=b, with L=24.5mm, W=9.5mm
(d) Variation wrt α = a, with L=24.5mm, W=9.5mm, b=10mm
(e) Variation wrt α = b, L=24.5mm, W=9.5mm, a=10mm

Numerical results show that a 57% change in W gives a fractional resonant frequency change of 1.1% and 5.2% respectively, at ports 1 and 2. Numerical and measured variation in frequency at the two ports for case D, is shown in

figure 5.2.10.b. Figures 5.2.10.c shows the variation in resonant frequency with respect to variations in α, where α = a = b(*i.e.* case E), keeping other dimensions constant. Numerically a 57% change in α results in a 5.4% and 7.05% change in port 1 and 2 resonant frequencies. Experimentally 5.71% and 6.92% fractional change in frequency is observed at the two resonances for a 50% change in α. Figure 5.2.10.d shows the variation in resonant frequency with respect to α, where α = a. With α = a, fractional change of 57% in α gives ~6% change in port 1 resonance both numerically and experimentally. At port 2, the resonance frequency remains nearly constant for α <L, but thereafter for higher values of α, frequency decreases steadily. With α = b, fractional change of 57% in α gives ~7% change in port 2 resonance both numerically and experimentally. At port 1, the resonance frequency remains nearly constant, as indicated in figure 5.2.10.e.The above discussed results are summarised in table 5.2.4.

Constant dimensions	Varied dimension	Fractional change expressed in %					
		CFDTD computed			Measured		
		% dimension change	% change in freq at port 1	% change in freq at Port 2	% dimension change	% change in freq at Port 1	% change in freq at Port 2
W=9.5mm α = a= b=10mm	L	57	5.5	2.2	30	5	2.6
L=24.5mm α = a= b=10mm	W	57	1.1	5.2	35	1.3	4.6
L=24.5mm W=9.5mm	α = a= b	57	5.4	7.1	50	5.7	6.9
L=24.5mm W=9.5mm b=10mm	α = a	57	6	Const for α < L, decreases thereafter	57	6	Const for α < L, decreases thereafter
L=24.5mm W=9.5mm a=10mm	α = b	57	7	Nearly const	57	7	Nearly const

Table 5.2.4 Summary of variations in the CFDTD computed and measured frequency at the two ports with respect changes in the dimensions of the Octagonal MPA

From the exhaustive numerical and experimental studies performed on the effect of antenna dimensions on resonant frequencies, the optimum patch dimensions suited for Mobile–Bluetooth dual band applications is identified

and studied in further detail .The radiation characteristics of such a configuration is discussed in section 5.3.

5.2.2 Variation in the input impedance at the ports with respect to feed position

The position of the open end of the feed lines, relative to the patch centre, corresponding to the two ports determines the impedance match at the ports. To ascertain the influence of feed end positions, the patch is positioned upon the feed line at different x and y offsets from the centre and the input characteristics are measured. Figures 5.2.11.a, b show the loci of feed points corresponding to the two ports.
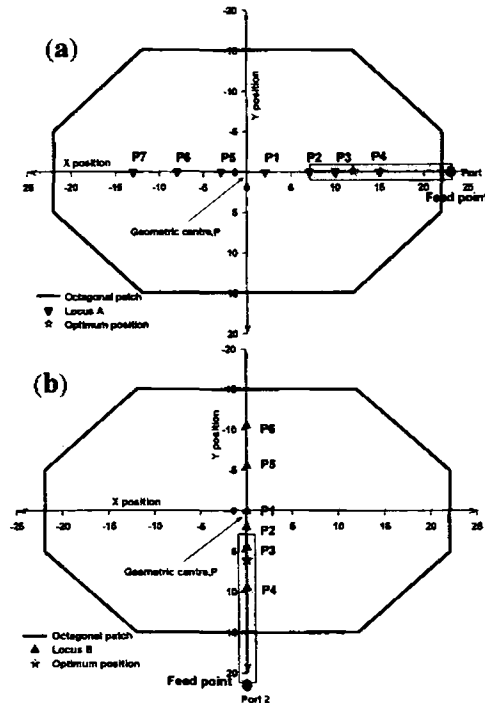
Figure 5.2.11 Loci of the to feed end position for the two ports
(a) Loci of port 1 feed points (b) Loci of port 2 feed points

The measured input impedance, within the two operating bands of the patch, for these feed points is indicated in figures 5.2.11.c,d. It is seen from the impedance chart that as the feed point moves away from the geometric centre of the patch the impedance increases.

(c)

O·· P1
O·· P2
O·· P3
O·· P4
★·· P5
★·· P6
★·· P7
▲·· Optimum
      position

Start 1.75GHz
Stop 1.87GHz
Step 15MHz

(d)

O·· P1
O·· P2
O·· P3
O·· P4
★·· P5
★·· P6
▲·· Optimum
      position

Start 2.365GHz
Stop 2.5GHz
Step 15MHz
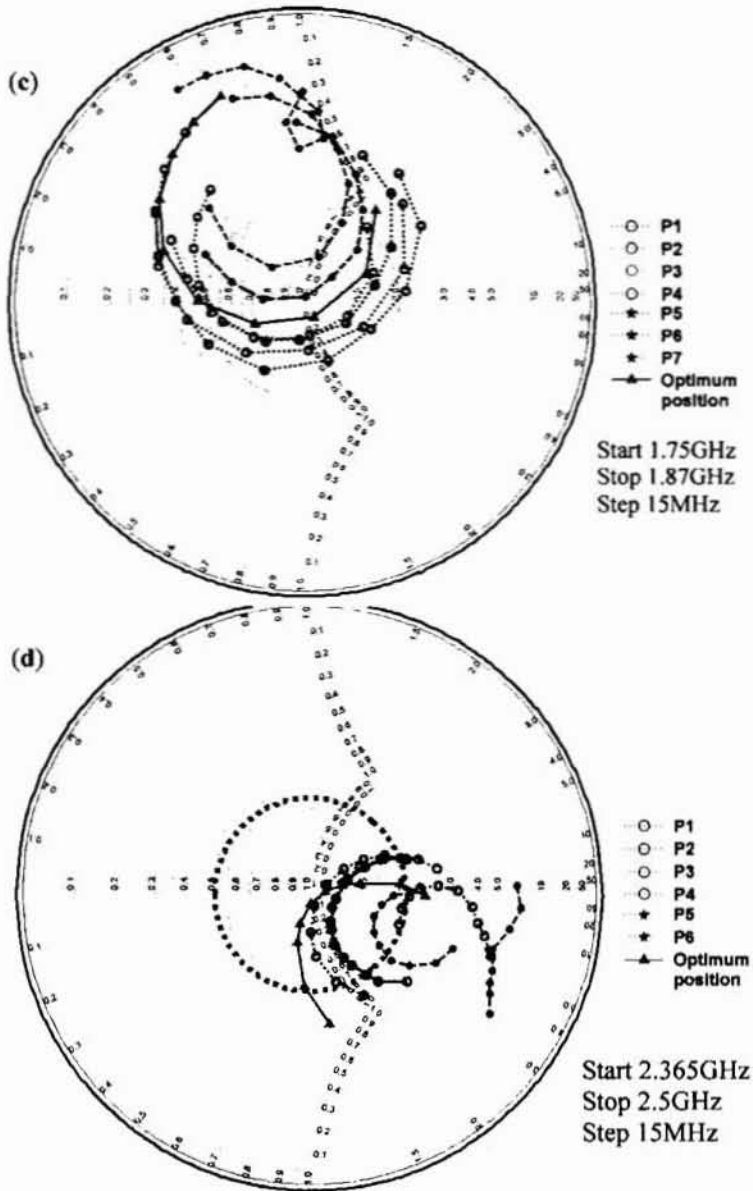
Figure 5.2.11 *(contd)* Input impedance variation at the ports wrt to feed point
(c)Port 1 input impedance variation along the port 1 feed loci
(d) Port 2 input impedance variation along the port 2 feed loci
L=24.5mm, W=9.5mm,a=10mm,b=10mm,h=1.6mm,ε_r=4.28

The optimum feed point is identified based on good impedance match and
better isolation between ports. The design parameters of the Octagonal patch
antenna suited for Mobile–Bluetooth application is inferred based on the
above results and verified experimentally as discussed in section 5.3.

5.3 Electromagnetically excited Octagonal patch antenna for Mobile and Bluetooth applications

Conformal FDTD techniques are used to predict the dimensions and characteristics of the Octagonal microstrip patch antenna excited electromagnetically. The Dual port Dual band Octagonal MPA configuration, on FR4 substrate, with resonance frequencies that suit the Mobile-Bluetooth application, optimized by CFDTD computation is

Patch dimensions: $L = 24.5mm, W = 9.5mm, a = 10mm, b = 10mm$

Feed parameters: $w = 3mm, FL_1 = 0.31\lambda_d, FL_2 = 0.42\lambda_d,$

      $Fd_1 = 12.5mm, Fd_2 = 6mm$

Substrate parameters: $h=1.6mm, \varepsilon_r=4.28$

Proximity coupling is a relatively simple feeding method that offers moderate 2:1VSWR bandwidth. It is also observed that dimensions of the coaxially excited Octagonal patch antenna are slightly larger than that for the proximity coupled case, for the same band of operation. This may be attributed to the increase in the total substrate thickness of the complete antenna configuration in proximity coupling over the single layer coaxial fed case.

5.3.1 Resonant frequency and bandwidth

The measured input characteristics for the prototype with above dimensions are compared with its predicted values in figure 5.3.1. Port 1 of the antenna exhibits resonance at 1.795GHz, with the 2:1VSWR band from 1.774GHz to 1.821GHz, and a fractional bandwidth of 2.6%. The second port shows, resonance at 2.455GHz and 3.2%BW, with the band from 2.422GHz to 2.5009GHz. The return loss characteristic at the two ports is illustrated in figure 5.3.1.a. Variation of the input impedance, normalized with respect to 50 Ohms, within the 2:1VSWR bands are plotted in figure 5.3.1.b.
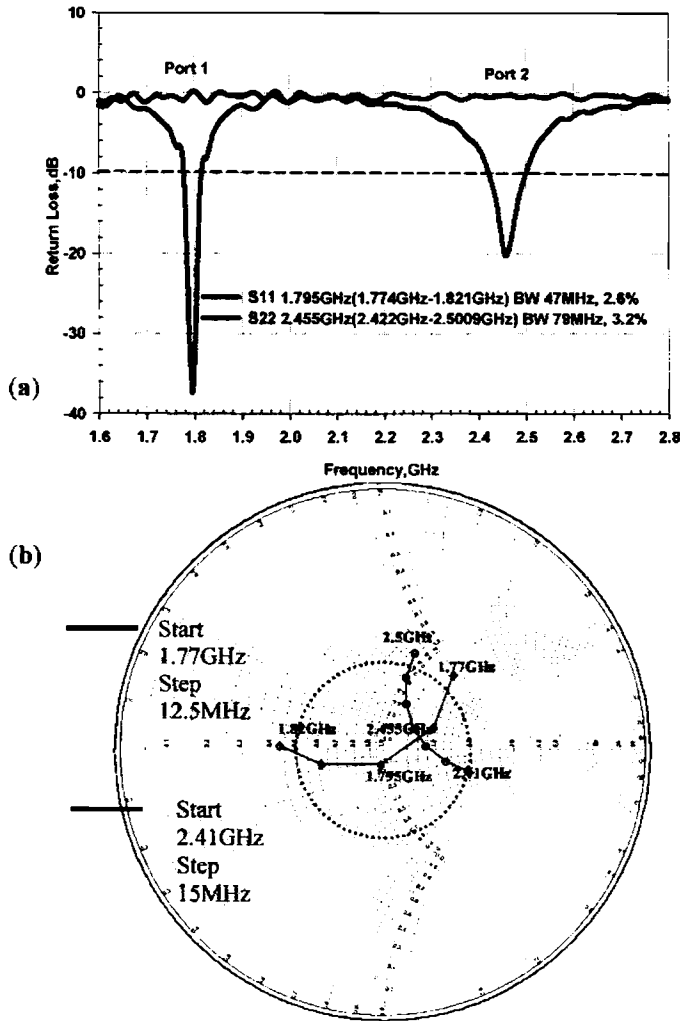
Figure 5.3.1 Reflection characteristics of Octagonal MPA optimized for Mobile and
Bluetooth Applications
(a)Return Loss measured at the two ports of the antenna.
(b)Normalized Input impedance loci within the two resonant bands
L = 24.5mm, W= 9.5mm, a= 10mm, b=10mm, w=3mm, FL_1= 0.31 λ_d, FL_2=0.42 λ_d,
h=1.6mm, ε_r=4.28

The Scattering parameters of the above antenna predicted by
conformal FDTD method are illustrated in figure 5.3.2, in comparison with
IE3D™ simulation results. CFDTD results indicate the resonant frequencies
for the two ports as 1.81GHz and 2.4297GHz respectively, at 0.8% and 1%
difference with respect to the measured values. The computed -10dB return
loss bands are 1.7644GHz-1.8628GHz and 2.3487GHz-2.5165GHz
respectively at the two ports. The port resonances observed in IE3D™

simulation are 1.805GHz and 2.46GHz respectively.
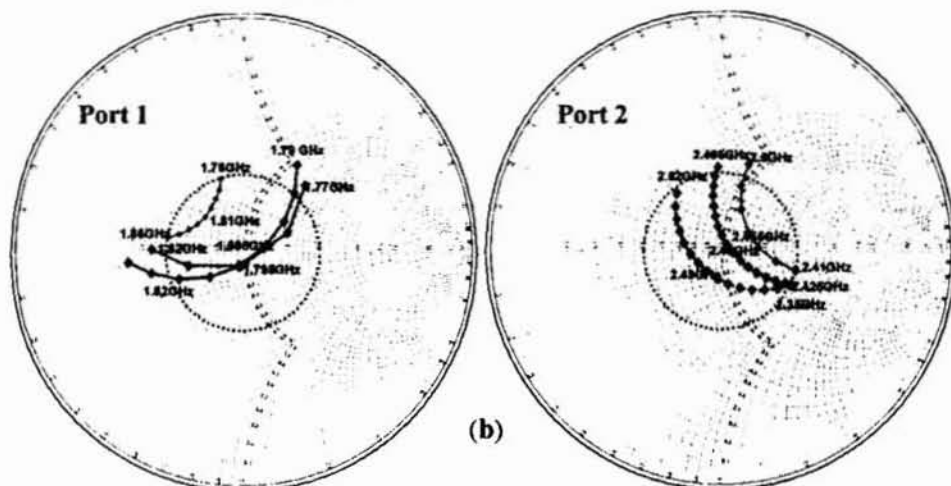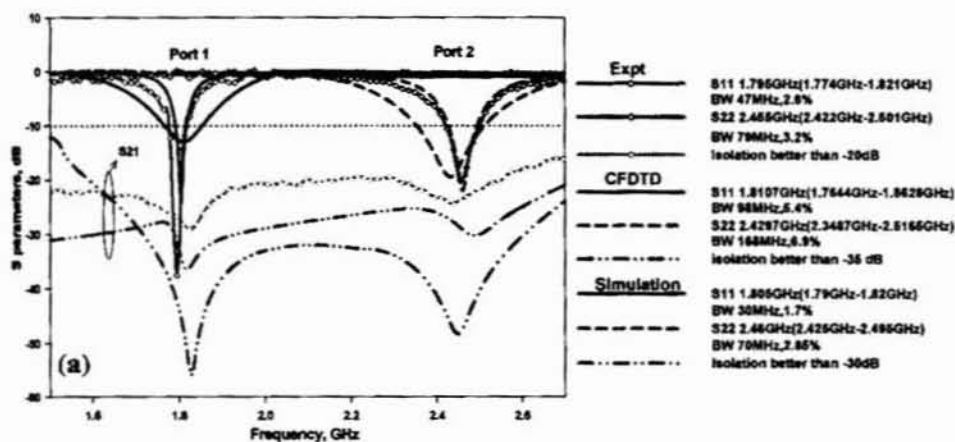
Figure 5.3.2 Measured, CFDTD Computed and Simulated S parameters and input
impedance variation of the Octagonal MPA optimized for Mobile and Bluetooth
application
(a)S parameters (b) Input impedance at Port 1 (c)Input impedance at Port 2
L = 24.5mm, W = 9.5mm, a = 10mm, b =10mm, w = 3mm, FL_1= 0.31λ_d
FL_2=0.42λd, h = 1.6mm, ε_r = 4.28

CFDTD computed band width is slightly wider than the experimentally
observed value for both ports. The small difference in these results may be
due to the assumptions involved in the analysis procedure (feed, ABC,
excitation etc), the error in the Conformal FDTD scheme itself, and due to
material inhomogeneity. Fabrication tolerances and experimental errors due
to probable imperfect soldering, ground connections etc are the other factors

that contribute to these deviations. Table 5.3.1 shows a comparison of the experimental observations against numerical and simulation results. It is seen that, percentage error between measured, computed and simulated frequencies at the ports is less than 1.0%.

	Characteristics	Measured	CFDTD (PMC)	IE3D simulation
Port 1	Fr	1.795GHz	1.8107GHz	1.805GHz
	%difference	-	-0.8%	-0.6%
	Band Band width	1.774 -1.821GHz 47MHz, 2.6%.	1.7644-1.8628GHz 98MHz, 5.4%	1.79-1.82GHz 30MHz, 1.66%
	Feed offset, Fd$_1$	12.5mm	12.5mm	12.5mm
Port 2	Fr	2.455GHz	2.4297GHz	2.46GHz
	%difference	-	1.0 %	-0.2%
	Band Band width	2.422-2.5009GHz 79MHz, 3.2%	2.3487-2.5165GHz 168MHz, 6.9%	2.425-2.495GHz 70MHz, 2.85%
	Feed offset, Fd$_2$	6mm	6mm	6mm

Table 5.3.1 Resonance characteristics of Octagonal patch antenna measured, CFDTD computed and IE3D simulated.
L= 24.5mm,W= 9.5mm, a=10mm,b=10mm,w=3mm,FL$_1$=0.31035λ_d, FL$_2$=0.4224 λ_d, h=1.6mm, ε_r=4.28
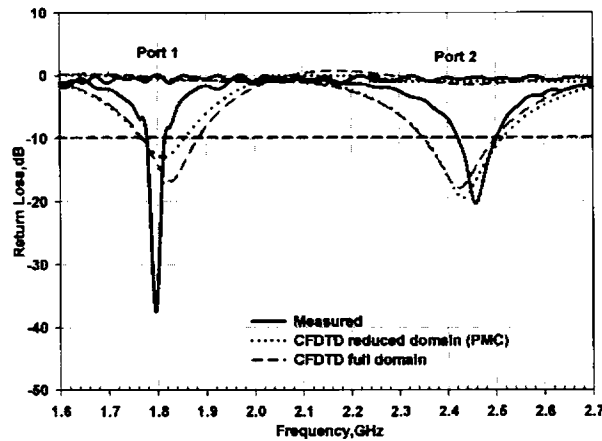
Figure 5.3.3 Measured and predicted Return loss characteristics of the Octagonal MPA
L = 24.5mm, W= 9.5mm, a= 10mm, b=10mm, w=3mm, FL$_1$= 0.31 λ_d, FL$_2$=0.42 λ_d
h=1.6mm, ε_r=4.28

On employing the *full domain* CFDTD computation the resonance frequencies obtained are 1.825GHz and 2.4239GHz respectively at the two

ports. Port 1 of the prototype exhibits a slightly higher value for the resonance frequency, whereas port 2 resonance is within limits of the desired band as shown in figure 5.3.3.

A comparison of the predicted results obtained from full domain computation and that from the PMC based reduced domain computation is presented in table 5.3.2. The percentage error between the measured and computed results in both approaches is below 2%.

	Characteristics	Measured	Predicted (CFDTD_PMC)	Predicted (CFDTD_ Full domain)
Port 1	Fr %difference	1.795GHz -	1.8107GHz -0.8%	1.825GHz -1.67%
	Band %Band width	1.774 GHz- 1.821 GHz 47MHz, 2.6%	1.7644 GHz- 1.8628GHz 98MHz, 5.4%	1.7876GHz- 1.9033GHz 116MHz,6.27%
	Feed offset, Fd_1 Feed patch overlap	12.5mm 0.0561 λ_d	12.5mm 0.0864 λ_d	12.5mm 0.0861 λ_d
Port 2	Fr %difference	2.455GHz -	2.4297GHz +1.0 %	2.4239GHz +1.27%
	Band %Band width	2.422GHz- 2.5009GHz 79MHz, 3.2%	2.3487GHz- 2.5165GHz 168MHz, 6.9%	2.3487GHz- 2.4991GHz 150MHz,6.2%
	Feed offset, Fd_2 Feed patch overlap	6mm 0.0773 λ_d	6mm 0.0904 λ_d	6mm 0.0889 λ_d

Table 5.3.2 Comparison of the measured and CFDTD results of the Octagonal patch antenna.
L=24.5mm,W=9.5mm,a=10mm,b=10mm,w=3mm,FL_1=0.31035λ_d,FL_2=0.4224λ_d, h=1.6mm, ε_r=4.28

5.3.2   Effect of feed length on resonant frequency and band width

The effect of feed length (FL_1 and FL_2) on the resonant frequency of the Octagonal patch is studied experimentally and using CFDTD. The feed line length is varied from 0.31 λ_d to 1.24 λ_d for port 1 and from 0.42 λ_d to 1.6895 λ_d for port 2 (*i.e.* from 25mm to 100mm). λ_d is the wavelength within the substrate, corresponding to the resonance frequency at the respective ports. The feed-patch overlap distance for good impedance match in each

case is also determined for the octagonal geometry. Variation of the feed length causes a small shift in the resonance frequency. The optimum feed length for the configuration is identified as 0.31035 λ_d and 0.4224 λ_d for ports 1 and 2 respectively. This allows the feed layer of the configuration to be of moderate size. Figures 5.3.4.a,b illustrate the measured variation in return loss characteristics at the two ports as the feed length is varied. Resonant frequency at port 1 is found to exhibit less than 2% shift, for a 3% variation in feed length expressed in λ_d, whereas at port 2 the frequency shift is around 4%. The result of the effect of feed length studied numerically is illustrated in figures 5.3.4.c,d.
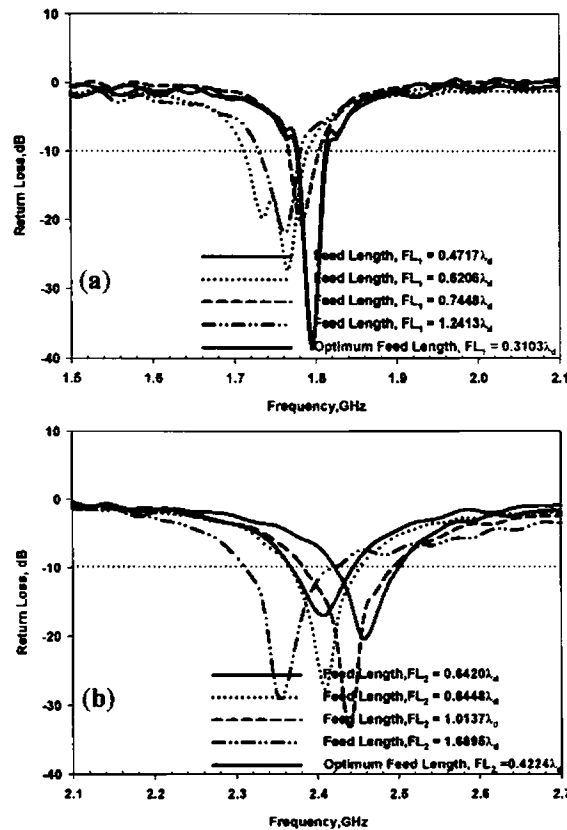
Figure 5.3.4 Effect of feed length on reflection characteristics of the Octagonal MPA. (a)Measured return loss at port 1 (b) Measured return loss at port 2 L = 24.5mm, W= 9.5mm, a= 10mm, b=10mm, w=3mm, h=1.6mm, ε_r=4.28

The %BW computed numerically at port1 of the geometry is between 5.4% and 7.5% whereas for port 2 it is between 5% and 7.2% for different feed lengths.
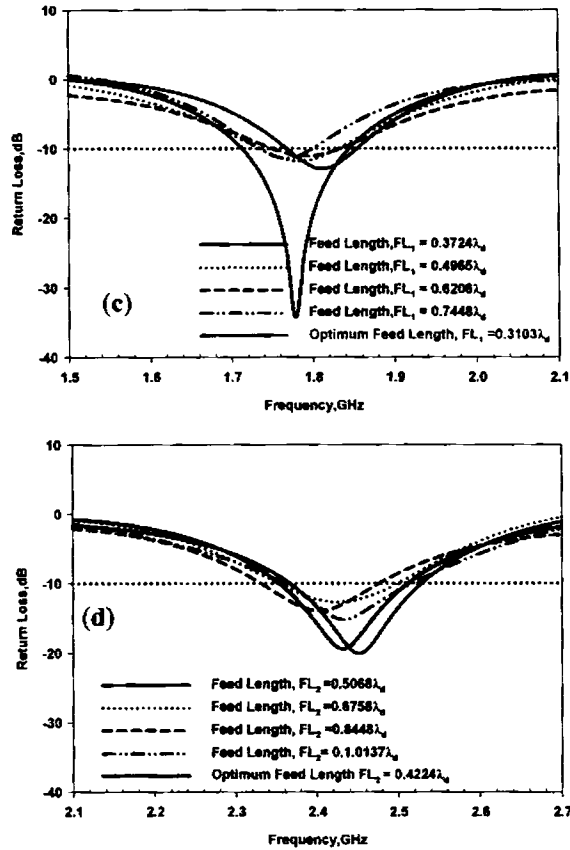
Figure 5.3.4 *(contd.)* Effect of feed length on reflection characteristics of the Octagonal MPA.
(c) Computed return loss at port 1 (d) Computed return loss at port 2
L = 24.5mm, W= 9.5mm, a= 10mm, b=10mm, w=3mm, h=1.6mm, ε_r=4.28

Variation in resonant frequency with respect to feed length, for the two ports is shown in figure 5.3.5.a and figure 5.3.5.b indicates the measured and computed variation in %BW. At port 1, the predicted values for %BW indicate large variations with respect to feed length, but the measured results show lesser fluctuations with the average fractional BW being 2.6%. CFDTD computed band width is slightly wider than the experimentally observed value for both ports for all feed lengths. A comparison of reflection characteristics of the two ports for varying feed lengths is given in table 5.3.3.The average feed – patch overlap distance for port 1 is $0.115\lambda_d$ and that

for port 2 is 0.156λ_d.
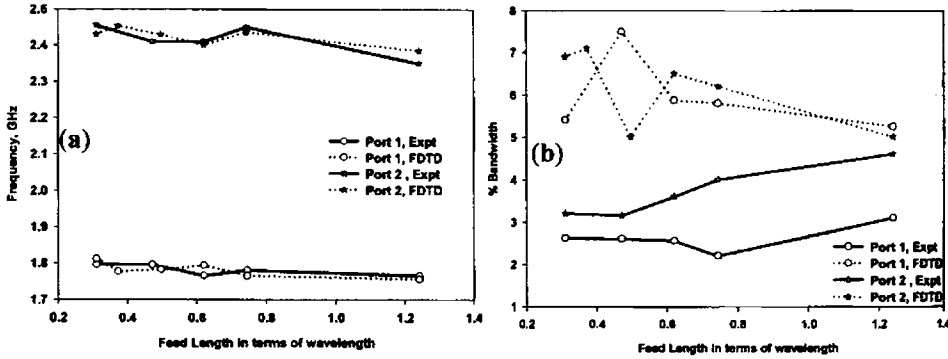
Figure 5.3.5 Effect of feed length on reflection characteristics of the Octagonal MPA.
(a) Measured and computed resonant frequency variation at both the ports
(b) Measured and computed % bandwidth variation at both the ports.
L = 24.5mm, W= 9.5mm, a= 10mm, b=10mm, w=3mm, h=1.6mm, ε_r=4.28

		Characteristics for different feed lengths					
Measured	**Port 1**	Feed length in lambda FL$_1$/ λ_d	0. 3103	0.4717	0.6206	0.7448	1.2413
		Fr1 %BW	1.795GHz 2.62%	1.795GHz 2.6%	1.765GHz 2.55%	1.78GHz 2.2%	1.765GHz 3.1%
		Feed patch overlap F$_1$ / λ_d	0.1207	0.0897	0.1491	0.1135	0.1004
	Port 2	Feed length in lambda FL$_2$/ λ_d	0.4224	0.6420	0.8448	1.0137	1.6895
		Fr2 %BW	2.455GHz 3.2%	2.41GHz 3.15%	2.41GHz 3.6%	2.44GHz 4%	2.35GHz 4.6%
		Feed patch overlap F$_2$ / λ_d	0.1481	0.1537	0.2036	0.1205	0.1537
CFDTD	**Port 1**	Feed length in lambda FL$_1$/ λ_d	0.3122	0.3674	0.4915	0.6184	0.7301
		Fr1 %BW	1.8107GHz 5.4%	1.776GHz 7.5%	1.782GHz 5.87%	1.793GHz 5.8%	1.7644GHz 5.25%
		Feed patch overlap F$_1$ / λ_d	0.1217	0.1133	0.12595	0.1515	0.1133
	Port 2	Feed length in lambda FL$_2$/ λ_d	0.4189	0.5019	0.6703	0.8278	1.008
		Fr$_2$ %BW	2.4297GHz 6.9%	2.453GHz 7.1%	2.43GHz 5%	2.4008GHz 6.5%	2.4355GHz 6.2%
		Feed patch overlap F$_2$ / λ_d	0.1466	0.1464	0.1804	0.1780	0.1464

Table 5.3.3 Effect of feed length on the reflection characteristics of Octagonal MPA.
L = 24.5mm, W= 9.5mm, a= 10mm, b=10mm, w=3mm, h=1.6mm, ε_r=4.28

Figure 5.3.6 illustrates the effect of varying the feed length, on the isolation

between the ports obtained experimentally and by CFDTD computation. For the optimum feed length, the port isolation predicted is better than -35dB for either bands. The experimentally measured value is slightly lesser than the computed value as indicated in figure 5.3.6.a. From the above results, it is seen that as feed length increases the port isolation deteriorates in general.
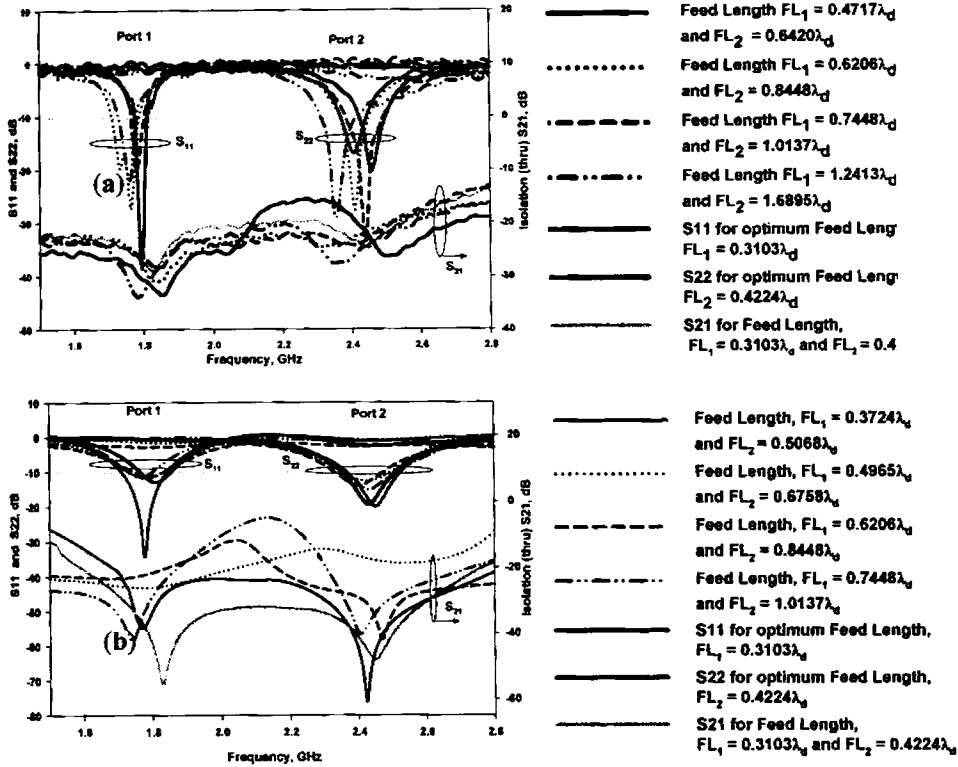
Figure 5.3.6 Effect of feed length on isolation characteristics of the Octagonal MPA. (a) Measured isolation between ports (b) CFDTD computed isolation between ports L = 24.5mm, W= 9.5mm, a= 10mm, b=10mm, w=3mm, h=1.6mm, ε_r=4.28

5.3.3 Radiation patterns

The measured radiation patterns of antenna for ports 1 and 2 are illustrated in figures 5.3.7.a and b. The geometry exhibits broad side radiation. At port 1, the Half Power Beam Widths (HPBW) measured in E and H planes are 85° and 95° respectively. Cross polar level (CPL) in the E plane is -20dB along the boresight direction and it is better than -15dB over the entire plane, while the minimum cross polar isolation of -14dB is at angle

of +16°. In the H plane, cross polar level along the zenith is -32dB. The cross polar isolation in the H plane is lowest at an elevation angle of -24° from the zenith. The patterns measured at port 2 exhibits HPBW of 100° and 85° respectively, in the E and H planes. The cross polar levels along the broadside direction in the E plane and H plane are -22dB and -20dB respectively, at port 2. In the E plane minimum cross polar isolation of -12dB is at elevation angle of +26° and for the H plane, minimum is -16dB at an angle of +31°. Hence it is observed that the antenna exhibits good cross polar characteristics.
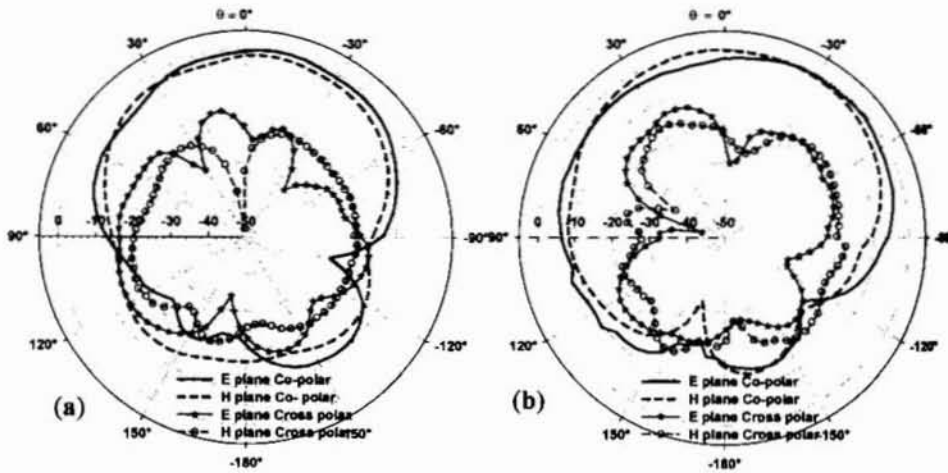
Figure 5.3.7 Measured radiation patterns of the Octagonal MPA
(a) 1.795GHz Port 1 (b) 2.455 GHz Port 2
L = 24.5mm, W= 9.5mm, a= 10mm, b=10mm, w=3mm, FL_1= 0.31 λ_d, FL_2=0.42 λ_d, h=1.6mm, ε_r=4.28

The edge diffraction due to the finite size of the ground plane used in the configuration results in a front to back ratio (FBR) of 20dB in E plane and 15dB in H plane for port 1. For port 2, the FBR are 16dB and 15dB respectively in the E and H planes. Broad radiation patterns in both principal planes coupled with reasonably good cross polar isolation makes the antenna attractive for dual frequency applications. The front to back ratio can be improved using large ground plane. The measured radiation patterns are compared with IE3D simulated and CFDTD results in figure 5.3.8 a and b. The direction of beam maxima and CPL for each case are shown in table

5.3.4. The differences between predicted values and measured results may be due to the finite size of feed layer of the configuration.

━━ Expt Co-polar ━━ Simu Co-polar ━━ CFDTD Co-polar
••••• Expt Cross polar •••• Simu Cross polar •••• CFDTD Cross polar
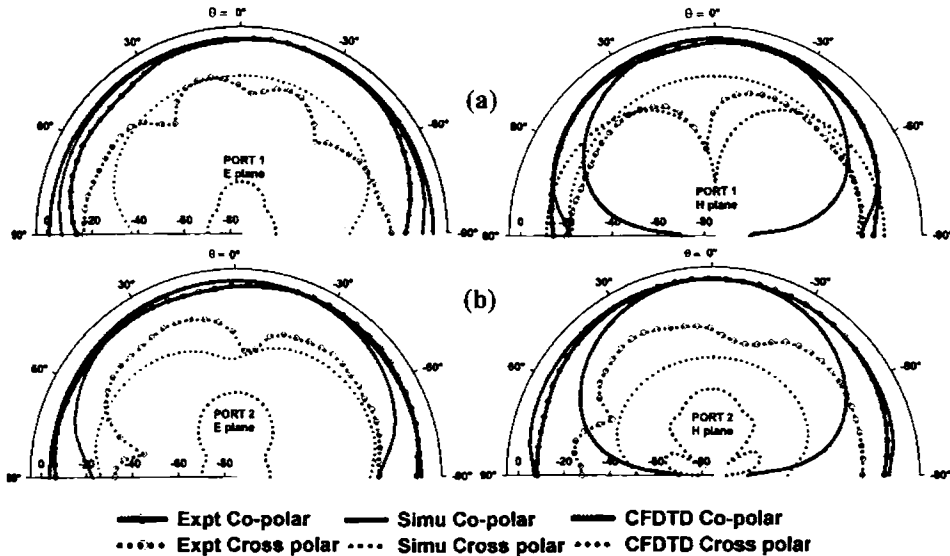
Figure 5.3.8 Measured, CFDTD computed and simulated radiation patterns (a) E plane and H plane patterns of Port 1 (b) E plane and H plane patterns of Port 2 L = 24.5mm, W= 9.5mm, a= 10mm, b=10mm, w=3mm, FL_1= 0.31 λ_d FL_2=0.42 λ_d h=1.6mm, ε_r=4.28

		Feed length, FL_1= 0.31 λ_d FL_2=0.42 λ_d						Feed length FL_1=0.7448 λ_d, FL_2=1.0137 λ_d	
		E plane			H plane			E plane	H plane
		Expt	Comp. CFDTD	Simu. IE3D	Expt	Comp. CFDTD	Simu. IE3D	Expt	Expt
Port 1	Direction of Beam maxima	-9°	Broad side	-5°	-9°	Broad side	Broad side	16°	11°
Port 1	Broad side CPL	-32 dB	-62 dB	-16.2 dB	-20 dB	-62 dB	-16.2 dB	-28 dB	-17.5 dB
Port 2	Direction of Beam maxima	-29°	Broad side	Broad side	-6°	Broad side	Broad side	26°	-4°
Port 2	Broad side CPL	-20 dB	-48 dB	-33.8 dB	-22 dB	-48 dB	-33.7 dB	-13.6 dB	-25.5 dB

Table 5.3.4 Comparison of far field characteristics of Octagonal MPA. L = 24.5mm, W= 9.5mm, a= 10mm, b=10mm, w=3mm, h=1.6mm, ε_r=4.28

At port 1 resonance wavelength, the ground dimension is only 0.29 λ_d by 0.29 λ_d, where as it is 0.395λ_d by 0.395 λ_d at the port 2 frequency. The finite size of the ground plane affects the E plane pattern more than the H plane pattern. The obvious asymmetry in the configuration, that results from the placement of patch on the *finite* size feed layer and the proximity of cable - SMA connector arrangement, accounts for the asymmetry and the deviation of the measured patterns from the predicted and simulated ones.

• Effect of feed length variation on radiation pattern

The length of the feed line is changed to study the effect of feed dimensions on the far field pattern. Figures 5.3.9.a-b illustrates the radiation patterns of the Octagonal MPA for feed lengths $FL_1= 0.7448 \lambda_d$ and $FL_2 =1.0137 \lambda_d$. The patterns are almost similar to the patterns of the optimized feed length discussed earlier. The direction of beam maxima and CPL in the principal planes for the increased feed length are shown in table 5.3.4 along with results for the optimum feed. The size of the ground plane is kept same as the previous case.
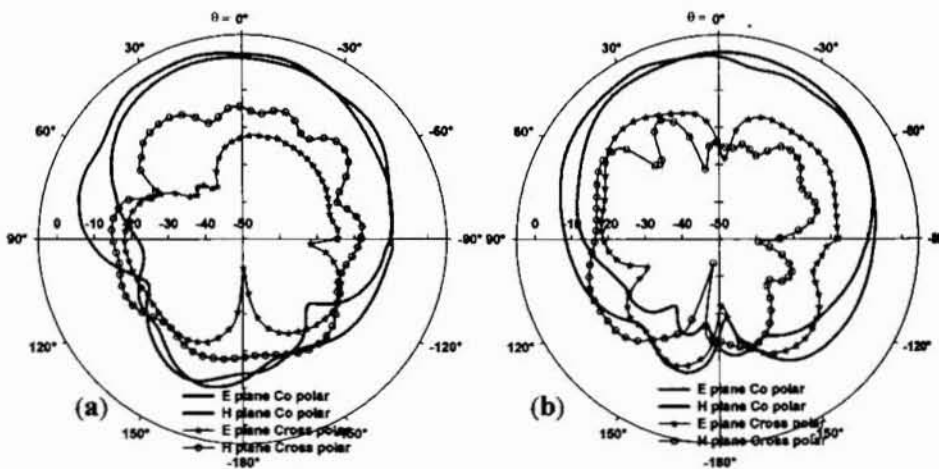
Figure 5.3.9 Radiation pattern with feed length FL_1=0.7448 λ_d, FL_2 =1.0137 λ_d
(a) E plane and H plane patterns of Port 1 (b) E plane and H plane patterns Port 2
L = 24.5mm, W= 9.5mm, a= 10mm, b=10mm, w=3mm, h=1.6mm, ε_r=4.28

5.3.4 Resonant modes

The resonant modes of the Octagonal microstrip patch antenna are identified from the electric field distribution in the near field aperture explained in section 4.6.

The modes of microstrip line fed rectangular microstrip antenna [Sheen *et al.* ref [2],ch.3] is studied initially based on the procedure outlined in section 4.6. The voltage distribution at the observation point in the CFDTD domain, illustrated in figure 5.3.10.a, indicates that the system has attained sinusoidal steady state.
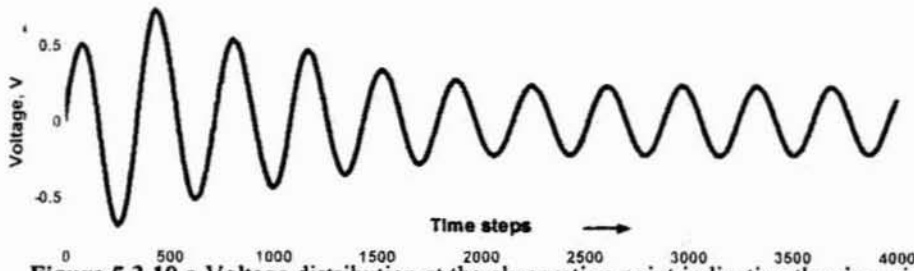
Figure 5.3.10.a Voltage distribution at the observation point indicating the sinusoidal steady state

The rectangular patch resonates at 7.474GHz. A pictorial representation of the field distribution corresponding to 7.474GHz, in the near field aperture is illustrated in figure 5.3.10.b.
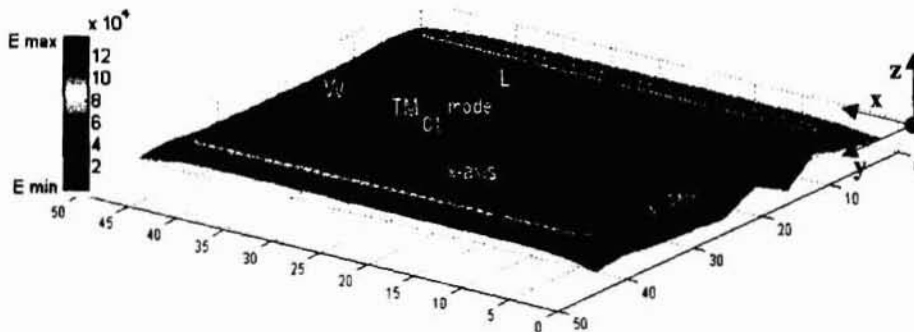
Figure 5.3.10.b Resonant modes in a rectangular MPA [Sheen *et al.*] computed using FDTD, at 7.474 GHz. E field shows constant distribution along x and one half cycle variation along y indicating TM_{01} mode
L = 16mm, W=12.45mm,h=0.794mm, ε_r=2.2

The field *along* the Length (L = 16mm) of the patch is constant (*no* variation along x), whereas the field along the width (W = 12.45mm) exhibits *one half*

cycle variation. Resonance mode of the rectangular patch is therefore identified as Transverse Magnetic, TM_{01}. The field distribution in the same patch corresponding to the lower resonance at 6.28GHz, shown in figure 5.3.10.c exhibits the dominant TM_{10} mode of the geometry.

(c)
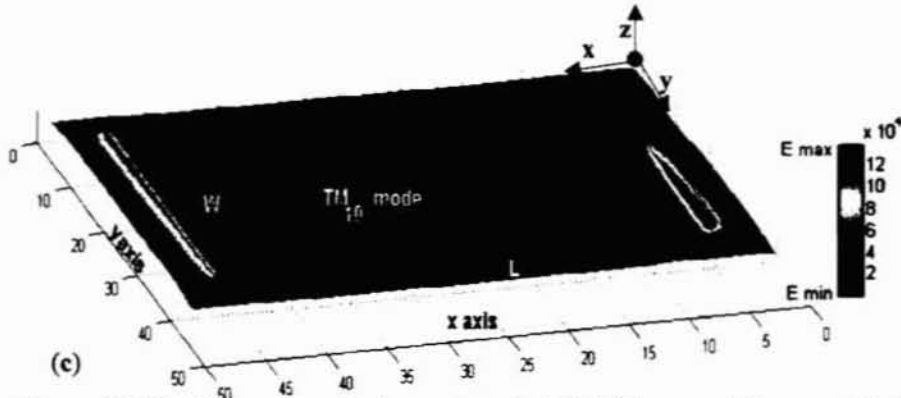
Figure 5.3.10.c Resonant modes in a rectangular MPA [Sheen *et al.*] computed using FDTD, at 6.280 GHz. E field shows constant distribution along y and one half cycle variation along x
L = 16mm, W=12.45mm,h=0.794mm, ε_r=2.2

Analogous to the conclusions derived for the rectangular MPA, modes of Octagonal MPA is interpreted based on the electric field distribution in the near field aperture depicted in figure 5.3.11 and 5.3.12. For the configuration with length L of the Octagonal MPA oriented along the x axis, the resonance mode at port 1 is identified as TM_{10}. It is seen from figure 5.3.11, that at port 1 electric field distribution exhibits *one half cycle* variation along x direction (5.3.11.a) and *no* variation along the y direction (5.3.11.b). The resonance at port 2 of the antenna corresponds to TM_{01} mode, where the electric field distribution exhibits *one half cycle* variation along y direction and *no* variation along the x direction of the configuration, as illustrated in figure 5.3.12.a and b respectively.

(a)

(b)
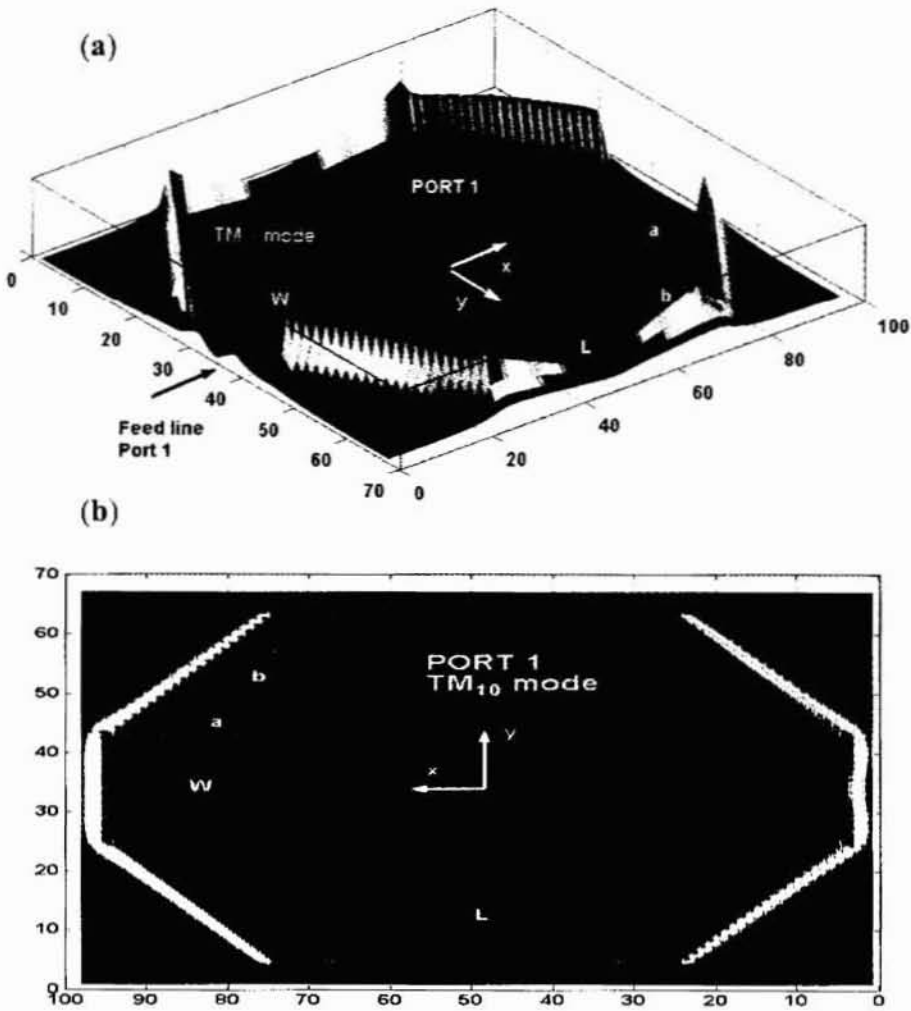
Figure 5.3.11 *Near field* distribution at port 1 resonant frequency of
Octagonal MPA, computed using CFDTD method.
(a) *exn* component of the aperture field indicating one half cycle variation
along *x*
(b) *eyn* component of aperture field indicating constant distribution along
y
L = 24.5mm, W = 9.5mm, a = 10mm, b = 10mm, w = 3mm,

(a)

(b)
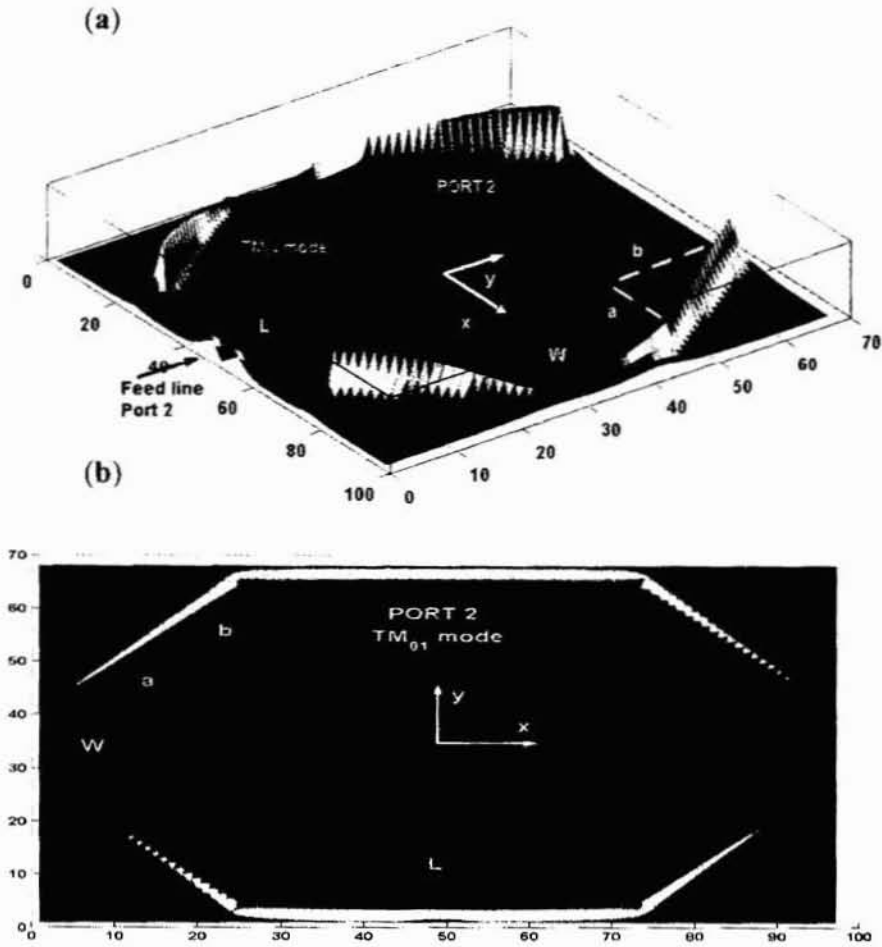
Figure 5.3.12 *Near field* distribution at port 2 resonant frequency of
Octagonal MPA, computed using CFDTD method.
(**a**) *eyn* component of the aperture field indicating one half cycle variation
along *y*
(**b**) *exn* component of aperture field indicating constant distribution along
x
L = 24.5mm, W = 9.5mm, a = 10mm, b = 10mm, w = 3mm,

5.3.5   Gain and Polarization patterns

Gain of the Octagonal microstrip patch antenna is determined using the gain transfer method explained in section 3.4.3. The antenna exhibits moderate gain in the 1.8GHz band as illustrated in figure 5.3.13.
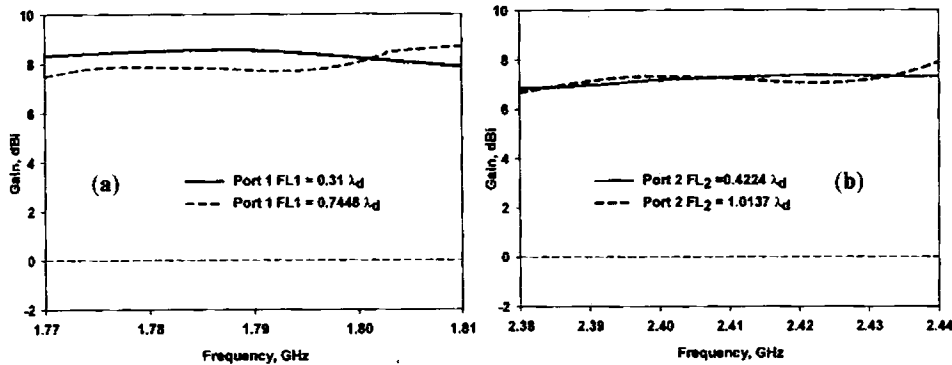
Figure 5.3.13 Measured Gain of Octagonal microstrip patch antenna
L = 24.5mm, W= 9.5mm, a= 10mm, b=10mm, w=3mm, h=1.6mm, ε_r=4.28
(a) Port 1 (b) Port 2

The gain in the port 2 resonance band is better than that of standard circular patch resonating at the same frequency. Average gains measured in the resonant bands of the Octagonal MPA are 7.29dBi and 7.05dBi respectively for ports 1 and 2, for the optimum feed length. The average and peak gains exhibited in the two resonant bands for two different feed lengths is shown in table 5.3.5.

	Feed length FL_1=0.31 λ_d, FL_2=0.42 λ_d		Feed length FL_1=0.7448 λ_d, FL_2=1.0137 λ_d	
	Avg Gain	Peak gain	Avg Gain	Peak gain
Port 1	7.288dBi	8.540dBi	7.482dBi	8.7dBi
Port 2	7.057dBi	7.3868dBi	6.9926dBi	7.9dBi

Table 5.3.5 Gain characteristics of Octagonal MPA.
L = 24.5mm, W= 9.5mm, a= 10mm, b=10mm, w=3mm, h=1.6mm, ε_r=4.28

Polarization characteristics of the Octagonal microstrip patch antenna are studied using the *Polarisation pattern* technique. Measured

polarization patterns of the antenna, along with the respective *polarization ellipse* at the two ports are shown in figure 5.3.14.
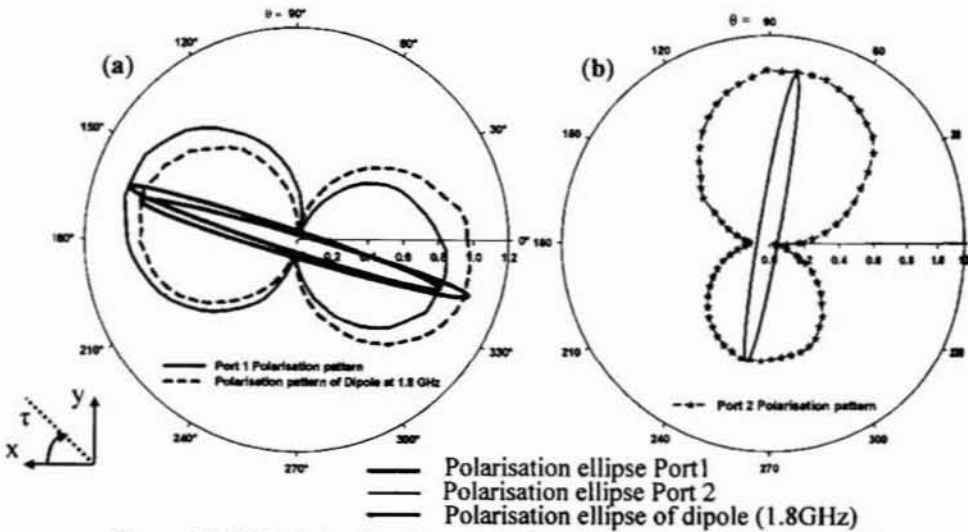
Figure **5.3.14** Polarization characteristics of Octagonal microstrip patch antenna (a)Polarization pattern and polarization ellipse at port 1 compared with that of a dipole resonating at 1.8GHz (b) Polarization pattern and polarization ellipse at port 2 Tilt angle τ is 180-θ

The *figure of eight* polarization patterns indicate that ports of the Octagonal geometry exhibit dual orthogonal *linear* polarizations. Axial ratio (AR $=10\log_{10}$(major axis / minor axis)) calculated from the respective *Polarization ellipse* for the two ports are 11.85dB and 11.46dB respectively. The value of AR is *not* infinity (∞) indicating that the polarization is not *purely* linear. The tilt angle, τ of the polarization ellipse are 18° and 100° respectively for the two ports.

The polarization states of the antenna in the two resonant modes are shown on the *Poincáre* sphere in figure 5.3.15.a. For a point, P on the sphere, Longitude is 2τ where τ is the tilt angle of the polarization ellipse. The latitude of the point is given by 2ζ where ζ = $\tan^{-1}$(1/axial ratio). The points on the sphere lie near the *equator* as is the case for linear polarization. They lie at diametrically opposite points on the sphere, indicating that the two ports are orthogonally polarized. The Axial ratio variation in the two resonant bands is depicted in figure 5.3.15.b.
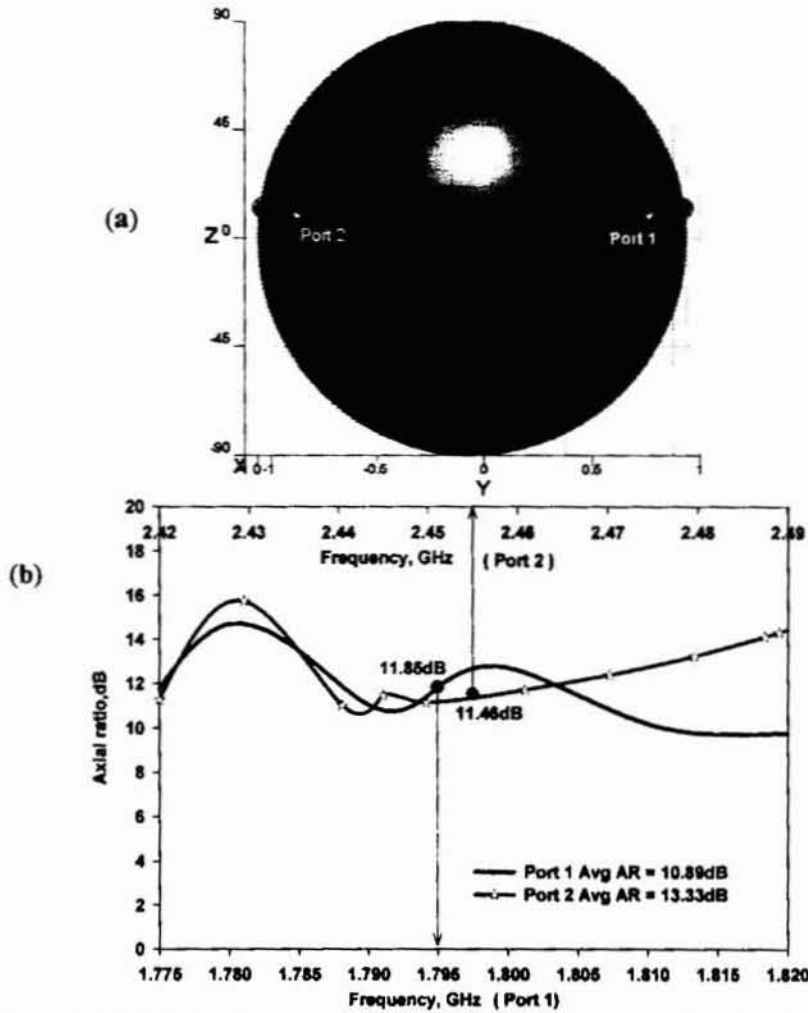
Figure 5.3.15 Polarization states and Axial Ratio in the two operating bands
of Octagonal MPA
(a) *Poincáre* sphere representing the polarization states
(b)Variation of Axial Ratio with frequency in the two resonant bands

5.3.6   Near field distribution of Electric and Magnetic fields

Electric and Magnetic field components extracted from the near
field aperture, as explained in section 4.6, is the basis for the interpretation of
resonant modes. The computed x, y and z components of E and H fields in
the aperture, at the respective resonant frequencies of port 1 and 2 are
illustrated in figures 5.3.16 and 17 respectively. The H field distribution
confirms the TM_{10} and TM_{01} modes of resonance of the geometry interpreted

based on E field analysis in section 5.3.4.

(a)   (b)
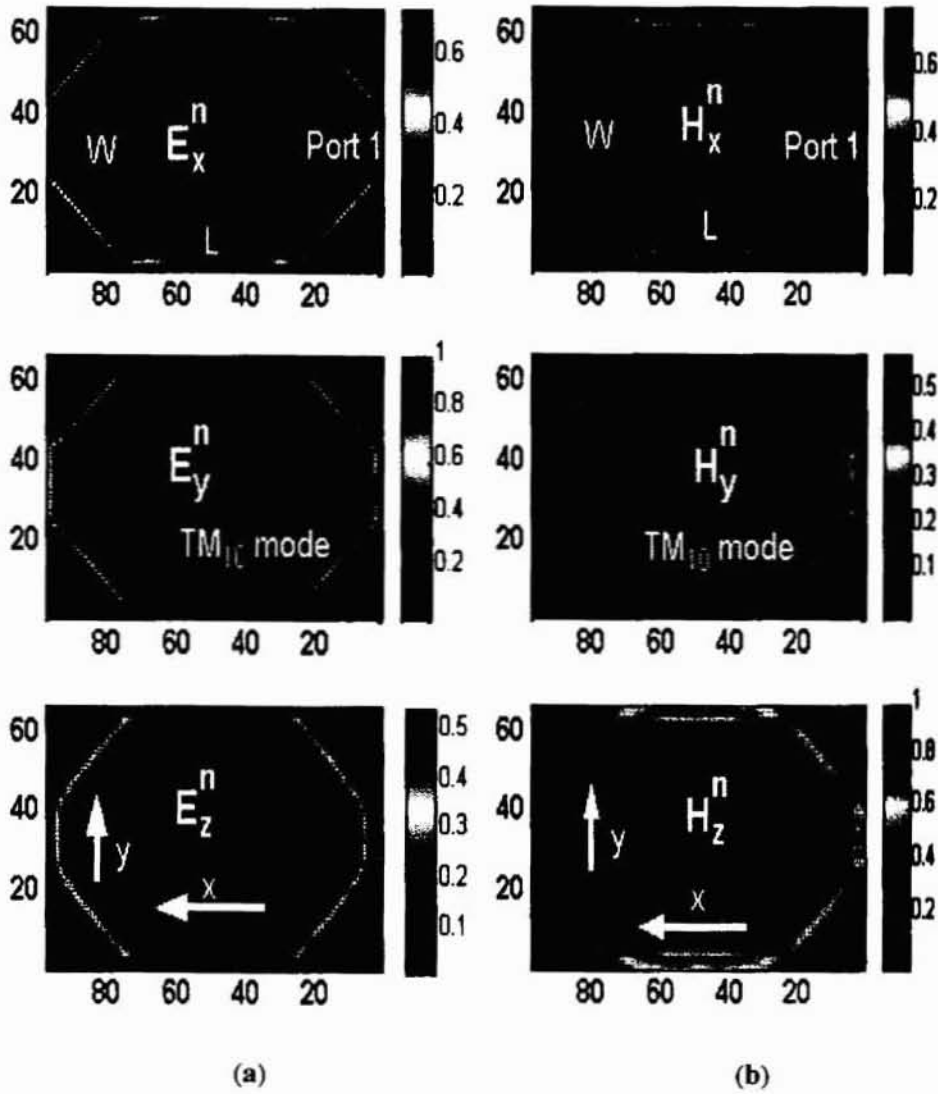
Figure 5.3.16 CFDTD computed Near field Electric and Magnetic distribution at port 1
resonance
(a)E field components (b) H field components
L = 24.5mm, W= 9.5mm, a= 10mm, b=10mm, w=3mm, FL_1= 0.31 λ_d, FL_2=0.42 λ_d
h=1.6mm, ε_r=4.28
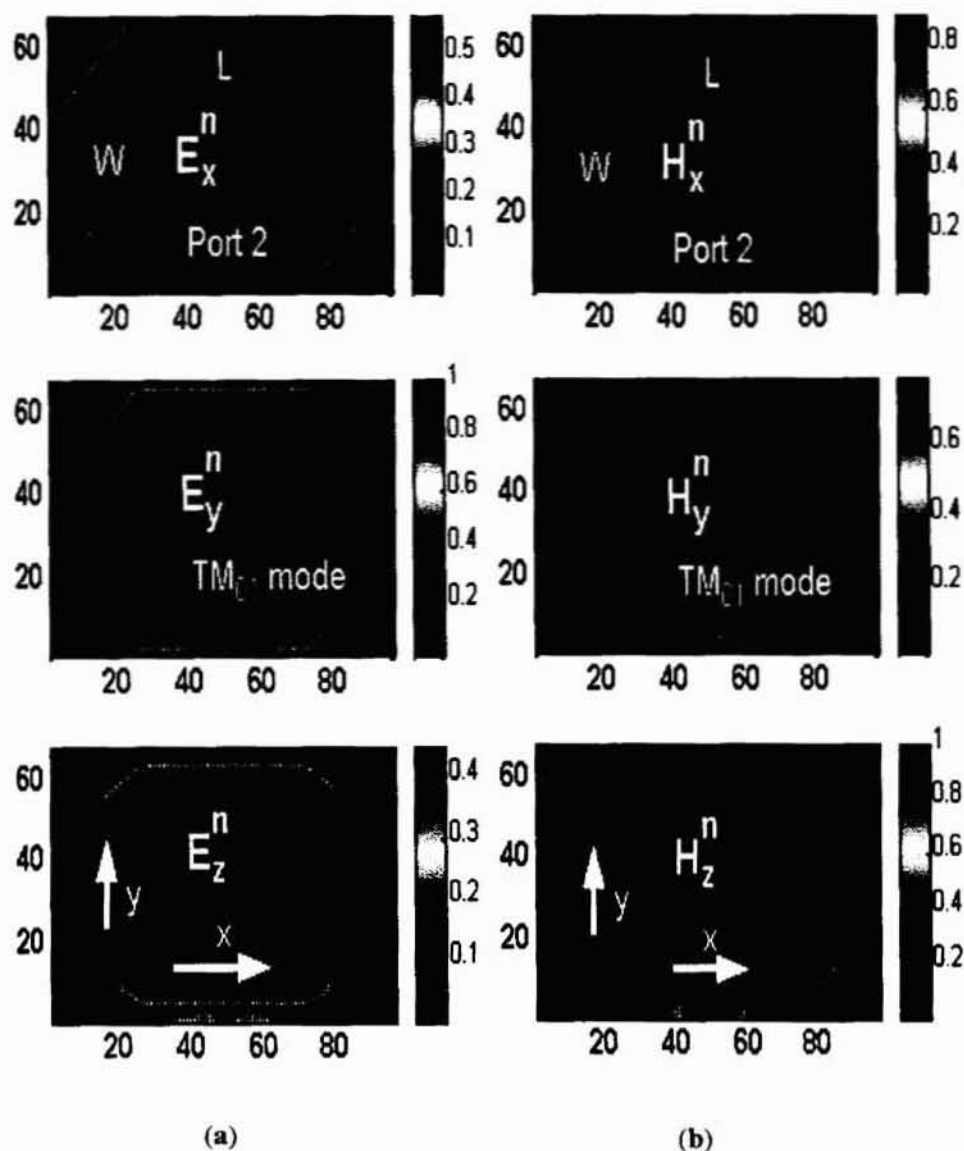
Figure 5.3.17 CFDTD computed Near field Electric and Magnetic distribution
at port 2 resonance
(a)E field components (b) H field components
L = 24.5mm, W= 9.5mm, a= 10mm, b=10mm, w=3mm, FL_1= 0.31 λ_d, FL_2=0.42 λ_d
h=1.6mm, ε_r=4.28

5.3.7   Comparison with conventional patches

The characteristics of the Octagonal microstrip patch antenna are compared with proximity coupled standard circular patches resonating at the same frequencies and with a rectangular patch resonating in the 1.8GHz / 2.45GHz bands.

- **Standard Circular patches resonating in the 1.8GHz and 2.45GHz bands**

The return loss characteristics of two electromagnetically excited circular patches resonating at 1.795GHz and 2.44GHz respectively, fabricated on the same substrate as the Octagonal microstrip patch antenna is shown in figure 5.3.18.a. The radiation patterns of the circular patch antennas in the principal planes are compared with respective patterns of Octagonal microstrip patch antenna in figure5.3.18.b. E plane pattern of Octagonal microstrip patch antenna at 1.795GHz is broad, just as in the case of standard circular patch. However in the H plane Octagonal geometry exhibits a wider beam. At 2.45GHz both patterns are broad. In the principal planes, along the broadside direction, cross polar levels of the Octagonal patch at 1.795 GHz is better than that of the corresponding circular patch. In general Octagonal MPA exhibits radiation characteristics comparable to that of standard circular patches.

The radii of standard circular microstrip patch antennas resonating at 1.795GHz and 2.44GHz are 23mm and 16.8mm respectively. The corresponding circular patch areas are 1660mm^2 and 890mm^2 whereas the area of the Octagonal geometry is 1110mm^2. The Octagonal geometry offers a physical area reduction of 33% with respect to the circular geometry.

A circular patch with its resonance characterized by a single dimension results in an electric field distribution that is uniquely characterized. The dominant mode in the geometry is well isolated from its harmonics, resulting in better performance at the fundamental mode. Hence circular patch is used as the reference.

Port 1
1.795GHz (1.785-1.825GHz) BW 40MHz, 2.2%
1.795GHz (1.774-1.821GHz) BW 47MHz, 2.6%

Port 2
2.44GHz (2.395-2.47GHz) BW 75MHz, 3.0%
2.455GHz (2.423-2.501GHz) BW 79MHz, 3.2%
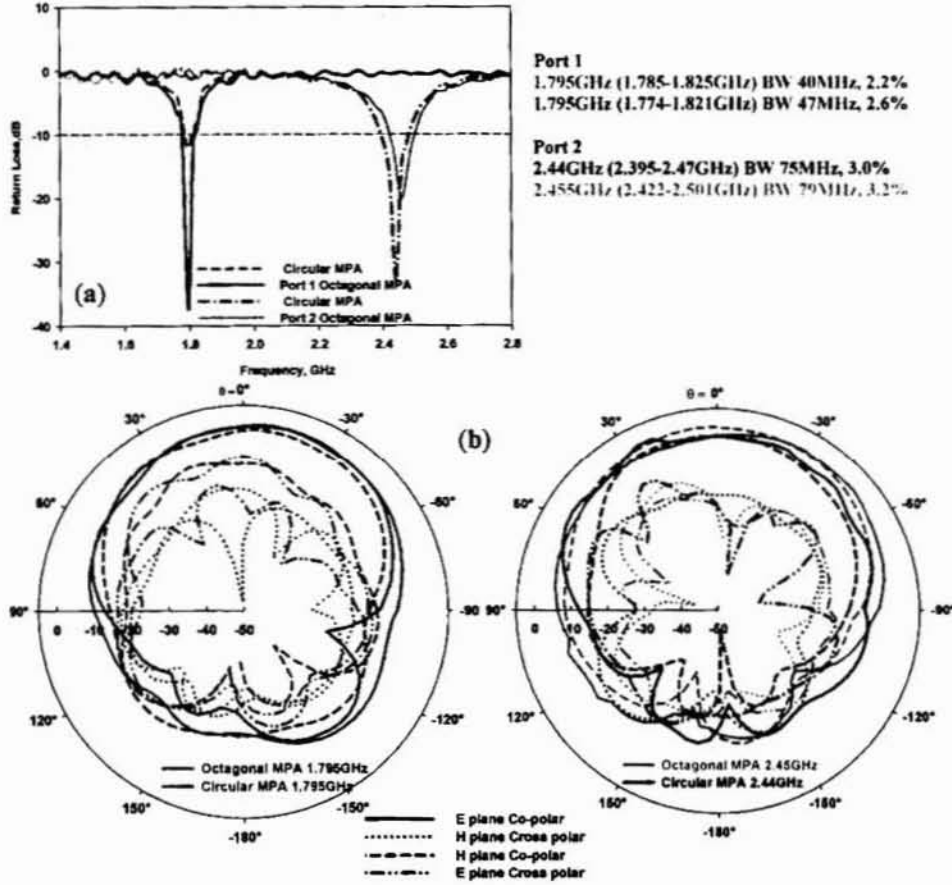
Figure 5.3.18 Measured Characteristics of Circular patches compared with
Octagonal MPA
(a)Return Loss characteristics (b) E plane and H plane patterns
Octagonal MPA: L = 24.5mm, W= 9.5mm, a= 10mm, b=10mm
Radii of the two Circular MPA: r_1=23mm (1.795GHz), r_2=16.8mm (2.44GHz),
h=1.6mm, ε_r=4.28

- **Rectangular patch resonating in the 1.8GHz / 2.45GHz bands**

A rectangular patch of dimensions length, L= 39.8mm and width,
W= 30.2mm, fabricated on FR4 substrate with h=1.6mm, ε_r=4.28 is fed
electromagnetically using two 50Ω orthogonal microstrip feed lines. The
feed-patch overlap distance for the two ports are 0.12λ_d and 0.102λ_d
respectively, λ_d being the respective wavelengths in the dielectric. Return
loss characteristics of the rectangular patch resonating at 1.81GHz and
2.425GHz, at the two ports, is shown in figure 5.3.19.a. Radiation patterns of

Octagonal microstrip patch antenna is compared with that of rectangular MPA in figure 5.3.19.b.

Port 1
1.810GHz (1.790-1.844GHz) BW 54MHz, 2.98%
1.795GHz (1.774-1.821GHz) BW 47MHz, 2.6%
Port 2
2.425GHz (2.410-2.470GHz) BW 60MHz, 2.47%
2.455GHz (2.422-2.501GHz) BW 79MHz, 3.2%
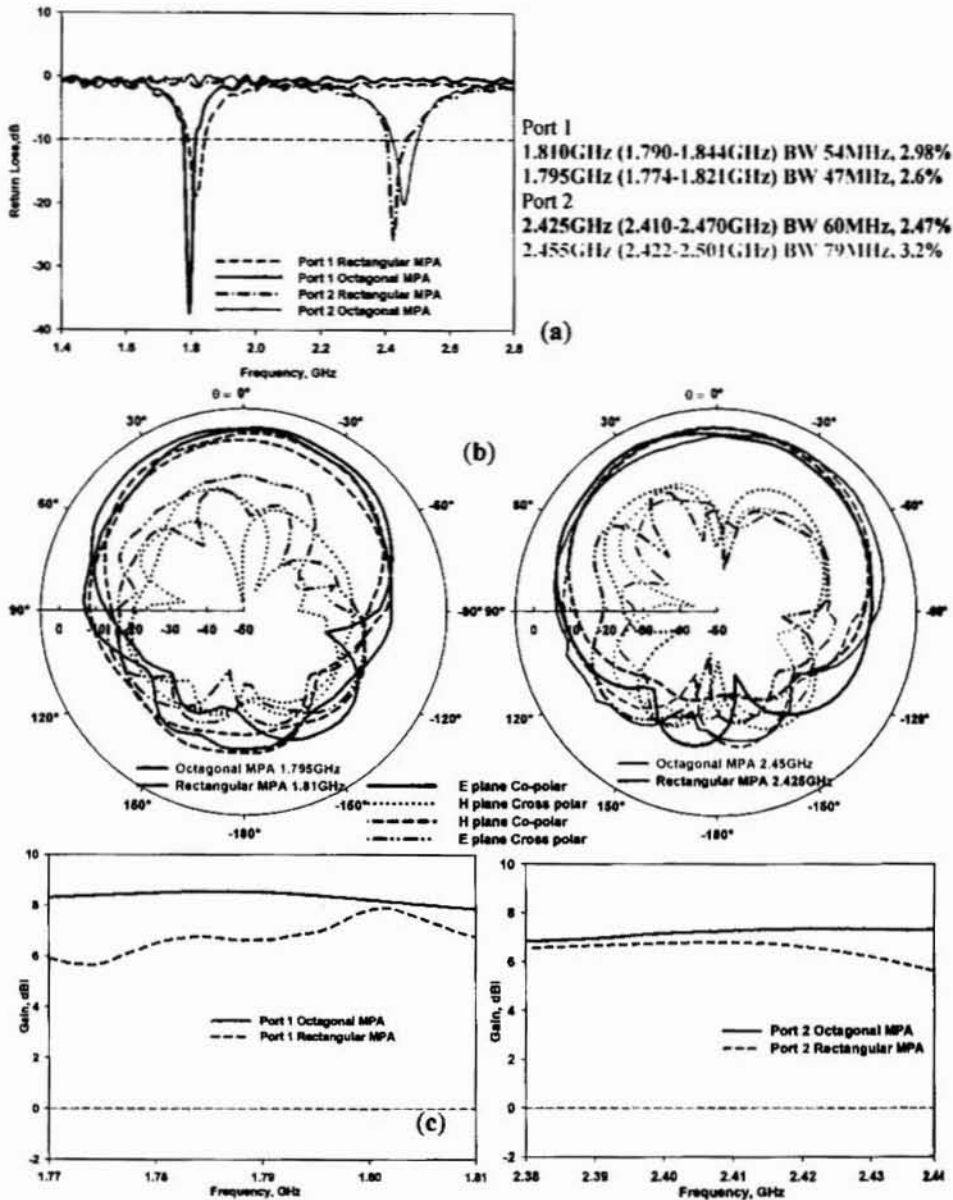
Figure 5.3.19 Measured Characteristics of Dual band Rectangular MPA
compared with Octagonal MPA
(a)Return Loss characteristics (b) E plane and H plane patterns (c) Gain
Octagonal MPA: L = 24.5mm, W= 9.5mm, a= 10mm, b=10mm, h=1.6mm, ε_r=4.28
Rectangular MPA: L= 39.8mm, W= 30.2mm, h=1.6mm, ε_r=4.28

At port 1, in the principal planes the Octagonal patch exhibits better cross polar isolation, along the bore sight, than the rectangular patch. At port 2,

both antennas exhibit broad patterns with CPL better than -20dB along the broad side direction. In general the Octagonal patch antenna offers wide beams in the principal planes. Theoretically, the maximum directive gain possible for the dual band Rectangular MPA at 1.8GHz and 2.45GHz, on the substrate presently employed for study, are 7.25dBi and 7.375dBi respectively. Gain of the Octagonal patch antenna measured in the bore sight direction is higher than that of the dual band Rectangular MPA in both resonant bands as shown in figure 5.3.19.c. The characteristics of Octagonal MPA, rectangular MPA and circular patches are compared in table 5.3.6.

Geometry	Port1				Port 2				Area of the patch (mm²)
	Freq (GHz)	Band (GHz) %BW	E plane HPBW	H plane HPBW	Freq (GHz)	Band (GHz), %BW	E plane HPBW	H plane HPBW	
Octagonal L=24.5mm, W=9.5mm, a=10mm, b=10mm	1.795	1.774-1.821, 2.6%	85°	95°	2.455	2.422-2.501, 3.2%	100°	85°	1100
Rectangular L=39.8mm, W=30.2mm	1.810	1.790-1.844, 2.98%	97°	90°	2.425	2.410-2.470, 2.47%	99°	90°	1202
Circular patch -1 r=23mm	1.795	1.785-1.825, 2.2%	90°	55°		--			1660
Circular patch -2 r=16.8mm		--			2.440	2.395-2.470, 3%	85°	80°	890

Table 5.3.6 Comparison of radiation characteristics of Octagonal microstrip antenna with standard microstrip antennas

5.3.8 Antenna on standard substrates

Based on CFDTD calculations the dimensions of Octagonal microstrip patch antenna, suitable for operation in the Mobile - Bluetooth bands is given in table 5.3.7, for standard laminates. The average value of patch feed overlap distance which offers good impedance matching is $0.0731\lambda_d$ and $0.114\lambda_d$ for ports 1 and 2 respectively. λ_d is the wavelength in the dielectric, corresponding to the resonant frequencies.

Substrate description			Antenna dimensions				Feed- patch overlap	
	ε_r	Thickness h (mm)	Length, L (mm)	Side, a (mm)	Side, b (mm)	Width W (mm)	F_1/λ_d	F_2/λ_d
RT Duroid 5880 0.010in	2.2	0.254	37.5	12	12	19.5	0.09	0.13
RT Duroid 5880 0.020in	2.2	0.508	37	12	12	19	0.1	0.14
GML 2032 0.030in	3.2	0.762	30	10.5	10	15.4	0.12	0.16
GML 1034 0.020in	3.38	0.508	32.4	9	12	10.7	0.06	0.11
Glass epoxy (local)	4.28	1.6	24.5	10	10	9.5	0.05	0.1
FR4 62 mil	4.35	1.5748	24	10	10	9	0.08	0.13
FR4 epoxy 0.030in	4.4	0.762	24.5	10	10	10.5	0.1	0.16
FR4 40mil	4.4	1	25.2	9.5	9.5	10.9	0.08	0.12
FR4 epoxy 0.060in	4.4	1.524	24.5	9.5	9.5	10	0.07	0.11
Alumina 0.010in	9.8	0.254	15.8	8	8	5.3	0.06	0.07
Alumina 0.025in	9.8	0.635	15.8	8	8	4.8	0.04	0.06
RT Duroid 6010 0.010in	10.2	0.254	11.4	10.5	8.5	4.6	0.06	0.1
RT Duroid 6010 0.025in	10.2	0.635	11.5	10.5	8.5	4	0.04	0.09

Table 5.3.7 Computed dimensions of Octagonal MPA on standard laminates

The measured and computed input characteristics of electromagnetically coupled Octagonal MPA suited for Mobile - Bluetooth application,

fabricated on GML 2032 substrate is shown in figure 5.3.20.a. The antenna exhibits resonance at 1.8125GHz and 2.425GHz respectively at the two ports while the corresponding CFDTD computed values are 1.795GHz and 2.45GHz. The antenna offers 2.43% and 3.25% BW in the two bands. The port isolation exhibited is also compared with the predicted values in figure 5.3.20.a. The measured values show a close agreement with the CFDTD computed results.
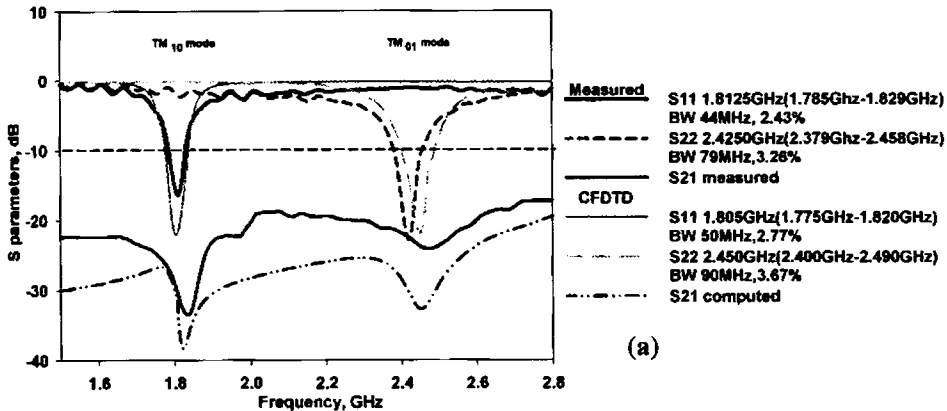
Figure 5.3.20.a Measured and Computed Input characteristics of the Octagonal MPA
L = 30mm, W= 15.4mm, a= 10.5mm, b=10mm, w=3mm, F_1= 0.12 λ_d, F_2=0.16 λ_d,
FL_1= 0.27 λ_d, FL_2=0.36 λ_d, h=0.762mm, ε_r=3.2

The measured radiation patterns of the above Octagonal MPA are illustrated in figure 5.3.20.b. The antenna exhibits broad side radiation. At port 1, HPBW measured in E and H planes are 105° and 75° respectively. CPL in the E plane is -28dB along the broadside direction and it is better than -18dB over the entire plane, while the minimum cross polar isolation of -35dB is at angle of -34°. CPL in the H plane is -24dB along the broadside direction, while the minimum cross polar isolation of -30dB is at angle of -19°. The patterns measured at port 2 exhibit HPBW of 115° and 90° respectively, in the E and H planes. The cross polar levels along the broadside direction in the E plane and H plane are -24dB and -30dB respectively, for port 2. In the H plane minimum cross polar isolation of -41dB is at elevation angle of -24°. The measured cross polar level along the broadside direction, in the two operating bands is illustrated in figure 5.3.20.c.
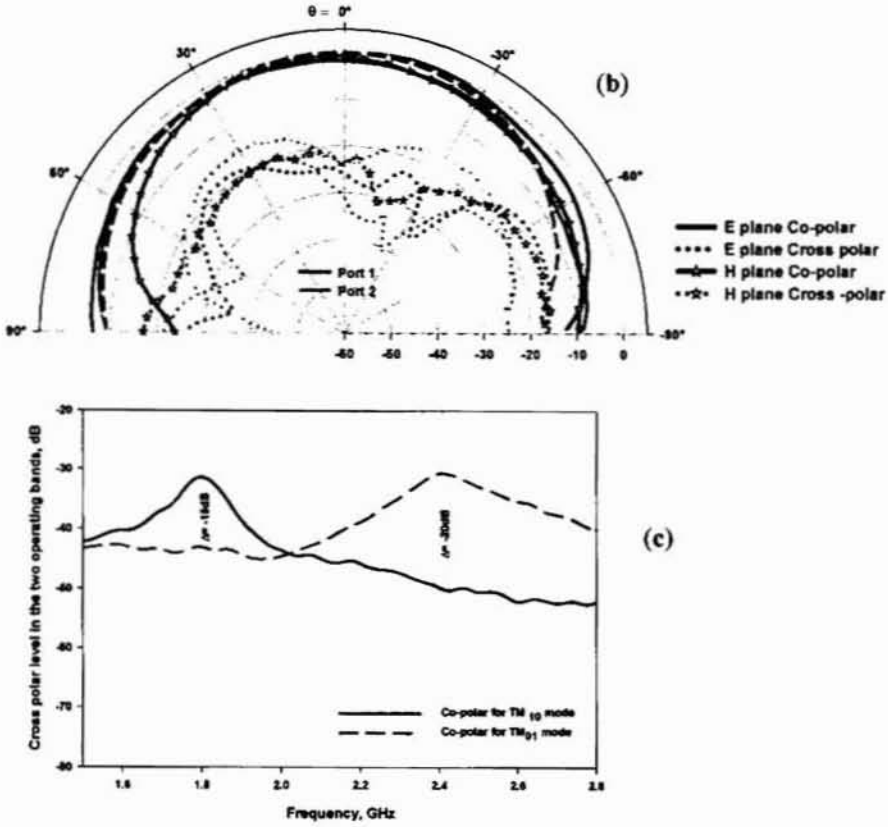
Figure 5.3.20 *(contd.)* **(b)** Measured radiation patterns of the Octagonal MPA
(c) Cross Polar isolation between ports
L = 30mm, W= 15.4mm, a= 10.5mm, b=10mm, w=3mm, F_1= $0.1\lambda_d$, F_2=$0.16\lambda_d$,
FL_1= $0.27 \lambda_d$, FL_2=$0.36 \lambda_d$,h=0.762mm, ε_r=3.2

5.4   Octagonal patch antenna for Mobile and GPS receiver applications

Operating band of *PCS 1900* is 1.85-1.99 GHz while GPS receiver works in the 1565-1585 MHz band. The dimensions of the Dual port Dual band Octagonal MPA configuration suitable for the above application, optimised from numerical investigations using CFDTD is

Patch dimensions: L = 30mm, W = 20mm, a = 9mm, b = 9mm

Feed parameters: w = 3mm, FL_1 = 0.541λ_d, FL_2 = 0.328λ_d,

                        Fd_1 = 12 mm, Fd_2 = 10 mm

Substrate parameters: h = 1.6mm, ε_r = 4.28

Characteristics of the antenna configuration fabricated on FR4 substrate are described below.

5.4.1   Input characteristics

The dimensions of the patch and feed suitable for GPS/PCS frequency bands are numerically determined and verified experimentally. The two ports of the antenna are energized electromagnetically using two orthogonal 50Ω microstrip feed lines with dimensions as given above.

• Return loss and isolation characteristics at the ports

The S parameters of the above described antenna configuration antenna is shown in figure 5.4.1. Port 1 of the antenna exhibits resonance at 1.57GHz, with the 2:1VSWR band from 1.548GHz-1.593GHz, and a fractional bandwidth of 2.86%. The second port shows, resonance at 1.9GHz with 2.16%BW, with the band from 1.881GHz-1.922GHz. The numerically computed S11 and S21 parameters of the antenna are illustrated in figure 5.4.1.a, in comparison with measured and simulated results. CFDTD based numerical computations indicate the resonance frequencies for the two ports as 1.5677GHz and 1.9206GHz respectively. The two frequencies are predicted within a tolerance of +0.15% and -1.07% respectively with respect

to the corresponding measured results. The computed -10dB return loss bands are 1.5041GHz-1.6372GHz and 1.8512GHz-1.99GHz respectively at the two ports. Input impedance loci, normalized with respect to 50 Ohms, within the 2:1VSWR bands are plotted in figure 5.4.1.b. The measured isolation between the ports is better than -25dB at port 1 and better than -30dB at port 2 whereas, CFDTD study indicated isolation better than -35dB and -40dB respectively.
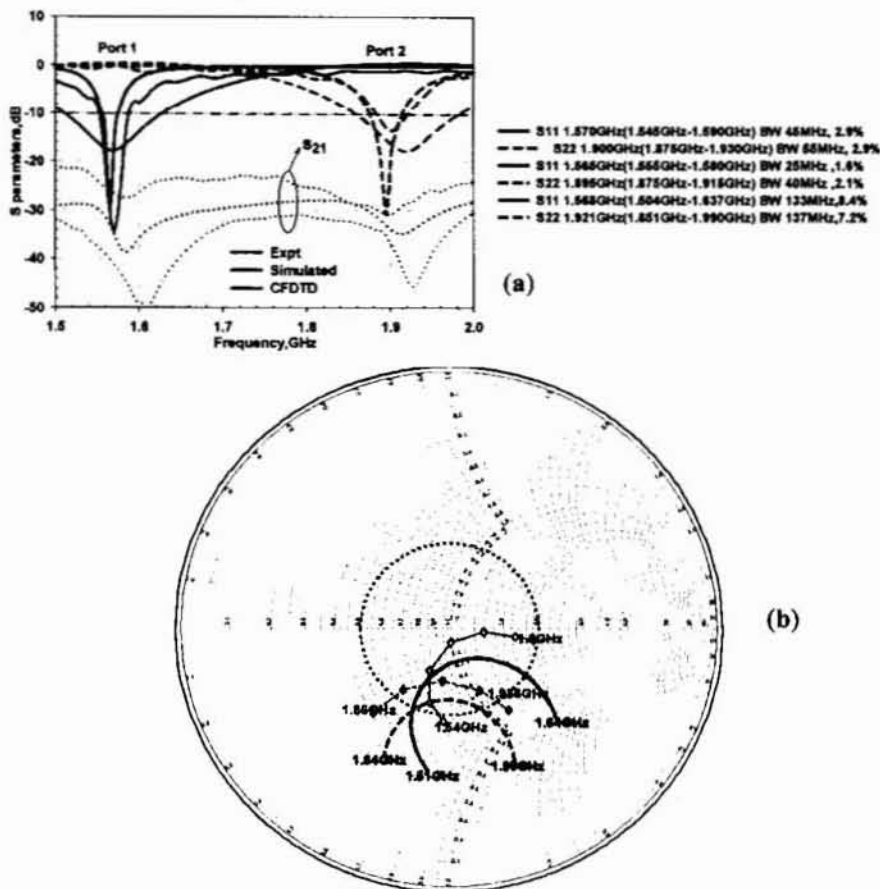
Figure 5.4.1 Input Characteristics of Octagonal MPA suitable
for GPS / mobile application
(a) Measured, CFDTD computed and simulated S parameters
(b) Measured and computed input impedance loci at the two ports
L = 30mm, W= 20mm, a= 9mm, b=9mm, w=3mm, FL_1=0.541 λ_d, FL2=0.328 λ_d
h=1.6mm, ε_r=4.28

The resonant frequency bands of the octagonal patch antenna can be fine tuned by the dimension α ($\alpha = a = b$). Figure 5.4.2.a illustrates the variation

in the resonant frequency of the two ports with respect to the dimension, α. As α is varied from 6 mm to 30 mm, the computed resonant frequency of the two ports varies from 1.7355GHz to 0.9719GHz and 2.22GHz to 1.0876GHz respectively *i.e* corresponding to 80% variation in the dimension α, the port 1 resonance frequency shows 44% variation whereas port 2 shows 51% variation. The corresponding values observed experimentally are 45.7% and 53.1% for the respective ports. As α is varied from 6mm to 30mm, the measured resonant frequencies of the two ports vary from 1.75GHz to 0.95GHz and from 2.19GHz to 1.0275GHz respectively. Good bandwidth characteristics are obtained when α = 9 mm, for both bands. This property is illustrated in figure 5.4.2.b.
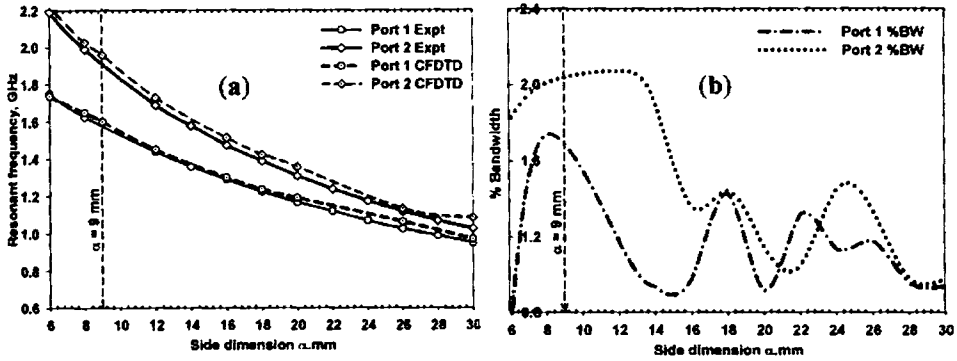
Figure 5.4.2 Variation of (a) resonant frequency (b) %BW with respect to dimension, α L = 30mm, W= 20mm, α=a=b, w=3mm, FL_1=0.541λ_d ,FL_2=0.328λ_d, h=1.6mm, ε_r=4.28

• **Effect of feed length on resonant frequency, band width and isolation characteristics**

The effect of feed length (FL_1 and FL_2) on the resonant frequency of the Octagonal patch is studied experimentally and using CFDTD. The feed line length is varied from 0.21λ_d to 1.07λ_d for port 1 and from 0.26λ_d to 1.34λ_d for port 2. λ_d is the wavelength within the substrate, corresponding to resonance frequency of the respective ports. The optimum feed lengths for maximum bandwidth for the two ports of the configuration identified numerically are 0.5465λ_d and 0.3311λ_d, whereas the measured values are

$0.541\lambda_d$ and $0.328\lambda_d$ respectively. Figure 5.4.3.a illustrates the computed return loss characteristics at the two ports as the feed length is varied. Figure 5.4.3.b illustrates the measured S parameters at the two ports for different feed lengths.
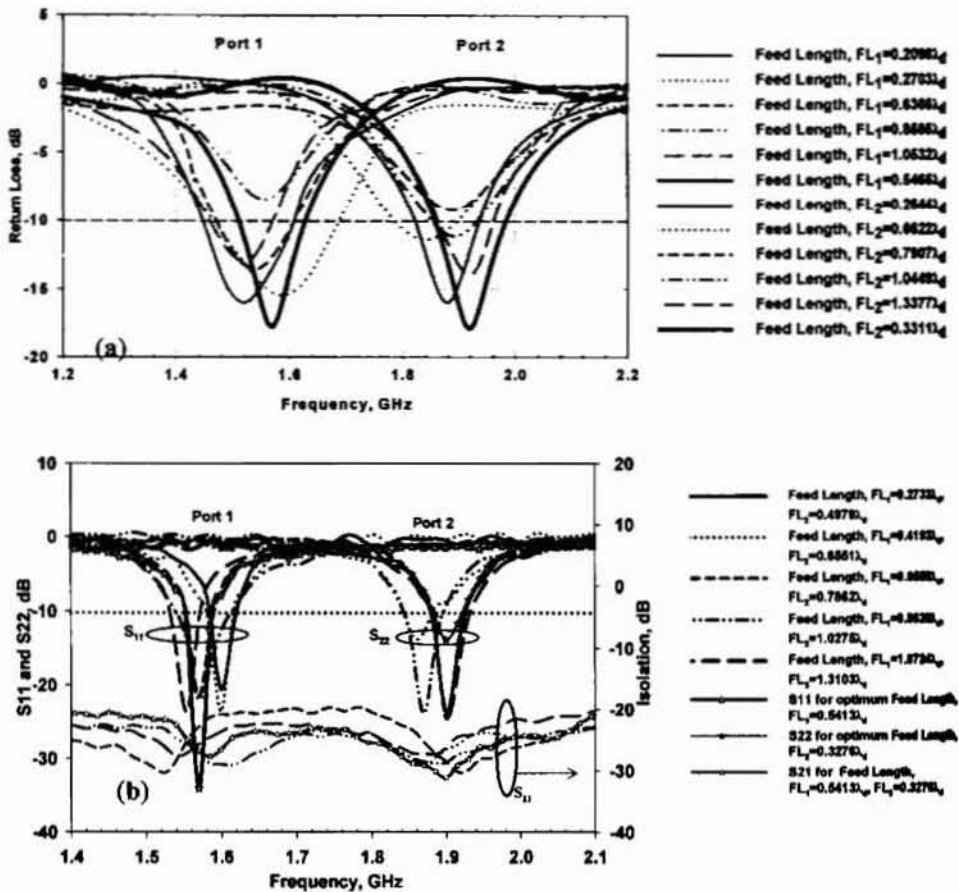
Figure 5.4.3 Influence of feed length on the input characteristics of Octagonal MPA for GPS-Mobile application
(a) CFDTD computed return loss characteristics at the two ports for different feed lengths (b) Measured S parameters at the two ports for different feed lengths (the optimum feed length is high lighted in both cases)
L = 30mm, W= 20mm, a= 9mm, b=9mm, w=3mm, h=1.6mm, ε_r=4.28

Figure 5.4.4 illustrates the influence of feed length on the resonant frequency. Resonant frequency at the ports is found to exhibit less than 2.5% shift, for a 80% variation in feed length. The average feed – patch overlap

distance for port 1 is $0.096\lambda_d$ and that for port 2 is $0.144\lambda_d$.
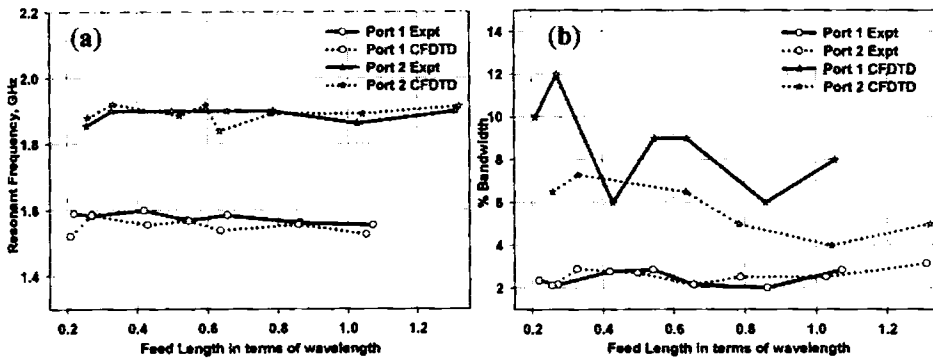
Figure 5.4.4 Influence of feed length on the resonant frequency and %BW of Octagonal MPA for GPS-mobile application.

(a) Variation of resonant frequency at the two ports for different feed lengths

(b) Variation of % BW at the two ports for different feed lengths

L = 30mm, W = 20mm, a = 9mm, b = 9mm, w = 3mm, h = 1.6mm, ε_r = 4.28

5.4.2 Far field Characteristics

• Radiation patterns

The antenna configuration exhibits broadside radiation. The computed 2D radiation patterns are compared with measured and IE3D simulation results in figures 5.4.5.a and b, at the resonance frequencies of ports 1 and 2 respectively. The direction of beam maxima and CPL for each case are shown in table 5.4.1. The differences between predicted values and measured results may be due to the finite size of feed layer of the configuration. The HPBW measured in the E plane and H plane at port 1 resonance are 92° and 78°. Cross polar level in the E plane is -29.4dB in the bore sight direction and it is better than -20 dB over the entire plane. In the H plane, cross polar level in the bore sight direction is -19dB, while the minimum cross polar isolation of -13dB is at an angle of +37°. At port 2, the patterns exhibit HPBW of 76° and 88° respectively, in the E and H planes. The corresponding cross polar levels along the broadside direction in the two planes are -18.5dB and -22dB respectively. In the E plane, minimum cross polar isolation of -17dB is at elevation angle of -19° and for the H plane, minimum is -19dB at an angle of +45°.
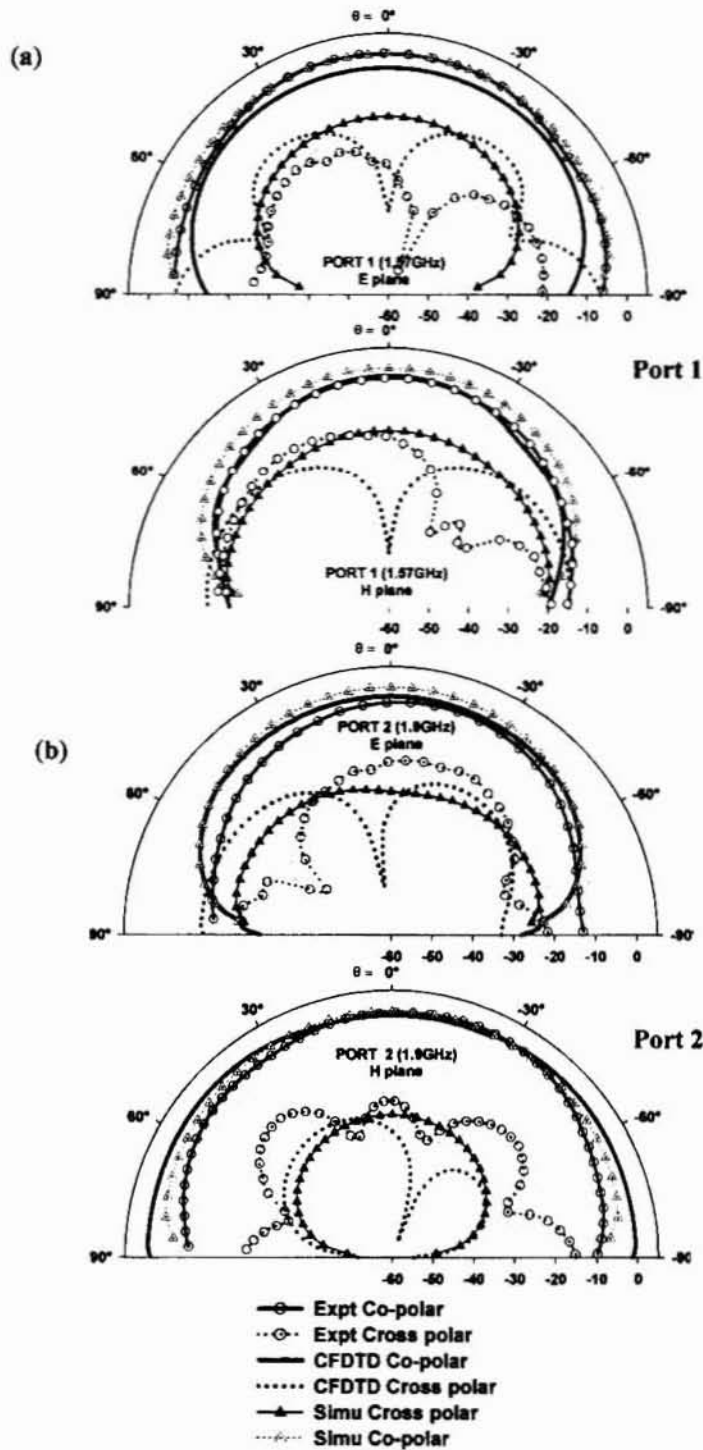
Figure 5.4.5 Radiation Patterns of Octagonal MPA for GPS/Mobile application
(a) E plane and H plane patterns of Port 1 (b) E plane and H plane patterns of Port 2
L = 30mm, W = 20mm, a = 9mm, b = 9mm, w = 3mm, $FL_1 = 0.541\lambda_d$, $FL_2 = 0.328\lambda_d$,
h=1.6mm, ε_r=4.28

3D E phi pattern
pattern

3D E theta

(c)

Port 1
1.57GHz

Complete 3D pattern

3D E phi pattern
pattern

3D E theta

(d)
Port 2
1.9GHz

Complete 3D
pattern
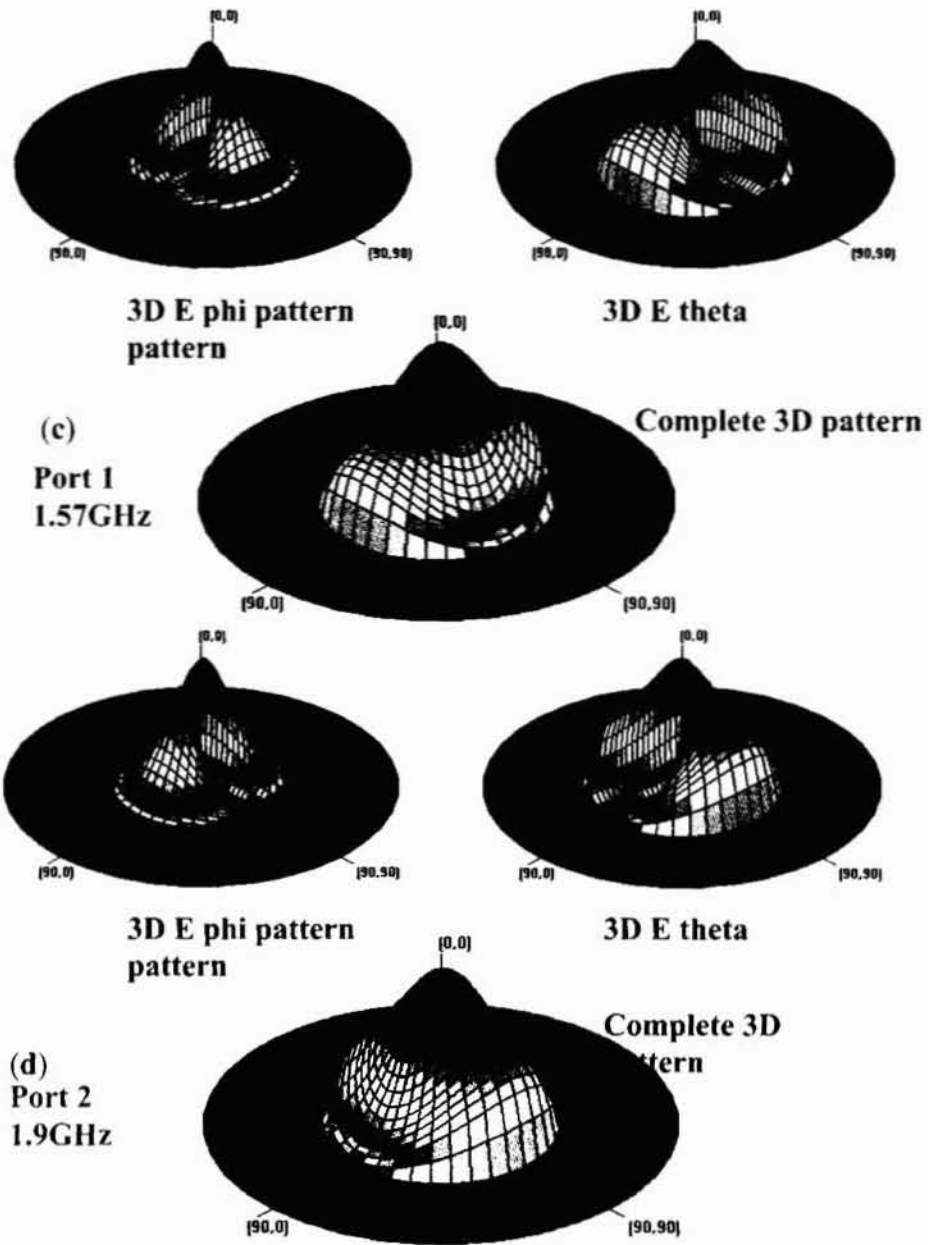
Figure 5.4.5*(contd)* Simulated 3D patterns of Octagonal MPA for
GPS/Mobile application
(c) E_φ, E_θ and E_{total} 3D patterns at Port 1 resonance frequency
(d) E_φ, E_θ and E_{total} 3D patterns at Port 2 resonance frequency
L = 30mm, W = 20mm, a = 9mm, b = 9mm, w = 3mm, $FL_1 = 0.541\lambda_d$,
$FL_2 = 0.328\lambda_d$, h=1.6mm, ε_r=4.28

(e)

(f)
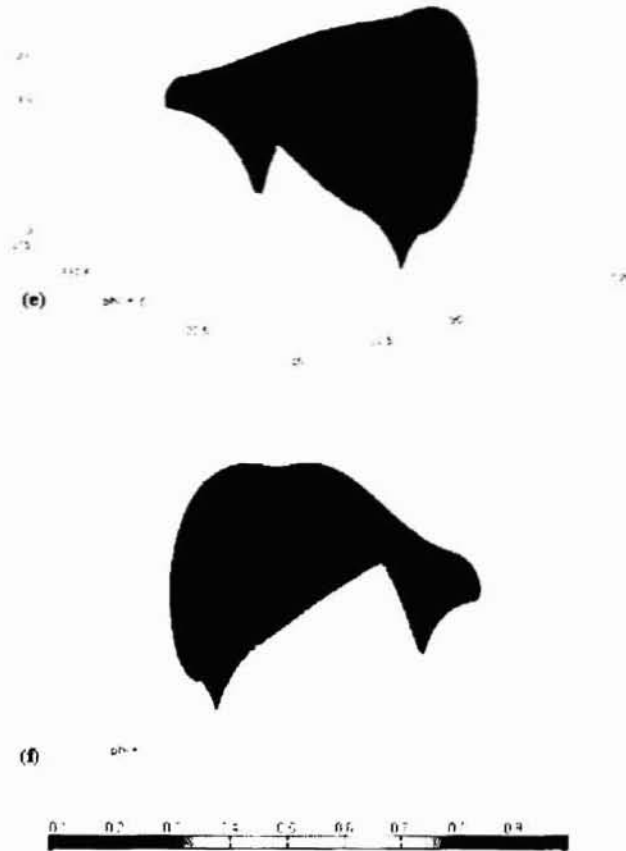
Figure 5.45 *(contd)* CFDTD computed normalized 3D pattern of Octagonal MPA for
GPS-Mobile application
(e) Pattern corresponding to 1.57GHz (f) Pattern corresponding to 1.9GHz
L = 30mm, W = 20mm, a = 9mm, b = 9mm, w = 3mm, $FL_1 = 0.541\lambda_g$, $FL_2 = 0.328\lambda_g$,
h = 1.6mm, $\varepsilon_r = 4.28$

		E plane			H plane		
		Expt	Predicted CFDTD	Simulated IE3D	Expt	Predicted CFDTD	Simulated IE3D
Port 1	Direction of Beam maxima	+9°	Broad side	Broad side	-7°	Broad side	Broad side
	Broad side CPL	-30dB	-39.5dB	-15.8dB	-19dB	-4dB	-15.8 dB
Port 2	Direction of Beam maxima	-12°	Broad side	Broad side	-21°	Broad side	Broad side
	Broad side CPL	-19dB	-30dB	-25dB	-22dB	-29.5dB	-25dB

Table 5.4.1 Comparison of far field characteristics of Octagonal MPA.
L = 30mm, W= 20mm, a= 9mm, b=9mm, w=3mm, h=1.6mm, ε_r=4.28,
FL_1 = 0.541λ_d and FL_2 = 0.328λ_d

The simulated 3D radiation patterns of the antenna corresponding to E_φ, E_θ and E_{total} at the two resonant frequencies is shown in figure 5.4.5.c -d respectively. The 3D patterns computed numerically for the configuration is illustrated in figure 5.4.5.e. It is observed that patterns are reasonably broad with radiation maxima in the broad side direction.

• **Gain and Polarization**

The antenna exhibits moderate gain in the lower band as illustrated in figure 5.4.6. The gain at port 2 resonance band is better than that of standard circular patch resonating at the same frequency. Average gains measured in the resonant bands of the Octagonal MPA are 7.25 dBi and 8.15dBi respectively for ports 1 and 2, for the optimum feed length. The antenna configuration offers linear orthogonal polarization at the two ports. The plane of polarization of the lower resonance mode of the antenna is tangential to the longer dimension, L of the geometry while, that of the higher resonance frequency is tangential to the dimension, W.

Port 1
Avg. Gain   6.652dBi
Peak gain 7.479dBi

Port 2
Avg. Gain   8.172dBi
Peak gain 8.312dBi
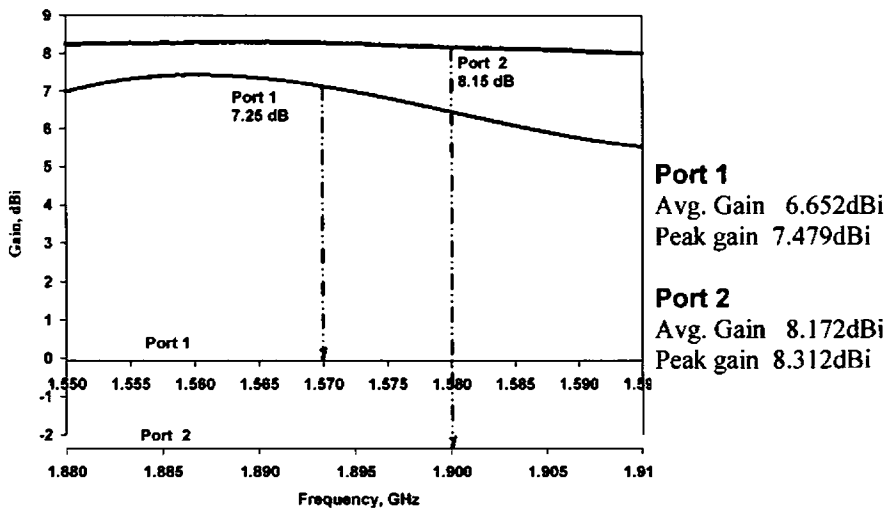
Figure 5.4.6 Measured gain of Octagonal MPA for GPS/Mobile application
L = 30mm, W = 20mm, a = 9mm, b = 9mm, w = 3mm, $FL_1 = 0.541\lambda_d$, $FL_2 = 0.328\lambda_d$, h=1.6mm, ε_r=4.28

• **Near field distribution and Resonant modes**

The CFDTD computed near field components at the two resonant frequencies of the antenna, is illustrated in figure 5.4.7.a-b. From these distributions, the resonance modes of the antenna are identified as TM_{10} and TM_{01} respectively for the two ports. Figure 5.4.7.c-d shows the average current

---

Development and Analysis of Microstrip Antennas for Dual Band Microwave Communication

Density on the patch surface obtained by IE3D simulation, illustrating the resonant modes.
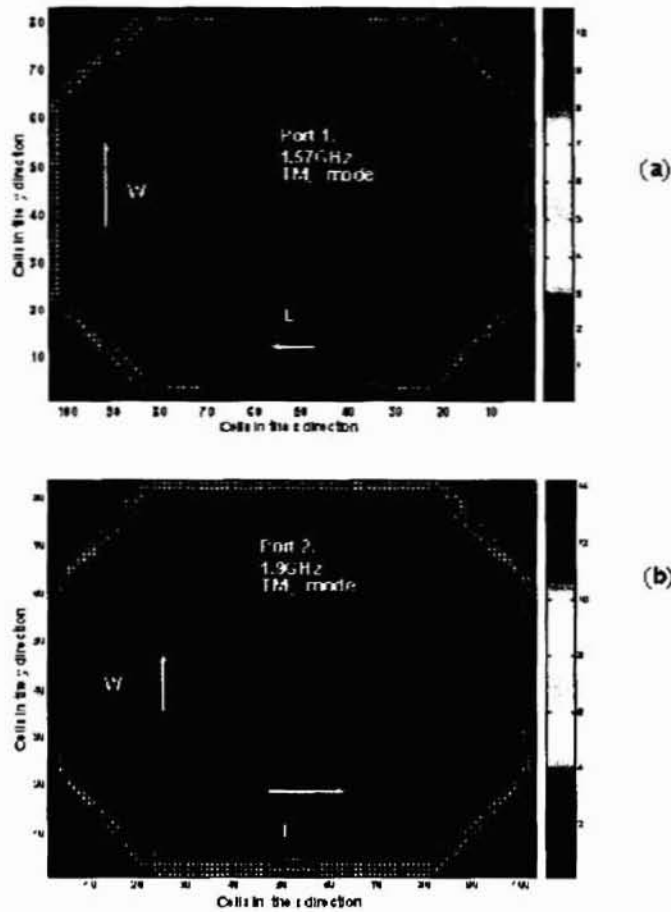
Figure 5.4.7 CFDTD Computed *Near field* distribution of Octagonal MPA for GPS/Mobile application
(a) Port 1 exhibiting TM_{10} mode (b) Port 2 exhibiting TM_{01} mode
$L = 30mm$, $W = 20mm$, $a = 9mm$, $b = 9mm$, $w = 3mm$, $FL_1 = 0.541\lambda_d$, $FL_2 = 0.328\lambda_d$, $h = 1.6mm$, $\varepsilon_r = 4.28$

Comparison with standard patches
Both resonant modes of the Octagonal MPA exhibits higher gain than the standard circular patches resonating at these frequencies. At 1.57GHz,

there is an area reduction of 15% and 31% with respect to standard circular and rectangular patches.
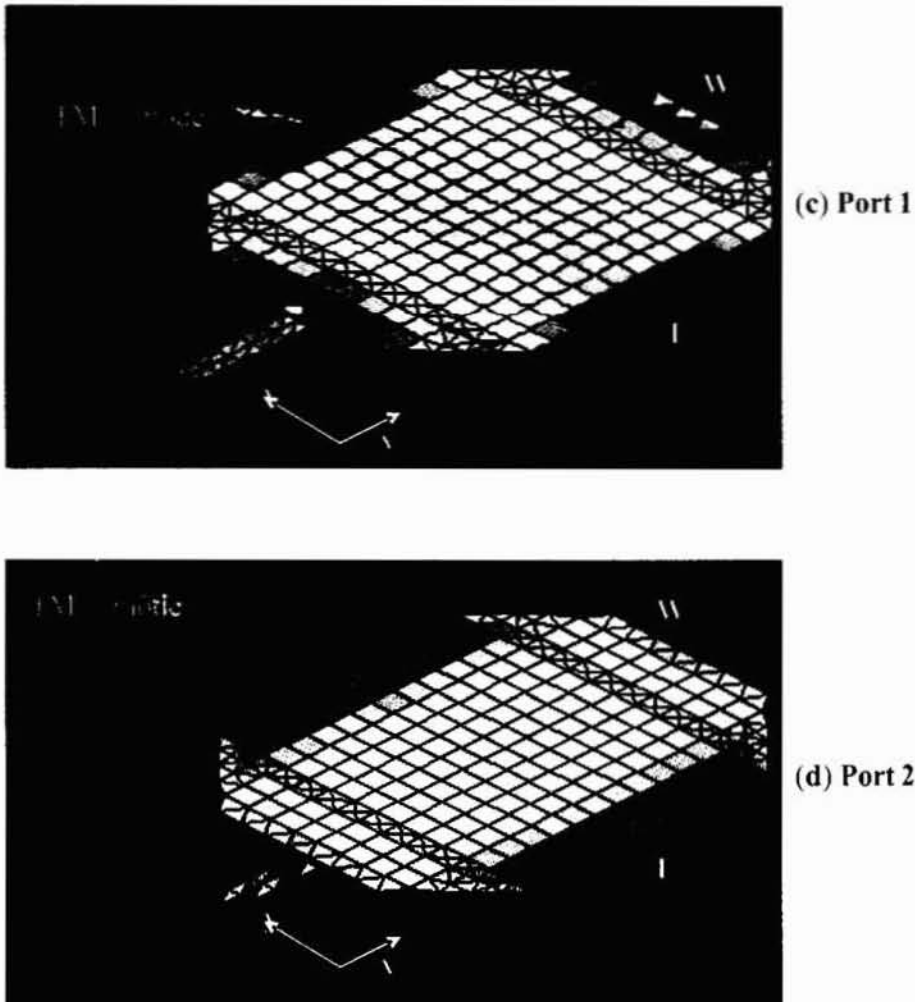
(c) Port 1

(d) Port 2

Figure 5.4.7 *(contd)* Surface current density obtained by IE3D simulation of Octagonal MPA configuration illustrating the resonant modes of the geometry.
(c)Port 1 resonating in TM_{10} mode (d) Port 2 resonating in TM_{01} mode
L = 30mm, W = 20mm, a = 9mm, b = 9mm, w = 3mm, FL_1=0.541λ_d

The above highlighted characteristics of the antenna suggest the suitability of the geometry for use in single module supporting the GPS and Mobile frequency bands of operation.

5.5 Slot loaded Octagonal patch antenna

The geometry of the Octagonal microstrip patch antenna is perturbed, by incorporating narrow meandering slits of appropriate dimensions, to achieve compactness.

5.5.1 Effect of slot parameters

The location of the slot is chosen based on exhaustive computations. The effect of a single perturbation on the side 'L' of the antenna, as shown in figure 5.5.1.a is predominant on the TM_{10} mode of resonance than on TM_{01} mode of the geometry, as shown in figure 5.5.2.a. The antenna with single perturbation on the side 'W' of the patch, shown in figure 5.5.1.b, modifies the field distribution corresponding to TM_{01} mode of the geometry. Figure 5.5.2.b illustrates the variation in the resonance with respect to dimensions of the slot.
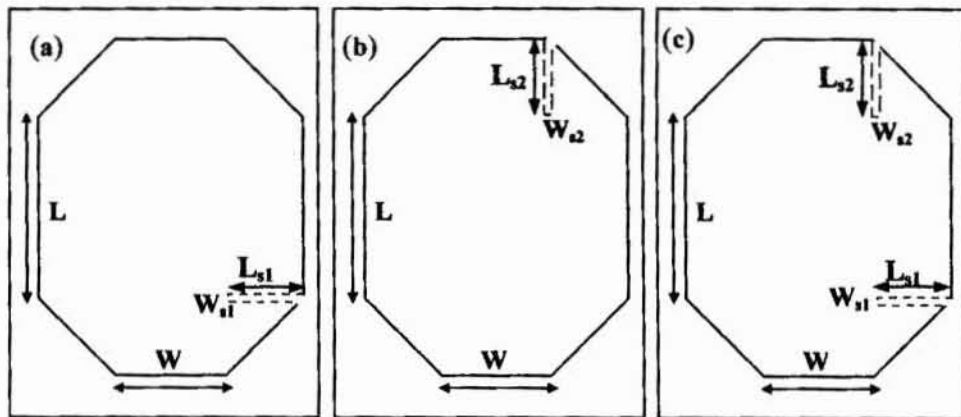
Figure 5.5.1 Top view of slot loaded Octagonal microstrip patch antenna
(a) slot on side L (b) slot on side W (c) slot on both L and W sides

The numerically computed resonant frequencies of an unperturbed Octagonal patch with dimensions L = 23.5mm, W = 9mm, a = 9mm, b = 9mm are 1.93GHz and 2.62GHz. Table 5.5.1 illustrates the computed variation in resonance frequencies of the two modes, when the patch is perturbed by narrow slots with lengths varying from 4mm to 18mm. These narrow slits increase the effective length of the resonant geometry. Figure 5.5.2.c

illustrates the variation in the return loss characteristics in the presence of both the slots. In the desired band of operation, the slot width shows a lesser influence on the resonant frequency in comparison with effect length of the slot. With slot1 of length 11mm and slot 2 of length 10mm, the computed resonance frequency of the patch lowered to 1.81GHz and 2.455GHz.

Slot 1 dimensions		Slot 2 dimensions		Resonant frequency	
Width W_{s1} (mm)	Length L_{s1} (mm)	Width W_{s2} (mm)	Length L_{s2} (mm)	Fr_{10} (GHz)	Fr_{01} (GHz)
1	4	No slot		1.9	2.65
	6			1.89	2.64
	8			1.88	2.63
	10			1.83	2.62
	11			1.81	2.61
	12			1.78	2.6
	14			1.71	2.58
	16			1.63	2.77
	18			1.53	2.73
No slot		1	4	1.91	2.63
			6	1.91	2.6
			8	1.91	2.54
			10	1.91	2.45
			11	1.91	2.37
			12	1.91	2.3
			14	1.89	2.16
			16	1.86	2.01
			17	1.83	1.97
			18	1.78	1.95
1	8	1	8	1.87	2.55
	11		10	1.81	2.455
	12		12	1.75	2.31

Table 5.5.1 Resonant frequency variation with respect to slot dimensions
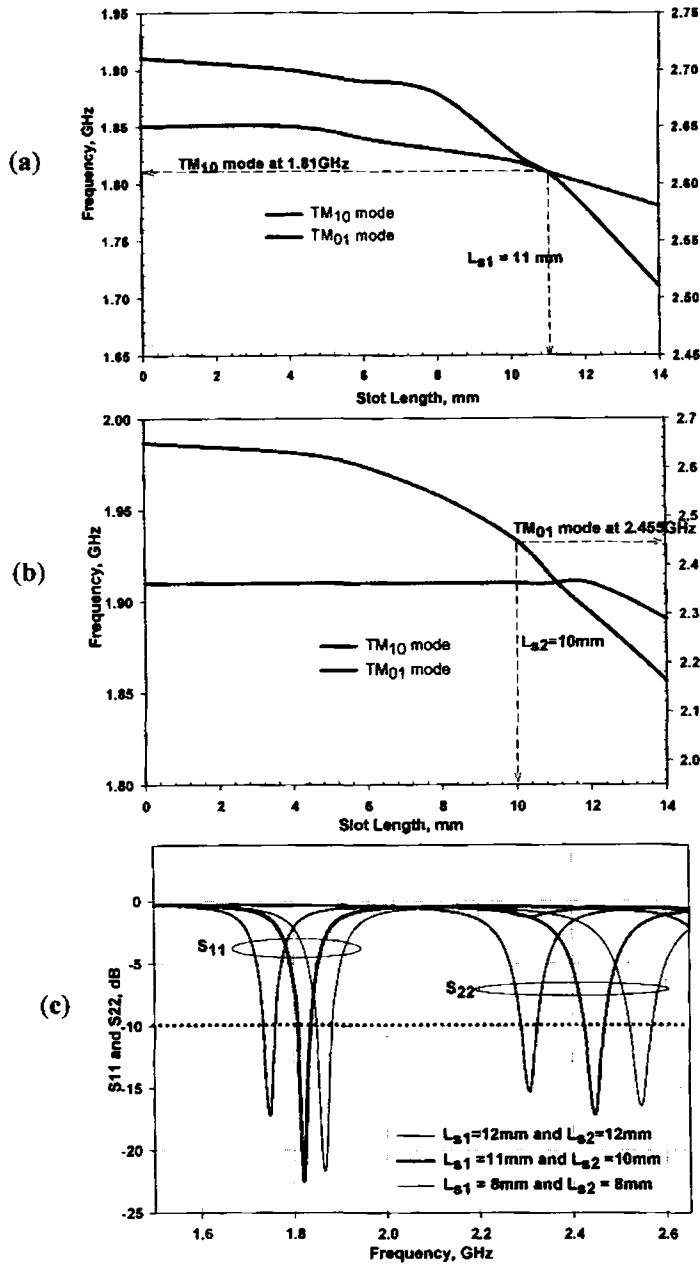
Figure 5.5.2 Computed variation in resonant frequency and Return Loss
with respect to slot dimensions
(a) Resonant frequency variation at either ports wrt varying Ls1
(b) Resonant frequency variation at either ports wrt varying Ls2
(c) Return Loss variation for different slot dimensions
$L = 23.5mm$, $W = 9mm$, $a = 9mm$, $b = 9mm$, $w = 3mm$, $FL_1 = 0.495\lambda_d$, $FL_2 = 0.502\lambda_d$,
$h = 1.6mm$, $\varepsilon_r = 4.28$

5.5.2   Compact slot loaded antenna for Mobile - Bluetooth application

Based on these numerical observations, perturbations of appropriate dimensions are introduced to both sides 'L' and 'W' as illustrated in figure 5.5.1.c, to achieve resonance at the desired frequencies. The resultant Octagonal patch offers area reduction with respect to the unloaded patch operating in the same band. The dimensions of the perturbed Dual port Dual band Octagonal MPA configuration suitable for the Mobile/Bluetooth application on FR4 substrate, obtained from numerical investigations is

Patch dimensions: $L = 23.5mm$, $W = 9mm$, $a = 9mm$, $b = 9mm$

Feed parameters: $w = 3mm$, $FL_1 = 0.495\lambda_d$, $FL_2 = 0.502\lambda_d$,

$\qquad\qquad\qquad$ $Fd_1 = 0.186\lambda_d$, $Fd_2 = 0.151\lambda_d$

The slot dimensions are $L_{s1} = 11mm$ and $L_{s2} = 10mm$. The perturbed antenna configuration with the two slots, is fabricated on FR4 substrate and verified experimentally. The antenna is energized electromagnetically using two orthogonal 50Ω microstrip feed lines with dimensions given above. Figure 5.5.3.a shows the computed, simulated and measured S parameters of the perturbed patch. The measured return loss characteristics of the perturbed patch is shown in comparison with normal patch with the above dimensions, in figure 5.5.3.b, illustrating the lowering of the resonance frequency due to the presence of the slot. At port 1 the measured resonance frequency lowered by 105MHz (*from 1.9 to 1.795*) whereas at port2 it shifted by 140MHz (*from 2.565 to 2.425*). The isolation between the two ports deteriorates when the slot length increases, as indicated in figure 5.5.3.c. For the optimum slot dimensions the computed isolation between ports is better than -20dB. The isolation measured between the ports for the optimum configuration is better than -23dB. At port 2 resonance frequency isolation between ports is low. The perturbed geometry offers an area reduction of ~15% with respect to the unperturbed Octagonal patch antenna operating in the same frequency bands.
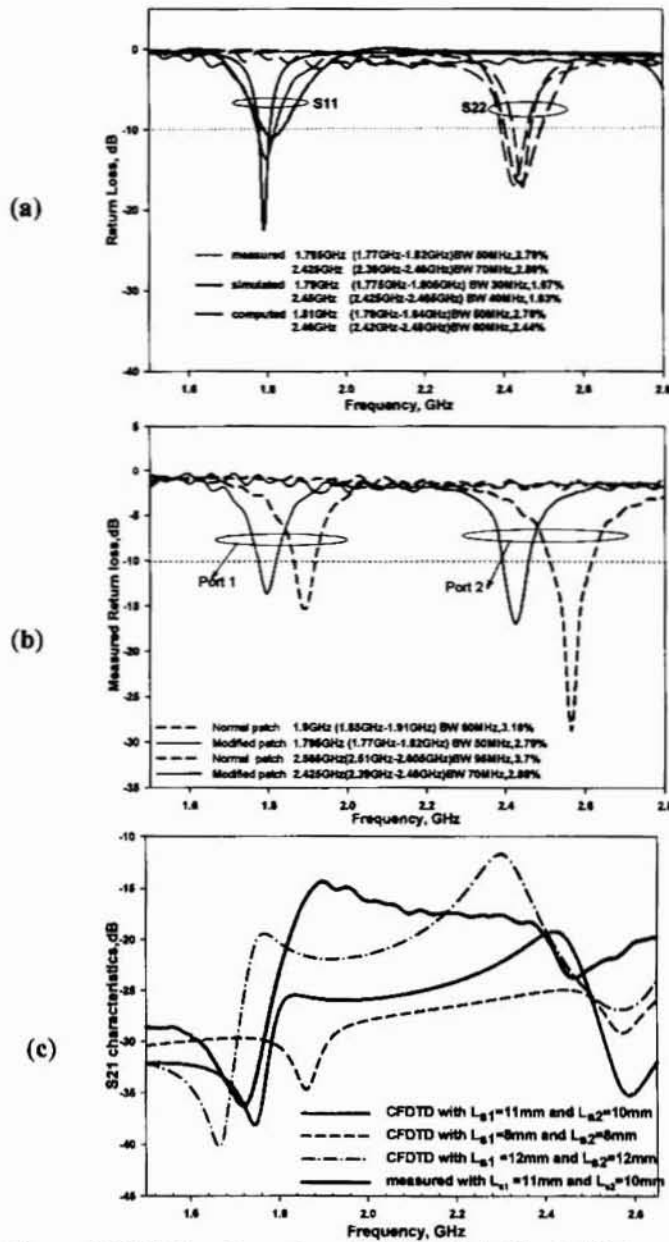
Figure 5.5.3 Return Loss characteristics of slot loaded Octagonal MPA
(a) Computed, Simulated and measured Return Loss at the ports of the antenna
(b) Comparison of the measured return loss of the normal patch and slot loaded patch
(c) S21 characteristics of the antenna
L = 23.5mm, W = 9mm, a = 9mm, b =9mm, w = 3mm, $FL_1 = 0.495\lambda_d$, $FL_2 = 0.502\lambda_d$,
h=1.6mm, ε_r=4.28

• Radiation characteristics at the two ports

Numerically computed resonance for port 1 is at 1.81GHz, with -10dB return loss band from 1.79GHz to 1.84GHz, exhibiting 50MHz bandwidth. Port 2 shows resonance at 2.46GHz, with a 60MHz band from 2.42GHz to 2.48GHz giving 2.44%BW. The measured resonance of the antenna for port 1 is at 1.795GHz, with the 2:1VSWR bandwidth of 50MHz, from 1.77GHz-1.82GHz, with a fractional bandwidth of 2.79%. Port 2 exhibits resonance at 2.425GHz, with the band from 2.39GHz to 2.46GHz offering 70MHz bandwidth and 2.89%BW. Simulated resonance for port 1 is at 1.79GHz, with the 2:1VSWR band from 1.775GHz to 1.805GHz, offering a fractional bandwidth of 1.68%. Port 2 of the geometry exhibits 1.63% bandwidth at 2.45GHz, with the 2:1 VSWR band of 2.425GHz-2.465GHz.
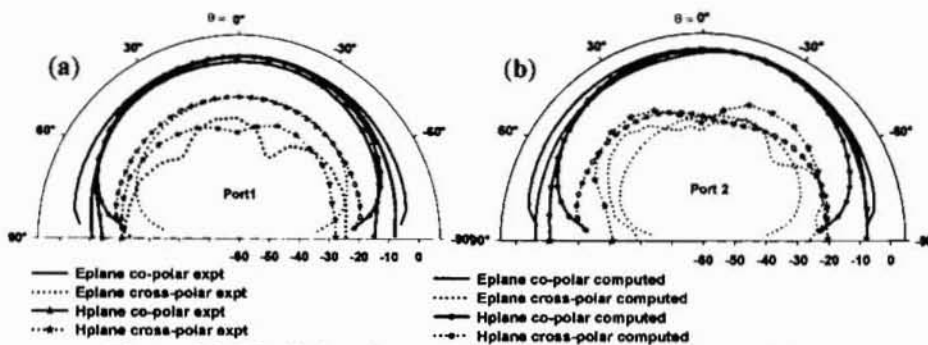
Figure 5.5.4 Radiation characteristics of slot loaded Octagonal MPA
(a)Port 1 patterns (b) Port 2 patterns
L = 23.5mm, W = 9mm, a = 9mm, b = 9mm, w = 3mm, FL_1 = 0.495λ_d, FL_2 = 0.502λ_d,
h=1.6mm, ε_r=4.28

The measured far field values indicate that radiation patterns of the perturbed geometry remain broadside, as shown in figure 5.5.4, but the cross polar level in the H plane increases slightly due to increased current in orthogonal directions *i.e.* perpendicular to side L and W for the two modes respectively. E plane pattern is broader than the H plane patterns and cross polar level in the H plane remains nearly same throughout the plane. The beam maxima is

in the bore sight direction port1 resonance whereas for port 2 resonance frequency the E plane and H plane patterns are tilted, by an angle of ~-10° and ~-14° respectively from the axis. The HPBW measured in the E plane and H plane at port 1 resonance are 95° and 90°. Cross polar level in the E plane is -22dB along the zenith and it is better than -20 dB over the entire plane. In the H plane cross polar level along the zenith is -23.7dB, while the minimum cross polar isolation of -14dB is at angle of +51°. At port 2, the patterns exhibit HPBW of 92° and 88° respectively, in the E and H planes. The corresponding cross polar levels along the broadside direction in the two planes are -24dB and -23dB respectively. In the E plane minimum cross polar isolation of -16dB is at elevation angle of +36° and for the H plane, minimum is -12dB at an angle of -34°. The on axis cross polar level at the two ports for the two operating bands is illustrated in figure 5.5.5.
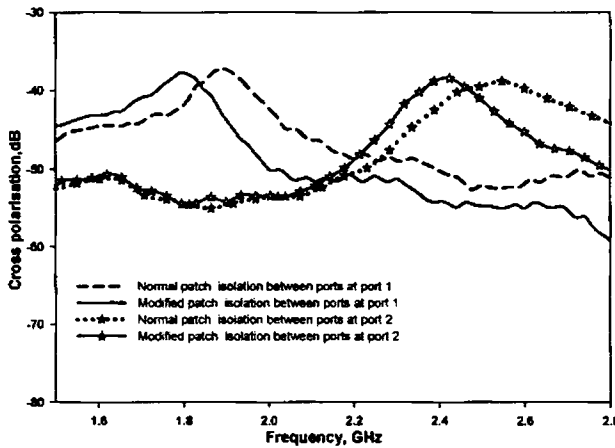
Figure 5.5.5 Cross polar level in the two operating bands of slot loaded Octagonal MPA
L = 23.5mm, W = 9mm,a = 9mm, b = 9mm, w = 3mm, FL$_1$ = 0.495λ_d ,FL$_2$ = 0.502λ_d,
h = 1.6mm, ε_r = 4.28

The simulated current density on the patch surface corresponding to the two resonant frequencies is illustrated in figure 5.5.6. It shows the meandering of the current along slot edges. The current density in slot one region dominate at lower resonance frequency while that at other slot dominate at the higher resonance, for the optimized slot position and dimensions. The modified antenna offers linear orthogonal polarization at the two ports. The plane of

polarization of the lower resonance mode of the antenna is along the longer
dimension, L of the geometry while, that of the higher resonance frequency
is along the dimension, W.
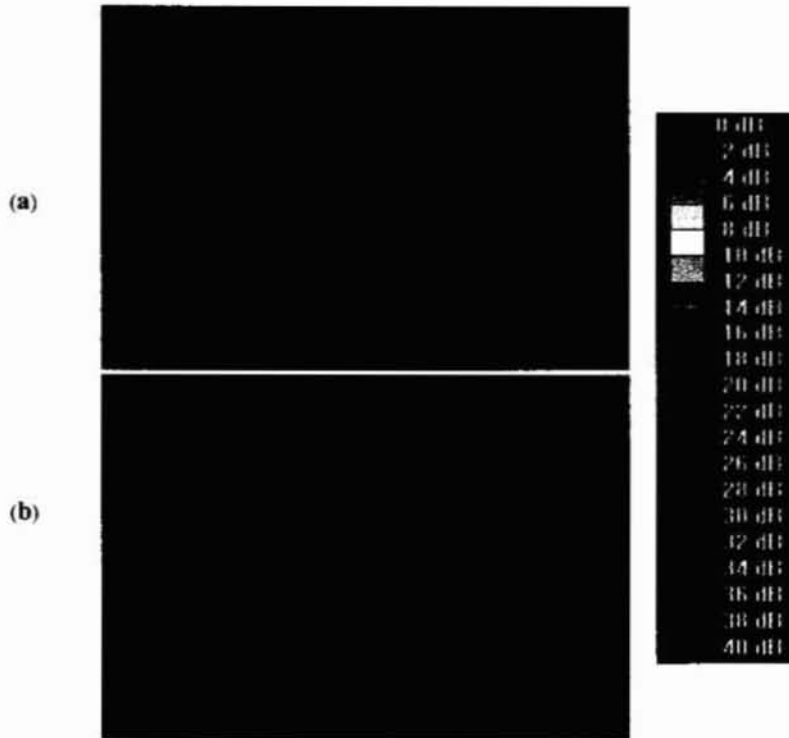
Figure 5.5.6 Current density on the surface of slot loaded Octagonal MPA
(a)Distribution at 1.79GHz (b)Distribution at 2.45GHz
L = 23.5mm, W = 9mm,a = 9mm, b = 9mm, w = 3mm, FL_1 = 0.495λ_d ,FL_2 = 0.502λ_d,
h = 1.6mm, ε_r = 4.28

The predicted and measured characteristics of the octagonal patch
antenna, with two narrow slots on the L and W sides of the geometry,
indicate the suitability of the configuration for Mobile-Bluetooth
applications. The area reduction offered by the presence of the slot is
advantageous since the physical area is a major design constraint. The
measured far field characteristics of the antenna show that the presence of
slots does not perturb the patterns much. Patterns are relatively broad and the
antenna offers broadside radiation. Filter circuitry may be incorporated in the
feed line of port 2 to improve the overall isolation between the ports.

5.6 Design formula for Octagonal patch antenna

The empirical formula for the design of Octagonal patch is developed by suitably modifying the standard equations available for a circular patch. Transmission line model, Cavity model and Full wave techniques are commonly employed for the analysis of microstrip patch antennas. Cavity model is relatively complex but widely accepted as an accurate and fast method to estimate the characteristics of patch geometries. In this approach the microstrip patch antenna is assumed to resemble a dielectric loaded cavity bounded by electric conductors on the top and bottom and by magnetic walls, simulating the open circuit condition, along the periphery of the patch. The dielectric material of the substrate is assumed to be isotropic and truncated and that it does not cover the ground plane beyond the patch edges. Another major assumption is that ground plane infinite. The presence of a dielectric covered ground plane modifies the reflection coefficient to some extent. A major draw back of the approach is its inability to model the feed structure.
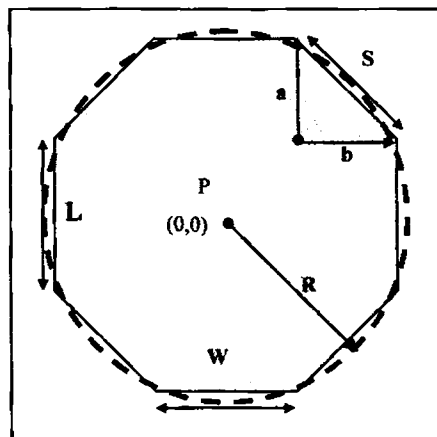
Figure 5.6.1 The Octagonal microstrip patch antenna superimposed
with the equivalent circle

There are several substrates having dielectric constant in the range $2.2 \leq \varepsilon_r \leq 12$, which can be used for the design of microstrip antennas. Though the microstrip antenna performs best on thicker substrates with low

dielectric constant, a compromise is reached considering the circuit integration factor.

In the development of a simple empirical relation, the geometry of the Octagonal microstrip patch antenna is approximated to that of an equivalent circular geometry as depicted in figure 5.6.1. The homogenous wave equation based on the vector magnetic potential A for the fields within the cavity is

$$\nabla^2 A + k^2 A = 0 \tag{5.6.1}$$

In cylindrical coordinates, the solution for the E_z field derived from the potential A based on m[th] order Bessel function of first kind (J_m) is

$$E_z = E_0 J_m(k_\rho \rho)\cos(m\varphi) \tag{5.6.2}$$

with the wave numbers subject to the constraint

$$k_\rho^2 + k_z^2 = \omega_r^2 \mu\varepsilon \tag{5.6.3}$$

On applying appropriate boundary conditions, for each mode configuration, a typical radius 'r' exists that gives resonance corresponding to zeros of the derivative of the Bessel function so that

$$k_\rho = \frac{X'_{mn}}{r} \text{ and } k_z = \frac{p\pi}{h} \tag{5.6.4}$$

where X'_{mn} represents the zeros of the derivative of the Bessel function $J_m(x)$, 'r' the radius of the cavity and 'h' the thickness of the dielectric substrate. The indices '$m\ n\ p$' are given as

m = 0,1,2,....

n = 1,2,3,.....

p = 0,1,2,.....

These indices are used to represent the modes within the cavity and p=0 for typical microstrip antenna substrates with h<< λ_o. The resonant frequency for the TM_{mn0} modes of a circular patch is thus computed from equations 5.6.3 and 5.6.4 as

$$(f_r)_{mn0} = \frac{1}{2\pi\sqrt{\mu\varepsilon}}(\frac{X'_{mn}}{r})$$

(5.6.5)

Since *field fringing* at the open ends of the patch make the geometry electrically larger, correction is introduced by incorporating *effective radius* 'r_{eff}' for circular patch as

$$r_{eff} = r\sqrt{\left\{1 + \frac{2h}{\pi\alpha\varepsilon_r}\left[\ln\left(\frac{\pi r}{2h}\right) + 1.7726\right]\right\}}$$

(5.6.6)

• Resonant frequency computation of Octagonal patch geometry

For an Octagonal patch with dimension α, (α=L=W=a=b) the resonant frequency is calculated, with the r_{eff} modified to suit the Octagon dimensions. Referring to figure 5.6.1, the Octagonal MPA geometry is superimposed by an equivalent circle with radius r,determined empirically as

$$r = 1.51\alpha + 0.48h$$

(5.6.7)

r_{eff} is then computed using eqn. 5.6.6. The resonance frequency of the Octagonal patch is then given by

$$f_r = \frac{1.841c}{2\pi r_{eff}\sqrt{\varepsilon_r}}$$

(5.6.8)

where c is the velocity of light in free space. The 'h' factor in eqn 5.6.7 obtained empirically accounts for *the increase in the spread of fringing field due to electromagnetic coupling employed in the study*. The above illustrated empirical relation is used iteratively to initially estimate the dimension α of the Octagonal patch for a typical resonance frequency, which is then, verified numerically using the CFDTD tool and finally established experimentally.

The table 5.6.1.a shows the comparison of resonant frequency estimated using the above relation for Octagonal geometry of different dimensions with measured results for antennas fabricated on FR4 substrate with ε_r=4.28, h=1.6mm. Table 5.6.1.b illustrates the comparison of

measured, empirical and CFDTD computed results.

Antenna dimension α (mm)	Resonant Frequency (GHz)		
	Measured	As per eqn 5.6.8	Fractional error
6	4.12	4.1261	-0.148
8	3.198	3.1825	0.485
10	2.59	2.5913	-0.05
12	2.19	2.1858	0.192
14	1.92	1.8903	1.547
16	1.675	1.6654	0.573
18	1.51	1.4884	1.43
20	1.355	1.3455	0.701
22	1.245	1.2276	1.398
24	1.135	1.1288	0.546
26	1.055	1.0447	0.976
28	0.985	0.97229	1.29
30	0.915	0.90928	0.625
32	0.865	0.85395	1.277
34	0.812	0.80497	0.866
36	0.772	0.76131	1.385
38	0.728	0.72215	0.804
40	0.6933	0.68683	0.933

Table 5.6.1.a Variation of resonant frequency for different values of ' α ' for the Octagonal MPA on FR4 (h =1.6mm, ε_r=4.28)

Antenna dimension α (mm)	Resonant Frequency (GHz)			Fractional error between measured and numerical results
	As per eqn. 5.6.8	Measured	CFDTD computed	
6	4.1261	4.12	4.21	-2.184
10	2.5913	2.59	2.5917	-0.066
16	1.6654	1.675	1.7066	-1.887
20	1.3455	1.355	1.38	-1.845
24	1.1288	1.135	1.1544	-1.709
30	0.90928	0.915	0.9019	1.432
36	0.76131	0.772	0.7752	-0.415
40	0.68683	0.6933	0.7011	-1.125

Table 5.6.1.b Variation of resonant frequency for different values of ' α ' for the Octagonal MPA on FR4 substrate (h =1.6mm, ε_r=4.28)

Figure 5.6.2 shows the variation of resonance frequency, for different values of the dimension α, estimated empirically, computed numerically by CFDTD and measured experimentally. It is observed that the fractional error in both predictions with respect experimental observations lies within ±2% validating the approaches. The mean error between the measured and empirically computed values is +0.824%.
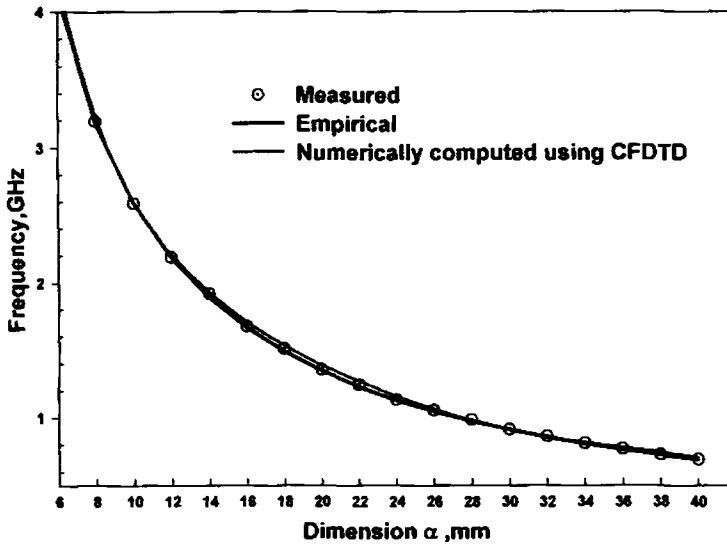
Figure 5.6.2 Variation of resonant frequency with respect to the dimension α
of the Octagonal patch antenna (h=1.6mm,ε_r=4.28)

Figure 5.6.3.a compares the resonance frequency for a typical patch (α = 10) predicted empirically and computed numerically with the measured value. Numerically computed resonance for the geometry is at 2.5917GHz, with -10dB return loss band from 2.5165GHz to 2.6553GHz, exhibiting 139MHz bandwidth. The measured resonance of the antenna is at 2.59GHz, with the 2:1VSWR bandwidth of 93MHz, from 2.536GHz-2.629GHz, with the fractional bandwidth corresponding to 3.59%. The mean feed patch overlap distance is 0.0983λ_d. Simulated resonance is at 2.585GHz, with the 2:1VSWR band from 2.56GHz to 2.63GHz, offering a fractional bandwidth of 2.71%. Measured variation in return loss with feed length is illustrated in figure 5.6.3.b. Variation in the resonance frequency and fractional bandwidth with respect to feed length is shown in Figure 5.6.3.c.
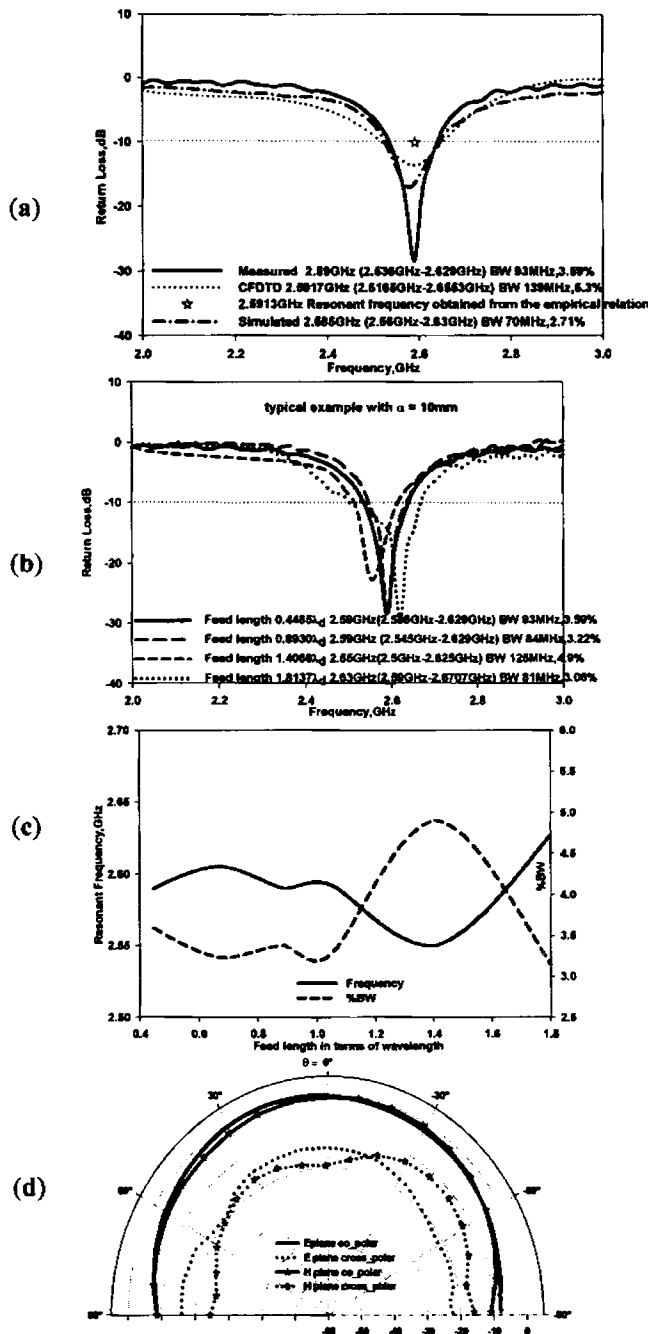
Figure 5.6.3 Characteristics of a typical Octagonal patch studied empirically and verified numerically and experimentally (h=1.6mm,ε_r=4.28,α = 10mm) (a)Return loss characteristics of a typical patch with α =10mm(b)Effect of feed length on the reflection characteristics for the typical patch(c)Variation in resonance frequency and %BW wrt to feed length(d)E plane and H plane patterns of the antenna

Measured radiation patterns in the E and H planes of the geometry

is shown in figure 5.6.3.d. Patterns are broad and the cross polar level in both the planes is relatively high. Table 5.6.2 presents simulated and experimentally computed results obtained for Octagonal patch antennas fabricated on laminates of different permittivity and thickness. In all cases the maximum % error is within ±2%. Figure 5.6.4.a-i illustrates empirically predicted, and simulated results exhibiting variation of resonant frequency of the Octagonal patch with respect to the dimension for various laminates.

Substrate parameters $\varepsilon_r = 2.2$	Antenna dimension α, mm	Resonant Frequency (GHz)		Fract-ional error (%)	Variation in resonant frequency (IE3D and empirical)
		IE3D	Empi-rical		
h = 0.254 mm	6	6.36	6.3092	0.799	
	8	4.795	4.7701	0.519	
	10	3.86	3.8352	0.632	
	12	3.23	3.207	0.712	
	16	2.435	2.4159	0.784	
	20	1.955	1.9381	0.864	
	24	1.63	1.6181	0.73	
	28	1.4	1.3888	0.8	
	32	1.225	1.2165	0.694	
	36	1.095	1.0822	1.169	
	40	0.99	0.97465	1.551	Figure 5.6.4.a
h = 0.508 mm	6	6.16	6.1262	0.549	
	8	4.68	4.6607	0.412	
	10	3.78	3.7622	0.471	
	12	3.18	3.1546	0.799	
	16	2.4	2.385	0.625	
	20	1.928	1.9176	0.539	
	24	1.615	1.6035	0.712	
	28	1.39	1.3779	0.871	
	32	1.21	1.208	0.165	
	36	1.085	1.0754	0.885	
	40	0.975	0.96904	0.611	Figure 5.6.4.b
h = 1.6mm	6	5.5	5.527	-0.491	
	8	4.28	4.2916	-0.271	
	10	3.5	3.5105	-0.3	
	12	2.98	2.9714	0.289	
	16	2.28	2.2747	0.232	
	20	1.84	1.8435	-0.19	
	24	1.56	1.5502	0.628	
	28	1.34	1.3376	0.179	
	32	1.18	1.1764	0.305	
	36	1.05	1.0499	0.01	
	40	0.95	0.94803	0.207	Figure 5.6.4.c

Table 5.6.2.a Variation of resonant frequency for different values of ' α ' for the Octagonal MPA on a substrate of ε_r =2.2

Substrate parameters ε_r _4.4	Antenna dimension α, mm	Resonant Frequency (GHz)		Fractional error (%)	Variation in resonant frequency (IE3D and empirical)
		IE3D	Empi-rical		
h = 0.762 mm	6	4.37	4.3275	0.973	
	8	3.33	3.2946	1.063	
	10	2.68	2.6604	0.731	
	12	2.256	2.2312	1.099	
	16	1.705	1.6872	1.044	
	20	1.38	1.3566	1.696	
	24	1.14	1.1344	0.491	
	28	0.985	0.97479	1.037	
	32	0.865	0.85458	1.205	
	36	0.77	0.76077	1.199	
	40	0.695	0.68553	1.363	**Figure 5.6.4.d**
h = 1.524 mm	6	4.08	4.0955	-0.38	
	8	3.16	3.1549	0.161	
	10	2.57	2.5666	0.132	
	12	2.18	2.1637	0.748	
	16	1.66	1.6473	0.765	
	20	1.34	1.3302	0.731	
	24	1.13	1.1156	1.274	
	28	0.97	0.96067	0.962	
	32	0.85	0.84358	0.755	
	36	0.76	0.75195	1.059	
	40	0.685	0.6783	0.978	**Figure 5.6.4.e**

Table 5.6.2.b Variation of resonant frequency for different values of ' α ' for the Octagonal MPA on a substrate of ε_r =4.4

Substrate parameters $\varepsilon_r = 9.8$	Antenna dimension α, mm	Resonant Frequency (GHz)		Fractional error (%)	Variation in resonant frequency (IE3D and empirical)
		IE3D	Empirical		
h = 0.254 mm	6	3.1	3.0422	1.865	
	8	2.33	2.2918	1.639	
	10	1.87	1.8384	1.69	
	12	1.56	1.5348	1.615	
	16	1.175	1.1537	1.813	
	20	0.94	0.92427	1.673	
	24	0.77	0.77095	-0.123	
	28	0.67	0.66127	1.303	
	32	0.59	0.57891	1.88	
	36	0.525	0.51479	1.945	
	40	0.472	0.46346	1.809	Figure 5.6.4.f
h = 0.635 mm	6	3.025	2.9664	1.937	
	8	2.29	2.2479	1.838	
	10	1.845	1.8097	1.913	
	12	1.54	1.5145	1.656	
	16	1.16	1.1421	1.543	
	20	0.935	0.91671	1.956	
	24	0.78	0.76564	1.841	
	28	0.67	0.65732	1.893	
	32	0.585	0.57586	1.562	
	36	0.52	0.51237	1.467	
	40	0.47	0.46149	1.811	Figure 5.6.4.g

Table 5.6.2.c Variation of resonant frequency for different values of ' α ' for the Octagonal MPA on a substrate of ε_r =9.8

Substrate parameters $\varepsilon_r = 10.2$	Antenna dimension α, mm	Resonant Frequency (GHz)		Fract-ional error (%)	Variation in resonant frequency (IE3D and empirical)
		IE3D	Empirical		
h = 0.254 mm	6	3.04	2.9826	1.888	
	8	2.28	2.2467	1.461	
	10	1.83	1.8022	1.519	
	12	1.53	1.5045	1.667	
	16	1.15	1.131	1.652	
	20	0.92	0.90603	1.518	
	24	0.766	0.75573	1.341	
	28	0.661	0.64821	1.935	
	32	0.575	0.56747	1.31	
	36	0.5135	0.50462	1.729	
	40	0.463	0.4543	1.879	Figure 5.6.4.h
h = 0.635 mm	6	2.965	2.9089	1.892	
	8	2.245	2.2041	1.822	
	10	1.81	1.7743	1.972	
	12	1.508	1.4849	1.532	
	16	1.14	1.1197	1.781	
	20	0.914	0.8987	1.674	
	24	0.76	0.75058	1.239	
	28	0.655	0.64438	1.621	
	32	0.574	0.56452	1.652	
	36	0.51	0.50227	1.516	
	40	0.4592	0.45239	1.483	Figure 5.6.4.i

Table 5.6.2.d Variation of resonant frequency for different values of ' α ' for the Octagonal MPA on a substrate of ε_r =10.2

Chapter Six

CONCLUSIONS

The conclusions drawn from the numerical and experimental investigations carried out on Octagonal microstrip patch antenna configurations are presented in this chapter. The salient features of the geometry are examined. Suggestions for future work in the field are also provided.

6.1 Thesis Highlights

This chapter brings the thesis to a close by presenting the conclusions drawn from the outcome of the Numerical and Experimental investigations of the radiation characteristics of the Octagonal microstrip patch antenna. Chapter one introduced the topic of research. Characteristic features of microstrip antennas and various feed techniques were also outlined followed by a brief description of various methods of computational electromagnetics for numerical analysis of antennas. Relevant work in related areas was discussed in Chapter two. Chapter three described the experimental setup and measurement methodology. The fundamentals of the Conformal FDTD method and its adaptation to the problem were discussed in Chapter four. The essence of the thesis is Chapter five. This chapter presented the outcome of the Numerical investigations and Experimental Observations. Octagonal microstrip patch antenna configurations suitable for Mobile-Bluetooth dual band communication applications were proposed. Appendix A of the thesis presents a compact planar multiband antenna for GPS,DCS,2.4/5.8GHz WLAN applications. A fully automated near field measurement set up driven by an indigenously developed user friendly MATLAB™ GUIDE based controlling and communication software is presented as Appendix B.

6.2 Inferences from Numerical Computation using FDTD method

The FDTD method models the propagation through the elements of the computational domain using the discrete form of Maxwell's equations. In the thesis the FDTD method is employed for the numerical computation of the radiation characteristics of the Octagonal microstrip patch antenna. Chapter four describes the 3D-FDTD modeller for the antenna configuration. The use of a Gaussian pulse excitation enables characterization of the model

over a broad frequency band. The input impedance (Zin) is calculated from the ratio of the FFT of the voltage derived from the E field values over the entire time steps to the FFT of the current derived from the H field values. The conformal FDTD based update equations are employed for modeling the slant edge of the geometry. The experimentally plotted return loss characteristics are akin to the numerically predicted figures as illustrated in section 5.3.1-2. The measured far field radiation patterns compare well against those computed from the tangential field components defined in an aperture in the near field. This is illustrated by the figures in section 5.3.3. Uniform gridding has been employed while modelling. The use of non-uniform gridding could improve the results further. However this calls for more complex modelling techniques. The CFDTD method is thus found to be a viable alternative to the conventional theoretical modelling techniques. This is also an efficient computational tool in visualizing the EM field distribution in and around the geometry. Resonant modes of the rectangular patch visualised using the FDTD based computation and illustrated in section 5.3.4 serves as the reference in identifying the modes of the geometry under investigation. The resonant frequency predicted using the CFDTD approach also matches reasonably well with the results from the design equations put forth in section 5.6.

6.3 Inferences from Experimental Observations

Measurements performed using HP 8510C Vector Network Analyzer validate the computed results. A comprehensive summary of the exhaustive investigations conducted on antenna feed configuration, feed position, feed length, patch dimensions and feed patch overlap distance is presented in sections 5.1-2. Microstrip feed lines varying in length from $0.3\lambda_d$ to $1.2 \lambda_d$ have been used for the study. The influence of the feed line length on the antenna properties was further confirmed by placing the antenna symmetrically to the feed line as described in section 5.3.2 and 5.3.3.

The patterns and gain are found to be nearly same. Nevertheless, an increase in feed length also results in an increase in the overall size of the antenna configuration.

Section 5.1.1 presented the results of the study performed on coaxial fed Octagonal microstrip patch antenna designed to operate in the Mobile-Bluetooth frequency bands. The characteristics of the antenna fabricated on two different substrates are presented in table 5.1.3. Though the coaxial feed excited both resonances at an optimum position, the bandwidth exhibited is of the order of 1-2% and hence this feed may not be much sought after. The single feed electromagnetically excited configuration is discussed in section 5.1.2. The influence of feed patch overlap distance upon excited frequencies is carefully observed for the laterally offset feed and corner fed configurations. In both cases, dual frequency excitation for an optimum position displayed reasonable bandwidth characteristics. However, the isolation performance between the two resonant modes is not appreciable (around -10dB), as indicated in figure 5.1.13.a and figure 5.1.16. Thus, the interest narrows down to the electromagnetically excited dual port dual feed configuration presented in section 5.2. In this configuration the resonant behaviour is somewhat similar to that of single feed electromagnetically excited case, but for the improvement in isolation characteristics as evident from figures 5.2.8,5.2.9,5.3.2,5.3.6,5.4.1 and 5.4.3. Table 5.2.4 summarises the influence of dimension variations on the antenna resonance. Based on the study performed on the effect of antenna dimensions on the resonant frequencies, Octagon dimensions suited for Mobile-Bluetooth dual band applications is identified and verified experimentally as L = 24.5mm, W = 9.5mm, a = 10mm, b =10mm with feed dimensions w = 3mm, FL_1= $0.31\lambda_d$ and FL_2=$0.42\lambda_d$. Antenna and feed laminate is FR4 with h = 1.6mm, ε_r = 4.28. The radiation characteristics of the configuration are discussed in detail in the subsections of section 5.3. The isolation offered is found to be better than -35dB and the optimum feed dimensions provide good bandwidth

behaviour. The patch was positioned at regular intervals symmetrically along the feed line and also laterally, to ascertain the importance of the relative position of feed and patch in exciting the dual frequencies. The return loss characteristics showed significant variation as illustrated in section 5.1.2 and 5.2.2. The dimensions predicted for GML 2032 laminate is also experimentally verified as shown in figure 5.3.20. Table 5.3.7 summarises the suitable dimensions of antenna on other laminates for the Mobile-Bluetooth application. Section 5.4 discusses the numerically predicted and experimentally obtained results for the configuration suited for GPS-Mobile dual band applications.

The electromagnetically coupled dual port-dual band Octagonal MPA configuration offers size reduction in comparison to a conventional circular and rectangular patch antennas operating in the same frequency bands. The additional frequency tuning offered by the slant dimension S of the octagonal geometry is an added attraction. Beam shaping may be achieved by varying the 'a/b' ratio of the slant dimension, without introducing much variation in the resonant behaviour of the geometry. Broad radiation patterns ensure the suitability of the configuration in a mobile gadget. Gain offered is better than that of the conventional patches. By introducing suitable feed alterations bandwidth enhancement can also be achieved. The polarization of both the excited modes is linear as indicated by the polarization patterns of figures 5.3.13-14. TM_{10} mode is linearly polarized along the direction tangential to L and TM_{01} mode is linearly polarized tangential to W. This suggests that array configurations may be easily realized for circular and/or elliptical polarisation by proper feed design. By incorporating the slot in the patch as discussed in section 5.5 further size reduction may be achieved. The simple design equation presented in section 5.6 predicts the resonant frequency of the patch within ±2%.

6.4 Salient features of the Electromagnetically excited dual band Octagonal patch antenna

The Electromagnetically excited Octagonal microstrip patch antenna investigated in this thesis is a suitable candidate for integrated mobile communication gadgets. The antenna offers a size reduction in comparison to conventional Rectangular and Circular Microstrip patch antennas without causing deterioration of the radiation properties. Moderate bandwidth, gain and broad radiation patterns are the salient features of this antenna. The simple geometry and ease of excitation are added attractions. Resonant frequency in the desired band may be obtained by choosing suitable material parameters and dimensions of the geometry with the slant dimension offering additional degree of freedom in determining the resonant frequency and beam shaping.

6.5 Suggestions for future work

The outcome of FDTD based studies show reasonable agreement with experimental observations. The discrepancies especially in bandwidth and magnitude of S parameters are presumably due to the simplifying approximations, truncation errors and round off errors in the numerical model. Future numerical and experimental investigations that may be sought after in continuation with the present work are cited below.

- The replacement of first order Mur ABC with second order ABC or Berenger's PML boundary conditions could be looked into.

- Finer grids may be employed to support high permittivity laminates.

- New feed models that best suit the electromagnetic coupling arrangement may be tried out instead of the resistive voltage gap feed model employed here.

- Algorithm for pattern computation may be modified further to include gain and directivity calculations.

- Bandwidth enhancement techniques may be looked into to realize a multiband or ultra wide band designs that suits the various mobile communication standards and WLAN standards while retaining the good gain and beam width. The Coplanar waveguide feed and monopole excited patch are possible alternatives in this direction, in addition to normal stub matching approaches.

- The feed layer modifications that allows *switching* between different polarizations (LP, RHCP, LHCP and elliptical) is another aspect that may be looked into.

- Radiation pattern beam shaping with minimum radiation directed towards the user, while retaining the nearly omni directional nature needed for WLAN applications is highly desirable.

Compact planar multiband antenna for GPS,DCS,2.4/5.8GHzWLAN applications

A compact single feed multiband planar antenna configuration suitable for GPS, DCS, 2.4/5.8GHz WLAN applications is presented. The antenna of dimensions 38mm x 3mm x 1.6mm offers good radiation and reflection characteristics in the desired frequency bands. The antenna has a simple geometry and can be easily fed using a 50Ω coaxial probe.

A.1 Introduction

The rapid progress in personal and computer communication technologies demand integration of more than one communication systems into a single compact module. To comply with the above requirements compact high performance multiband planar antennas with good radiation characteristics are needed. A planar single feed dual L antenna of dimensions 30.5mm x 21.5mm x 13mm operating in GPS and PCS bands is proposed in [1]. The dual band antenna for the ISM band (2.4/5.8GHz) using a backed microstrip line proposed in [2] has an overall dimension of 30 x 20 mm^2 on FR4 substrate and offers a maximum gain of 4dBi. Dual frequency antenna configuration proposed in [3] uses triple stacked microstrip patch antennas with a slot in the middle patch, to achieve triple band operation. A compact single feed planar antenna with three wide 2:1 VSWR operating bands around 1.8GHz, 2.4GHz and 5.8GHz respectively, covering four useful frequency bands namely GPS (1575.4MHz), DCS (1800MHz), 2.4GHz (2400-2484) and 5.8GHz (5725-5825) WLAN is presented.

A.2   Antenna design

The geometry of the proposed antenna is shown in figure A.1. It is etched on FR4 substrate of relative permittivity, ε_r = 4.7 and thickness h = 1.6mm. The antenna has two arms of lengths l1 = 38mm, l2 = 33mm and widths w1 = w2 = 1mm placed symmetrically on either side of a middle element of length l3 = 17mm, and width w3 = 1mm. The feed point of the antenna is experimentally optimized to be at the middle of edge AB. Good impedance matching is achieved by embedding a reflector of dimensions L = 40mm and W = 25mm on the bottom side of the substrate at an offset d = 0.5mm from the edge AB as shown in figure A.1.

From the experimental and simulation results it is understood that the lower resonant mode can be tuned by varying the length l1 of arm 1. Resonance in the 2.4GHz band is influenced by the length l1 + l2 - 2 l3. When

---

length l3 of the middle element is increased, the second resonance shifts upwards whereas, it gets lowered when the length l2 is increased. Dimensions of the reflector affect both the resonance frequency and impedance matching in the 5.8GHz band. For l1=79.4mm,l2=77.48mm and l3=60.54mm, the resonance is achieved at 940MHz,1850MHz and 5.2GHz respectively suitable for GSM/DCS/5.2GHz WLAN applications.
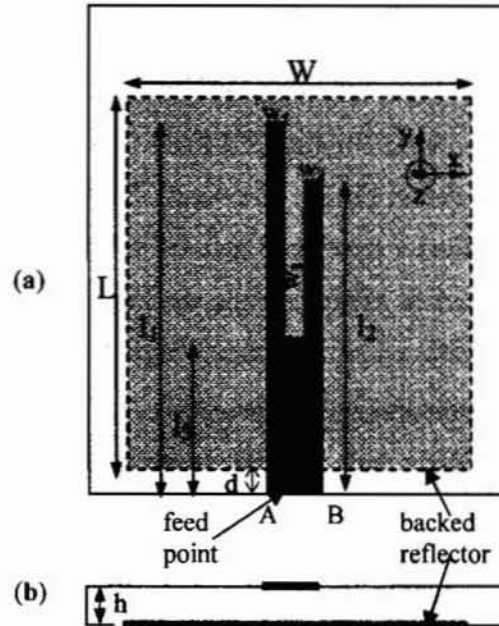
Figure A.1 Geometry of the compact planar multiband antenna
(a) Top view (b) Side view
L=40mm,l₁=38mm,l₂=33m,l₃=17mm,W=25mm,w₁=w₂=w₃=1mm,d=0.5mm

A.3   Results

The measured return loss characteristic of the proposed antenna is shown in figure A.2. Three resonant modes are observed at frequencies 1.75 GHz, 2.45 GHz and 5.76 GHz with 2:1 VSWR bandwidths of 23%, 5% and 4.5% respectively. The lower resonant mode with 406MHz (1466MHz-1872MHz) bandwidth is wide enough to cover the GPS/DCS bands. The upper resonant modes with 124 MHz (2372-2496) and 260 MHz (5630-5890) bandwidths cover the 2.4 GHz and 5.8 GHz WLAN bands respectively.
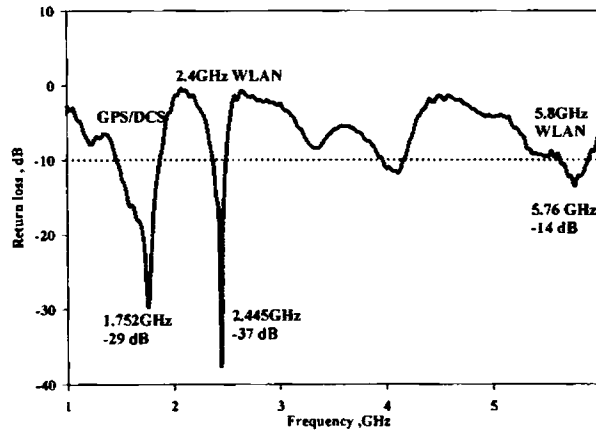
Figure A.2 Return Loss characteristics of the compact planar antenna
L=40 mm, l₁=38mm, l₂=33mm, l₃=17mm, W=25 mm, w₁= w₂=w₃=1mm, d=0.5mm
h=1.6 mm, εᵣ=4.7

The normalized E-plane and H-plane radiation patterns measured at the centre frequencies of the respective bands are shown in figure A.3. The patterns are observed to be omni directional in the H-plane, with a cross polar level better than -15 dB in the broad side direction. The antenna exhibits similar radiation characteristics in all the desired bands. The measured antenna gain against frequency is presented in figure A.4. The antenna offers a peak gain of 7 dBi in the GPS band. The maximum gain observed in the DCS, 2.4GHz WLAN, 5.8 GHz WLAN bands are 3.8dBi, 4.2dBi and 4.5dBi respectively.

The radiation performance of the antenna in all the above bands is summarized in table A.1. It is observed that all bands except the 5.8GHz band are linearly polarized along Y direction. The 5.8GHz band is orthogonal to the other bands.

A.4 Conclusions

A compact multiband planar antenna with reflector backing suitable for GPS/DCS/2.4GHz N/5.8GHz WLAN applications is presented. The wide 2:1 VSWR bandwidths at the three resonant modes along with moderate gain and radiation characteristics make the proposed antenna an ideal choice for multiband wireless communication gadgets.
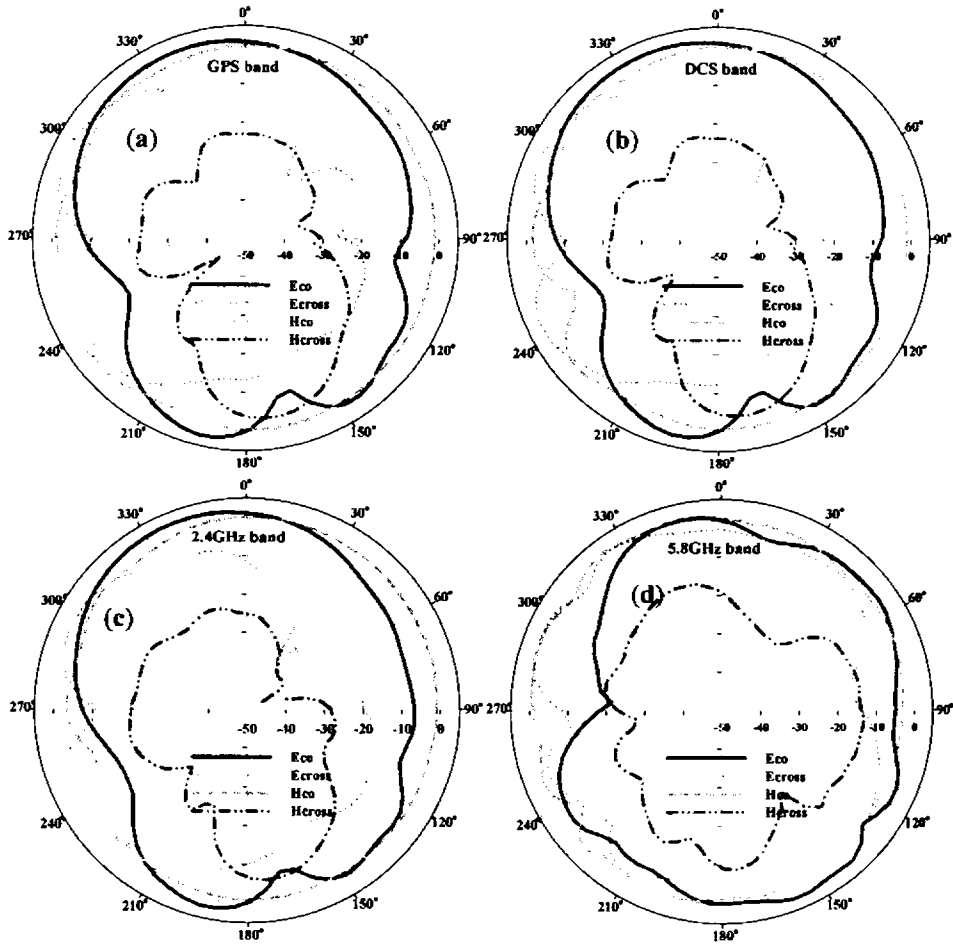
Figure A.3 Radiation patterns of the antenna in the four application bands.
(a) GPS band (b) DCS band (c)2.4GHz band (d)5.8GHz band
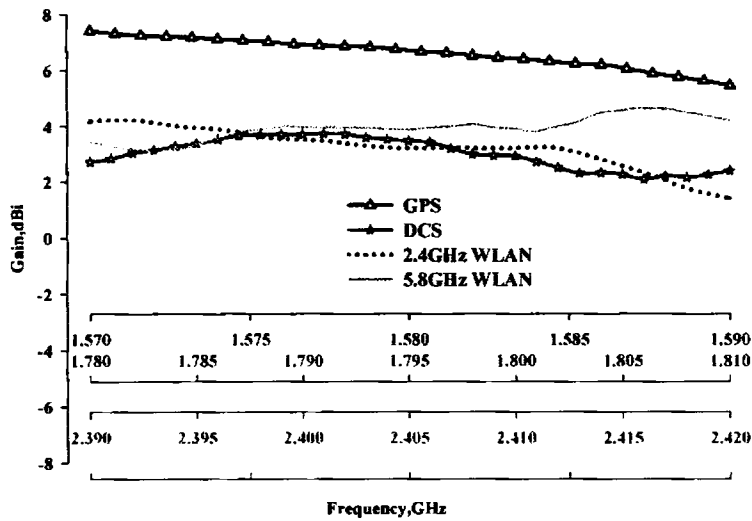
Figure A.4 Reflection characteristics of the antenna
L=40 mm, l_1=38mm, l_2=33mm, l_3=17mm, W=25 mm, w_1= w_2=w_3=1mm, d=0.5mm

Band and Application	Peak Gain (dBi)	Polarisation	Cross Polar level (dB)	Radiation pattern	
				H-plane	E-plane
1.46GHz-1.89GHz **GPSand DCS**	7.0	Linear along Y direction	-23	Omni directional	HPBW=90⁰ at 1.75 GHz
2.37GHz-2.49GHz **2.4 GHz WLAN**	4.2	Linear along Y direction	-25	Omni directional	HPBW=80⁰ at 2.45 GHz
5.63GHz-5.89GHz **5.8 GHz WLAN**	4.5	Linear along X direction	-19	Omni directional	HPBW=126⁰ at 5.76 GHz

Table A.1 Radiation characteristics of the compact planar multi band antenna

References:

1. Zhizhang Chen, Acep D. Ganjara and Xiaomin Chen, "A dual-L antenna with a novel tuning technique for dual frequency applications," *IEEE. Trans. Antennas. Propagat.*, vol.50, no.3, pp. 402 - 403, 2002.

2. Seok H. Choi, Jong K.Park, Sun K .Kim, and Hak S. Kim, "Design of dual-band antenna for the ISM band using a backed microstrip line," *Microwave. Opt. Technol. Lett.*, vol 41, no. 6, pp.457-460, 2004.

3. Han-Cheol Ryu, Hee-Ran Ahn, Sang-Hwa Lee and Wee Sang Park, "Triple-stacked microstrip antenna for multiband system," *Electron. Lett.*, vol.38, no.24, pp. 1496-1497, 2002.

Automated Planar Near field measurement

The complex boundary conditions to be applied while modelling, discontinuities like open end of waveguides, radiation from the radiating aperture of planar antennas or propagation along a simple microstrip line, increases the computational complexity of the systems when analysed numerically. In view of the approximations taken up in such analysis, an accurate experimental investigation of near filed characteristics could be of great help. An experimental setup is developed indigenously to facilitate planar (2D) near field scanning mechanism incorporating two stepper motors. The scanner assembly provides a spatial coverage of 20 x 20- cm^2 with grid resolution as small as 0.02 x 0.02 mm^2. The experimental procedure outlined here performs the Near field scanning using a field probe mounted on the moving platform of the stepper assembly. The outcome of measurement performed at the open end of a X band rectangular wave guide is presented.

B.1 Introduction

The history of near field measurement dates back to 1950's when Barett and Barnes built an *automatic wave front plotter* to plot the phase and amplitude contours of a 10λ reflector antenna [1]. Near field measurement is advantageous in case where the antenna return loss characteristics may be shadowed by the parasitic or active elements present in the configuration and also in case where placement of antenna and other modules of the system are crucial from EMC point of view.

In 1961 Clayton *et al.* computed the principal far field E plane pattern of reflector antenna of diameter 14λ. They obtained good agreement with the direct far field measurements over the main beam and first few side lobes [1]. Later, better understanding of antenna – antenna interactions paved the way to planar near field measurements with three dimensional probe corrections. Expensive, fully automated and sophisticated near field test facilities are commercially available. They employ Lasers for accurate probe positioning and are backed by efficient post processing tools. A simple set up indigenously developed for automated planar near field measurement is presented here.

B.2 Experimental apparatus

The automated planar near field measurement set up employs an electric probe mounted on a two-dimensional linear translational stage to spatially scan the DUT. The scanner assembly is driven by two stepper motors.

• **Scanner assembly**

The stepper motors in the scanner assembly are unipolar with 1.2A/phase and 12V bias. Both motors have a resolution 7.5°/step (*i.e* ~ 0.02mm/step) and are operated in the full step mode. Photographs illustrating the scanner and the measurement set up is presented as figures B.1-2.

The controller is built around the 28 pin, 8 bit CMOS FLASH microcontroller, Microchip - PIC 16F870. The microcontroller is clocked at 8MHz. The LCD display is connected to port B of the PIC. The control pins RB_{4-7} drive the data lines (D_{4-7}) of the display. Motor A is driven by Port C (RC_{2-5}) and Motor B is interfaced to RC_{0-1}, RA_5 and RB_0 lines. Port C lines RC $_{6-7}$ is used as Tx and Rx lines. The motors are MOSFET driven. Maxim – MAX 232 is used for serial communication with the PC. Additional ball bearings given to the rails of the assembly ensure smooth translational movement.

- **Electric probe**

The *Electric probe* antenna is fabricated by removing the outer conductor and Teflon dielectric of a long semi rigid coaxial cable [2-4]. The length of the stripped section is 2 mm as shown in figure B.3. The dimensions of the probe plate is 8 x 8cm^2. The DUT is mounted on a stationary platform and connected to Port 1 of the S parameter test set while the probe mounted on the moving platform of the stepper assembly is connected to port 2. HP 8510C network analyzer produces and detects microwave energy. The system operates at a transmit power of 10dBm in stepped frequency mode with frequencies spaced between 8 and 12 GHz. The probe assembly is aligned 5mm away from the open end of the X band rectangular wave guide (RWG). The probe is initially moved along the longer edge of the RWG aperture and positioned where the measured field strength is a maxima. A *THRU RESPONSE* calibration is performed in the 8-12GHz band and saved by invoking the *S21 cal* option in the *CremaSoft* command window. Several factors influence the probe performance. These include the probe impedance variation with proximity to DUT, capacitive coupling between probe and the field source and non uniform illumination of the elements that constitute the probe. Recommended distance between probe and DUT is therefore 2-3 times probe dimensions.
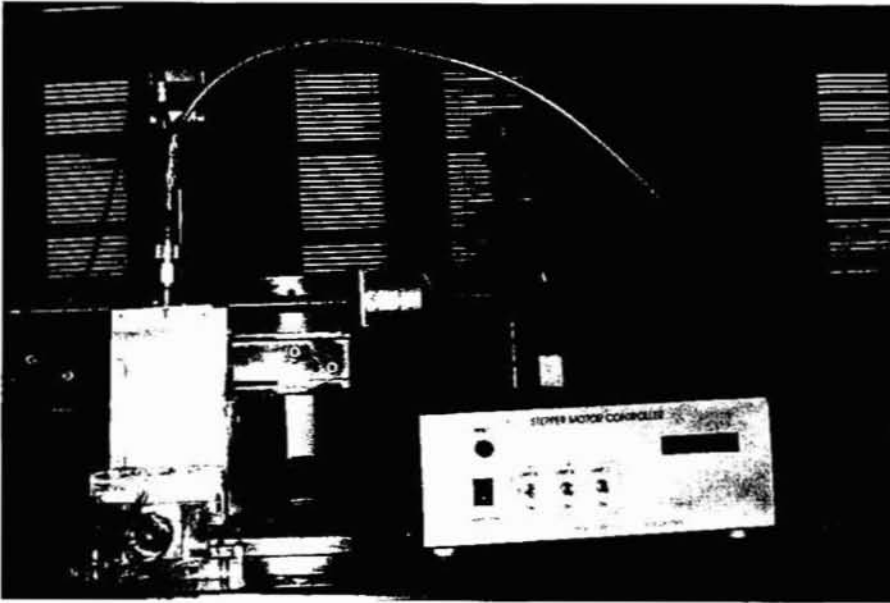
The scanner assembly along with the stepper motor controller
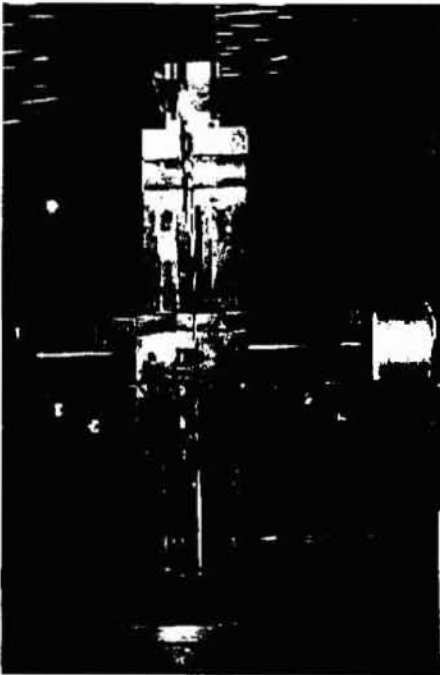
Front view
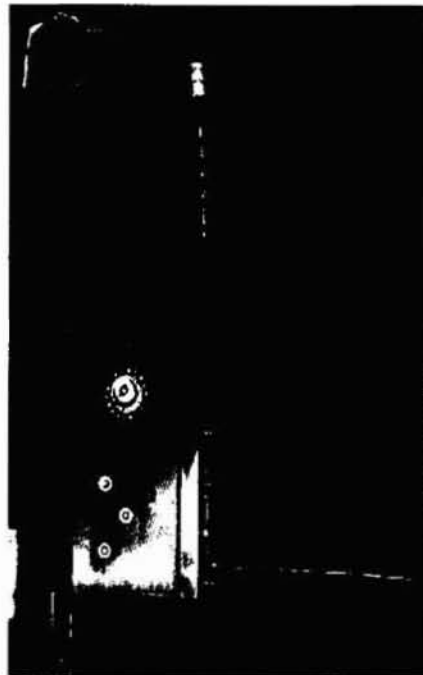
Side view

Figure B.1 Planar Near field scanner
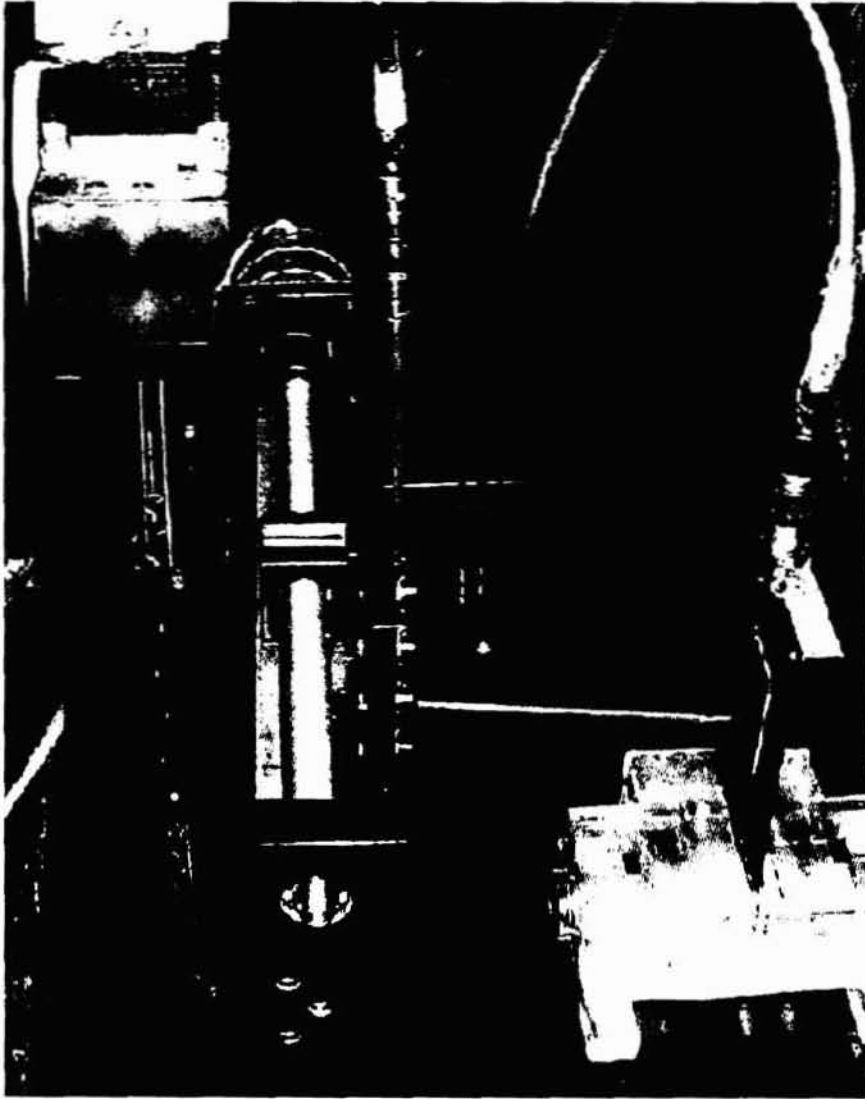
Figure B.2 Set up for planar *Near* field measurement
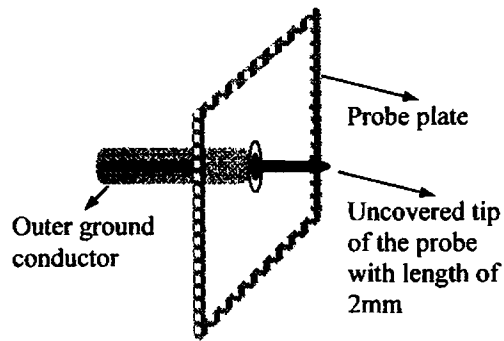
Figure B.3 Electric probe assembly.

- *Crema Soft*

The user friendly software, *CremaSoft* is built in the MATLAB™ environment. The powerful instrument control tool box of the package is used for communicating with the stepper motor control and the Network Analyser (NWA) using the USB/GPIB interface. Figure B.4 shows the *Main measurement window* and figure B.5 shows the *near field measurement window* of *CremaSoft* developed using GUIDE feature of MATLAB.

The computer to stepper motor controller communication is via the serial port for which a *serial object* S is defined in the workspace. The baud rate, parity, number of data bits, no: of stop bits etc are initialized directly from the MATLAB™ environment as.

```
S = serial ('COM1');
set(S,'Baudrate',2400,'Databits',8, 'Parity','none','Stopbits',1,'Terminator','LF');
fopen(S)
```

The communication between the computer and NWA, is established via the USB/GPIB adapter 82357A, from Agilent Technologies, which has a data transfer rate of 750kbps. The communication between source, S parameter test set up and other modules of the analyzer configuration is established through the HPIB bus which supports upto 14 instruments. The following MATLAB code

```
g=gpib('AGILENT',7,16);
```

```
set(g,'InputBufferSize',4096);
set(g,'Timeout',1000);
fopen(g)
```

initializes NWA as an object module with name *g*. All subsequent commands are sent to this object using *fprintf*. The following set of commands reads the Start frequency, Stop frequency and *no of frequency sampling points* option set in the NWA for S21 measurement.

```
fprintf(g,'S21')
pause (.1)
fprintf(g,'STAR;OUTPACTI;');
startf =str2num(fscanf(g));
fprintf(g,'STOP;OUTPACTI;');
stopf =str2num(fscanf(g));
fprintf(g,'POIN;OUTPACTI;');
pts=str2num(fscanf(g));
```

Finally the *fscanf* command allows to fetch the measured data from the NWA to the MATLAB workspace which is then processed and stored appropriately.

```
fprintf(g,'FORM4;OUTPDATA;')
a =fscanf(g);
b=str2num(a);
```

The probe is moved from *xmin* to *xmax* in the horizontal direction and from *ymin to ymax* in the vertical direction at the specified spatial increments by issuing necessary commands to the PIC controlled stepper assembly. It is positioned accurately at each grid point in scan area and the S21 data is acquired. The probe traces a scan path as illustrated in figure B.6, covering the RWG aperture along locus A-D. For traversing locus A and B, the stepper A of the assembly is moved forward and reverse respectively using the commands

```
fprintf(S,'mAfd,%f',step);  %Stepper A forward
fprintf(S,'mArv,%f',step); % Stepper a reverse
```

Figure B.4 *CremaSoft* main window
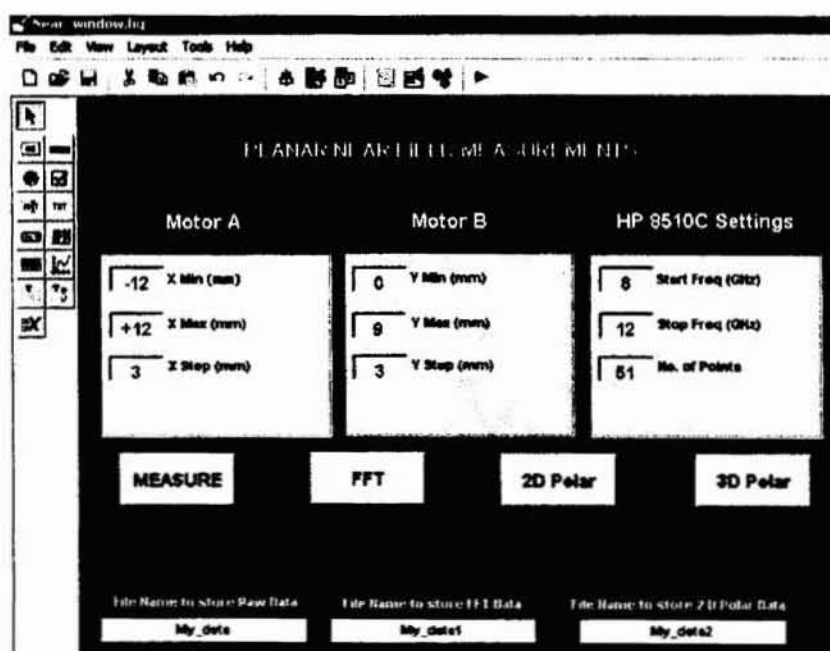
Figure B.5 Near field window

At each forward/reverse step data is acquired and stored. The vertical downward movement from locus A to locus B is performed by rotating motor B of the assembly in reverse direction by issuing the command,

          fprintf(S,'mBrv,%f',step);

The saved data is suitably processed to display the field strengths about the aperture. From the measured near field data, far field pattern is computed using suitable far field transformations.
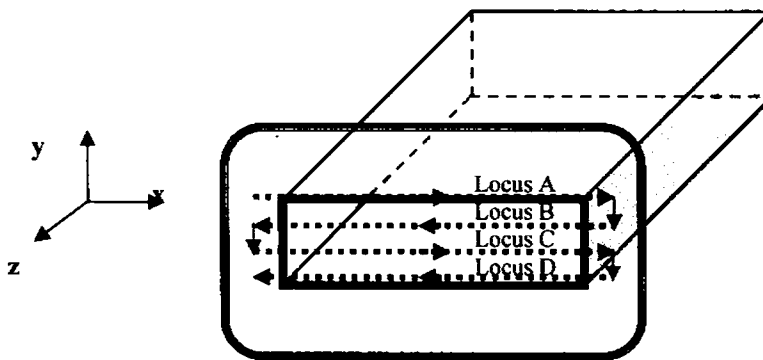
Figure B.6 The loci traversed by the *near* field probe scanning the open end of RWG.

B.3   Measured near field and computed far field data of RWG

The S21 data acquired by scanning the open end of the X band rectangular waveguide for a coarse grid size of 3mm x 3mm (~ $\lambda/10$ x $\lambda/10$ at the centre frequency of the band) is plotted as figure B.7. The measured values in dB are normalised and plotted in comparison with the theoretical TE_{10} mode distribution of the RWG, for different frequencies in the X band, namely 8.5GHz, 10GHz and 11.5GHz. It is observed from the figure that the simple set up reveals the near field behaviour of the DUT with reasonably good accuracy. The field distribution in the aperture is observed to vary slightly with respect to frequency within the X band. The normalized radiation patterns at different frequencies computed from these observations is illustrated as figure B.8. The side lobe level and beam width varies with frequency as expected from the observed near field variations.
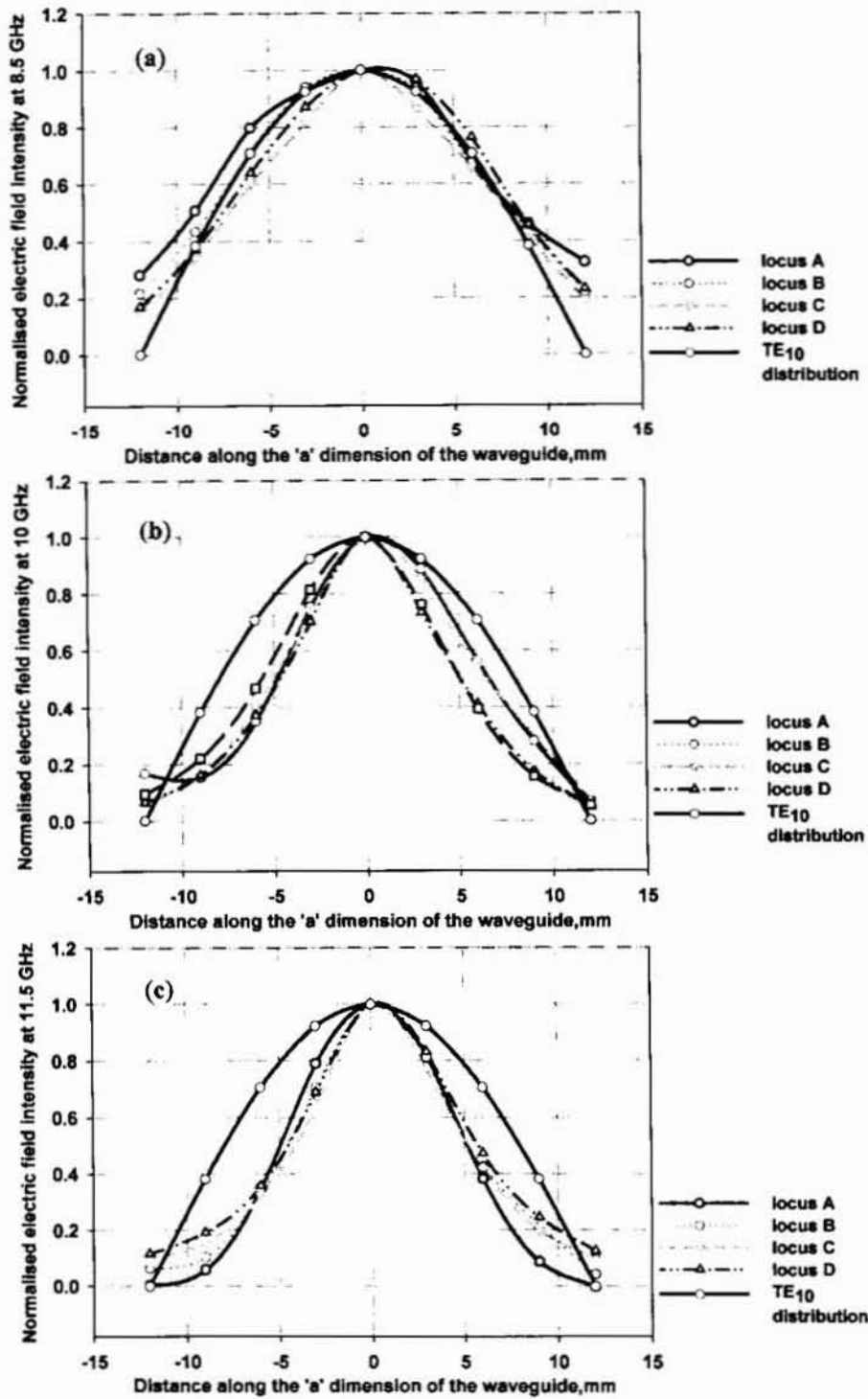
Figure B.7 Measured S21 data along the different loci in the open end of X band RWG
(The values are normalized wrt maxima for each locus, for each frequency)
(a) 8.5GHz(b) 10GHz(c)11.5GHz
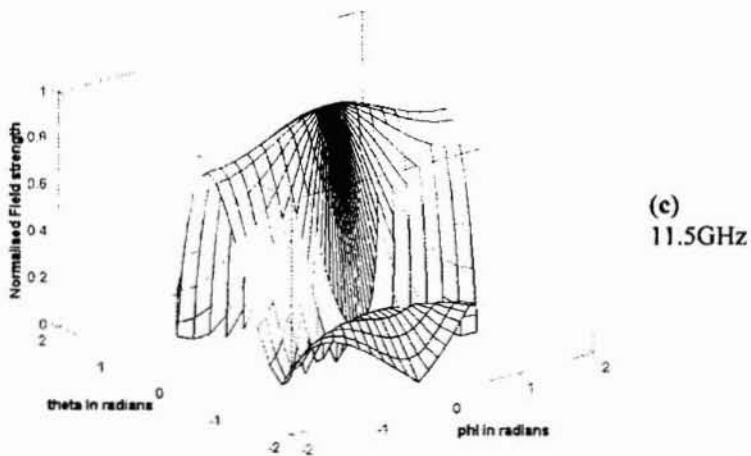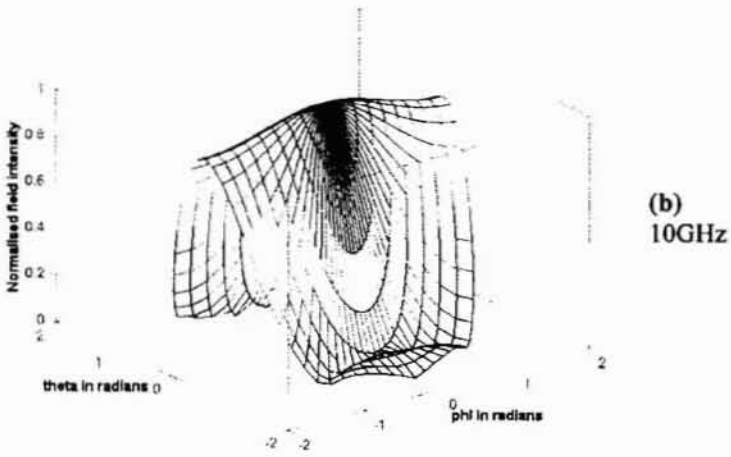
Figure B.8 Far field patterns computed from the measured near filed data of X band
RWG, for different frequencies
(a) 8.5GHz(b) 10GHz(c)11.5GHz

B.4 Conclusions

The set up measures the near field with reasonably good accuracy. The finite size and near field distance of the measurement probe must be considered and appropriate correction factors are to be applied to refine the procedure. The computed far field patterns reveal the radiation characteristics of the DUT. The stepper assembly gives a very fine spatial resolution of 20μm. The method is useful in studying non-reciprocal antennas that must be measured in the transmitting mode and hence may be inconvenient to perform the far field measurement. Increasing the scan area beyond the aperture can reduce the errors introduced [5] into the far field patterns at larger angles from the boresight.

References:

1. A.D.Yaghjian, "An overview of near field antenna measurements," *IEEE. Trans. Antennas. Propagat.*, vol.34, no.1, pp. 30 - 46, 1986.
2. S.A.Bokhari, J.F.Zuricher, J.R.Mosig and F.E.Gardiol, "Near fields of microstrip antennas," *IEEE. Trans. Antennas. Propagat.*, vol.43, no.2, pp. 188-197, 1995.
3. J.S.Dahele and A.L.Cullen, "Electric probe measurements on microstrip," *IEEE Trans. Microwave Theory Tech.*, vol. MTT-28(7), pp. 752-755, July 1980.
4. Jacob George, "Development and analysis of a drum shaped compact microstrip antenna," Ph.D thesis, Cochin University of Science and Technology, July 1998.
5. A.D.Yaghjian, "Antenna coupling and near field sampling in plane polar coordinates," *IEEE. Trans. Antennas. Propagat.*, vol.40, no.3, pp. 304-312, 1992.

International Journal

1. **Binu Paul**, S. Mridula, C.K.Aanandan and P.Mohanan, "A new Microstrip Patch Antenna for Mobile Communications and Bluetooth applications," **Microwave and Optical Technology letters**, Vol.33, No.4, pp. 285 – 286, May 20 2002.

2. S.Mridula, Sreedevi.K.Menon, B.Lethakumary, **Binu Paul**, C.K.Aanandan and P.Mohanan, "Planar L–Strip fed broadband Microstrip Antenna," **Microwave and Optical Technology letters**, Vol. 34, No.2, pp.115-117, July 20 2002.

3. **Binu Paul**, S.Mridula, P.Mohanan, P.V.Bijumon and M.T.Sebastian, "A compact very-high-permittivity Dielectric-eye Resonator Antenna for multiband wireless applications," **Microwave and Optical Technology letters**, Vol. 43, No.2, pp.118-121, October 20 2004.

4. Rohith.K.Raj, Manoj Joseph, **Binu Paul** and P.Mohanan, "Compact planar multiband antenna for GPS,DCS,2.4/5.8GHz WLAN applications," **IEE Electronics Letters**, Vol. 41, No.6, pp.290-291, 17th March 2005.

International Conference

1. **Binu Paul**, Jacob George, C.K.Aanandan, P.Mohanan, K.G.Nair, H.Sreemoolanadhan and M.T.Sebastian, "Investigations on the bandwidth enhancement effect of dielectric resonator loaded microstrip antenna", Proc. **Asia-Pacific Microwave conference, APMC(1996), New Delhi,** December 17-20 1996.

2. S.Mridula, **Binu Paul**, C.K.Aanandan and P.Mohanan, "Octagon Shaped Microstrip Patch Antenna for dual band applications," Proc. **IEEE Antennas and Propagation Society International Symposium, Texas,** July 2002.

3. S.Mridula, Sreedevi.K.Menon, **Binu Paul**, C.K.Aanandan K.Vasudevan, P.Mohanan P.V.Bijumon and M.T.Sebastian, "Experimental investigations on a Microstrip fed compact Rectangular Dielectric Resonator Antenna," Proc. **International Conference on Computers and Devices for Communication (CODEC–04), Institute of Radio Physics and Electronics, University of Calcutta,** January 1-3 2004.

4. **Binu Paul**, S.Mridula, Sreedevi.K.Menon, C.K.Aanandan, P.Mohanan, P.V.Bijumon and M.T.Sebastian, "Time Domain Analysis of a Microstrip Line excited compact Rectangular Dielectric Resonator Antenna," Proc. **20th Annual Review of Progress in Applied Computational Electromagnetics (ACES-04), Syracuse, New York,** April 19-23 2004.

5. S. Mridula, **Binu Paul**, Sreedevi.K.Menon, C.K.Aanandan, P.Mohanan, P.V.Bijumon and M.T.Sebastian "Wideband Rectangular Dielectric Resonator Antenna for W-LAN applications," Proc. **IEEE Antennas and Propagation Society International Symposium, Monterey,** July 2004.

6. **Binu Paul**, S.Mridula, C.K.Aanandan, K.Vasudevan and P.Mohanan, "Electromagnetically Coupled Dual Port, Dual Band, Octagonal Patch Antenna," Proc. **IEEE International conference on Personal Wireless Communication (ICPWC 2005), New Delhi,** January 23-25 2005. [Paper presented]

7. Manoj Joseph, Rohith.K.Raj, **Binu Paul** and P.Mohanan "Compact planar multiband antenna," Proc. **IEEE Antennas and Propagation Society International Symposium, Washington DC,** July 3-8, 2005.

8. S.Mridula, **Binu Paul**, K.Vasudevan P.Mohanan, P.V.Bijumon and M.T.Sebastian, "Rectangular Dielectric Resonator Antenna configurations for Mobile Communication applications," accepted for

poster presentation at **XXVIII**[th] **URSI GA 2005, New Delhi**, October 2005.

9. **Binu Paul**, S.Mridula, C.K.Aanandan, K.Vasudevan and P.Mohanan, "Octagonal Microstrip Patch Antenna for dual band applications," accepted for poster presentation at **XXVIII**[th] **URSI GA 2005, New Delhi**, October 2005.

National Conference

1. I.Shyju Mon, **Binu Paul**, S.Mridula, C.K.Aanandan, K.Vasudevan and P.Mohanan, "Rectangular Microstrip Antenna for Mobile Communications and Bluetooth Applications," Proc. **National Conference on Microwaves, Antennas and Propagation (MICROWAVE 2001), Jaipur,** pp. 24-26, November 2-4 2001.

2. S.Mridula, **Binu Paul**, I.Shyju Mon, C.K.Aanandan and P.Mohanan, "Dual Polarized Electromagnetically coupled Microstrip Antenna," Proc. **National Conference on Microwaves, Antennas and Propagation (MICROWAVE 2001), Jaipur,** pp. 145- 147, November 2-4 2001.

3. S.Mridula, **Binu Paul**, C.K.Aanandan, K.Vasudevan and P.Mohanan, "Dual Band Octagonal Patch Antenna suitable for PCS and Bluetooth Applications," Proc. **Interactive Integrated Technological Advancement-Recent Trends (IITART), College of Engineering, Trivandrum,** pp. 88-95, July 5-6 2002.

4. **Binu Paul**, S.Mridula, C.K.Aanandan and P.Mohanan, "Dual Band Octagonal Patch Antenna," Proc. **National Symposium on Antennas and Propagation (APSYM 2002), Cochin,** pp. 245-248, December 9-11 2002.

   [Paper presented]

5. **Binu Paul**, S.Mridula, C.K.Aanandan, K.Vasudevan and P.Mohanan, "Time domain analysis of Octagonal Microstrip Patch Antenna by

conformal FDTD method," Proc. **National Symposium on Antennas and Propagation (APSYM 2004), Cochin,** pp. 117–121, December 21-23 2004.

[Paper presented]

6. S.Mridula, **Binu Paul,** C.K.Aanandan, H.Sreemoolanadhan, V.Chandrasekaran and P.Mohanan, "Rectangular Dielectric Resonator Antenna for 2.4 GHz W-LAN Applications," Proc. **National Symposium on Antennas and Propagation (APSYM 2004), Cochin,** pp. 215–218, December 21-23 2004.

7. Manoj Joseph, Rohith.K.Raj, **Binu Paul,** K.Vasudevan, C.K.Aanandan, P.Mohanan and K.G.Nair, "Compact Wide band antenna for BLUETOOTH™ applications," Proc. **National Symposium on Antennas and Propagation (APSYM 2004), Cochin,** pp. 64–67, December 21-23 2004.

Citation – International Journal

➢ Remarks on the paper:

Binu Paul, S. Mridula, C.K.Aanandan and P.Mohanan, "A new Microstrip Patch Antenna for Mobile Communications and Bluetooth Applications," **Microwave and Optical Technology letters,** Vol.33, No.4, pp. 285-286, May 20 2002.

Microwaves and RF, R&D round up column, pp. 54, August 2002.

➢ Reference to the paper:

S. Mridula, **Binu Paul,** Sreedevi.K.Menon, C.K.Aanandan, P.Mohanan, P.V.Bijumon and M.T.Sebastian "Wideband Rectangular Dielectric Resonator Antenna for W-LAN applications," Proc. IEEE **Antennas and Propagation Society International Symposium, Monterey,** July 2004 in the paper entitled

"Strip fed Rectangular Dielectric Resonator Antennas with/ without a parasitic patch", *IEEE Trans. Antennas Propagat.,* vol.AP-53,no:7,pp. 2200-2207,authored by Bin Li and Kwok Wa Lueng.

➢ Reference to the paper

Binu Paul, S. Mridula, C.K.Aanandan and P.Mohanan, "A new Microstrip Patch Antenna for Mobile Communications and Bluetooth Applications," **Microwave and Optical Technology letters,** Vol.33, No.4, pp. 285-286, May 20 2002 in the paper entitled

"A new compact printed antenna with coplanar configuration," Proc. **IEEE Antennas and Propagation Society International Symposium, Washington DC,** July 3-8, 2005, authored by Rohith.K.Raj, Manoj Joseph, C.K.Aanandan, K.Vasudevan and P.Mohanan.

BINU PAUL

Research Scholar

CREMA, Department of Electronics

Cochin University of Science and Technology

Kochi – 682 022, INDIA

Phone: 91-484-2576418

E-mail: binupaul@cusat.ac.in

Objective:

> *To pursue research activities in the field of multi band mobile communication antennas and electromagnetic computation.*

Education:

M.Tech Electronics

Specialization: Microwave and Radar Electronics

Cochin University of Science and Technology (1996)

Score: 79% - First class

B. Tech Electronics

Model Engineering College, Thrikkakara

Cochin University of Science and Technology (1993)

Score: 82% - First class with Distinction and Second Rank

Research Experience:

Worked as project associate in the Malaysian consultancy project entitled, "Antenna Design, Fabrication and Testing for a pseudo random polarization hopping communication system" from July 2003 to January 2005.

Participation in Conferences:

Participated and presented research papers at 4 National conferences and at the "**IEEE International conference on Personal Wireless Communication (ICPWC 2005),** " held at New Delhi during January 23-25 2005.

Publications:

International Journal   : 4

International Conference   : 9

National Conference   : 7

Citation:

➢ Remarks on the paper

   Binu Paul, S. Mridula, C.K.Aanandan and P.Mohanan, "A new Microstrip Patch Antenna for Mobile Communications and Bluetooth Applications," **Microwave and Optical Technology letters,** Vol.33, No.4, pp. 285-286, May 20 2002.

   Microwaves and RF, R&D round up column, pp. 54, August 2002.

➢ Reference to the paper

   S. Mridula, **Binu Paul**, Sreedevi.K.Menon, C.K.Aanandan, P.Mohanan, P.V.Bijumon and M.T.Sebastian "Wideband Rectangular Dielectric Resonator Antenna for W-LAN applications," Proc. **IEEE Antennas and Propagation Society International Symposium, Monterey,** July 2004 in the paper entitled

   "Strip fed Rectangular Dielectric Resonator Antennas with/ without a parasitic patch", *IEEE Trans. Antennas Propagat.,* vol.AP-53, no:7,pp. 2200-2207,authored by Bin Li and Kwok Wa Lueng.

➢ Reference to the paper

   Binu Paul, S. Mridula, C.K.Aanandan and P.Mohanan, "A new Microstrip Patch Antenna for Mobile Communications and Bluetooth Applications," **Microwave and Optical Technology letters,** Vol.33, No.4, pp. 285-286, May 20 2002 in the paper entitled

"A new compact printed antenna with coplanar configuration," Proc. **IEEE Antennas and Propagation Society International Symposium, Washington DC,** July 3-8, 2005, authored by Rohith.K.Raj, Manoj Joseph, C.K.Aanandan, K.Vasudevan and P.Mohanan.

Computer Proficiency:

Assembly level programming, C, MATLAB

Simulation Software: IE3D, Fidelity, Microwave Office, Microstripes

Work experience:

10+ years teaching experience

➢ Lecturer in Electronics (December 1994 – January.1999)

(at College of Engineering, Chengannur and Model Engineering College, Thrikkakara)

Institute of Human Resource Development (IHRD)

Govt. of Kerala

➢ Lecturer in Electronics (January.1999 onwards)

Division of Electronics and Communication Engineering

School of Engineering

Cochin University of Science and Technology, Kochi – 682 022

Member- Indian Society for Technical Education (ISTE)

Index

G9075